

Micromechanical properties of inorganic multiphase materials

A dissertation submitted to partial fulfillment of the requirements for the degree of Doctor of Philosophy by

Hossein Besharatloo

Department of Materials Science and Engineering
Doctorate program in Materials Science and Engineering
Universitat Politècnica de Catalunya – BarcelonaTech

Advisors: Prof. Luis Miguel Llanes Pitarch
Prof. Joan Josep Roa Rovira



UNIVERSITAT POLITÈCNICA DE CATALUNYA
BARCELONATECH

Departament de Ciència i Enginyeria
dels Materials

Barcelona, Spain

January 2021



UNIVERSITAT POLITÈCNICA
DE CATALUNYA
BARCELONATECH

Micromechanical properties of inorganic multiphase materials

Hossein Besharatloo

ADVERTIMENT La consulta d'aquesta tesi queda condicionada a l'acceptació de les següents condicions d'ús: La difusió d'aquesta tesi per mitjà del repositori institucional UPLCommons (<http://upcommons.upc.edu/tesis>) i el repositori cooperatiu TDX (<http://www.tdx.cat/>) ha estat autoritzada pels titulars dels drets de propietat intel·lectual **únicament per a usos privats** emmarcats en activitats d'investigació i docència. No s'autoritza la seva reproducció amb finalitats de lucre ni la seva difusió i posada a disposició des d'un lloc aliè al servei UPLCommons o TDX. No s'autoritza la presentació del seu contingut en una finestra o marc aliè a UPLCommons (*framing*). Aquesta reserva de drets afecta tant al resum de presentació de la tesi com als seus continguts. En la utilització o cita de parts de la tesi és obligat indicar el nom de la persona autora.

ADVERTENCIA La consulta de esta tesis queda condicionada a la aceptación de las siguientes condiciones de uso: La difusión de esta tesis por medio del repositorio institucional UPLCommons (<http://upcommons.upc.edu/tesis>) y el repositorio cooperativo TDR (<http://www.tdx.cat/?locale-attribute=es>) ha sido autorizada por los titulares de los derechos de propiedad intelectual **únicamente para usos privados enmarcados** en actividades de investigación y docencia. No se autoriza su reproducción con finalidades de lucro ni su difusión y puesta a disposición desde un sitio ajeno al servicio UPLCommons. No se autoriza la presentación de su contenido en una ventana o marco ajeno a UPLCommons (*framing*). Esta reserva de derechos afecta tanto al resumen de presentación de la tesis como a sus contenidos. En la utilización o cita de partes de la tesis es obligado indicar el nombre de la persona autora.

WARNING On having consulted this thesis you're accepting the following use conditions: Spreading this thesis by the institutional repository UPLCommons (<http://upcommons.upc.edu/tesis>) and the cooperative repository TDX (<http://www.tdx.cat/?locale-attribute=en>) has been authorized by the titular of the intellectual property rights **only for private uses** placed in investigation and teaching activities. Reproduction with lucrative aims is not authorized neither its spreading nor availability from a site foreign to the UPLCommons service. Introducing its content in a window or frame foreign to the UPLCommons service is not authorized (*framing*). These rights affect to the presentation summary of the thesis as well as to its contents. In the using or citation of parts of the thesis it's obliged to indicate the name of the author.

Cover photo: H/E map of duplex stainless steel plotted from data attained by means of massive nanoindentation techniques.

“What we know is a drop, what we do not know is an ocean.”

-Sir Isaac Newton

تقدیم به حضرت مولانا، او که مرا راه زندگی و عشق آموخت.

تا در هوس لقمه ی نانی نانی
هر چیز که در جستن آنی آنی

مولانای جان

تا در طلب گوهر کانی کانی
این نکته ی رمز اگر بدانی دانی

Dedicated to his majesty Rumi, who shed the light on my path through life and love.

“What you seek is seeking you.”

-Rumi

Preface

This dissertation is an original intellectual product of the author and ultimately based on the research work conducted by the author. It is submitted for the degree of Doctor of Philosophy in Materials Science and Engineering at the Universitat Politècnica de Catalunya - BarcelonaTech. The research described herein was directed under the supervision of Professors Luis Miguel Llanes Pitarch and Joan Josep Roa Rovira between February 2016 and March 2021. The experimental works were mainly carried out within the Centre d'Integritat Estructural, Micromecànica i Fiabilitat dels Materials (CIEFMA) group from the Departament de Ciència i Enginyeria de Materials (CEM) of the Universitat Politècnica de Catalunya (UPC) and the Laboratory for Nanometallurgy from the Department of Materials of ETH Zürich. The presented work is original unless otherwise detailed references are provided.

This Ph.D. dissertation is presented as a compendium of published articles and is formed of six chapters, which are described hereafter. *Chapter 1* provides a general introduction of studied composite systems as well as descriptions of the main microstructural parameters and mechanical properties. *Chapter 2* presents the aim and objectives of the work. *Chapter 3* includes detailed information such as constitutive elements and production processing routes of the studied materials. Moreover, techniques for microstructural characterization and evaluation of mechanical properties are described in this chapter. Published scientific articles, in which the first author is H. Besharatloo, are included in *Chapter 4*. The obtained results, focusing on the main idea behind the thesis, are provided in *Chapter 5*. Finally, general conclusions and the future outlook of this Ph.D. thesis are summarized in *Chapter 6*.

Abstract

Multiphase systems include a wide variety of engineering materials that are extensively used in industrial applications owing to their structures. They may be described as composites whose microstructure consists of different phases with distinct mechanical properties. Accordingly, the mechanical behavior of these materials is dictated by the intrinsic response of each constitutive phase as well as the fashion in which they interact with each other. Therefore, an accurate and detailed assessment of both microstructural characteristics and small-scale mechanical properties becomes key for understanding the macroscopic behavior of these materials. Obtaining this knowledge means predicting the macroscopic response of a multiphase system from the behavior exhibited by its constitutive phases, which leads to optimize its microstructural design.

Within the above context, the current study is intended to offer a systematic investigation, aiming to assess small-scale mechanical properties of multiphase materials through a protocol based on massive nanoindentation and statistical analysis. It consists of three sequential stages: *(i) microstructural characterization, (ii) micromechanical evaluation (massive indentation and statistical analysis), and (iii) correlation between microstructure and mechanical properties using advanced characterization techniques.*

Microstructural characterization of studied systems was carried out through extensive and detailed field emission scanning electron microscopy analysis. This is an essential step for determining testing parameters to be used when implementing massive indentation, particularly penetration depth of performed imprints; and consequently, corresponding applied load and proper space between indentations (grid spacing). Based on the acquired information, massive indentation testing and statistical analysis of experimentally gathered data were implemented. Main outcome of this second step was to determine the local properties of several unidentified phases. Such data analysis was then complemented by the use of different advanced characterization techniques for deeper inspection of microstructural features. Main goal of this final step was to define the unidentified mechanically distinct phases, on the basis of physically-based correlations between microstructure features and small-scale properties.

The proposed and described protocol has been implemented on three different materials: Duplex Stainless Steels (DSS), Polycrystalline cubic Boron Nitride (PcBN) composites and Ti(C,N)-FeNi cermets. They are representative of metal-metal, ceramic-ceramic, and ceramic-metal systems, respectively.

This Ph.D. thesis is presented as a compendium of scientific publications in which several specific objectives are studied, using the proposed testing protocol, for each multiphase system. Regarding the metal-metal system, the influence of the processing route on the local mechanical properties (hardness and elastic modulus) of austenitic and ferritic phases of a DSS was successfully evaluated in the first article. It was found that cold work effects on the small-scale properties of both austenite and ferrite phases were more pronounced than those promoted by the other processing routes studied. Moreover, a novel *2D* histogram of hardness and elastic modulus was introduced and validated as a suitable and effective tool to correlate microstructure and intrinsic mechanical properties of the constitutive phases of DSSs.

The second article was devoted to extracting the small-scale mechanical properties of a PcBN composite. The superhard material consists of cBN ceramic particles embedded within a TiN binder. Moreover, the correlation of relative B/N ratio and local hardness for individual cBN particles was studied and understood, through complementary analysis by means of electron probe X-ray microanalysis of the data attained using the proposed testing protocol. In doing so, five mechanically distinct phases were defined, based on chemical nature, TiN/cBN interface presence, and phase stoichiometry. It was discerned that the hardness of cBN had a direct relationship with the N amount presented in each cBN particle.

The influence of ceramic/metal phase ratio and carbon addition on the local mechanical properties of Ti(C,N)–FeNi cermets have been assessed in the third and fourth articles. It was derived that both composite hardness and elastic modulus of cermets are inversely related to the ceramic/metal phase ratio. Furthermore, carbon addition was found to exhibit a direct relationship with hardness and elastic modulus of the studied cermets. Regarding the small-scale properties of the constitutive phases, the intrinsic hardness of both Ti(C,N) particles and FeNi metallic binder were determined using massive nanoindentation and statistical analysis. In doing so, a thin-film model was used as a complementary analysis step to assess the effective hardness of the constrained metallic binder. Additionally, toughening action of FeNi binder in the studied Ti(C,N)-based cermets was evidenced by studying deformation, damage, and fracture mechanisms evidenced in resulting imprints.

As a general conclusion, it has been proven that the proposed methodology can be considered as a successful testing protocol for determining small-scale mechanical properties (hardness and elastic modulus) of the studied multiphase systems. Nevertheless, successful implementation requires careful consideration of testing parameters used, on the basis of microstructural, residual imprint, and plastic flow length scales.

Resumen

Los sistemas multifásicos incluyen un abánico amplio de materiales utilizados en una gran variedad de aplicaciones industriales. En términos de ciencia e ingeniería de los materiales, ellos pueden ser descritos como composites cuya microestructura consta de fases diferentes con propiedades mecánicas distintas. En consecuencia, la respuesta intrínseca de cada fase constitutiva, así como la forma en que ellas interactúan entre sí, dictan el comportamiento mecánico de estos materiales. Por lo tanto, una evaluación precisa y detallada tanto de las características microestructurales como de las propiedades mecánicas a pequeña escala emerge como una acción crítica para comprender el comportamiento macroscópico de estos materiales. La adquisición de este conocimiento significa poder predecir la respuesta macroscópica de un sistema multifásico a partir del comportamiento intrínseco de las fases constitutivas; y con ello, finalmente optimizar el diseño microestructural de estos materiales.

En el contexto descrito previamente, se propone realizar una investigación sistemática con el objetivo de evaluar las propiedades mecánicas a pequeña escala de diferentes materiales multifásicos a través de un protocolo que se basa en la implementación de técnicas de nanoindentación masiva y, a continuación, el análisis estadístico de los datos experimentales obtenidos. Esta metodología consta de tres etapas secuenciales: (i) caracterización microestructural, (ii) evaluación micromecánica (indentación masiva y análisis estadístico), y (iii) correlación entre microestructura y propiedades mecánicas mediante técnicas avanzadas de caracterización complementarias.

La caracterización microestructural de los sistemas estudiados se llevó a cabo a través de una inspección extensa y detallada mediante microscopía electrónica de barrido. Este es un paso esencial para determinar los parámetros de ensayo que se utilizarán al implementar técnicas de nanoindentación masiva, particularmente la profundidad de penetración de las impresiones a realizar; y, en consecuencia, la carga que se debe aplicar y el espaciamiento adecuado que debe existir entre las huellas. Teniendo en cuenta la información obtenida, se realizaron entonces los ensayos de nanoindentación masiva, y acto seguido, el análisis estadístico de los datos experimentales recopilados. El resultado principal de este segundo paso fue determinar las propiedades locales de varias fases no identificadas individualmente. Este análisis de datos se complementó con el empleo de diferentes técnicas de caracterización avanzadas que permitieron una inspección en mayor detalle de las características microestructurales. El objetivo principal de este estadio final fue definir las fases mecánicamente distintas y no identificadas, teniendo en

consideración correlaciones físicas entre las características microestructurales y las propiedades a pequeña escala determinadas.

El protocolo propuesto y descrito se implementó en tres materiales diferentes: aceros inoxidable dúplex (DSS), compuestos basados en partículas de nitruro de boro cúbico (PcBN) y cermets del tipo Ti(C,N)-FeNi. Estos materiales representan ejemplos idóneos de sistemas multifásicos metal-metal, cerámica-cerámica y cerámica-metal, respectivamente.

Esta tesis doctoral se presenta como un compendio de publicaciones científicas en las que se abordan varios objetivos específicos, utilizando el protocolo de ensayo y análisis propuesto, para cada sistema multifásico. En cuanto al sistema metal-metal, en el primer artículo se evaluó satisfactoriamente la influencia de la ruta de procesamiento en las propiedades mecánicas a pequeña escala (dureza y módulo elástico) de las fases austenítica y ferrítica de un DSS. Los resultados obtenidos permiten concluir que los efectos de la deformación en frío sobre las propiedades a nivel local de las fases austenítica y ferrítica son más pronunciados que los inducidos por las otras rutas de procesamiento investigadas. Adicionalmente, en esta parte del trabajo se introduce y valida un nuevo histograma 2D de dureza y módulo de elasticidad como una herramienta adecuada y eficaz para correlacionar la microestructura y las propiedades mecánicas intrínsecas de las fases constitutivas de los DSS.

La segunda publicación se centró en la extracción de las propiedades mecánicas a pequeña escala de un composite de PcBN. Este material de extremada dureza consiste en partículas cerámicas de cBN inmersas en una fase aglutinante de TiN. En este artículo también se evaluó y comprendió la correlación entre el cociente B/N y la dureza local de partículas de cBN individuales, complementando el estudio mediante microanálisis de rayos X con sonda electrónica. Para ello, se definieron cinco fases mecánicamente distintas, teniendo en cuenta factores diversos tales como la naturaleza química, la presencia de interfaces TiN/cBN y la estequiometría (relación cuantitativa entre los contenidos de B y N) de las partículas de cBN. Los resultados obtenidos permitieron concluir que existe una relación directa entre la dureza del cBN y la cantidad de N presente en cada partícula de esta fase cerámica.

La influencia de la cantidad relativa de fases (cerámica y metal) y la adición de carbono sobre las propiedades mecánicas locales de cermets de Ti(C,N)-FeNi se estudiaron en el tercer y cuarto artículo. A través de estos trabajos se evidenció que tanto la dureza como el módulo elástico de los cermets se relacionan de forma inversamente proporcional al cociente metal/cerámica correspondiente a la proporción relativa de las fases presentes. Asimismo, se llegó a la conclusión que la adición de carbono resulta en un incremento tanto de la dureza como del módulo elástico de los cermets estudiados. Con respecto a las propiedades a pequeña escala de las fases constitutivas, se determinó la dureza intrínseca tanto de las partículas de Ti(C,N) como del aglutinante metálico FeNi, mediante nanoindentación masiva y el posterior análisis estadístico de

los datos experimentales obtenidos. En este sistema, y para el caso particular de la evaluación de la dureza efectiva de la fase metálica, se utilizó un modelo de película delgada como herramienta de análisis complementaria. Adicionalmente, el estudio de los mecanismos de deformación, daño y fractura en los cermets investigados permitió evidenciar el endurecimiento de la fase ligante de FeNi, asociado directamente al constreñimiento ejercido por las partículas cerámicas adyacentes.

En términos generales, el estudio realizado y los resultados obtenidos permiten concluir que la metodología propuesta se ha implementado y validado con éxito como protocolo de ensayo para la determinación de propiedades mecánicas a pequeña escala (dureza y módulo elástico) de los sistemas multifásicos investigados. En este contexto, se debe indicar que la implementación satisfactoria de esta metodología requiere una consideración minuciosa de los parámetros de ensayo utilizados, en particular en lo que refiere a la relación entre las escalas dimensionales representativas de la plasticidad y las huellas residuales inducidas con respecto a las características microestructurales del material bajo estudio.

Resum

Els sistemes multifàsics inclouen un ampli ventall de materials emprats en una gran varietat d'aplicacions industrials. En termes de ciència i enginyeria dels materials, aquests sistemes poden ser descrits com materials compostos amb una microestructura i propietats mecàniques diferents per cadascuna de les fases. Com a conseqüència, la resposta intrínseca de cada constituent, així com la forma en què interactuen, dicten el comportament mecànic d'aquests materials. Per tant, una avaluació precisa i detallada de les característiques microestructurals i de les propietats mecàniques a petita escala emergeix com una acció crítica per comprendre el comportament macroscòpic d'aquests materials. L'adquisició d'aquest coneixement significa poder predir la resposta macroscòpica d'un sistema multifàsic a partir del comportament intrínsec de cadascun dels constituents; i amb això, finalment optimitzar el disseny microestructural d'aquests materials.

En aquest context descrit prèviament, es proposa realitzar una investigació sistemàtica amb l'objectiu d'avaluar les propietats mecàniques a petita escala de diferents materials multifàsics a través d'un protocol que es basa en la implementació de tècniques de nanoindentació massiva i, a continuació, l'anàlisi estadístic a partir de les dades experimentals obtingudes. Aquesta metodologia consta de tres etapes seqüencials: (i) caracterització microestructural, (ii) avaluació micromecànica (indentació massiva i anàlisi estadístic), i (iii) correlació entre microestructura i propietats mecàniques mitjançant tècniques avançades de caracterització complementaries.

La caracterització microestructural dels sistemes estudiats es va portar a terme a través d'una inspecció extreta i detallada mitjançant microscòpia electrònica d'escombrat. Aquest és un pas essencial per determinar els paràmetres d'assaig que s'utilitzaran per implementar tècniques de nanoindentació massiva, particularment la profunditat de penetració de les impressions a realitzar; i en conseqüència, la càrrega que s'ha d'aplicar i l'espaiat adequat que ha d'existir entre les empremtes. Tenint en compte la informació obtinguda, es van realitzar els assajos de nanoindentació massiva, i tot seguit, l'anàlisi estadístic de les dades experimentals recopilades. El resultat principal d'aquest segon pas, va ser determinar les propietats locals de diferents fases no identificades individualment. Aquests anàlisis de dades es va complementar utilitzant diferents tècniques de caracterització avançada que van permetre una inspecció amb major detall de les característiques microestructurals. L'objectiu principal d'aquest estudi final va ser definir les diferents fases mecànicament no identificades, tenint en consideració correlacions físiques entre les característiques microestructurals i les propietats a petita escala determinades.

El protocol proposat i descrit es va implementar en tres materials diferents: acer inoxidable dúplex (DSS), compostos basats en partícules de nitrur de bor cúbic (PcBN) i cermets de tipus Ti(C,N)-FeNi. Aquests materials representen exemples idonis de sistemes multifàsics metall-metall, ceràmic-ceràmic i ceràmic-metall, respectivament.

Aquesta tesi doctoral es presenta com un compendi de publicacions científiques en les quals s'aborden diferents objectius específics, utilitzant el protocol d'assaig i anàlisi proposat, per cada sistema multifàsic. Referent al sistema metall-metall, en el primer article es va avaluar satisfactòriament la influència de la ruta de processament en les propietats mecàniques a petita escala (duresa i mòdul elàstic) de les fases austenita i ferrita d'un DSS. Els resultats obtinguts permeten concloure que els efectes de la deformació en fred sobre les propietats a nivell local de les fases austenítica i ferrítica són més pronunciades que els inclosos en altres rutes de processament investigats. Addicionalment, en aquesta part del treball s'introdueix i es valida un nou histograma 2D de duresa i mòdul d'elasticitat com una eina adequada i eficaç per correlacionar la microestructura i les propietats mecàniques intrínseques de les fases constitutives dels DSS.

La segona publicació es va centrar en l'extracció de les propietats mecàniques a petita escala d'un compost de PcBN. Aquest material d'extremada duresa està constituït per partícules ceràmiques de cBN immerses en una fase aglutinant de TiN. En aquest article també es va avaluar i comprendre la correlació entre el quocient B/N i la duresa local de partícules de cBN individuals, complementant l'estudi mitjançant microanàlisis de rajos X amb sonda electrònica. Per això, es van definir cinc fases mecànicament diferents, tenint en compte factors diversos tals com la naturalesa química, la presència d'interfases TiN/cBN i l'estequiometria (relació quantitativa entre els continguts de B i N) de les partícules de cBN. Els resultats obtinguts permeten concloure que existeix una relació directa entre la duresa del cBN i la quantitat de N present en cada partícula d'aquesta fase ceràmica.

La influència de la quantitat relativa de fases (ceràmica i metàl·lica) i l'addició de carboni sobre les propietats mecàniques locals de cermets de Ti(C,N)-FeNi es van estudiar en el tercer i quart article. A través d'aquest treball es va evidenciar que tant la duresa com el mòdul elàstic dels cermets es relacionen en forma inversament proporcional al quocient metall/ceràmic corresponent a la proporció relativa de les fases presents. Tanmateix, es va arribar a la conclusió que l'addició de carboni resulta en un increment tant de la duresa com del mòdul elàstic dels cermets estudiats. Respecte a les propietats a petita escala de les fases constitutives, es va determinar la duresa intrínseca tant de les partícules de Ti(C,N) com de l'aglutinant metàl·lic FeNi, mitjançant nanoindentació massiva i un posterior anàlisi estadístic de les dades experimentals obtingudes. En aquest sistema, i pel cas particular de l'avaluació de la duresa efectiva de la fase metàl·lica, es va utilitzar un model de pel·lícula fina com una eina d'anàlisi complementaria. Addicionalment, l'estudi dels mecanismes de deformació, dany i fractura en els cermets estudiats va permetre

evidenciar l'enduriment de la fase lligant de FeNi, associat directament al constrenyiment exercit per les partícules ceràmiques adjacents.

En termes generals, l'estudi realitzat i els resultats obtinguts permeten concloure que la metodologia proposada s'ha implementat i validat amb èxit com a protocol d'assaig per la determinació de propietats mecàniques a petita escala (duresa i mòdul elàstic) dels sistemes multifàsics investigats. En aquest context, s'ha d'indicar que la implementació satisfactòria d'aquesta metodologia requereix una consideració minuciosa dels paràmetres d'assaig utilitzats, en particular referint-se a la relació entre les escales dimensionals representatives de la plasticitat i les emprems residuals induïdes respecte a les característiques microestructurals del material estudiat.

List of publications

This Ph.D. thesis is accomplished as a compendium of articles presented in the following list (sorted by published date). Impact factor (IF) and quartile of the published articles are included based on information available in the Journal Citation Reports (JCR) 2019.

Article 1.

H. Besharatloo, M.de Nicolás, J.J. Roa, M. Dios, A. Mateo, B. Ferrari, E. Gordo, L. Llanes, *Assessment of mechanical properties at microstructural length scale of Ti(C,N)–FeNi ceramic-metal composites by means of massive nanoindentation and statistical analysis*. *Ceramics International* 45 (2019) 20202-20210. <https://doi.org/10.1016/j.ceramint.2019.06.292>. IF: 3.83. Q1 (2/28) in Materials Science, Ceramics.

Article 2.

H. Besharatloo, S. Gordon, T. Rodriguez-Suarez, A. Can, W.C. Oliver, L. Llanes, J.J. Roa, *Small-scale mechanical properties of constitutive phases within a polycrystalline cubic boron nitride composite*. *Journal of the European Ceramic Society* 39 (2019) 5181-5189. <https://doi.org/10.1016/j.jeurceramsoc.2019.08.023>. IF: 4.495. Q1 (1/28) in Materials Science, Ceramics.

Article 3.

H. Besharatloo, M. de Nicolás, J.M. Wheeler, A. Mateo, B. Ferrari, E. Gordo, L. Llanes, J.J. Roa, *Carbon addition effects on microstructure and small-scale hardness for Ti(C,N)-FeNi cermets*. *International Journal of Refractory Metals and Hard Materials* 85 (2019) 105064. <https://doi.org/10.1016/j.ijrmhm.2019.105064>. IF: 3.407. Q1 (11/79) in Metallurgy & Metallurgical Engineering.

Article 4.

H. Besharatloo, M. Carpio, J.M. Cabrera, A. Mateo, G. Fargas, J.M. Wheeler, L. Llanes, J.J. Roa. *Novel mechanical characterization of austenite and ferrite phases within a duplex stainless steel*. *Metals* 10 (2020) 1352. <https://doi.org/10.3390/met10101352>. IF: 2.259. Q1 (18/79) in Metallurgy and Metallurgical & Engineering.

Other contributions

Sorted by published date

Article 5.

Y.F. Zheng, G. Fargas, **H. Besharatloo**, M. Serra, J.J. Roa, E. Armelin, O. Lavigne, L. Llanes. *Assessment of corrosion-induced changes on the mechanical integrity of cemented carbides at small length scales*. International Journal of Refractory Metals and Hard Materials 84 (2019) 105033. <https://doi.org/10.1016/j.ijrmhm.2019.105033>. IF: 3.407. Q1 (11/79) in Metallurgy & Metallurgical Engineering.

Article 6.

M. de Nicolás, **H. Besharatloo**, J.M. Wheeler, M. de Dios, P. Alvaredo, J.J. Roa, B. Ferrari, L. Llanes, E. Gordo. *Influence of the processing route on the properties of Ti(C,N)-Fe15Ni cermets*. International Journal of Refractory Metals and Hard Materials 87 (2020) 105046. <https://doi.org/10.1016/j.ijrmhm.2019.105046>. IF: 3.407. Q1 (11/79) in Metallurgy & Metallurgical Engineering.

Article 7.

M. de Nicolás, **H. Besharatloo**, P. Alvaredo, J.J. Roa, L. Llanes, E. Gordo. *Design of alternative binders for hard materials*. International Journal of Refractory Metals and Hard Materials 87 (2020) 105089. <https://doi.org/10.1016/j.ijrmhm.2019.105089>. IF: 3.407. Q1 (11/79) in Metallurgy & Metallurgical Engineering.

Article 8.

Yuan Xiao, **Hossein Besharatloo**, Bin Gan, Xavier Maeder, Ralph Spolenak, Jeffrey M. Wheeler. *Combinatorial investigation of Al–Cu intermetallics using small-scale mechanical testing*. Journal of Alloys and Compounds 822 (2020) 153536. <https://doi.org/10.1016/j.jallcom.2019.153536>. IF: 4.650. Q1 (8/79) in Metallurgy & Metallurgical Engineering.

Oral presentations

Sorted by presented date

International

H. Besharatloo, J.J. Roa, M. Dios, A. Mateo, B. Ferrari, E. Gordo, L. Llanes. *Micromechanics of Ti(C,N)-FeNi composites: statistical analysis and flow stress determination for the FeNi binder*. Europe's annual powder metallurgy congress and exhibition (EuroPM) 2017. Oral presentation. (Milan, Italy, 1st – 5th October 2017).

H. Besharatloo, J.J. Roa, X. Gil, G. Fargas, A. Mateo, L. Llanes. *Characterization of the anisotropy of the duplex stainless steels by means of micromechanical evaluation*. 10th European Solid Mechanics Conference – ESMC2018. Oral Presentation. (Bologna, Italy, 2nd - 6th July 2018).

H. Besharatloo, J.J. Roa, M. de Dios, M. de Nicolas, A. Mateo, B. Ferrari, E. Gordo, L. Llanes. *Micromechanics of Ti(C,N)-FeNi composites*. World Conference on Powder Metallurgy (WorldPM) 2018. Oral presentation (presented by J.J. Roa) (Beijing, China, 16th – 20th September 2018).

H. Besharatloo, J.M. Wheeler, M. de Nicolas, E. Gordo, A. Mateo, L. Llanes, J.J. Roa. *Hardness and elastic modulus map cartography on Ti (C,N)-FeNi composites: evaluation of the carbon effect of metallic binder*. 11th International Conference on the Science of Hard Materials. Oral presentation. (Khao Lak, Thailand, 25th – 29th March 2019).

National

H. Besharatloo, J.J. Roa, M. Dios, A. Mateo, B. Ferrari, E. Gordo, L. Llanes. *Micromechanical properties of a Ti(C,N)-FeNi composite: statistical method*. 34th XXXIV Encuentro del Grupo Español de Fractura. (Santander, Spain, 29th – 31st March 2017).

H. Besharatloo, J.J. Roa, V. Lamelas, L. Llanes. *Mechanical properties of the constitutive phases of polycrystalline cubic boron nitride*. VI Congreso Nacional de Pulvimetalurgia y I Congreso Iberoamericano de Pulvimetalurgia. (Ciudad Real, Spain, 7th – 9th June 2017).

H. Besharatloo, J.J. Roa, W.C. Oliver, A. Can, L. Llanes. *Hardness and stiffness map cartography on a cBN-TiN composite*. 35th XXXV Encuentro del Grupo Español de Fractura. (Málaga, Spain, 14th – 16th March 2018). (**This work won the best presentation award at this conference**)

Table of contents

Preface.....	I
Abstract.....	III
Resumen.....	V
Resum	VIII
List of publications	XI
Other contributions	XII
Oral presentations	XIII
Table of contents.....	XV
List of figures	XIX
List of tables.....	XXIV
Glossary of symbols and abbreviations	XXVI
Glossary of symbols.....	XXVI
Glossary of abbreviations	XXVII
1 Chapter 1. Introduction	2
1.1 Multiphase systems under consideration in this work	5
1.1.1 Metal – Metal system.....	5

1.1.2	Ceramic – Ceramic system	9
1.1.3	Ceramic – Metal system.....	13
1.2	Assessing the influence of microstructure-processing correlations on bulk mechanical properties of multiphase systems	18
1.3	Microstructural parameters	18
1.3.1	Phase content	19
1.3.2	Grain size	20
1.3.3	Binder content.....	21
1.3.4	Contiguity	22
1.3.5	Mean free path	23
1.4	Length scale issues on the measurement of hardness, as a representative mechanical property of multiphase systems	24
1.5	Challenges of using nanoindentation technique to evaluate the local mechanical properties of multiphase systems	32
1.5.1	Nanoindentation technique as applied to multiphase materials	32
1.5.2	Statistical analysis.....	35
1.5.3	High-speed nanoindentation technique.....	37
2	Chapter 2. Aim and scope of the work	39
3	Chapter 3. Materials and methods	43
3.1	Materials and sample preparation	43
3.1.1	Duplex stainless steel (Metal-Metal system)	43

3.1.2	Polycrystalline cubic boron nitride composite (Ceramic-Ceramic system)	44
3.1.3	Ti(C,N)-FeNi cermets (Ceramic-Metal system).....	45
3.1.4	Sample preparation	47
3.2	Microstructural characterization techniques	48
3.2.1	Scanning electron microscopy (SEM)	48
3.2.2	Electron probe microanalysis (EPMA).....	50
3.2.3	Electron backscatter diffraction (EBSD)	51
3.2.4	Focused ion beam (FIB).....	54
3.3	Mechanical characterization techniques.....	57
3.3.1	Nanoindentation: equipment and testing conditions.....	57
3.3.2	Macroindentation: equipment and testing conditions	59
4	Chapter 4. Scientific articles presentation	61
	Article I: Novel mechanical characterization of austenite and ferrite phases within a duplex stainless steel.....	62
	Article II: Small-scale mechanical properties of constitutive phases within a polycrystalline cubic boron nitride composite.....	78
	Article III: Assessment of mechanical properties at microstructural length scale of Ti(C,N)-FeNi ceramic-metal composites by means of massive nanoindentation and statistical analysis	88
	Article IV: Carbon addition effects on microstructure and small-scale hardness for Ti(C,N)-FeNi cermets	98
5	Chapter 5. Summary of main results.....	109

5.1	Microstructural characterization	109
5.1.1	Duplex stainless steel (Metal-Metal system)	109
5.1.2	Polycrystalline cubic boron nitride composite (Ceramic-Ceramic system)	111
5.1.3	Ti(C,N)-FeNi cermets (Ceramic-Metal system)	112
5.2	Micromechanical characterization	114
5.2.1	Duplex stainless steel (Metal-Metal system)	115
5.2.2	Polycrystalline cubic boron nitride composite (Ceramic-Ceramic system)	118
5.2.3	Ti(C,N)-FeNi cermets (Ceramic-Metal system)	121
5.3	Correlation between microstructure and micromechanical properties.....	125
5.3.1	Duplex stainless steel (Metal-Metal system)	125
5.3.2	Polycrystalline cubic boron nitride composite (Ceramic-Ceramic system)	128
5.3.3	Ti(C,N)-FeNi cermets (Ceramic-Metal system)	131
6	Chapter 6: General conclusions and future work.....	135
6.1	General conclusions	135
6.2	Future work	139
	Acknowledgments.....	141
	Bibliography	144

List of figures

- Figure 1.1.** Bonding behavior present in different groups of engineering materials [2]..... 2
- Figure 1.2.** The "iterative tetrahedron" representing the four main components describing materials science and engineering (adapted from [3])...... 3
- Figure 1.3.** A typical microstructure of a rolled duplex stainless steel [35]. 5
- Figure 1.4.** Section through the Fe-Cr-Ni ternary phase diagram (at 68% iron content) [52]...... 8
- Figure 1.5.** Transformation of hBN to cBN (adapted from Refs. [63,66]). 10
- Figure 1.6.** Pressure vs. temperature diagram for BN [69]. 11
- Figure 1.7.** Micrographs of PcBN grades corresponding to (a) low cBN (60 *vol. %*) and (b) high cBN (90 *vol. %*) contents [90]. 12
- Figure 1.8.** (a) Evolution of the contact angle of liquid Fe, Ni and Fe-15Ni in contact with Ti(C,N) substrate with the residence time. (b) Camera shots of the evolution of liquid drop with time. (c) Micrographs of the interface of the systems Fe/Ti(C,N), Fe-15Ni/Ti(C,N) and Ni/Ti(C,N) after high temperature wetting experiments [128]. 16
- Figure 1.9.** Influence of the microstructure on the mechanical properties of cemented carbides: (a) hardness, (b) fracture toughness, (c) compressive strength, and (d) wear resistance, as a function of the binder content for different carbide mean grain sizes [149]. 17
- Figure 1.10.** Main microstructural parameters for (a) DSS (adapted from [154]), (b) PcBN and cermets. 19
- Figure 1.11.** Linear-intercept lines drawn across idealized: (a) metal structures, (b) cermet microstructure (adapted from [156] and [155] respectively). 21

Figure 1.12. Scheme of indentation hardness of a polycrystalline/multiphase material at (a) macro-scale, (b) micro-scale, and (c) nano-scale [165].	26
Figure 1.13. Typical $P-h$ curve obtained during loading and unloading of the indentation process [165]......	28
Figure 1.14. (a) Elasto-plastic deformation at the maximum applied load P_{max} . (b) Plastic deformation after releasing the load [165]......	28
Figure 1.15. Schematic representation of the indentation size effect [165]......	31
Figure 1.16. Mechanical properties evaluation of multiphase material by (a) and (b) performing deep indentation, (c) and (d) shallow imprints.	33
Figure 1.17. (a) Confined indentation within a WC grain of a WC-Co system. (b) Minimum penetration depth obtained from plotting P/S^2 as a function of displacement into the surface [188].	34
Figure 1.18. Experimental CDF value plotted by Origin Pro software for a cermet.	36
Figure 2.1. (a) Elastic modulus and (b) hardness cartography maps assessed for two multiphase materials studied in this work: DSS and cermet respectively.	40
Figure 2.2. Schematic flowchart indicating the different steps followed to acquire local mechanical properties of each constitutive phase within the multiphase materials studied in this work.	41
Figure 3.1. Schematic diagram of the industrial processing route (including individual and sequential stages) associated with DSS specimens investigated in this study.	44
Figure 3.2. (a) Scheme of the PcBN cutting tool, where the encircled region is magnified in (b), aiming to show the assemblage of the insert's tip: WC-Co structure where PcBN is placed, brazing region and PcBN itself, consisting of cBN particles bonded by a TiN matrix.	45
Figure 3.3. SEM scheme [201].	49
Figure 3.4. Schematic of detectors and signals of EPMA [206]......	51

Figure 3.5. (a) Scheme of the formation of Kikuchi patterns. (b) Kikuchi pattern of Cadmium [207].	52
Figure 3.6. Schematic of the EBSD technique [208].	53
Figure 3.7. (a) Quality image, (b) phase map, and (c) IPF map of DSS, obtained by means of EBSD technique.	54
Figure 3.8. FIB scheme [213].	55
Figure 3.9. Scheme of cross-section milling by FIB.	56
Figure 3.10. Cross-section view of different samples obtained by FIB technique: (a) PcBN composite, and (b) Ti(C,N)-FeNi cermet.	57
Figure 3.11. Hardness cartography map, obtained by NanoBlitz technique using iNano for a studied cermet.	58
Figure 5.1. Phase map and corresponding quality images for studied DSS samples.	110
Figure 5.2. (a) Volume fractions of both constitutive phases for all the studied samples. (b) Grain size histogram for the HR sample, with 250 nm of bin size, computed from at least 2000 counted grains. (c) Surface fraction occupied by different grain size ranges of each phase for all the studied samples.	111
Figure 5.3. (a) FESEM micrograph of PcBN microstructure. (b) Magnified micrograph of the red marked region where microstructural parameters of PcBN composite are indicated.	112
Figure 5.4. Micrographs of Ti(C,N)-FeNi cermets with different <i>vol. %</i> and carbon addition of the metallic binder.	113
Figure 5.5. P/S^2 ratio versus penetration depth for indentations on CR DSS sample.	116
Figure 5.6. $P-h$ curves, obtained from different imprints performed on different phases, performed at 4 mN.	116
Figure 5.7. Phase map of an indented area in a DSS sample.	117

- Figure 5.8.** (a) and (b) *CDF* fittings for obtained experimental *H* and *E* of the HR DSS sample, respectively. (c) and (d) Fitted Gaussian distributions (obtained from *CDF* plot) on hardness and elastic modulus histogram, respectively. 117
- Figure 5.9.** (a) FESEM micrograph of performed imprints on different phases of PcBN composite. (b),(d) Residual imprints performed on cBN and TiN binder, respectively. (c) and (d) cross-section view of figures (b) and (d), respectively, in which the estimated plastic flows for both phases are shown. 119
- Figure 5.10.** (a) Hardness histogram with a constant bin size of 1.8 GPa computed from imprints performed by high-speed indentation technique. (b) Hardness evolution against displacement into surface, obtained from dynamic indentations performed on different phases. 120
- Figure 5.11.** Hardness histogram obtained from the same data as shown in **Figure 5.10**, plotted with a constant bin size of 1 GPa. 121
- Figure 5.12.** (a) and (c) FESEM micrographs of residual imprints performed at 2000 nm. (b) Magnified image of residual imprint shown in (a). (d) FIB-milled cross-section of residual imprint shown in (c), under the region of interest indicated by the white dash line. 122
- Figure 5.13.** (a) Hardness and (b) Elastic modulus evolution against penetration depth for all the investigated cermets. 122
- Figure 5.14.** (a) SEM micrograph of a cropped region of the indented area on a cermet sample. (b) Hardness histogram of 15FeNi+C samples with a constant bin size of 0.5 GPa and fitted Gaussian distribution, corresponding to the mechanical properties of each phase. 124
- Figure 5.15.** EBSD maps of indented surfaces and corresponding mechanical cartography maps of the indicated region for HR and CR samples. 126
- Figure 5.16.** 2D histograms of Hardness (y-axis) vs Elastic Modulus (x-axis) acquired from 10,000 indentations on each HR and CR sample. 127
- Figure 5.17.** Final hardness and elastic modulus histogram of HR sample. 128
- Figure 5.18.** Hardness cartography map of PcBN composite obtained from nanoindentations performed at 25 mN. 129

- Figure 5.19.** EPMA analysis performed on PcBN sample: (a) SEM micrograph of the analyzed region, (b) N map for high N grains marked by red lines in SEM image, and (c) N map for low N grains marked by yellow lines in the SEM image. 130
- Figure 5.20.** (a) FESEM micrograph of performed indentation matrix at 200 nm on the marked region of PcBN sample. (b) N map of microstructure, and corresponding indentations, attained by EPMA analysis..... 130
- Figure 5.21.** (a) Hardness evolution against penetration depth for cBN grains with different N (and B) content. (b) Hardness histogram of PcBN composite with five fitted mechanically distinct phases (the updated version of **Figure 5.11**). 131
- Figure 5.22.** (a) FESEM micrograph on an indented surface of 20FeNi+C cermet. (b) Corresponding H cartography map of the indented surface. (c) Overlay of FESEM micrograph and H cartography maps. 132
- Figure 5.23.** Magnified region of hardness histograms of studied samples for $H < 4$ GPa, corresponding to the porosity level. 133

List of tables

Table 1.1. Basic composition and mechanical properties of three types of stainless steel [37]. ...	6
Table 1.2. Summary of the main physical and mechanical properties of abrasive materials [59,61].	10
Table 1.3. Comparison of high-temperature properties of TiC- and Ti(C,N)-based cermets [118].	14
Table 1.4. Summary of the main physical and mechanical properties of Ti(C,N) [69].	15
Table 1.5. Grain size classification of cemented carbides [144].	17
Table 1.6. Name, application, shape and contact area of the different indenters used in this work.	25
Table 3.1. Chemical composition (in <i>wt. %</i>) of the studied duplex stainless steel EN 1.4462. ...	43
Table 3.2. Characteristics of the as-received powders.	46
Table 3.3. Chemical formulation of suspensions.	47
Table 3.4. Polishing steps for surface sample preparation.	47
Table 3.5. Vibratory finishing condition.	48
Table 3.6. Micro-indentation testing conditions.	59
Table 5.1. Microstructural parameters of studied cermets.	113
Table 5.2. Testing conditions and achievements of each set of indentation tests performed by Nanoindenter XP.	115

Table 5.3. Testing conditions and achievements of each set of indentation tests performed by iNano [®] nanoindenter.....	115
Table 5.4. Summary of H and E values of the unidentified phases in each processing condition of DSS, determined from statistical analysis.	118
Table 5.5. Hardness values for each mechanically distinct phase of PcBN composite, obtained from statistical analysis.....	120
Table 5.6. Mechanical properties data assessed at different length scales for the studied Ti(C,N)–FeNi composites.....	123
Table 5.7. Hardness mean values for each phase of the investigated samples, obtained through statistical analysis.....	124
Table 5.8. Corrected hardness values of metallic binder assessed by thin-film method (Korsunsky <i>et.al</i> [218]).....	125
Table 5.9. Summary of hardness and elastic modulus values for defined phases of studied duplex steels computed by statistical analysis.....	128
Table 5.10. Intrinsic hardness values for five mechanically different phases of the studied PcBN composite.....	131

Glossary of symbols and abbreviations

Glossary of symbols

$2D$	Two-dimension
$3D$	Three dimension
A	Projected area of the indent
A_c	Actual surface area (contact area)
A_i	Area occupied by each phase
A_p	Cross-sectional area of the indenter
A_s	Contact area at maximum load
A_{total}	Total area occupied by all phases
A_5	The ratio of the original specimen gauge length to diameter ratio of 5
C	Contiguity
$C_{hard\ phase}$	Contiguity of the hard phase
D	Characteristic size of the phase
D_{BET}	Brunauer-Emmett-Taller diameter
D_{V50}	Particle size distribution (average particle size in volume)
d_{grain}	Grain size of ceramic particles
E	Elastic modulus
E_{eff}	Effective Young's modulus
E_i	Young's modulus of the diamond tip
F	Applied force
F_{ag}	Agglomeration factor
f_i	Relative fraction occupied by each phase
H	Hardness
H_c	Hardness of composite
H_f	Hardness of thin-film
H_s	Hardness of substrate
HV	Vickers hardness
H_0	Hardness in the limit of infinite depth
h	Penetration depth or displacement into the surface
h^*	Characteristic length
h_c	Contact depth
h_{final}	Final penetration depth

h_{max}	Maximum penetration depth
h_{min}	Minimum penetration depth
h_s	Amount of sink-in
k_k	Fitting parameter of film thickness
m	Power law constant
N	Number of phases
N_g	Number of grain boundaries
N_i	Number of indentation
P	Applied load
P_i	Phase content
P_{max}	Maximum applied load
p_i	Properties of individual phase
R^2	Ultimate coefficient in cumulative distribution function fitting
S	Stiffness
T	Temperature
V_{binder}	Binder volume content
vol. %	Volume fraction (volume percent)
wt. %	Mass fraction (weight percent)
α	Ferrite
β	Indenter geometry parameter
γ	Austenite
ε	Constant of the geometry of indenter
λ	Thermal conductivity
λ_{binder}	Binder mean free path
λ_{FeNi}	Mean free path of FeNi metallic binder
λ_{TiN}	Mean free path of TiN ceramic binder
ρ_c	Density of composite
$\rho_{Ti(C,N)}$	Density of Titanium carbonitride
σ_i	Standard deviation
ν	Poisson's ratio
ν_i	Poisson's ratio of the diamond tip
χ^2	Tolerance of cumulative distribution function fitting

Glossary of abbreviations

AS	Array size
BCC	Body centered cubic
BN	Boron nitride
BSE	Backscattered electron

cBN	Cubic boron nitride
<i>CDF</i>	Cumulative distribution function
CR	Cold roll
CSM	Continuous stiffness measurement
DSS	Duplex stainless steel
EBSD	Electron back-scattered diffraction
EMPA	Electron microprobe analysis
EN	European standard
FCC	Face centered cubic
FESEM	Field emission scanning electron microscopy
FIB	Focused ion beam
FP	Final product
GIS	Gas injection system
hBN	hexagonal boron nitride
HR	Hot roll
HRA	Hot roll annealed
IPF	Inverse pole figure
IS	Indentation spacing
ISE	Indentation size effect
LI	Linear interception
PcBN	Polycrystalline cubic boron nitride
PEI	Polyethylenimine
PVA	Polyvinyl alcohol
QI	Quality image
R&D	Research and development
RVE	Representative volume element
SE	Secondary electrons
SEM	Scanning electron microscopy
SSA	Specific surface area
STEM	Scanning transmission electron microscopy
TEM	Transmission electron microscopy
TMAH	Tetramethylammonium hydroxide
TRS	Transverse rupture strength
TWIP	Twinning induced plasticity
UTS	Ultimate tensile strength
wBN	Wurzite boron nitride
WDS	Wavelength dispersive spectroscopy
YS	Yield strength

Chapter 1

Introduction

Chapter 1.

Introduction

Proper performance of any engineered device, structure or product requires the use of the right materials. The group of materials that are used in the production of man-made assemblies and components are called engineering materials and may be classified into four large groups: metals, polymers, ceramics, and semiconductors. The primary function of an engineering material depends on its properties, for instance, the capability to withstand applied loading without breaking and/or exhibiting excessive deflection. On the other hand, the effective properties of engineering materials are directly linked to their chemical nature as well as the arrangement and morphology of the constituting particles and/or phases [1,2]. Metallic, ionic and covalent are the types of bonds mainly found in metals and their alloys, ceramics, and semiconductors, respectively. Ceramics usually exhibit a mixture of ionic and covalent bonding. Meanwhile, in polymers weak secondary forces of attraction (Van der Waals forces) are present between the extended covalently bound hydrocarbon chains (**Figure 1.1**) [2].

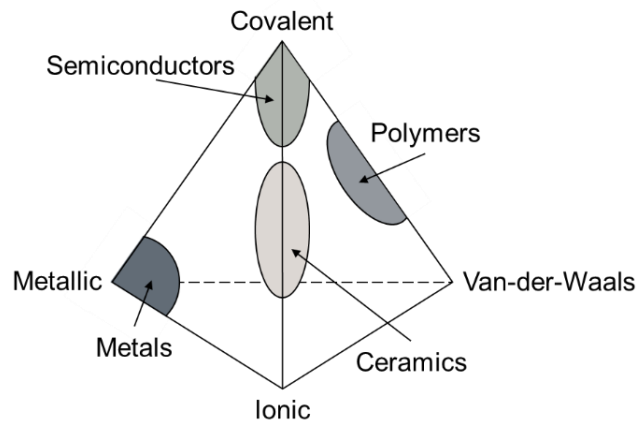


Figure 1.1. Bonding behavior present in different groups of engineering materials [2].

The arrangement of constituting particles and phases may be described at different levels. At the lowest one, atoms may position each other following some order. In the case of inorganic materials (metals and ceramics), the main subject of this Ph.D. dissertation, it usually takes place as crystal or lattice structures where atoms are arranged in periodically repeating arrays. However, even though these materials are referred to as crystalline ones, the order is neither perfect nor unlimited.

In the first case, it results in a variety of crystal imperfections which are classified as point (vacancies, interstitial atoms), line (dislocations), planar (stacking faults, twin boundaries), and volume (voids, cavities) defects. In the second case, it implies a jump into a microscopic structural level, i.e. one involving large groups of atomic arrangements separated by either grain or phase boundaries. These are interfaces that separate two adjoining grains (or phases) having different crystallographic orientations and, in the case of phases, different crystal structures and/or chemical compositions [2]. This scenario by itself defines the key “microstructure of engineering materials” which is critical to control the resulting properties. Hence, the microstructural design is key for tailoring the properties of a material to fit the requirements of a certain application. Effective implementation of this approach requires an in-depth understanding of the processing-structure-property relationships. These three main factors and the links among them are shown in **Figure 1.2**, and they are the pillars supporting the foundations and success of materials science and engineering [3].

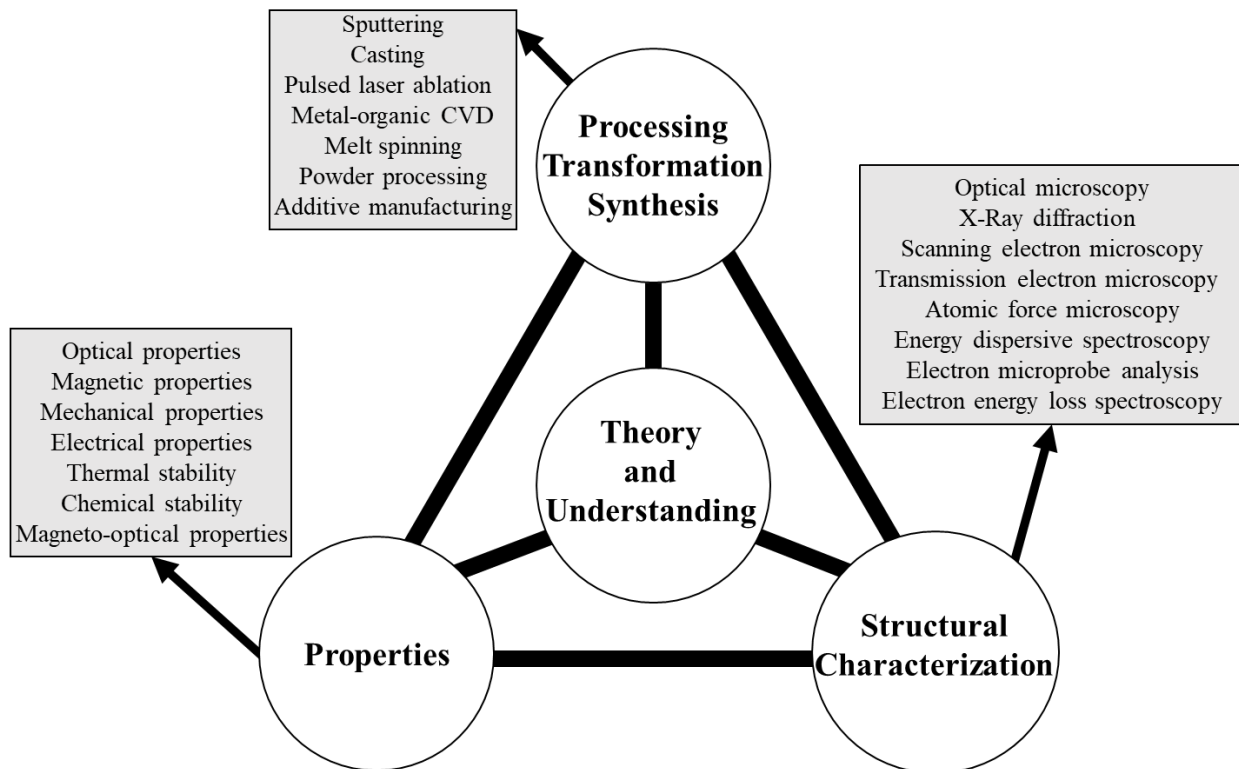


Figure 1.2. The "iterative tetrahedron" representing the four main components describing materials science and engineering (adapted from [3]).

As it is seen in **Figure 1.2** the amount of data that might be scrutinized to obtain comprehensive knowledge of the materials is almost unlimited. Depending on the application, the required factors which have to be taken into consideration can be varied. Accordingly, identifying and analyzing them needs extensive knowledge and expertise, which may involve different materials science and

engineering criteria. This implies combined multiscale theoretical, analytical and experimental efforts. In this regard, and within the scope of this Ph.D. thesis, assessment of mechanical properties at the micrometric length scale is proposed as a key issue towards the optimized microstructural design of inorganic multiphase composites.

As it has been described above, the microstructure of a material could be comprised of one or several phases. Although remarkable properties may be achieved in single-phase materials through combined processing and thermal treatments, tailoring them for desired applications might be limited. Meanwhile, property windows may be widened by using multiphase systems. In this regard, assuming that processing requirements and challenges may be satisfied and overcome respectively, the achievement of targeted properties by tailoring the microstructure of multiphase materials would be more flexible than attempting it by using single-phase ones (e.g. Refs. [4–9]). However, it requires access and implementation of advanced characterization techniques for precise and reliable assessment of both microstructural features and micromechanical properties for all the present phases (e.g. Refs. [10–13]). This would help to discern how structure-property correlations at small scales affect the macroscopic behavior of the bulk material. Such knowledge is recognized as critical for the effective microstructural design of multiphase materials, as it aids to understand the physical micro-mechanisms as well as enhances the prediction (simulation) capability of the macroscopic response of these materials, on the basis of those exhibited by its constitutive phases (e.g. Refs. [14–18]). Inorganic multiphase materials have a vast variety of industrial applications. Therefore, investigation and analysis of their effective properties are crucial not only for the optimization of their performance but also for designing new materials (e.g. Refs. [19–24]). Moreover, research in such a field may give insights into further developments of the related mathematical, physical, and engineering theories about multiphase systems (e.g. Refs. [9,18,22]).

The above definition of multiphase system includes a wide variety of engineering materials. Within the framework of this Ph.D. thesis, we are limiting the study to inorganic composites. Inorganic materials are generally derived from non-living sources, such as rocks or minerals, and encompass such categories as ceramics, glass and metals. Furthermore, materials chosen for the investigation correspond to different multiphase systems: metal-metal, ceramic-ceramic, and ceramic-metal, all of them being successfully implemented in industrial applications as engineering components and tools.

1.1 Multiphase systems under consideration in this work

In this section, general information about constitutive phases/elements, microstructure, processing, properties and applications will be provided for the different multiphase systems under consideration in this work. They refer to Duplex Stainless Steels (DSS), Polycrystalline cubic Boron Nitride (PcBN) composite, and Titanium Carbonitride/Iron-Nickel [Ti(C,N)-FeNi] cermets as representative examples of metal-metal, ceramic-ceramic and ceramic-metal systems, respectively.

1.1.1 Metal – Metal system

DSSs are chromium-nickel-molybdenum-iron two-phase alloys. They usually have a heterogeneous microstructure consisting of approximately equal phase amounts of austenite and ferrite (e.g. **Figure 1.3**), obtained by controlling chemical composition and heat treatments. As a result, they combine some of the features of austenitic and ferritic stainless steels, becoming the optimum selection for certain applications. On one hand, they are resistant to corrosion as the former, although not as resistant as the ferritic stainless steels. On the other hand, they exhibit a toughness superior to that of the latter, but lower than the one shown by austenitic stainless steels [25–34].

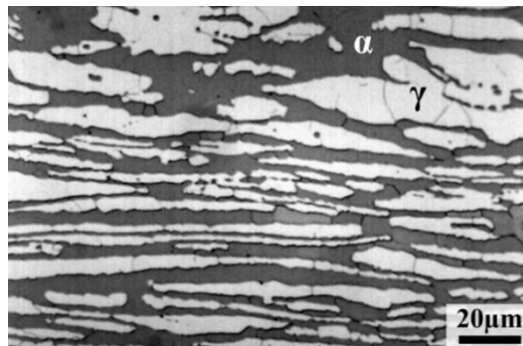


Figure 1.3. A typical microstructure of a rolled duplex stainless steel [35].

DSSs have existed since the early 1930s. They were developed to reduce the intergranular corrosion problems present in the early high-carbon austenitic stainless steels, particularly in terms of resistance to chloride stress-corrosion cracking. This advantage of DSSs over austenitic steels has been exploited by engineers since then. The first-generation DSSs were produced in high-frequency induction furnaces using precisely weighed alloying additions. Partial vacuum ensured carbon removals, rudimentary de-oxidation and restricted nitrogen ingress. Although these DSSs provided good performance characteristics, they had limitations in the as-welded condition. As a consequence, the use of the first-generation DSSs was confined to a few specific applications, usually in the non-welded condition [29–32].

The use of DSSs became extensive from the late 1970s on. The main reasons behind it were a nickel shortage which pushed up the price of austenitic steels, demand for stainless steel grades able to perform under extreme service conditions typical of a rising offshore oil industry, and the introduction of the vacuum and argon oxygen decarburization practices. As a result, the second generation of much cleaner DSSs emerged. They exhibit improved welding properties mainly through nitrogen alloying. A well-controlled addition of nitrogen and lowering of carbon content improved corrosion resistance and high-temperature stability of the duplex structure, e.g. the heat-affected-zone by stabilizing the austenite [29–32]. One of these second-generation DSSs EN 1.4462 or 2205 (UNS S31803/S32205) – with a nominal composition of 22% Cr, 5% Ni, 3% Mo, and 0.16% N – is the metal-metal system to be studied in this thesis. It is the most common grade today and is used in a great number of applications in a wide variety of product forms.

The success of the EN 1.4462/2205 (UNS S31803/S32205) grade led to the development of an entire family of duplex alloys, which range in corrosion resistance depending on their alloy content. The modern DSSs can be divided into three groups [36]: (1) lean and/or first-generation DSSs, with 0.05-0.6 wt. % of Mo [34]; (2) standard or second-generation DSSs, from which the 2205 grade is the work-horse one, accounting for more than 80% of duplex use; and (3) super DSSs, the most highly alloyed grade for wrought products (25% Cr, 6.8% Ni, 3.7% Mo and 0.27% N, with or without Cu and/or W additions) [27,28].

The mechanical properties (high yield strength and ductility) and corrosion resistance of DSSs make them suitable for many industrial applications involving stringent service conditions, e.g. the oil and gas, the pulp and paper, chemical industries, and chemical tankers. Most of these applications require relatively simple forming, such as the rolling of cylindrical sections, press forming, and vessel and tank head forming by pressing or rolling. Moreover, in all these applications, properties such as welding, corrosion resistance, and mechanical strength, are crucial. In this regard, DSSs exceed the mechanical properties of the completely ferritic or austenitic alloys. **Table 1.1** provide some information and comparison between DSS and single-phase stainless steels [25,26,28,31,37,38].

Table 1.1. Basic composition and mechanical properties of three types of stainless steel [37].

Structure	Cr (wt. %)	C (wt. %)	Ni (wt. %)	Short name	YS Rp _{0.2} (MPa)	UTS R _m (MPa)	Elongation A ₅ (%)
Ferrite	13 - 30	< 0.1	< 1.0	X8Cr18	345	540	20
Austenite	17 - 26	< 0.1	7 - 26	X5CrNi18-10	190	450	45
Duplex	24 - 28	< 0.1/0.4	4 - 7	X2CrNiMoN22-5-3	450	700	25

YS Rp_{0.2}: Yield strength the amount of stress that will result in a plastic strain of 0.2%.

UTS R_m: Ultimate tensile strength.

A₅: The ratio of the original specimen gauge length to diameter ratio of 5.

Considering the multiphase system definition of DSSs, their final bulk properties would be mainly attributed to properties and fraction of each constitutive phase (austenite “ γ ” and ferrite “ α ”). Regarding the influence of γ - and α - phase fractions, it has been claimed that duplex microstructures with an equal fraction of austenite and ferrite offer the optimum combination of corrosion resistance and mechanical properties. High ferrite fractions decrease toughness and elongation, whereas low ones increase the susceptibility to chloride stress corrosion cracking [39–43]. Therefore, it seems clear that ferrite-austenite balance has a critical influence on the properties of DSSs, and determining a method to obtain an optimum combination of properties is of great interest [44]. In this regard, the influence of alloying elements becomes critical for DSSs.

Apart from Fe and C, as any other stainless steel, DSSs contain additional alloying elements (Cr, Mo, N, and Ni) which can tailor the microstructure and the amount of constitutive phases within these materials [45–53]. As a consequence, they also affect the mechanical, physical and corrosion properties of DSSs, as will be briefly explained below.

Chromium comprises at least 20% of DSS grades, which enhances both corrosion and oxidation resistance at elevated temperatures. It is a ferrite former, which means that its addition promotes the BCC structure of iron. At higher Cr contents, more nickel is necessary to form a duplex (austenite-ferritic) structure. Moreover, Cr may also promote the formation of intermetallic phases [29,44,45].

Molybdenum enhances pitting and crevice corrosion resistance of DSSs. It is a ferrite former (similar to Cr) and also increases the tendency of a stainless steel to form detrimental intermetallic phases. Therefore, the amount of Mo addition in DSS is usually limited to less than 4% [29,45,46,54,55].

Nitrogen is a low-cost alloying element that also increases, as it is the case for Mo and Cr, the corrosion resistance of DSSs. It is a strong FCC austenite former which provides the toughness of the DSS. Nitrogen raises the strength of the austenite phase by solid solution and work-hardening mechanisms. Moreover, N could delay the formation of detrimental intermetallic phases at elevated temperatures, which lets the processing and fabrication of the DSS grades be accomplished with the desired structure. Therefore, nitrogen-bearing DSSs display good toughness owing to their higher austenite fraction and reduced intermetallic contents [29,45,54,55].

Nickel is an austenite stabilizer that promotes a change of the crystal structure of stainless steel from BCC (ferrite) to FCC (austenite). The amount of Ni content ranges from 1.5 to 7%. Ni could also delay the formation of detrimental intermetallic phases, while the effectiveness of N is much higher in DSS [29,44,45].

Besides the alloying elements, other factors such as heat treatment and processing route might have relevant influences on the fraction of constitutive phases [37,40,41]. **Figure 1.4** displays the Fe-Cr-Ni ternary phase diagram, which is the guideline of the metallurgical behavior of DSSs. It illustrates that these alloys solidify as ferrite, which then partially transforms to austenite as the temperature falls, depending on the alloy composition. Moreover, it is shown that nitrogen raises the initiation temperature of $\alpha \rightarrow \gamma$ phase transformation which leads to increase the $\alpha \rightarrow \gamma$ transformation rate (see the colored region in **Figure 1.4**). Therefore, even at relatively rapid cooling rates, the equilibrium level of austenite can nearly be reached if the grade has sufficient nitrogen, which improves the structural stability of the DSS grade [27,49,52,53].

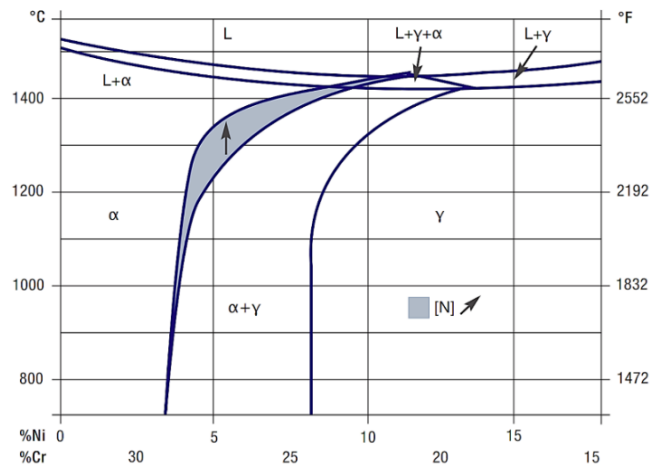


Figure 1.4. Section through the Fe-Cr-Ni ternary phase diagram (at 68% iron content) [52].

From the phase diagram shown in **Figure 1.4**, it may be discerned that small changes in composition can significantly affect the relative volume fraction of austenite and ferrite. The influence of each alloying element on the formation and consequently phase balance of ferrite/austenite in the microstructure might be predicted with multivariable linear regression, as follows:

$$Cr_{eq} = Cr + 1.73 Si + 0.88 Mo \quad \text{Equation 1.1}$$

$$Ni_{eq} = Ni + 24.55 C + 21.75 N + 0.4 Cu \quad \text{Equation 1.2}$$

$$\% \text{ Ferrite} = 4.01 Cr_{eq} - 5.6 Ni_{eq} + 0.016 T - 20.93 \quad \text{Equation 1.3}$$

where T is the annealing temperature, ranging from 1050 to 1150 °C, and the elemental compositions are in *wt. %* [47].

The goal of achieving the desired phase balance of austenite and ferrite is attainable by first adjusting the contents of N and Ni (as austenite stabilizers) as well as of Cr and Mo (as ferrite

formers), and then by tailoring the thermal history. Controlling these variables, besides other factors such as metal forming aspects (not detailed here), lead to develop the desired DSSs structure [37,44].

Finally, another microstructural factor that should be taken into account is the grain size of each phase. Depending on the desired application and formability of DSS, different manufacturing routes are applied to DSSs. These forming processes may also change the grain size of each phase, due to grain refinement or recrystallization processes induced by cold and hot rolling respectively [48,50].

1.1.2 Ceramic – Ceramic system

This set of systems are used in a wide variety of advanced engineering applications. Understanding the relationship between microstructure and properties can help to enhance the design of these materials which may have a significant influence on the corresponding industrial applications. In this regard, a PcBN composite was chosen to be studied as a representative example of an inorganic multiphase ceramic–ceramic system in this Ph.D. thesis. The functionality of PcBN mainly resides in its composite nature: a polycrystalline two-phase structure consisting of micron-sized grains of cubic boron nitride (cBN) held together by a binder material of ceramic chemical nature. PcBN is extensively used in highly demanding applications, such as tooling for high precision abrasive machining processes of alloys employed in the automotive and aerospace industries, due to superior thermal and chemical stability of cBN compared to diamond [56,57].

The extreme hardness of PcBN is the main characteristic of this ceramic-ceramic system. It is provided by cBN, which is the second hardest material only after the diamond. Therefore, since cBN is playing a key role to determine the bulk properties of PcBN, knowledge about its structure and properties becomes critical for optimizing the microstructural design of this composite material.

Excellent properties of cBN and diamond such as high hardness, thermal conductivity and chemical stability make them widely used in industrial applications, like cutting tools. Diamond-based cutting tools are employed for shaping hard materials (concrete, stones, ceramics and non-ferrous metals, among others) which have a low chemical reactivity with carbon. Machining iron-base alloys at high-temperature damages the diamond cutting tools due to the tendency of the diamond to react with those materials [58]. On the other hand, cBN is chemically inert to iron and is thermally stable to temperatures as high as 1000°C, i.e. better than diamond. Moreover, cBN can also form passive oxide layers at high temperatures when in contact with oxygen. Thus, it is suitable for the machining of hard ferrous alloys. Regarding technological progress, cBN tools represent a big advance in terms of tool life and operational performance in front of its competitors and previous solutions, as hardmetals or even diamond tools [58–60]. **Table 1.2** shows a

comparison between the basic properties and characteristics of cBN and other typical abrasive materials.

Table 1.2. Summary of the main physical and mechanical properties of abrasive materials [59,61].

Properties	cBN	Diamond	WC
Density (gr/cm^3)	3.5	3.5	14.7
Vickers hardness (GPa)	50	110	20
Fracture toughness ($\text{MPa}\cdot\sqrt{\text{m}}$)	5	3	3
Young's modulus (GPa)	600 – 800	1140	600
Compressive strength (GPa)	5.3	8.7	4.5
Thermal conductivity ($\text{W}/\text{m}\cdot\text{K}$)	150 – 700	500 – 2000	100
Thermal expansion ($10^{-6}\cdot\text{K}^{-1}$)	1.5	1.5 – 4.8	5.4

The outstanding properties listed for cBN in **Table 1.2** are directly related to its structure. It is a synthetic allotrope of boron nitride (BN) with a three-dimensional network of short and strong covalent bonds, which is critical for its properties. BN consists of equal amounts of boron and nitrogen atoms and has a structure similar to carbon. Thus, BN has different allotropes: hexagonal BN (hBN), cubic BN (cBN) and wurtzite BN (wBN), although the former two are the most common forms [62]. BN is usually found in nature (atmospheric conditions) as a hexagonal lattice (analogous to graphite in diamond). Meanwhile, cBN is formed by the conversion of hBN. The hexagonal lattice shown in **Figure 1.5** consists of a stacking arrangement along the c-axis of planar layers of hexagonal rings where boron (B) and nitrogen (N) occupy the edges. The layer sequence is ABAB... with B and N atoms also alternating along the c-axis [59,63,64]. cBN was first synthesized in 1957 by Wentorf [65]. It was found that high-temperature and high-pressure conditions, similar to those needed for the synthesis of diamond, could be used to convert hBN to cBN (**Figure 1.5**).

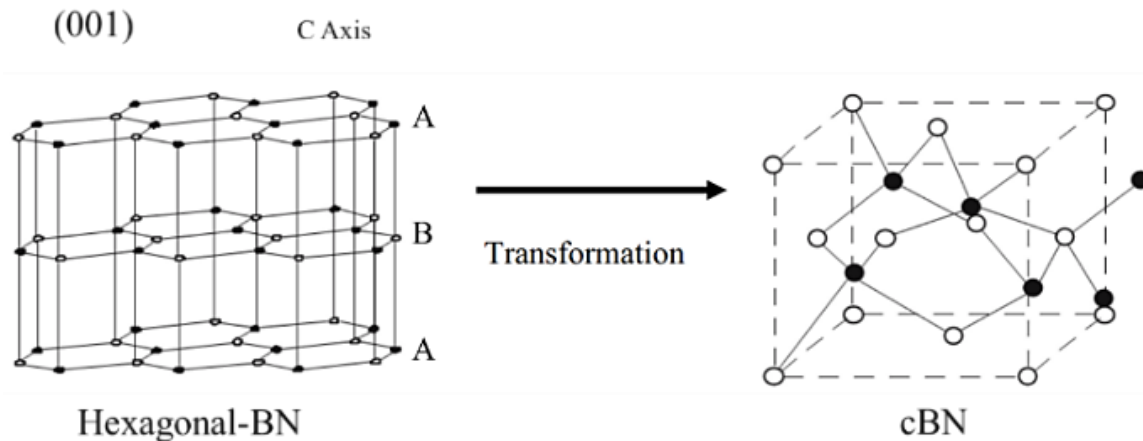


Figure 1.5. Transformation of hBN to cBN (adapted from Refs. [63,66]).

There are two main industrial ways to process cBN materials/tools. Both of them involve high pressure and temperature but include their particularities. They are:

- *Direct conversion from hBN to cBN*: This is the primary method, as developed by Wentorf, in which just high pressure and temperature were applied. The direct conversion of hBN to cBN can be done with pressure of up to 18 GPa and temperatures between 1750 and 3023°C. In this process, some parameters such as starting hBN particle size and crystallinity are very important factors for the resulting cBN grains. This method is the most basic and unrefined way of obtaining cBN, and in this sense, the transition from hBN to cBN is done in small volumes [65,67].
- *hBN to cBN conversion using a catalyzed process*: Commercially cBN is synthesized by a mixture of hBN and various catalysts/solvents, such as lithium-, calcium- and magnesium-nitride. The main reason for using catalyzers is to enhance the kinetics of the transformation, in order to boost the production rates. Catalysts/solvents assist sintering process, consolidating cBN much faster at lower pressures (around 4.5 – 5.5 GPa) and temperatures (between 1200 and 1700°C) [59,66,68]. **Figure 1.6** shows the pressure-temperature diagram for BN and sets the regions at which hBN and cBN are thermodynamically stable. Typically, the processing values of pressure and temperature are around 6 GPa and 1350°C, respectively [69].

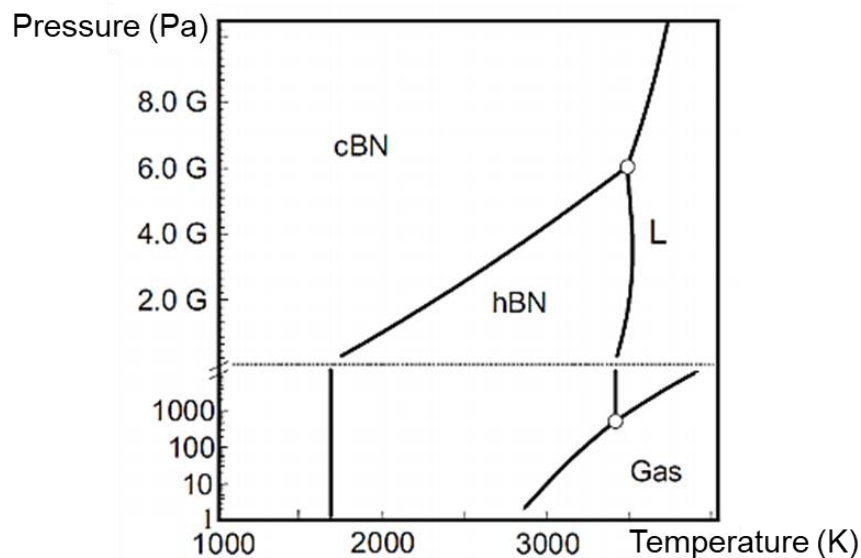


Figure 1.6. Pressure vs. temperature diagram for BN [69].

Although cBN is a useful material, its direct application as a single crystal is rather limited, since it can just be produced as small size particles ($< 60 \mu\text{m}$). Hence, it is rather used within materials

containing multiple crystals of cBN joined together with a binder. The resulting materials are usually termed Polycrystalline cubic Boron Nitride (PcBN) composites, and exhibit exceptional combinations of extreme hardness and moderate fracture toughness, the latter linked to the addition of different binder phases [59,70–72]. The commercial method of PcBN production is done by processing together cBN and sintering additives or binder materials at pressures about 4 – 6 GPa and temperatures ranging between 1200 and 1500°C [59].

Following the above ideas, the properties of the PcBN composites would then be determined by the final microstructure (structure) formed during sintering (processing). For PcBN composites, cBN content and mean grain size of cBN particles can be considered as the main microstructural parameters which then define their mechanical properties and tribological responses [73–80].

Commercially manufactured PcBN tools are available with different cBN contents and some additives. In this regard, they are usually categorized as either high or low cBN content grades (see **Figure 1.7**). High cBN content usually means values of the volume fraction (*vol. %*) of this phase above 80 – 90. In these cases, the binder phase could be of either ceramic or metallic nature, e.g. Co, W-Co-Al, Ti-Al and Al₂O₃. On the other hand, low cBN content refers to grades where the *vol. %* of cBN ranges between 40 and 70. Here, the binder is always of ceramic nature, usually aluminum nitride (AlN), titanium nitride (TiN) or titanium carbide (TiC) [67,81–84]. Since the introduction of Ti-base binders in the early 1980s [85,86], PcBN grades containing TiN and TiC as matrix have shown to be quite successful, because it enhances thermal stability and wear resistance of the composites [87–89]. One of those TiN-containing PcBN grades is the ceramic-ceramic system chosen for the investigation presented in this Ph.D. thesis.

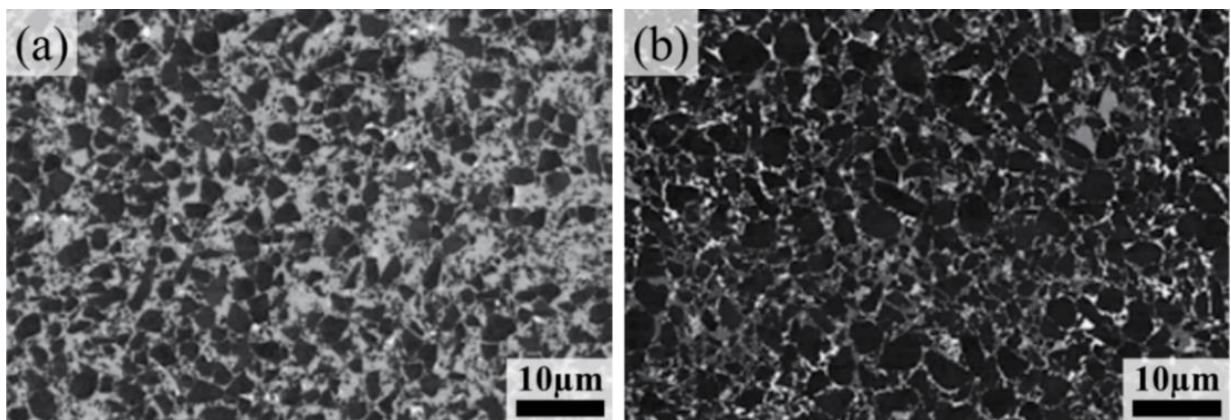


Figure 1.7. Micrographs of PcBN grades corresponding to (a) low cBN (60 *vol. %*) and (b) high cBN (90 *vol. %*) contents [90].

Depending on the chemical nature of the binder and cBN content, mechanical properties like hardness and strength are strongly affected [73–75,79,91]. High cBN content and Co matrix are recommended for interrupted cutting, while low cBN content and ceramic-based binders are

preferred options for finishing (continuous turning) operations. Research to date has found that low cBN content materials provide the best performance in hard turning, in terms of tool life and surface finish [61,82,92,93].

Regarding the physical dimensions of the hard particles, cBN grain size has shown to exert a great influence on the bulk properties of PcBN composites. Similar to other brittle materials, the relationship between hardness and size of the cBN grains can be approximated by the Hall-Petch relation, i.e. hardness is found to be inversely proportional to the square root of the grain size ($H \propto \sqrt{d_{grain}}$) [94]. This has been confirmed by several works reported in the literature [76,77,79].

Fracture toughness generally rises with increasing cBN grain size for low binder contents, because larger particles, for a fixed binder amount, leads to thicker binder layers, i.e. higher mean free paths between cBN grains [77,79].

In the literature, parameters such as the cutting edge geometry, cBN content, coating type, grain size of cBN, type of binder, use of cooling methods and variation in cutting parameters have also been reported to exhibit a significant influence on cBN tool performance [95–97]. However, detailed analysis and understanding of these correlations are beyond the scope of the present research work.

1.1.3 Ceramic – Metal system

The name Cermet is composed of the syllables “cer” from ceramics and “met” from metals. It is an artificial word that designates the combination of brittle hard phases (oxides, carbides, borides or similar inorganic compounds) with a ductile binder metallic phase to form a composite material. Cermets combine hardness, wear, and high-temperature resistance of ceramics with toughness of metals. They are generally hard, refractory and chemically resistant [69,98–101].

Cermets are widely applied in wear components, in chemical-resistant and high-temperature applications, and as insulators. Another application that is making cermets one of the most widespread powder metallurgy products refers to their use as cutting tools. In the metal cutting industry, the term “cermet” is usually recalled for designating TiC- or Ti(C,N)-based composites with a Co-, Ni-, or Co/Ni-based binder phase. On the other hand, “cermet” is rarely used for tagging WC-base composites, which are often referred to as “hardmetals” (Europe) or “cemented carbides” (Northamerica) within the tooling industry. Both cermets and hardmetals are extensively employed in metal cutting processes [101]. The reason for this is their outstanding combination of hardness and toughness compared to other cutting materials, such as tool steels or diamond [100,102–106]. In 1927 the German company Friedrich Krupp marketed worldwide the first cemented carbide composed of WC and cobalt, and its properties have been improving since then [107]. However, in recent years, there has been growing interest in finding alternative materials to

conventional hardmetals due to the high and fluctuating price of Co, which is a reflection of its low abundance as well as its toxicity. In this respect, in 2011 WC–Co was included in the “12th Report on Carcinogens” of the US Department of Health & Human Services as one of 240 substances that may increase the risk for cancer as powder material [108–111]. In this regard, Ti(C,N)-based cermets are considered an interesting alternative to conventional WC–Co systems. Although cermets show lower toughness, they exhibit superior properties over cemented carbides in terms of hardness, wear and oxidation resistance [98,101,112,113].

In general, the toughness of cermets is reduced when a selection of the materials and the blending method are chosen to attain better hardness. On the contrary, hardness decreases when aiming to higher toughness [114]. Considering the nature of constitutive phases of cermets, ceramics and metals are mainly responsible for hardness and toughness respectively. This is the most general view of the influence of each phase on the mechanical properties of cermets. However, in order to optimize the microstructural design of cermets for a desired application (e.g. cutting tool), some microstructure-processing correlations have to be taken to account, and they are briefly discussed below.

Ti(C,N)-based cermets have gained considerable attention from researchers since TiC emerged as a potential replacement for WC in the cutting tool field. Furthermore, the beneficial effects of nitrogen in TiC systems have spurred research into the design of materials for new cermet systems. It is known that the presence of nitrogen in the form of Ti(C,N) refines the microstructure and improves the mechanical properties of TiC-based cermets (see Refs. [69,98,101,115–117]). The use of Ti(C,N) is preferred to TiC due to its greater hardness, strength, higher thermal conductivity, and lower mass gain at higher temperatures. **Table 1.3** summarizes some mechanical, chemical and physical properties of both TiC- and Ti(C,N)- based cermets [118].

Table 1.3. Comparison of high-temperature properties of TiC- and Ti(C,N)-based cermets [118].

Cermet	Micro-hardness at 1000 °C (0.2 kg force) (kg/mm ³)	TRS at 900°C (MPa)	Oxidation rate at 1000°C mg/cm ² ·h	λ at 1000 °C (W /m·°C)
TiC-based	500	1050	11.8	24.7
Ti(C,N)-based	600	1360	1.6	42.3

λ : Thermal conductivity

TRS: Transverse rupture strength

Ti(C,N) as the hard phase is a ceramic material with a wide composition range dependent on the ratio of C:N, usually expressed as TiC_{1-x}N_x. The nitrogen content in Ti(C_{1-x}N_x) has a significant effect on the microstructure by changing the stability of Ti(C_{1-x}N_x), resulting in different rates of dissolution. Hard Ti(C,N) particles are combined with a ductile binder phase to yield ceramic-metal composites with capabilities beyond those exhibited by standard WC–Co grades for their application as cutting tools. The stringent demands linked to this application require the use of

Ti(C,N) powder with very fine size and narrow distribution. Various processing strategies are currently used to get Ti(C,N) powder, and detailed information about such production routes can be found in Refs. [119,120]. It has been reported that Ti(C_{0.3}N_{0.7}) is the most stable compound in the 1400 – 1600 °C range [69]. The main physical and mechanical properties of Ti(C,N) are listed in **Table 1.4** [69].

Table 1.4. Summary of the main physical and mechanical properties of Ti(C,N) [69].

Property	Ti(C,N)
Molecular weight (gr/mol)	59.9 – 61.9
Crystallographic structure	FCC
Density (gr/cm ³)	6.0 – 6.8
Melting point (°C)	2950
Microhardness <i>HV</i> 30	1400 – 1750
Transverse rupture strength (MPa)	1400 – 1900
Thermal expansion coefficient (K ⁻¹)	9.0×10 ⁻⁶
Thermal conductivity (W/m.K)	10

The metallic matrices used in Ti(C,N)-based cermets commonly contain Co, which shows a risk of toxicity [108–111]. There are several studies [121–124] that propose the use of Fe as a metallic matrix for cermets, as it is non-toxic and cheaper than Co, with the additional advantage of being able to be hardened by heat treatment. However, the use of Fe as a matrix makes processing more difficult because of the poor wettability of the liquid phase of Ti(C,N) particles during the sintering step (see **Figure 1.8**). Some alloying elements and compounds, such as Ni, Cr, Mo, Mo₂C, and W have been reported to improve the wettability by decreasing the contact angle between the liquid metallic matrix and the ceramic particles (see **Figure 1.8b**) [125–128]. Improvement of the wettability enhances the adhesion between ceramic particles and metallic binder; and thus, the fracture toughness of the composite [124,129]. In cermets, the state of aggregation of the ceramic phase varies not only due to the processing history but also with the binder content. It then ranges from isolated ceramic particles dispersed in the binder to a highly connected skeleton of contiguous ceramic particles, for high binder content to low binder content, respectively [130]. Therefore chemical nature and amount of binder affect directly and indirectly the properties of cermets.

Recent investigations have demonstrated that processing of Ti(C,N) with FeNi alloy by powder metallurgy results in fully-dense cermets with final properties comparable to some cemented carbides [131,132]. Such cermets will be the ceramic-metal multiphase materials to be studied in this thesis.

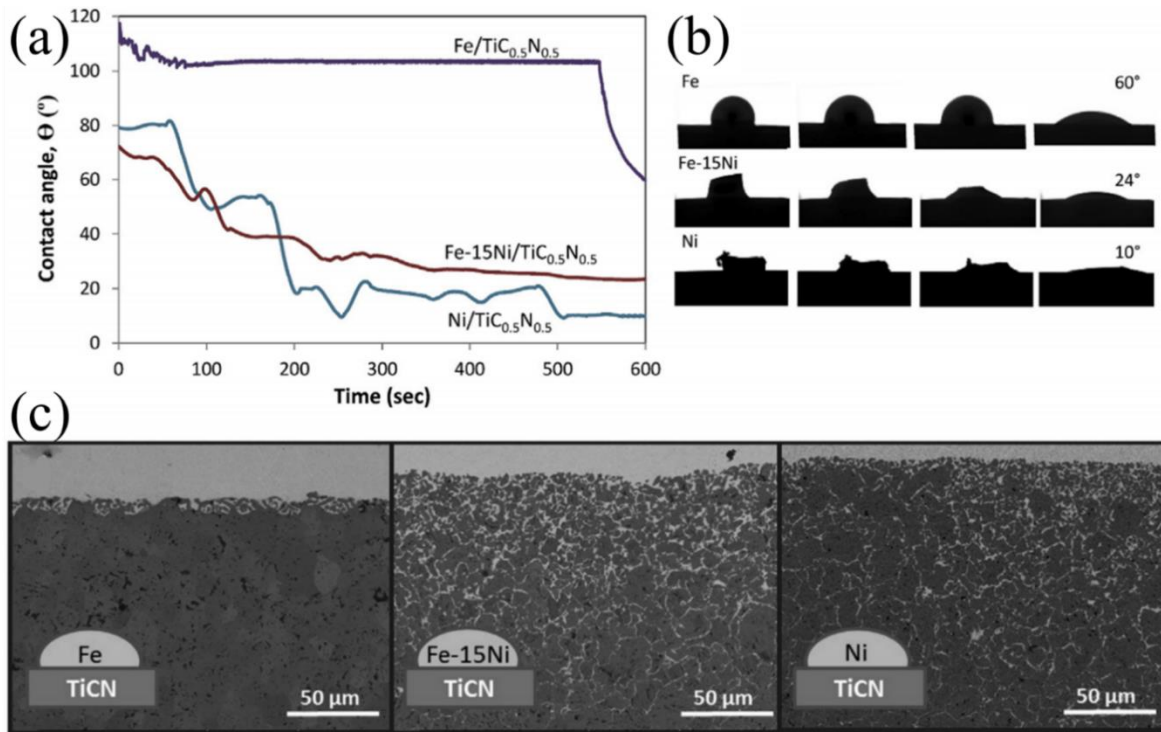


Figure 1.8. (a) Evolution of the contact angle of liquid Fe, Ni and Fe-15Ni in contact with Ti(C,N) substrate with the residence time. (b) Camera shots of the evolution of liquid drop with time. (c) Micrographs of the interface of the systems Fe/Ti(C,N), Fe-15Ni/Ti(C,N) and Ni/Ti(C,N) after high temperature wetting experiments [128].

In the case of using iron-base alloys as the metallic matrix, the carbon content becomes of particular significance too. The addition of a conservative amount of extra carbon has shown to play a dramatic role during the sintering stage, by lowering solidus-liquidus temperatures and improving densification. Moreover, it induces phase transformations in the steel matrix. Therefore, the correlation hardness-fracture toughness of the steel-matrix cermet could be improved by changing the carbon content [133–135]. This aspect will also be addressed in this study. Each alloy and additive has its own effects on processing towards the achievement of the ceramic-metal composite microstructure of the final product.

The interaction of ceramic particles and metallic binder determines the final microstructure of cermets and consequently the mechanical properties. Different variables can be considered as important factors for describing the microstructure of cermets. On one hand, there are single-phase parameters, i.e. grain size of ceramic particles and volume fraction of the metallic constituent. However, in the case of cermets (and cemented carbides), the two phases are often assembled as continuously inter-dispersed networks. Then, other two-phase microstructural parameters, i.e. contiguity of the ceramic phase and binder mean free path (the effective thickness of the metallic phase) are best-suited variables for providing a full description of the microstructure [106,130,136–140]. Detailed information about the microstructural characteristics of cermets is provided in *Section 1.3*.

Binder content and size of the ceramic particles directly affect both hardness and toughness of cermets. Since the metallic phase within these composites is the toughening agent, increasing the binder content definitely raises toughness, and consequently decreases hardness, or vice versa [106,141]. With respect to the influence of the mean grain size of the ceramic particles on the final properties of cermets, it is reported that, for a given binder content, finer microstructures yield higher hardness values than coarser ones [106,141–147]. Classification of the mean grain size of ceramic particles is summarized in **Table 1.5**. The final mean grain size and distribution of the ceramic particles within ceramic-metal composites depend on the size of the starting powders, the milling and sintering conditions, and the composition of the binder [69]. Following the above ideas, it can be stated that high binder contents and coarse grain sizes are the proper microstructural selection in applications requiring a high toughness level and enhanced damage tolerance; whereas low binder contents and fine grain sizes are the best choices in those materials demanding wear resistance and high hardness values [106,148]. **Figure 1.9** shows an example of hardness, fracture toughness, compressive strength and wear resistance evolution of cemented carbides as function of binder content (in *wt. %*) for different ceramic mean grain sizes (in this case WC) [106].

Table 1.5. Grain size classification of cemented carbides [144].

Designation	Ultrafine	Submicron	Fine	Medium	Coarse	Extra coarse
Grain size (μm)	0.2 – 0.5	0.5 – 0.9	0.9 – 1.3	1.3 – 2.5	2.5 – 6	> 6

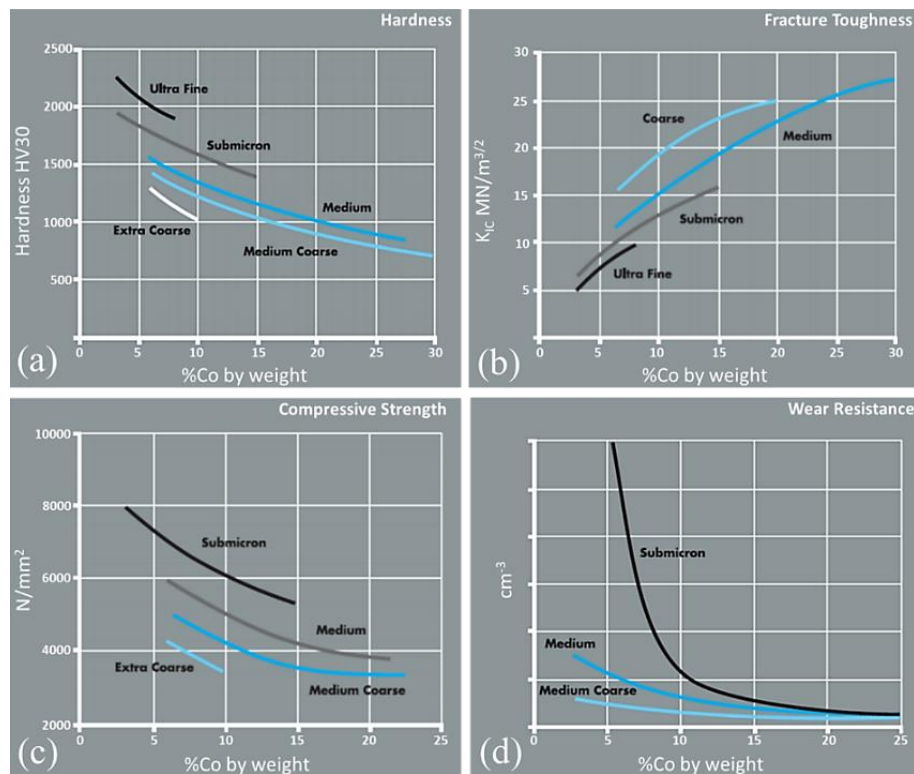


Figure 1.9. Influence of the microstructure on the mechanical properties of cemented carbides: (a) hardness, (b) fracture toughness, (c) compressive strength, and (d) wear resistance, as a function of the binder content for different carbide mean grain sizes [149].

1.2 Assessing the influence of microstructure-processing correlations on bulk mechanical properties of multiphase systems

In the previous section different studied multiphase materials, intrinsic microstructure-processing correlations that may affect their bulk properties, and their main applications have been introduced and briefly discussed. Although it is evident that microstructural and processing aspects affect the final properties of the considered materials, assessment of the specific influence of a given factor in the mechanical response of multiphase systems is rather complicated.

Regarding the metal-metal system chosen for this study. It has been proven that some alloying elements like nitrogen can change the hardness of the DSS grade, by modifying the phase content and local hardness of each constitutive phase [29,150–152]. However, the effective influence of nitrogen on modifying phase content and/or intrinsic hardness of ferrite and austenite is somehow unknown, and the corresponding assessment is not trivial.

Concerning the ceramic-ceramic system to be addressed in this thesis, synthesis temperature and/or pressure can modify the density and assemblage of the cBN grains as well as their reaction with the corresponding binder; and thus, the final hardness of PcBN composites [59,70,72,77]. Within this context, evaluation of the effective influence of individual microstructural and/or processing parameters, including their interactions with others, on final hardness is complex.

Finally, the above ideas also apply to cermets. It has been reported that heat treatment or carbon addition can modify the hardness of Ti(C,N)-Fe based cermets, by improving the microstructure assemblage (enhance the homogeneity and densification) and also work hardening of the metallic binder [121–124]. However, knowledge and understanding of the metallic binder contribution, in terms of phase content and work hardening, to increase the global hardness of cermets is quite scarce.

Within the above framework, it is clear that proper and satisfactory assessment of the local mechanical properties of each constitutive phase and their interactions is required to enhance the microstructural design of multiphase materials. In this regard, a clear definition and reliable characterization of the most relevant microstructural parameters which can affect the mechanical properties, specific for each multiphase system under consideration, is also needed.

1.3 Microstructural parameters

Microstructural characterization of materials definitely has played an important role in solving important problems in the fields of solid-state physics and chemistry, as well as materials research and technology during the past decades. Based on the close correlation between microstructure

and properties of materials, characterization at the sub-micrometric length scale is one of the key tasks in these fields [153].

There are different microstructural parameters in the material science realm, depending on the research field and studied material. Regarding the microstructural design of multiphase materials, the main microstructural parameters which need to be taken into account will be introduced in this section.

The principal and common parameters to characterize the microstructure of the studied inorganic multiphase systems are the content and characteristic physical dimension of each phase. Some of these systems, as it could be the case of the “ceramic-ceramic” and “ceramic-metal” composites addressed in this work, involve interpenetrating phase networks. Under these conditions, additional two-phase microstructural parameters may be defined aiming to capture the concomitant effects of the independent single-phase variables. They are usually referred to as binder mean free path (λ_{binder}) and contiguity of the hard phase ($C_{hard\ phase}$) [136,137,145]. **Figure 1.10** displays the main microstructural parameters of the studied multiphase materials.

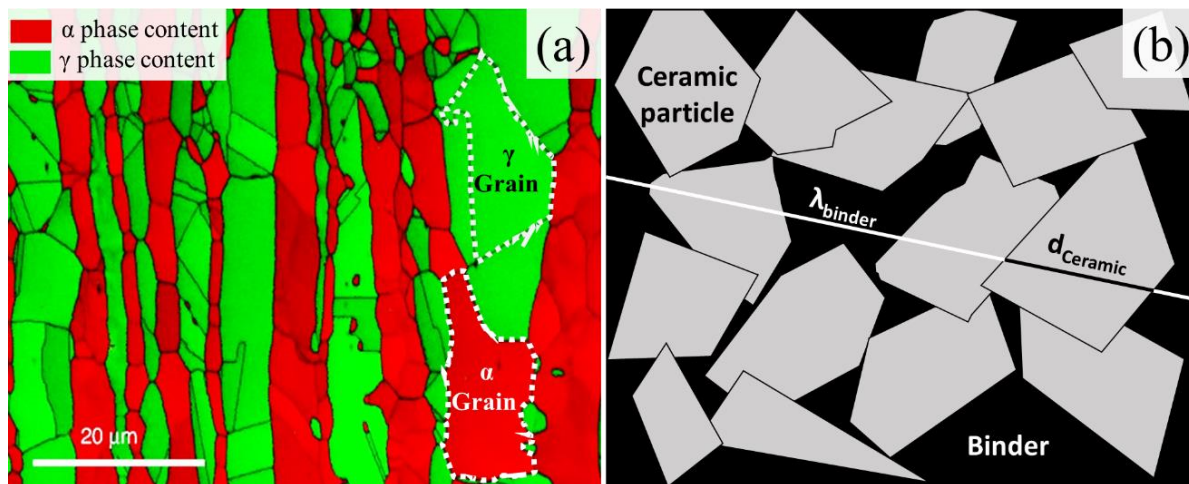


Figure 1.10. Main microstructural parameters for (a) DSS (adapted from [154]), (b) PcBN and cermets.

1.3.1 Phase content

Phase content may be defined as the area occupied by each phase on the studied surface of micrographs of a multiphase system. The surface fraction can be considered as a $2D$ parameter, which can be taken as a representative measurement of the volume content of each phase (binder content for PcBN composite and cermets, which will be discussed further below). As explained before, depending on the multiphase system, phase content can be tailored by alloying elements and/or processing routes. Since each phase has its own influence on the final mechanical properties of multiphase systems, phase content (or surface fraction) in conjunction with the corresponding

intrinsic mechanical response, may help us to find the correlation between local and bulk mechanical properties. The surface/volume fraction of each phase can be determined by using the following equation:

$$P_i = \frac{A_i}{A_{total}} \quad \text{Equation 1.4}$$

where P_i is the content of i phase, A_i is the total area occupied by phase i , and A_{total} is the total calculated area, composed from constitutive phases within the micrograph. The total phase fraction of constitutive phases is 1, which means:

$$P_1 + P_2 + P_3 + \dots + P_n = \sum P_i = 1 \quad \text{Equation 1.5}$$

1.3.2 Grain size

Mean grain size is a statistical concept that refers to the average dimension of a characteristic length for the system under consideration. In the case of DSS, it must be recalled for both γ - and α - phases, whereas for PcBN composite and cermet, it is mainly assessed on the hard ceramic particles. Grain size may be considered as one of the most important microstructural parameters to be characterized as its influence on mechanical properties is quite relevant. As a consequence, the effect of processing routes and alloying elements on grain size for the different multiphase systems under consideration becomes then significant, from a microstructural design viewpoint.

The most commonly used method to determine the grain size is the linear interception (LI) method, implemented on images obtained by means of the scanning electron microscope (SEM). LI method is the simplest procedure to use and has the added advantage of providing data that can be used to quantify distribution width. This method requires a straight line to be drawn across a calibrated image. In a single-phase material the length of the line (L), starting at a random position, traversing a number of grain boundaries (N_g), and ending at another random position, is measured (see **Figure 1.11a**). The mean-linear-intercept distance LI is thus [155]:

$$LI = L/N_g \quad \text{Equation 1.6}$$

As can be seen from the above equation, only the mean-linear-intercept distance is calculated. On the other hand, there is not any information obtained on grain-size distribution. For a nominally two/multi-phase material such as DSSs (γ - and α - phases), PcBN composite, or cermets, the LI technique is less straightforward, because each phase has to be measured independently, but it can provide information on grain-size distribution. It is advisable to count a relatively large number of

grains, i.e. between 100 and 200 grains, in order to reduce the uncertainty to relatively low values, i.e. below 10%. The mean-linear-intercept grain size (d_{grain}) is defined as [155]:

$$d_{grain} = \sum l_i / n \quad \text{Equation 1.7}$$

where l_i (linear-intercept length) is defined by the measured length of line overlaying each metallic phase or ceramic particle, such that $i = 1, 2, 3 \dots n$, refers to the 1st, 2nd, 3rd, ..., nth grain. The length of each interval (l_i) is measured using a calibrated rule (see **Figure 1.11b**).

Figure 1.11 shows lines drawn across the micrographs of metallic and cermet microstructure. Lines are numbered from 1-10 (L_1 - L_{10}) which are shown on the right side of **Figure 1.11**.

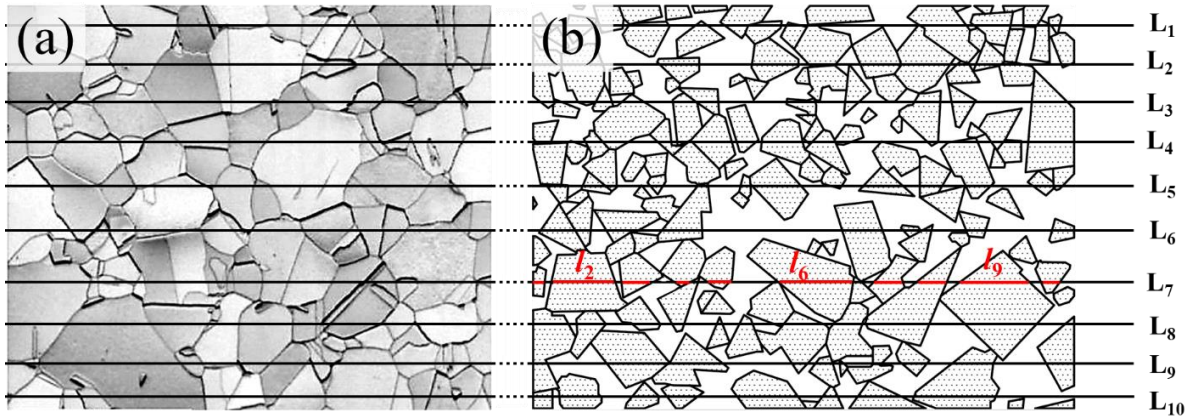


Figure 1.11. Linear-intercept lines drawn across idealized: (a) metal structures, (b) cermet microstructure (adapted from [156] and [155] respectively).

Generally, grain sizes of studied multiphase materials can vary over a wide range, from less than 1 μm up to 20 μm . Because of the uncertainties of measurement, it is good practice to report the mean-linear-intercept grain size to one decimal place for values $> 1.0 \mu\text{m}$ and to two decimal places for values $< 1.0 \mu\text{m}$ [155].

1.3.3 Binder content

Binder is a constitutive phase whose main function is to stick or mix together the other phases. This definition is applicable for PcBN composite and cermets, in which ceramic particles are held by a connected network of other material which is the binder. The quantity of binder (binder content) is another main microstructural parameter, as its influence on the mechanical properties (mainly hardness and toughness) of PcBN composite and cermets is quite significant. Binder content is commonly given in weight percentage (*wt. %*), but the use of the volume percentage (*vol. %*) or the volume fraction (V_{binder}) can be a more informative value [137]. In the case of the

cermet systems studied in this work, conversion of *wt. %* to V_{binder} can be done by applying the following expression:

$$V_{binder} = \frac{1 + \frac{1 - V_{binder}^{wt}}{V_{binder}^{wt} \rho_{Ti(C,N)}} (\rho_{Ti(C,N)} - \rho_c)}{1 + \frac{1 - V_{binder}^{wt}}{V_{binder}^{wt}}} \quad \text{Equation 1.8}$$

where V_{binder} is the binder content in volume, V_{binder}^{wt} is the binder content in weight, $\rho_{Ti(C,N)}$ is the density for the Ti(C,N) (6.0 – 6.8 gr/cm³ [69]) and ρ_c is the experimental density of the composite system.

1.3.4 Contiguity

Contiguity (C_i) is a measure of the proportion of the ceramic/ceramic particle contacts in the microstructure, which effectively form a skeleton of the hard phase (in PcBN and cermets). Contiguity was defined by Gurland for the WC-Co system as “the fraction of the total internal surface area of a phase that is shared by particles of the same phase” [106,130,157]. It somehow measures the extent of the ceramic grain boundary area relative to the total surface area of the hard phase grains [130]. Therefore, by definition, the C_i can vary between 0 and 1. In ceramic-metal systems, the contiguity of the ceramic phase has been assumed to tend to zero when the metallic binder volume fraction tends to one, and vice versa. Measured values of contiguity have confirmed that the contiguity of the ceramic phase in ceramic-metal composite decreases as the metallic binder content rises [158].

In a two-phase composite of constituents A and B, **Equation 1.9** provides the contiguity of phase A (C_A):

$$C_A = \frac{2N_{AA}}{2N_{AA} + 2N_{AB}} \quad \text{Equation 1.9}$$

where N_{AA} is the intersection points of the contact surface of A phase sectioned with test lines, and N_{AB} is the intersection points of the contact surface between phases A and B sectioned with test lines [157]. Values of contiguity for a fixed volumetric content of binder are extremely scattered. It could be attributed to the grain size distribution of the ceramic phase, the shape of the grains or the binder content [137,158–160].

Roebuck and Bennett [161] studied the contiguity as a function of the binder content (V_{binder}) for a series of hardmetals, and proposed the following empirical relation:

$$C_c(V_{binder})^n = D \quad \text{Equation 1.10}$$

where the best fitting is obtained when n and D constants take values of 0.45 and 0.20, respectively.

The contiguity is also simply related to the binder volume fraction (V_b) and the mean free path in the binder phase l_b and ceramic grains l_c^G [158], as presented in **Equation 1.11**

$$C = 1 - \frac{V_b}{\frac{l_b}{l_c^G}(1 - V_b)} \quad \text{Equation 1.11}$$

It is necessary to highlight that contiguity is a two-phase microstructural parameter, which is mainly used for hardmetals (WC-Co). In general, it is not considered in ceramic-ceramic systems like PcBN composites, because they may not exhibit interpenetrated phase networks, particularly for the intermediate or low volume fraction of cBN grains (40 – 60%). When the volume fraction of the cBN grains in PcBN cutting tools is less than 70%, ultrafine powders of a secondary hard phase are purposely incorporated in the binder phase as grain growth inhibitors, to prevent or reduce grain growth of the latter during the high temperature – ultra high pressure process [162].

1.3.5 Mean free path

The mean free path is also called the mean linear intercept in the binder phase (λ_{binder}). It is used to describe the effective size of this phase, under constraining conditions, in cemented carbides. It is the most important parameter to characterize the length scale of the binder phase, due to its inverse relationship with the specific surface of the binder phase (ceramic/binder interface per unit volume of binder) [136]. This microstructural parameter along with contiguity of the ceramic phase and volume fraction of binder, constitute the primary microstructural parameters of cermets. They are interrelated, similar to the description proposed by Lee and Gurland for hardmetals [158], according to **Equation 1.12**, even for varying binder phase content and sintering conditions, as follows:

$$\lambda_{binder} = \frac{1}{1 - C_{Ti(C,N)}} \frac{V_{binder}}{V_{Ti(C,N)}} d_{Ti(C,N)} \quad \text{Equation 1.12}$$

where $V_{Ti(C,N)}$ is the volume fraction of Ti(C,N) particles. The λ_{binder} increases when rising the Ti(C,N) mean grain size and/or the volume fraction of binder. An increase in λ_{binder} results in higher fracture toughness of the composite; and thus, in lower hardness [137].

The mean free path values could be also measured by the LI method, particularly for PcBN composite, where there is no specific correlation to estimate this parameter. In this regard, the LI method is also recommended as it is a direct one and might be more accurate.

1.4 Length scale issues on the measurement of hardness, as a representative mechanical property of multiphase systems

As it was explained before, the properties of a material are critical to assert whether the material is eligible for a given application. Within this context, focusing on the typical applications of DSSs, PcBN composite and cermets, mechanical properties become critical for the effective implementation of these materials. Moreover, it has been mentioned that, besides the mechanical response at the bulk level, intrinsic properties of the constitutive phases play a crucial role towards optimization of the microstructural design of multiphase systems. However, assessment of these small-scale mechanical properties is challenging, particularly in terms of identification and availability of advanced techniques to measure them at different length scales. This requires a critical analysis of physical and microstructural length scales, which may be different for the multiphase systems under consideration.

Within the above framework, mechanical and physical reactions of the materials induced by indentation have proven to be effective for supplying broad ranges of information to characterize the structure and mechanical properties of the materials along different length scales, from macro- to pico metric levels.

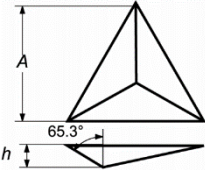
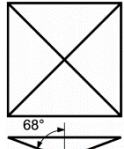
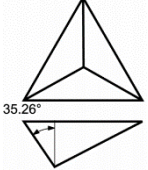
Indentation testing is one of the most common techniques to characterize the hardness (H) of a given material. Hardness has been defined as “material's resistance to plastic deformation”, although it is also used to recall resistance to scratching, abrasion or cutting. In metals, ceramics, and most of polymers, the hardness is related to the plastic deformation of the surface. This property is somehow referred to as representative of the mechanical response of a structural material, as it has – directly or indirectly – a close relation to other properties like strength and ductility. Moreover, hardness testing is extensively used in the industry as it is a relatively simple, fast and cheap quality control method for materials.

Depending on the characteristics of the indentation (indenter size and geometry, the value of applied load and displacement into the surface) and the strain field (i.e. plastic response of the bulk material, a phase or a particle), indentation testing methods can be classified as macro-, micro-, nano- and pico-indentation [163,164].

The usual method to assess a hardness value is to measure the depth or area of an imprint left by an indenter of a specific shape, with a specific force applied for a specific time [165,166]. The

shape of the indenters can be divided into two main types: blunt and sharp. Blunt types comprise spherical indenters, flat punches, sphero-conical indenters, among others, and they are characterized by the fact that during the first stages of contact with the material, they produce an elastic response on it. It means that, within an instrumented indentation test, the unloading curve is equal to the loading curve, and there the material is not permanently deformed. Upon further loading, the response of the material becomes elasto-plastic producing a residual imprint. Sharp probes, on the other hand, induce an elasto-plastic imprint from the beginning of the loading cycle, due to the fact that, in theory, the indenter tip has a null area, producing a stress singularity in the material. Sharp probes usually present a constant face angle; hence, the response of the material is self-similar for all penetration depths. Sharp tips are usually conical or pyramidal, being Vickers (4-side), cube-corner (3-side) and Berkovich (3-side) the most usual ones. Regarding the desired information and mechanical properties required, three different indenters: Vickers, Berkovich and cube-corner, have been employed in this work. They are briefly explained in **Table 1.6**.

Table 1.6. Name, application, shape and contact area of the different indenters used in this work.

Indenter	Application	Shape and contact area [167]
Berkovich	Three-face design allows grinding the tip to a sharp point. Mainly used for carrying out nanoindentation to measure hardness and elastic modulus. It is also suitable for bulk materials, thin-films, polymers, scratch and wear testing [168].	 $A=24.56h^2$
Vickers	Pyramidal diamond tip. Used for evaluating micro-hardness of different systems (HV), as well as scratch and wear testing, of bulk materials, films and foils [168].	 $A=24.50h^2$
Cube-corner	Three-sided pyramidal tip with perpendicular faces. It is suitable for thin-film scratch testing, indentation fracture toughness and wear testing [168].	 $A=24.60h^2$

Indentation hardness measurement could be performed at macro-, micro- and nanometric length scales. Hardness values at different length scales may follow an increasing or decreasing trend. This phenomenon is called the indentation size effect (ISE) and will be discussed later.

For macro-scale indentation, as shown in **Figure 1.12a**, the large Vickers residual imprint interacts with a relatively large number of grains, which then averages the sample in homogeneity. Therefore, a mean bulk hardness value is obtained. In the case of a micro-scale indentation, as indicated in **Figure 1.12b**, Vickers indenter probes fewer grains/crystals; thus, mean hardness

values could be attained, while variations in small areas can also be assessed. Micro-scale indentations tests could be implemented to characterize segregation and banding, identify constituents, and characterize surface hardness/microstructure [165]. Finally, black triangles, which are shown in **Figure 1.12c**, represent nanoindentations performed by Berkovich or cube-corner indenter. These imprints (nanoindentations) can be confined within different grains/phases (A and B imprints) and measure the hardness/elastic modulus of each one (local mechanical properties), or probe some interphase-like regions (imprint C), and assess the average/composite mechanical properties of different grains/phases.

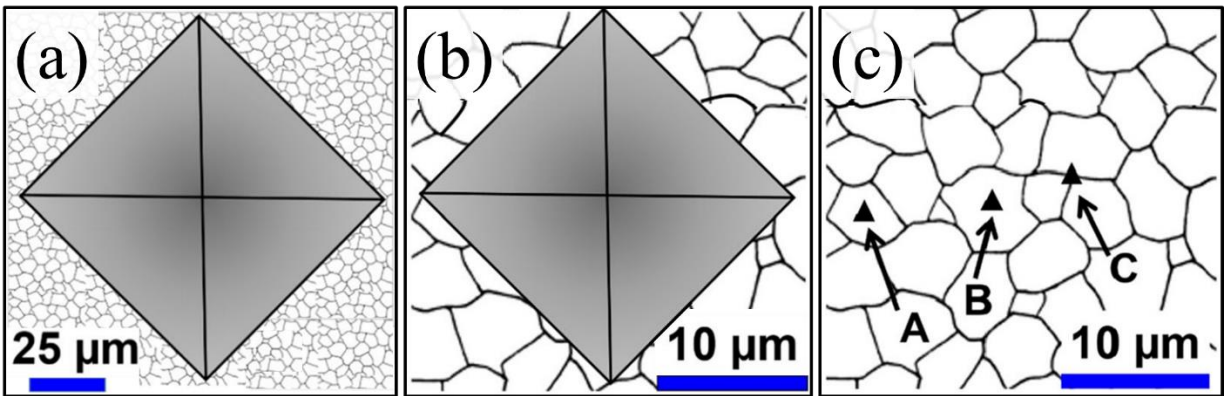


Figure 1.12. Scheme of indentation hardness of a polycrystalline/multiphase material at (a) macro-scale, (b) micro-scale, and (c) nano-scale [165].

Micro-indentation tests are characterized by indentations loads (P) in the range of $P < 2$ N and penetrations $h > 0.2$ μm [169]. There are two main methods used at this scale: Vickers and Knoop indentation tests. These indentation hardness tests determine the material resistance to the penetration of a diamond pyramid-shaped indenter. Micro-hardness is correlated with the depth that indenter will sink into the material, under a given load, during a specific period of time [165].

Vickers Hardness (HV) test was performed due to its advantages compared with other methods. For instance, the HV test leaves only tiny indentations that are usually not a problem for final components or tools, making it suitable for quality control. The other advantage of the Vickers system, besides the increased degree of accuracy, is that it provides simple data and does not have several different scales and indenters, as does Rockwell and Brinell scales. It also has a constant hardness value for homogeneous materials, regardless of the size of the applied load. It is suitable for testing small parts, thin plates, metal foils, electroplated layers and non-metallic materials such as glass. It can be used for extremely soft and hard materials [170].

HV is determined by using the following **Equations 1.13** and **1.14**:

$$A = \frac{d^2}{2 \sin(136^\circ/2)} \approx \frac{d^2}{1.8544} \quad \text{Equation 1.13}$$

$$HV = \frac{F}{A} = \frac{1.8544 F}{d^2} \quad \text{Equation 1.14}$$

where d is the diagonal of the residual imprints (mm), F is the applied force by the diamond tip in kilograms-force (kgf), and A is the surface area of the resulting indentation in square millimeters (mm^2).

As the length scale decreases, nanoindentation emerges as the appropriated technique. It is similar to the macro- and micro-hardness tests, in which an indenter of known geometry is pressed into a material and produces both elastic and plastic deformation into it. The main advantage of the nanoindentation technique is that it allows probing small volumes of material. Thus, the local mechanical properties of each phase (in multiphase materials) may be determined by performing shallow imprints. Moreover, this technique gives information about the mechanical response of the surface, which is crucial to understand the behavior of the material in applications where concentrated surface loadings are expected [167]. The first technical difference with macro- or micro-indentation tests is that nanoindentation machines continuously records the displacement/penetration depth (h) and the applied load (P) with high precision for both the loading and the unloading cycles [165,167]. Moreover, compared with traditional hardness testing, nanoindentation presents several advantages: evaluation of the mechanical response of the constitutive phases heterogeneously distributed in the bulk; possible setting of penetration depth (h) and/or maximum applied load (P_{max}); direct determination of the elastic modulus (E); testing of specimens whose volume may be as small as tens of cubic microns; and measurement of the mechanical properties without the need to visualize the residual imprint [164].

Figure 1.13 shows a typical P - h curve performed with a sharp indenter. It is appreciated that the unloading curve (generally associated with a pure elastic deformation) is different from the loading one (linked to an elasto-plastic deformation) as it returns to a residual depth (h_{final}) different from zero. This indicates a permanent deformation which results in a hardness imprint. By recurring to different analysis methodologies of the P - h curves it is possible to extract material parameters, such as instrumented indentation testing hardness and elastic modulus, without the visualization of the residual imprint. During the nanoindentation process, the indenter will penetrate the sample until a predetermined maximum load P_{max} is reached, where the corresponding penetration depth is h_{max} . When the indenter is withdrawn from the sample, the unloading displacement is also continuously monitored until the zero load is reached and a final or residual penetration depth

(h_{final}) is measured. The slope of the upper portion of the unloading curve, denoted as $S = dP/dh$, is called the elastic contact stiffness [165].

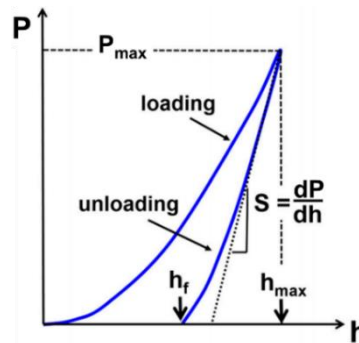


Figure 1.13. Typical P - h curve obtained during loading and unloading of the indentation process [165].

Hardness (H) and elastic modulus (E) are the most commonly measured properties as a function of the displacement into the surface (h), determined by virtue of the continuous stiffness module (CSM). The indented area after unloading will be extremely small (nanometers or few micrometers size); therefore, calculating the area by optical methods is not appropriated. However, several methods have been proposed to calculate the area directly from the loading-unloading curve. Oliver and Pharr developed a method [171,172] to calculate H and E accurately from the indentation load-displacement data (P - h curve), without any need to measure the deformed area with a microscope [165]. Oliver and Pharr's method was originally implemented for application with sharp indenters, like Berkovich [168]. The exact procedure used in order to measure H is based on the unloading process shown schematically in **Figure 1.14** in which it is assumed that the behavior of the Berkovich indenter can be modeled as it will be a conical indenter [168].

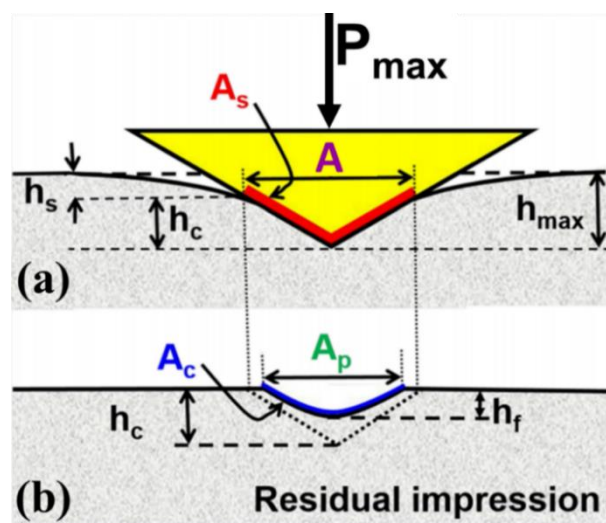


Figure 1.14. (a) Elasto-plastic deformation at the maximum applied load P_{max} . (b) Plastic deformation after releasing the load [165].

Regarding nanoindentation hardness measurement, and referring to **Figure 1.14**, H is defined as:

$$H = \frac{P_{max}}{A(h_c)} \quad \text{Equation 1.15}$$

where P_{max} is the maximum applied load and $A(h_c)$ is the projected area of contact at P_{max} .

The analysis used by Oliver and Pharr to determine the hardness and the elastic modulus is essentially an extension of the method proposed by Doener and Nix [173]. This is based on the fact that unloading curves are distinctly curved in a manner that cannot be accounted for by a simple flat punch approximation. These authors considered that the contact area remains constant as the indenter is withdrawn, and the resulting unloading curve is linear. The Oliver and Pharr method [171,172] begins by fitting the unloading portion of the P - h curve to a power-law relation of type:

$$P = B \cdot A \cdot (h - h_{final})^m \quad \text{Equation 1.16}$$

where B and m are power-law fitting constants, and h_{final} is the displacement after complete unloading, also determined from the curve fit. Contact stiffness (S) can be obtained by differentiating the unloading curve fit, and evaluating the result at the maximum depth of penetration ($h = h_{max}$), which gives:

$$S = B \cdot m \cdot (h_{max} - h_f)^{m-1} \quad \text{Equation 1.17}$$

Consequently, S can be determined with **Equation 1.17**, to fit only the upper portion of the unloading curve. Moreover, the value of S determined from this fit should be checked by comparing the curve fit to the data. Fitting the upper 25 to 50% of the data (the linear part) is usually sufficient.

This allows to calculate the contact depth h_c , which for elastic contact is less than the total depth of penetration (h_{max}), as illustrated in **Figure 1.14**. The basic assumption is that the contact periphery sinks in a manner that can be described by models of indentation of a flat elastic half-space by rigid punches of simple geometry [174]. This assumption limits the applicability of the method because it does not account for the pile-up material at the contact periphery that occurs on some elastic-plastic materials. However, assuming that pile-up is negligible; the elastic models show that the amount of sink-in, h_s , is given by the following equation:

$$h_s = \varepsilon \cdot \frac{P_{max}}{S} \quad \text{Equation 1.18}$$

where ε is a constant that depends on the geometry of the indenter. Typical values are 0.72 for a conical punch indenter, 0.75 for a parabolic of revolution (Berkovich and cube-corner) one, and 1 for a flat punch. From the geometry of **Figure 1.14**, the depth along contact made between the indenter and the specimen and **Equation 1.18**, h_c can be calculated by:

$$h_c = h_{max} - h_s = h_{max} - \varepsilon \cdot \frac{P_{max}}{S} \quad \text{Equation 1.19}$$

The projected contact area (A) is calculated by evaluating an empirically determined indenter area as a function of $A=f(h)$ at the contact depth h_c ; that can be re-written as $A=f(h_c)$ [168]. Therefore, for Berkovich indenter, the one used in this work, the projected area of contact will be:

$$A = 3\sqrt{3}h_c^2 \tan^2 \theta = 24.5h_c^2 \quad \text{Equation 1.20}$$

where $\theta = 130.6^\circ$ is the angle of the Berkovich indenter.

One interesting characteristic of the Oliver and Pharr method is the possibility to calculate elastic modulus in addition to the hardness of the material. Therefore, the effective Young's modulus (E_{eff}) can be determined as a function of S , A and β constant, which depends on the geometry of the indenter ($E_{eff} = f(S, A, \beta)$).

$$E_{eff} = \frac{\sqrt{\pi}}{2 \cdot \beta} \cdot \frac{S}{\sqrt{A}} \quad \text{Equation 1.21}$$

Equation 1.21 is found in elastic contact theory and holds for any indenter that can be described as a body revolution of a smooth function. Since this equation was derived for an axisymmetric indenter, it formally applied only to circular contacts, for which the indenter geometry parameter is $\beta = 1$. However, it has been shown that the equation works equally well when the geometry is not axisymmetric, provided that different values of β are used [174]. For indenters with triangular cross-sections, like Berkovich and the cube-corner ones, $\beta = 1.034$ [171].

An effective modulus (E_{eff}) is used in **Equation 1.21** to account for the fact that elastic displacements occur in both the indenter and the sample. The elastic modulus of the studied material (E) may be obtained from E_{eff} as follows:

$$\frac{1}{E_{eff}} = \frac{1 - \nu^2}{E} + \frac{1 - \nu_i^2}{E_i} \quad \text{Equation 1.22}$$

where ν and E are the Poisson's ratio and the elastic modulus for the test material respectively. The sub-index i denote the value of the indenter, which in the case of being made of diamond are: $E_i = 1141$ GPa and $\nu_i = 0.07$ [175,176].

Indentation size effect (ISE) is a representative example of “smaller is stronger” in materials. It is well established that, in general, the hardness increases with the decrease in the applied load (**Figure 1.15**). Through the use of geometrically self-similar indenters such as cones and pyramids, the size effect is manifested as an increase in hardness with decreasing depth of penetration and becomes important at depths of less than approximately $1 \mu\text{m}$. At low applied loads i.e. low penetration depths, hardness values are higher than those obtained at higher loads; this phenomenon is referred to as ISE [164,177].

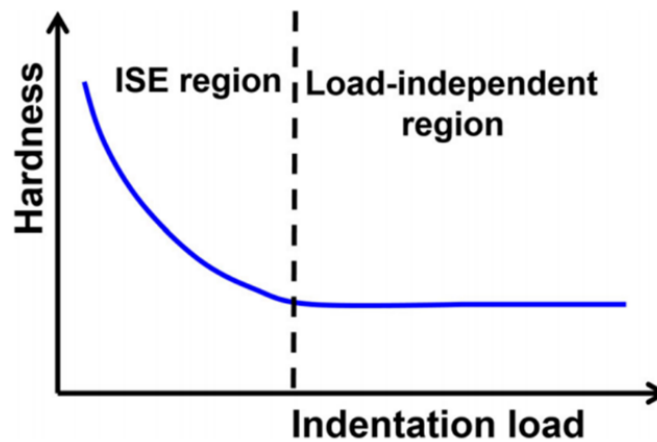


Figure 1.15. Schematic representation of the indentation size effect [165].

Nix and Gao [178] proposed the following relation (**Equation 1.23**) to determine accurately the hardness (H) taking into account ISE effect:

$$\frac{H}{H_0} = \sqrt{1 + \frac{h^*}{h}} \quad \text{Equation 1.23}$$

where H is the hardness for a given depth of indentation h , H_0 is the hardness in the limit of infinite depth, and h^* is a characteristic length that depends on the shape of the indenter [178]. This phenomenon is caused by possible combinations of several mechanisms as strain gradients effects, the roughness of specimen surface, irregularities of the deformed volume, and activation of different mechanisms in the elastic/plastic deformation [164,178].

1.5 Challenges of using nanoindentation technique to evaluate the local mechanical properties of multiphase systems

As discussed in the previous section, the nanoindentation technique could be a suitable option to evaluate the mechanical properties of materials through different length scales. Consequently, it may provide the local mechanical response of individual grains/phases and lead to evaluate small-scale properties of multiphase systems.

Typically in order to evaluate the mechanical properties of any single-phase material by nanoindentation technique, there are some general aspects, which can make this method challenging to use under specific conditions [179], as follows:

- Thermal drift: It is very important to perform the test in as short a time as possible to avoid any thermal drift [180]. For instance, for a maximum penetration depth of about 50 nm and testing time of 1 minute, error due to thermal drift may completely swamp the true penetration reading.
- Indenter tip radius: The objective is to have a fully-developed plastic zone in the material whose properties are to be measured. In this regard having a sharp tip for performing the test is vital [180].
- Good surface finish (surface roughness): A mirror surface finish of a sample is required prior to the nanoindentation test [180]. In the case of surface roughness being too high, relative to the maximum penetration and also tip radius, then the assumption of a semi-infinite specimen embodied in the contact equations will be invalid.

1.5.1 Nanoindentation technique as applied to multiphase materials

Apart from the mentioned challenges of indentation tests, it has to be mentioned that implementing **Equations 1.15, 1.21 and 1.22** on multiphase materials is challenging since the underlying contact mechanics analyses are based on the self-similarity of indentation test on an infinite half-space. This is particularly applicable for homogenous materials that obey the separation of scale conditions:

$$D \ll \mathcal{L} \ll h \quad \text{Equation 1.24}$$

where \mathcal{L} is the representative volume element (RVE). It has to be higher than D , i.e. the characteristic size of the microstructural/mechanical heterogeneity contained in the RVE; and considerably smaller than indentation depth (h), which defines the order of the length magnitude

of the strain gradient variation in the microstructure. Therefore, obtained mechanical properties from indentation data are averaged quantities characteristic of a material length scale defined by the penetration depth of the performed indentation (h). The characteristic size of the indented area is of the order of $3h$ for Berkovich indentation. Thus, the penetration depth of applied indentation plays the main role to evaluate the mechanical properties of composite or its constitutive phases [181,182].

For a multiphase material that is composed of N phases (with different mechanical properties), as far as the maximum penetration depth of performed indentation (h) is much larger than the characteristic size (D) of the individual phases – such that the ratio of penetration depth and characteristic size of each phase is greater than 6 ($h/D > 6$) –, the extracted properties correspond to the average response of the composite material (**Figures 1.16a** and **1.16b**). On the other hand, as long as the maximum penetration depth is much smaller than the characteristic size of individual phases – such that $h/D < 0.1$ –, then a single imprint can determine the mechanical properties of the indented phase i (**Figures 1.16c**, **1.16d** and **1.17a**) [182–184].

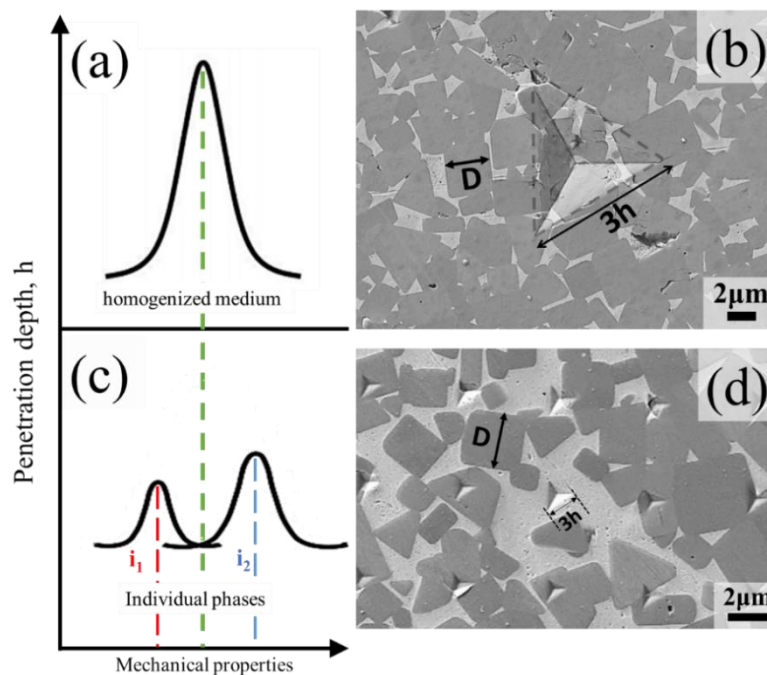


Figure 1.16. Mechanical properties evaluation of multiphase material by (a) and (b) performing deep indentation, (c) and (d) shallow imprints.

Although the chosen penetration depth has to obey the 1/10-rule of Buckle ($h/D < 0.1$) [183], it has to be considered that in the case that penetration depth is very small, the obtained values can be affected by ISE. The minimum penetration depth (h_{min}) is a value for which ISE and tip defects may be disregarded. Such a value is attained by plotting the ratio between applied load and stiffness squared (P/S^2), as a function of the displacement into the surface, and corresponds to the

penetration depth wherein the ratio will reach to a plateau (see **Figure 1.17b**). In general, it is recommended to keep the minimum penetration depth higher than 150 nm ($h_{min} \geq 150$ nm), to avoid any ISE [185–187].

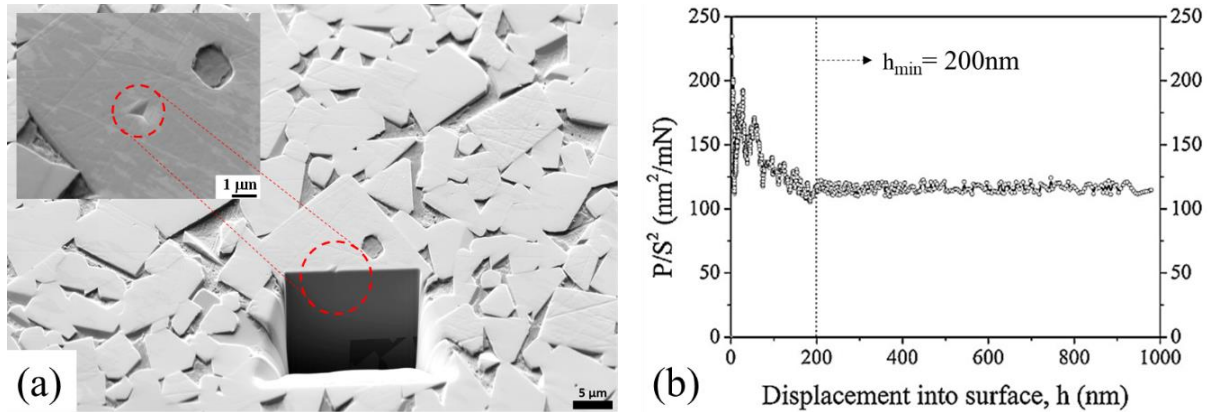


Figure 1.17. (a) Confined indentation within a WC grain of a WC-Co system. (b) Minimum penetration depth obtained from plotting P/S^2 as a function of displacement into the surface [188].

Therefore the suitable penetration depth to extract the intrinsic properties of each phase has to be chosen by satisfying the following condition:

$$h_{min} < h < h_{max} \quad \text{Equation 1.25}$$

Moreover, considering a matrix of indentations involving a large number of imprints ($N_i \gg 1$) that is performed (**Figure 1.16d**) on the surface of a multiphase material, it should be aimed that the grid spacing (ℓ) is greater than the characteristic size of the imprint to guarantee that no overlapping/ neighboring effect (interference) of the residual imprints occurs. It has been reported that the distance between each imprint has to be *i*) kept 10 times more than the penetration depth [189], and *ii*) much larger than the characteristic size of individual phases ($\ell/\sqrt{N} \gg D$). In doing so, the probability of indenting each phase is related to the surface fraction occupied by each of them on the indented surface. Therefore, as far as the grid size is large enough, a similar distribution of different phases (surface fraction) can be determined on the indented surface; and consequently, the surface fraction can be assimilated with the volume fraction of the multiphase (isotropic) material [181,182], as:

$$f_i = \frac{N_i}{N}; \quad \sum_{i=1}^n N_i = N \quad \text{Equation 1.26}$$

where f_i is the volume fraction of each mechanically distinct phase, and N_i is the number of imprints performed on phase i [181,182].

Taking into account all the above conditions, the gedanken experiment can be considered as a suitable test that contains all ingredients of statistical indentation analysis to be implemented on multiphase materials, in order to obtain the local mechanical properties of each constitutive phase. The gedanken experiment is based on the premise that each phase (i) has different properties (p_i) of sufficient contrast, such that these can be separated in small-scale indentation tests. Composite materials are generally more complex, requiring the use of some elementary statistics relations to analyze the indentation data [181,182].

1.5.2 Statistical analysis

Matrices of indentations have to be performed on multiphase materials with different fixed variables (penetration depth/applied load, array size and spacing between imprints). Consequently, the statistical method proposed by Ulm *et al.* [10,181,182,190] will be implemented on obtained results from massive indentation tests to determine the mechanical properties of each constitutive phase within multiphase systems studied.

As mentioned above, in order to execute the statistical analysis, it is assumed that the studied samples have a heterogeneous microstructure composed of various (i) constitutive phases that are mechanically distinct. In addition, the desired mechanical properties of each constitutive phase are assumed to follow a Gaussian distribution (p_i) (**Figure 1.16c**) described by **Equation 1.27**.

$$p_i = \frac{1}{\sqrt{2\pi\sigma_i^2}} \exp\left(-\frac{(p-p_i)^2}{2\sigma_i^2}\right) \quad \text{Equation 1.27}$$

where σ_i is the standard deviation and p_i is the arithmetic mean value of mechanical properties (H or E) for all indentation N_i in phase i . Mean values of p_i and σ_i have to be acquired, but the probability density function (**Figure 1.16c**) may not be appropriated for performing such deconvolution as it is dependent on the bin size. In this regard, Ulm and co-workers [10,181,182,190] suggested that since the cumulative distribution function (CDF) is independent of bin size, mean values of p_i and σ_i can be extracted from fitting CDF by means of a sigmoid shape error function, written as:

$$CDF = \sum_i \frac{1}{2} f_i \operatorname{erf}\left(\frac{p-p_i}{\sqrt{2}\sigma_i}\right) \quad \text{Equation 1.28}$$

where f_i is defined as the relative surface fraction occupied by each constitutive (i) phase. Hence, the measured values of desired mechanical properties p_x , $x \in [1, \dots, N]$ were sorted in ascending

order, while N is the total number of measured properties, and the experimental CDF was computed using the condition described by **Equation 1.29** and plotted in **Figure 1.18**:

$$D(p_x) = \frac{x}{N} \quad \text{for } x \in [1, \dots, N] \quad \text{Equation 1.29}$$

Consequently, by fitting the experimental CDF (**Equation 1.29**) using **Equation 1.28**, different mechanical and microstructural parameters of multiphase systems could be deconvoluted. These parameters include mean H or E values of constitutive phases, the surface fraction of each phase, and the standard deviation of desired properties (see the information box in **Figure 1.18**). Accordingly, software Origin[®] Pro (Northampton, MA, USA) was used to analyze the obtained data by fitting and deconvolution process following **Equation 1.30**, considering the existence of a number of different phases higher than two. For instance, in the cermet system under study three peaks were identified, linked to Ti(C,N) particles, FeNi binder and regions containing interphase boundaries, corresponding to imprints that were probing ceramic particles, metallic binder, and composite-like behavior of constitutive phases, respectively (**Figure 5.14**).

$$D_{fit}(p) = \frac{1}{2}f_1 \left(1 + \operatorname{erf} \left(\frac{p - p_1}{\sqrt{2}\sigma_1} \right) \right) + \frac{1}{2}f_2 \left(1 + \operatorname{erf} \left(\frac{p - p_2}{\sqrt{2}\sigma_2} \right) \right) + \frac{1}{2}(1 - f_1 - f_2) \left(1 + \operatorname{erf} \left(\frac{p - p_3}{\sqrt{2}\sigma_3} \right) \right) \quad \text{Equation 1.30}$$

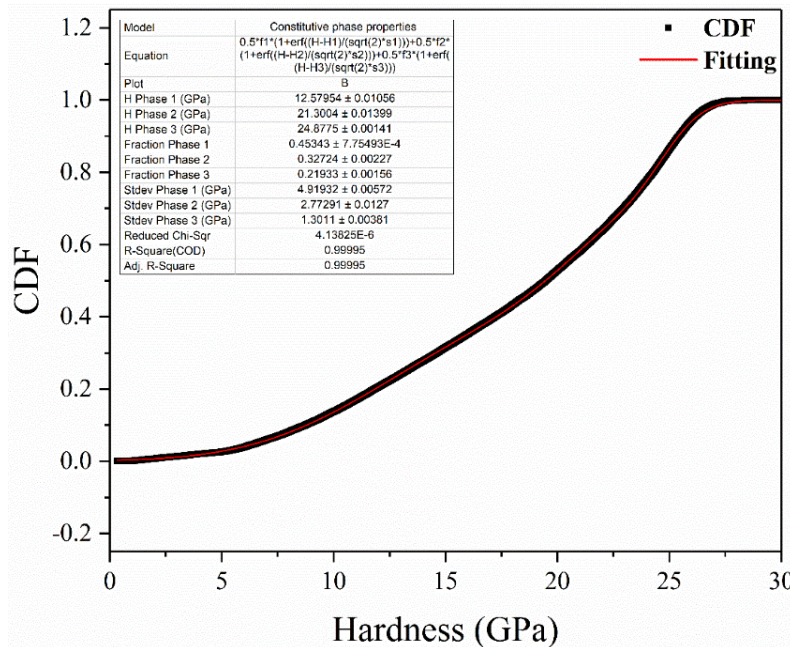


Figure 1.18. Experimental CDF value plotted by Origin Pro software for a cermet.

In order to acquire reliable values, several restrictions were programmed during the deconvolution process. In this regard, the total volume fraction of constitutive phases was fixed at 1, while the fitting process was set to finalize when the chi-square (χ^2) tolerance was less than 10^{-15} , with an ultimate coefficient of determination (R^2) of 0.9998 (see the information box in **Figure 1.18**).

1.5.3 High-speed nanoindentation technique

As discussed in previous sections, in order to evaluate the local mechanical properties of each constitutive phase of a multiphase material, it is necessary to perform grids of indentations with a great number of test ($N_i \gg 1$) on the surface of interest, while the space between imprints ℓ is large enough to avoid any interference between individual tests. Thereby the probed area would be much larger than the characteristic size of constitutive phases ($\ell\sqrt{N} \gg D$). Therefore, the locus of indentation would not have a statistical bias regarding the spatial distribution of the constitutive phases, the probability of probing each phase is equal to the surface fraction occupied by each phase on the indented surface [181]. In this regard, as long as the characteristic sizes of individual phases are in the range of micrometers, an extremely large amount of indentations has to be performed (in the form of grids with a fixed spacing value) to obtain statistically enough data to extract the mechanical properties of each constitutive phase. On the other hand, performing each regular dynamic nanoindentation test may take sometimes between 5 - 7 minutes (depending on the strain rate and penetration depth). Accordingly, performing massive numbers of indentations may take hundreds of hours. Thus, expediting the indenting process plays a pivotal role in the assessment of local mechanical properties of multiphase materials.

Within the above framework, the NanoBlitz 3D technique (KLA-Tencor, Milpitas, CA, USA) can be considered as a proper option. It is an advanced indentation technique that has proven to be successful for mapping the mechanical properties of composites, solders and multiphase materials. The main advantage of the NanoBlitz 3D technique is its suitability for expediting the indentation testing process, as compared with regular indentation testing. In particular, it offers the capability of accessing a tremendous amount of data to be analyzed by statistical analysis (see *Section 1.5.2*) to attain the H and E of each constitutive phase for different composite systems. Moreover, this fast testing technique may avoid ambient errors that may occur during long tests, such as thermal drift or vibration. More information about this technique is provided in *Section 3.3.1*.

Chapter 2

Aim and scope of the work

Chapter 2.

Aim and scope of the work

Scientific value and attitudes of an investigation are crucial for convincing the scientific, industrial and commercial “stakeholders” to be involved in a project. Therefore a proper and convincing justification for the questions about the reason and importance of the investigation is vital.

Understanding the correlation between microstructure and local mechanical properties of the individual phases that constitute a multiphase material may give us information to predict the behavior of such material at the macroscopic length scale and under real service conditions, with the aid of finite element analysis.

The relevance and functionality of multiphase materials were introduced and extensively discussed in the previous chapter. Available and appropriated microstructural and micromechanical characterization techniques, at different length scales, have been also revised and shown to be key for improving our knowledge towards enhancing the microstructural design of multiphase materials. In this regard, apart from advanced characterization techniques which yield required information about microstructural aspects, the nanoindentation technique has been highlighted as one of the most reliable methods to assess the small-scale mechanical properties of individual phases of multiphase systems and thin-films, along with providing critical information on deformation process rate. Particularly, the nanoindentation technique is used to extract basic mechanical parameters such as hardness and elastic modulus. Moreover, it has become an effective characterization tool for investigating insights about plastic deformation induced under applied stress, including shear instability initiation, the formation of lattice dislocations and phase transformation [191].

Nanoindentation testing has been recently combined and equipped with different systems (including facility and accessories) and techniques, yielding then different testing variants, e.g. in-situ nanoindentation, high-temperature nanoindentation and high-speed nanoindentation mapping. This wide range of options, in conjunction with different indenters (tips), may provide information about small-scale mechanical properties of materials at the micrometric scale on the basis of attained and gathered massive data sets (see **Figure 2.1**).

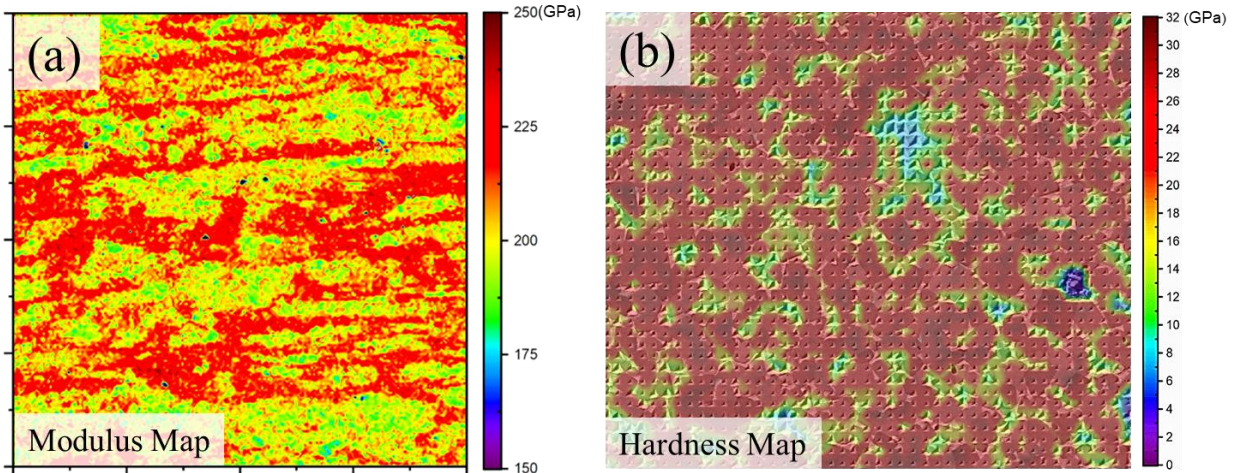


Figure 2.1. (a) Elastic modulus and (b) hardness cartography maps assessed for two multiphase materials studied in this work: DSS and cermet respectively.

In this work, all the studied systems are representative of R&D or industrial cases. Although specific techniques or approaches may be implemented in different materials, the general idea of the investigations is similar and transversal in all the cases. Within this context, the main objective of this study is to achieve a consistent and solid methodology to evaluate the local mechanical properties (mainly hardness and elastic modulus) of each constitutive phase and find the correlations among such intrinsic parameters and the effective microstructural assemblage of the studied multiphase systems.

The methodology consists of different steps which are schematically described in **Figure 2.2**. These proposed steps have to be followed in order to achieve the main objective of this study. The first step refers to the systematic and detailed microstructural characterization of the materials under consideration. In doing so, field emission scanning electron microscopy (FESEM) is implemented for all studied systems. However, the outcomes of such characterization are slightly different depending on the microstructural scenario of each multiphase material. The characteristic size of each phase/grain defines the conditions and initial parameters of the small-scale mechanical tests. Once massive nanoindentation testing is conducted, the obtained mechanical properties (H and E) are statistically analyzed, following the methodology proposed by Ulm and co-workers [10,181,182,190]. Corresponding deliverables are the properties of (N) unidentified phases. The latter refers to mechanically distinct phases, whose definition includes the consideration of not only the chemical nature of the constituents but also single-phase variables, such as crystallographic orientation, or two-phase ones, as the presence of phase boundaries. In this regard, complementary advanced characterization techniques are recalled in some cases for final optimization of the aimed linking between microstructural and mechanical property characterization. This is particularly the case for DSSs and PcBN composite where Electron Back Scattered Diffraction (EBSD) and Electron Probe X-ray Microanalysis (EPMA) are found to be

critical for rationalizing the experimental findings. For the cermets investigated, additional advanced characterization techniques are not required for discerning between the two quite different, from a mechanical viewpoint, constitutive phases: Ti(C,N) and metallic binder. However, the determination of a more realistic value of the intrinsic hardness for the constrained FeNi binder does require additional data analysis by the implementation of established thin-film models. **Figure 2.2** schematically shows the workflow followed in this investigation for acquiring the small-scale mechanical properties of the constitutive phases of the different multiphase systems considered.

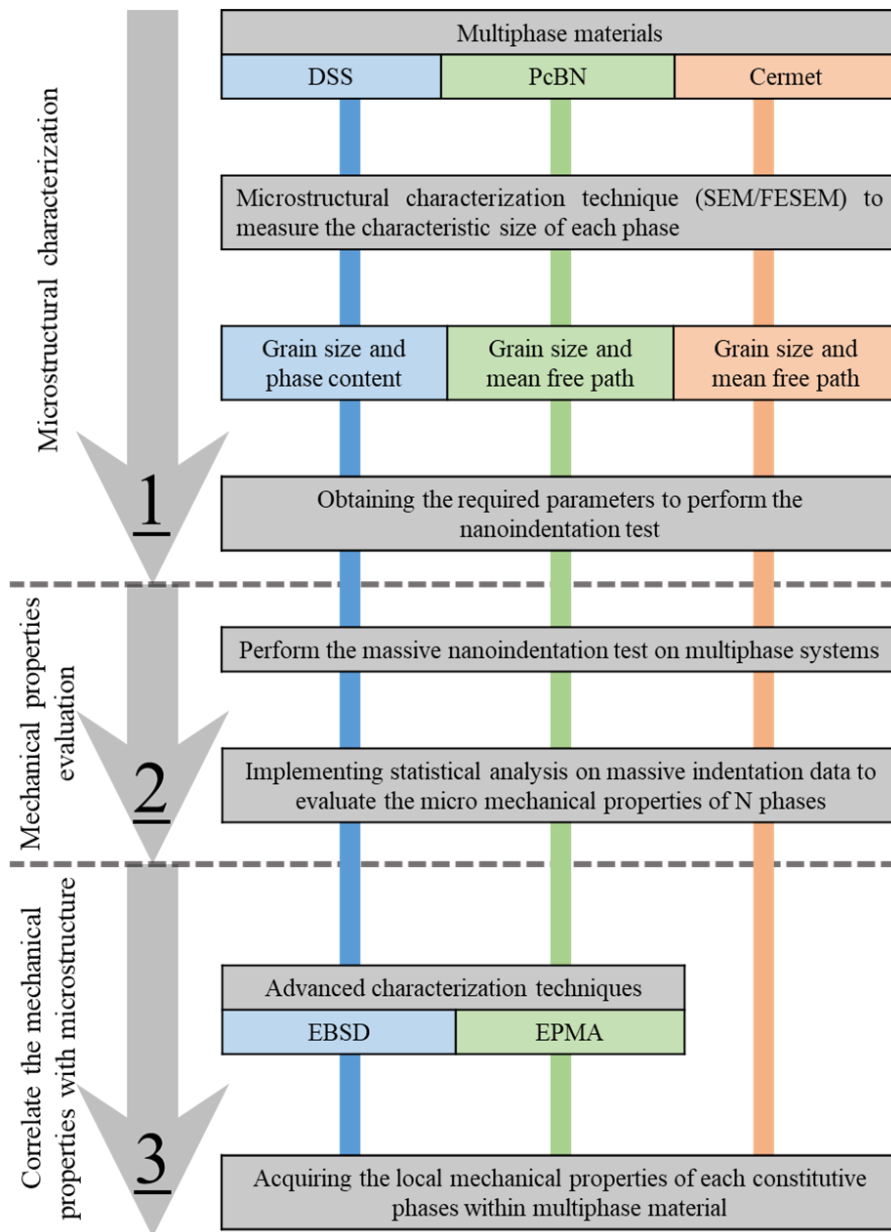


Figure 2.2. Schematic flowchart indicating the different steps followed to acquire local mechanical properties of each constitutive phase within the multiphase materials studied in this work.

Chapter 3

Materials and methods

Chapter 3.

Materials and methods

3.1 Materials and sample preparation

As it was introduced within *Chapter 1*, microstructural design optimization of the different multiphase inorganic systems to be studied requires consideration of several factors: (I) processing and chemical composition, (II) microstructural assemblage, and (III) small-scale mechanical properties of the constitutive phases as well as of the composites themselves. In this chapter, we will introduce the materials chosen for the investigation: grades, chemical composition and processing route. Furthermore, experimental methods implemented for effective microstructural and mechanical characterization will be described. The multiphase systems under consideration are DSSs, PcBN composite and Ti(C,N)-FeNi cermets. It should be highlighted that DSS and PcBN investigated are industrial materials, whereas the cermets studied are experimental grades supplied by the University Carlos III of Madrid (Getafe, Spain). Within this context, information about the processing of industrial samples is not as extensive as that of cermets, because of intellectual property restrictions. Nevertheless, for all the multiphase systems considered a systematic and detailed characterization has been conducted for each of the materials and variants studied, aiming to describe, as effectively as possible, their microstructural scenarios.

3.1.1 Duplex stainless steel (Metal-Metal system)

The metal-metal system studied was a duplex stainless steel EN1.4462 produced by UGINE & ALZ (ArcelorMittal Group, Luxembourg). The chemical composition of the DSS studied is summarized in **Table 3.1**, and a typical processing route for this material is schematically shown in **Figure 3.1**. Within this framework, four DSS variants were investigated, each of them corresponding to the product resulting after each of the stages detailed in **Figure 3.1**. They are referred to as HR, HRA, CR and FP in this study.

Table 3.1. Chemical composition (in wt. %) of the studied duplex stainless steel EN 1.4462.

C	Mn	P	S	Si	Cr	Ni	Mo	N	Fe
0.023	2.55	0.026	0.006	0.45	22.62	5.92	3.02	0.158	Bal.

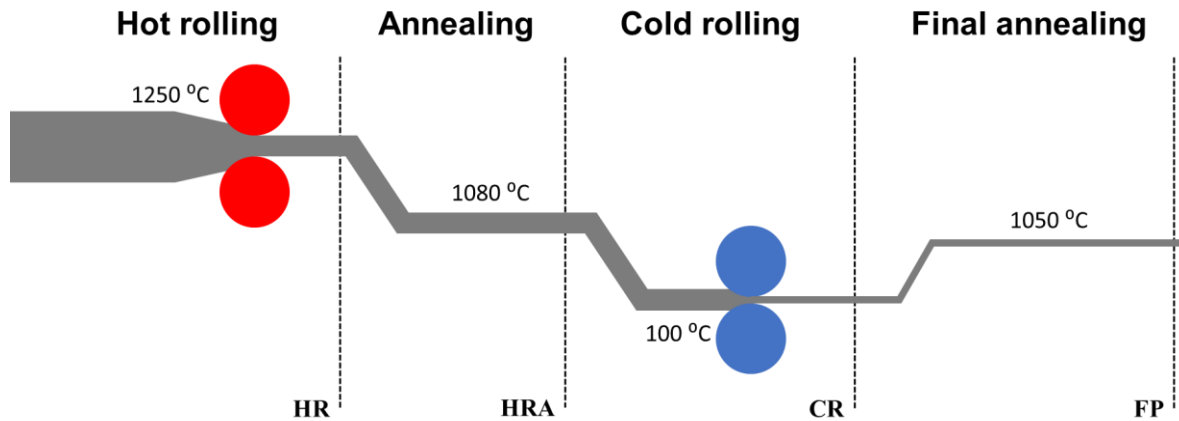


Figure 3.1. Schematic diagram of the industrial processing route (including individual and sequential stages) associated with DSS specimens investigated in this study.

Hot-rolled sample defines the first condition (HR). It was supplied in the form of plates of 300×400 mm and a thickness of 6 mm. They were obtained following a two-step industrial hot rolling schedule. First, cast slabs with 250 mm of thickness were reheated to $1250\text{ }^{\circ}\text{C}$ and then pre-rolled to a thickness reduction of 25% (150 mm). Before the second step, the slabs were cooled down to room temperature and the surface was ground. The final rolling operations started with a reheating at $1250\text{ }^{\circ}\text{C}$. Slabs were then rough rolled with a total thickness reduction of 80% (from 150 to 30 mm). Finally, the rough rolled sheets were hot rolled until a final 6 mm thickness, which corresponded to a total reduction of 96%. Typical finishing temperatures are between $975\text{ }^{\circ}\text{C}$ and $1000\text{ }^{\circ}\text{C}$. At the end, sheets were rapidly cooled to $650\text{ }^{\circ}\text{C}$, using water sprays in the run-out table, and coiled. The second supplied condition (HRA) was that corresponding to annealing of the HR product described above. Thermal treatment was done at around $1080\text{ }^{\circ}\text{C}$ for 15 min. There were no dimensional changes of the sheet, as compared to the HR condition. Cold rolling (CR) of the HRA product yielded the third condition studied. In this case, the sheet (600×150 mm) reached a thickness of 2 mm. The fourth and last condition investigated was the final product (FP) of the industrial process. It corresponds to the annealing treatment at $1050\text{ }^{\circ}\text{C}$ for around 10 min of CR condition. As for the case of going from HR to HRA, there were not any dimensional changes when annealing the CR product to yield the fourth FP condition [50].

3.1.2 Polycrystalline cubic boron nitride composite (Ceramic-Ceramic system)

The ceramic-ceramic system investigated was a polycrystalline cubic boron nitride (PcBN) composite corresponding to an industrial-grade included as a part of a machining chip breaker tool. The motivation for development and production of the selected grade is linked to their use in the automotive industry, wherein a trend is seen for acceleration of automakers' transferring production to developing countries. There, an increasing number of production lines are unmanned or operated by a small number of people. As a consequence, customer's demands for cutting tools

have shifted from “high-efficiency cutting” to “long and stable tool life”. Furthermore, the requirement for high-precision cutting has become stronger against the background of an increase of high-functional automotive parts. To satisfy such demand, different functional aspects are taken into consideration within the tool, such as geometry, design of the cutting edge and optimal microstructural design of the PcBN insert. In this work, evaluation of the microstructure and micromechanical properties of the PcBN tip of a commercial chip breaker tool is considered as the main objective.

The region of interest is a small ($1.0 \times 1.7 \times 2.0$ mm approx.) PcBN insert brazed to a hardmetal (WC-Co) structure (**Figure 3.2a**). A magnified view of the tip of such an insert, containing the cBN-TiN ceramic-ceramic system is shown in **Figure 3.2b**. The studied PcBN composite is the dark grey region in **Figure 3.2a**, obtained by the catalyzed conversion process. It consists of cBN grains which act as reinforcement bonded by a TiN matrix.

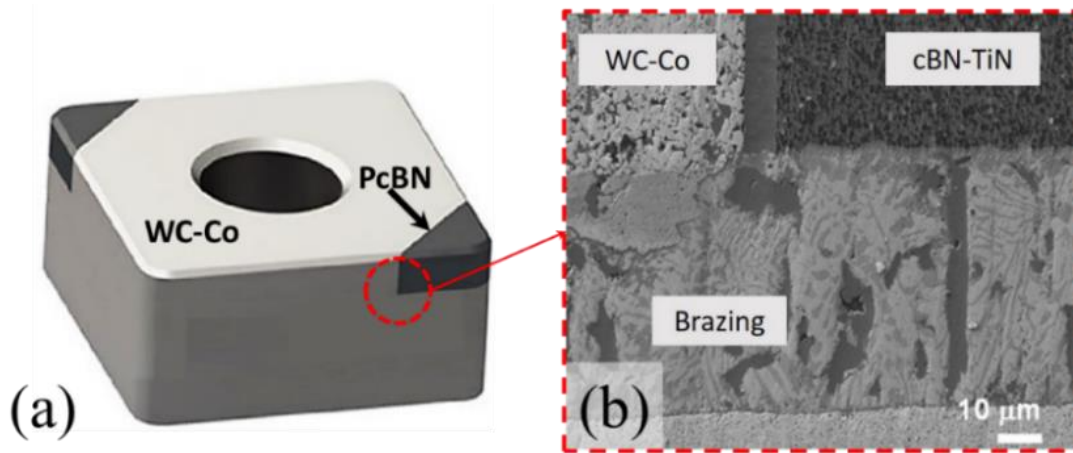


Figure 3.2. (a) Scheme of the PcBN cutting tool, where the encircled region is magnified in (b), aiming to show the assemblage of the insert's tip: WC-Co structure where PcBN is placed, brazing region and PcBN itself, consisting of cBN particles bonded by a TiN matrix.

3.1.3 Ti(C,N)-FeNi cermets (Ceramic-Metal system)

The ceramic-metal system investigated is a Ti(C,N)-FeNi cermet. This material is quite attractive because of its exceptional combination of properties as well as the growing interest in finding alternative materials to conventional cemented carbides (WC-Co system), as referred to in *Chapter 1*. Here, the processing route followed for manufacturing the material studied will be briefly presented. For the interested reader, detailed information on the fabrication of these materials may be found in Refs. [124,131,132,192].

Submicron powders used in this study were titanium carbonitride (Ti(C,N), Ti(C_{0.5}N_{0.5}) and iron (Fe, Fe SM), both provided by H.C. Starck (Germany), and nickel (Ni, Ni 210H) supplied by INCO

(Canada). The density of the powders was calculated employing a Helium Monosorb Multipycnometer (Quantachrome Corporation, USA). Particle size distribution (average particle size in volume) (D_{V50}), Brunauer-Emmett-Taller diameter (D_{BET}) and the agglomeration factor ($F_{ag} = D_{V50}/D_{BET}$) was measured with a laser analyzer (Mastersizer S, Malvern Instruments Ltd., UK). Specific surface area (SSA) was characterized by means of one-point nitrogen absorption (Monosorb Surface Area, Quantachrome Corporation, USA). All the mentioned parameters are summarized in **Table 3.2**.

Table 3.2. Characteristics of the as-received powders.

Characteristics		Powder		
		Ti(C,N)	Fe	Ni
Density (gr/cm ³)		5.1	7.8	8.9
Size	D_{v50} (μm)	2.1	3.5	1.7
	D_{BET} (μm)	0.4	1.2	0.2
	F_{ag} (-)	5.0	3.0	10
SSA (m ² /g)		3.0	0.6	4.0

A combination of powder metallurgy and colloidal processing was used to manufacture the powder compacts, following the procedure described in [132]. From these powders, high solid content suspensions were formulated using water as a dispersion medium [193]. Deionized water with tetramethylammonium hydroxide (TMAH) was used to prepare the suspensions which help to modify the pH up to 10-11, where surfaces are chemically stable [194,195]. Then 0.4 wt. % of polyethyleneimine (PEI) was added as a dispersant. Ti(C,N) and Fe/Ni slurries with different ratios (85/15, 80/20, and 70/30 vol. %) were prepared separately and milled in a ball mill for 1 hour, using Si₃N₄ and nylon balls, respectively. When the milling process finished, Ti(C,N) and Fe/Ni suspensions were mixed to get the final specimens (**Table 3.3**). Once the suspensions were prepared, 2 wt. % of polyvinyl alcohol (PVA) was added as a binder [196]. After PVA addition, the suspensions remained 20 min under mechanical stirring before they were sprayed. For the extra carbon addition, a 10 gr/L graphite suspension was prepared in another vessel, mixing ethanol and Black Carbon (ISTA, Germany), with a mean particle size of 18 μm and density of 2.24 gr/cm³. The ceramic, metallic and graphitic suspensions were blended according to the formulations collected in **Table 3.3**. Before spray-drying, a 2 wt. % of PVA was added to the mixture slurries to enable the formation of agglomerates. An Atomizer LabPlant SD-05 (North Yorkshire, UK) was used, with a modified nozzle design to obtain easy-to-press spherical granules, with inlet and exhaust temperatures held constant at 190 and 100 °C respectively, a slurry pump rate of 2 L/h, and an airflow rate of 29 m³/h. After atomization, the mixed agglomerates were uniaxially pressed at 600 MPa into 16 mm-diameter disks. The green bodies were sintered in a high-vacuum furnace (10⁻⁵ mbar) using the following heating cycle: 800°C – 30 min, and 1450°C – 2 h (5°C/min). More information about the mentioned processing route can be found in Ref. [192].

Table 3.3. Chemical formulation of suspensions.

Specimen	Volume (vol. %)		Weight (wt.%)	
	Ti(C,N)	FeNi	Ti(C,N)	FeNi
15FeNi	85	15	78.2	21.8
20FeNi	80	20	71.7	28.3
30FeNi	70	30	59.7	40.3

3.1.4 Sample preparation

All samples investigated along this work were prepared by a chemo-mechanical polishing process. Prior to the polishing process, the specimens were embedded and mounted in Bakelite in order to get a plane-parallel surface. This protocol was similar for all multiphase systems investigated here. In this section, such a sample preparation procedure will be explained in detail.

In order to get reliable results for microstructural and mechanical characterization, it is important to have a mirror-like surface, which can be obtained by chemo-mechanical polishing. The same steps were taken according to standard ASTM E3-01 [197] for all samples (time for some steps were different for each composite). More information about the chemo-mechanical polishing process is summarized in **Table 3.4**. During this process is necessary to control the planarity of the specimens as well as the applied force, in order to avoid any superficial modification during the polishing process.

Aiming to avoid any tiny scratches, all the grinding papers were wetted at the starting point of the polishing process. At the end of each step, during the last polishing minute, at least 1 liter of distilled water was used to clean both the polishing nap and the polishing specimen. After that, the different specimens were cleaned with a tens active liquid (TRITON x-100 polyethylene glycol mono (4,1,1,3-tetramethyl butyl)-phenyl ether,) and subsequently dried with pure air.

Table 3.4. Polishing steps for surface sample preparation.

Step	Time (min)			Disc/Cloth	Force (N)	Speed (rpm)
	MM ^a	CC ^b	CM ^c			
1	-	5	-	MD Piano 500	15	150
2	5	10	5	MD Piano 1200	15	150
3	15	20	20	Diamond paste 30 μm	15	150
4	15	20	20	Diamond paste 6 μm	15	150
5	15	20	20	Diamond paste 3 μm	15	100
6	15	20	20	Diamond paste 1 μm	20	100

^a Metal-Metal system (DSS)

^b Ceramic-Ceramic system (PcBN composite)

^c Ceramic-Metal system (Ti(C,N)-FeNi cermet)

Finally, in order to attain a high quality, polished surface and diminish the roughness and work hardening induced during the grinding and polishing process, all the samples were polished using a vibratory polisher unit (VibroMet 2, Buehler, USA) with a 30 nm silica solution. The vibratory finishing conditions are summarized in **Table 3.5**.

Table 3.5. Vibratory finishing condition.

Sample	Time (h)	Weight (gr)	Frequency (Hz)
DSS	4	800	60
PcBN	4	1200	60
Ti(C,N)-FeNi	3	1000	60

3.2 Microstructural characterization techniques

3.2.1 Scanning electron microscopy (SEM)

The electron microscope uses electrons instead of light to create an image of the sample. Its resolving power is much higher than a light microscope, allowing then to see finer features. Therefore, SEM plays a key role in the characterization of materials by providing high-resolution images that could range from micro to nanometric length scale. SEM could be combined with other techniques/detectors to provide complementary information about the microstructure of different multiphase systems.

The functionality of SEM is based on a focused beam of high-energy electrons to generate a variety of signals at the surface of solid specimens. The image is formed in an SEM unit by the collection of signals derived from electron-sample interactions when an electron beam crosses and scans the sample. These interactions reveal important microstructural features, such as texture, chemical composition, crystalline structure and orientation of materials. SEM is also capable of performing analyses of selected point locations on the sample. This approach is especially useful in qualitatively or semi-quantitatively determining chemical compositions, crystalline structure and crystal orientation. Interaction between sample and incident electrons produces different signals. They include secondary electrons (SE), backscattered electrons (BSE), diffracted backscattered electrons, photons, visible light, and heat. Furthermore, morphology and topography characteristics are obtained by secondary electrons [198–200].

In standard electron microscopes, electrons are mostly generated by “heating” a tungsten filament (electron gun). They are also produced by a special crystal, which results in a higher electron density in the beam and a better resolution compared with the conventional device. **Figure 3.3** exhibits a basic structure of this equipment [201].

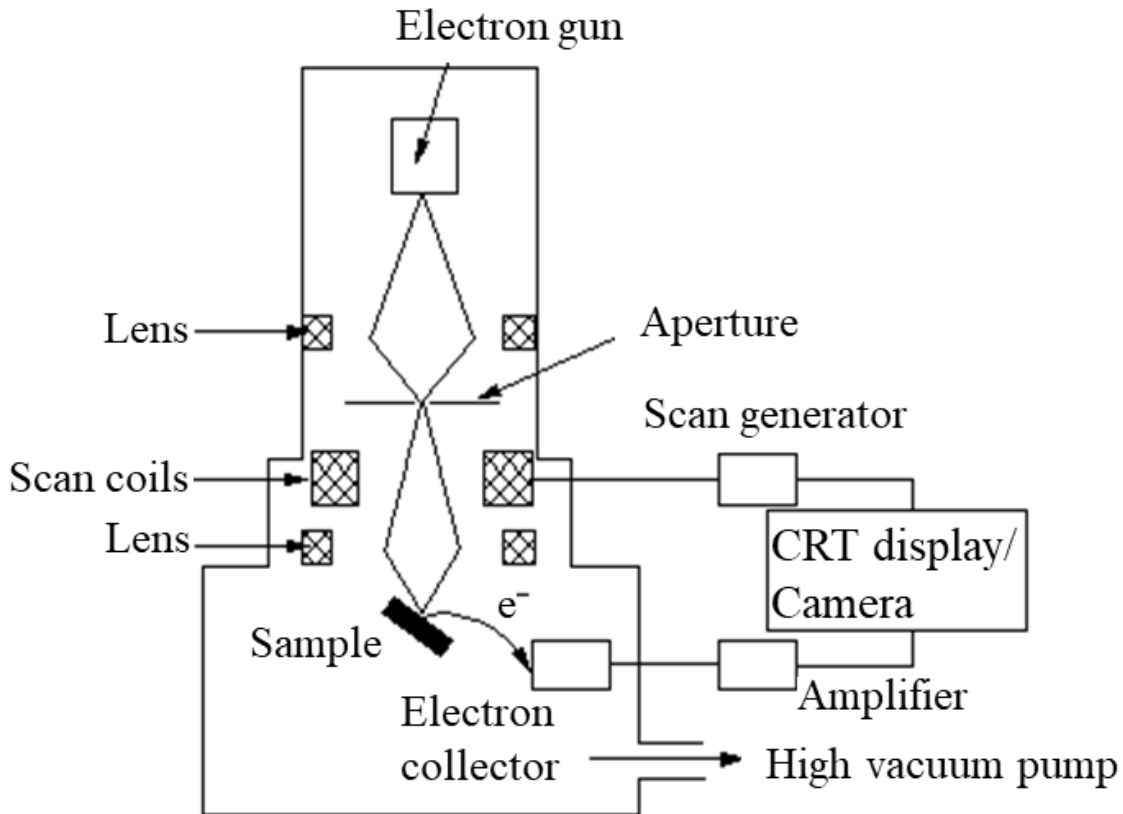


Figure 3.3. SEM scheme [201].

Field emission scanning electron microscopy (FESEM) is an SEM-based technique, which employs a beam of highly energetic electrons to analyze materials on a very fine scale. The term “field emission” is adapted due to the emission of electrons from the surface of a conductor, which is generated by a strong electric field. For this process, the equipment requires an extreme vacuum level in the column of the microscope (around 10^{-6} Pa). FESEM involves an electron emission cathode and anodes, wherein the acceleration voltage between these electrodes is commonly in the range of 0.5 to 30 kV [198–200]. In our cases, the acceleration voltage was kept at 5 kV to obtain the high-resolution FESEM images. Compared with conventional SEM, FESEM produces clearer and less electrostatically distorted images. Therefore, this technique is a very useful tool for high-resolution surface imaging [198,200].

The electron beam interacts with atoms on the surface and inside the volume of the specimen. SEs and BSEs could provide topographical and phase/crystal orientation information, respectively. SE gives contrasts with a variation of height in the surface of the samples; and subsequently, the attained image in return corresponds to the topography of the surface. BSEs reveal a distinction between different elemental compositions according to their molecular weight. Accordingly, constitutive phases of the different systems (mainly for DSS samples) could be defined by different color/grey tones [199].

Three different scanning electron microscopes were used in this study, depending on the required information to attain.

1. ZEISS NEON 40EsB Crossbeam (Oberkochen, Germany): this microscope can be considered as a “Swiss army knife” of microscopy, since it is equipped with different detectors and gadgets which provide wide varieties of information, such as:
 - Field emission electron column which is used for direct observation of the surface by virtue of BSE, SE, and Scanning transmission electron microscopy (STEM) detectors.
 - Gallium (Ga) ion beam column, for milling the material with different purposes: micromachining to obtain a particular shape for certain applications (especially for electronic applications), preparing samples for nanometric scale tests, and tomography-like cross-sectioning to attain 3D reconstruction of the material under consideration.
 - Gas injection system (GIS) for depositing different elements (e.g. platinum) to cover the surface of interest.
2. JEOL Model JSM-7001F (Tokyo, Japan): this microscope is mainly used for observation and characterization of materials using high-resolution X-ray energy dispersive spectrometry. It offers quantitative and qualitative chemical analysis (including linear profiles) and simultaneous surface distribution of chemical elements (up to 32). It is equipped with an electron backscattered diffraction (EBSD) detector to determine crystallographic orientation, phase map, and textures.
3. Phenom XL Desktop SEM (Eindhoven, Netherlands): this SEM is also used for surface characterization. However, different from the other ones referred to above, it is a semi-automatic microscope that is equipped with BSE and SE detectors. It is extremely user-friendly. Moreover, the dimension of studied samples can be up to 100 mm × 100 mm which is a nice feature to simply mount and characterize large samples.

3.2.2 Electron probe microanalysis (EPMA)

This technique, also known as electron microprobe analysis (EMPA), allows quantitative analysis of the chemical composition of samples on a micro-scale ($\sim 1 \mu\text{m}$) by irradiating electron beams onto the substance surface and measuring the characteristic X-ray that is generated. It can be used on a wide variety of materials such as metals, ceramic, minerals and semiconductors [202].

EPMA works similar to SEM, i.e. the sample is bombarded by a focused electron beam with an accelerating voltage ranging between 5 and 30 keV. As a result, X-ray photons are emitted from the specimens. The wavelengths of these X-rays are characteristic of the emitting species; thus,

the composition of the specimen is identified by recording wavelength dispersive spectroscopy (WDS) spectra [199,203].

When accelerated electrons hit the sample, apart from X-rays, particles and electromagnetic waves which are carrying different kinds of information are also emitted. Therefore, various signals such as the characteristic X-rays, SEs, BSEs, are detected (**Figure 3.4**). The attained information is then used to analyze the composition of the probed region [203–205].

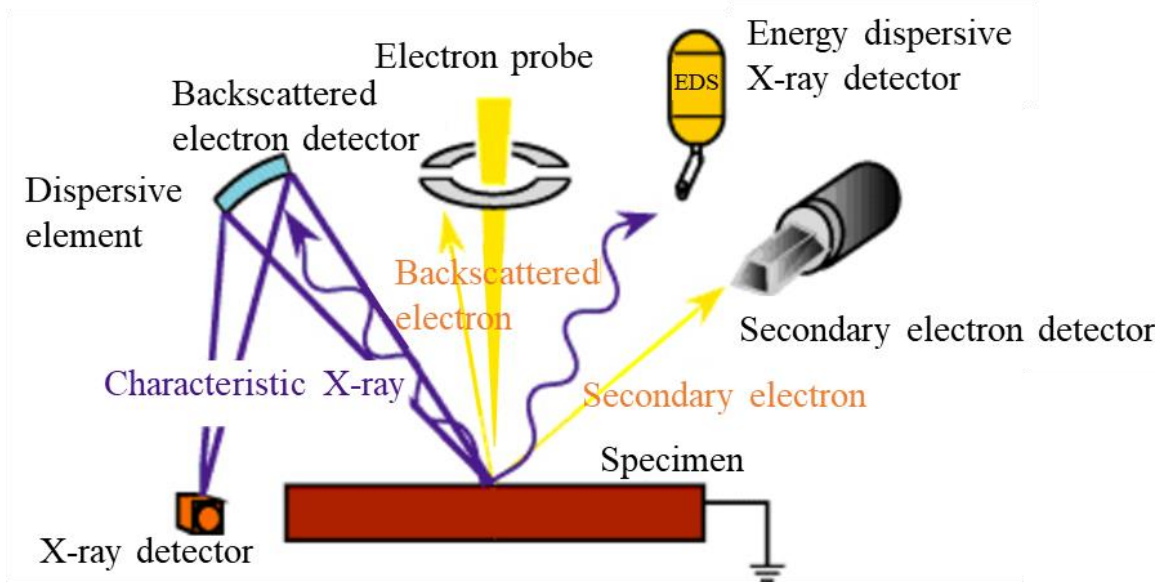


Figure 3.4. Schematic of detectors and signals of EPMA [206].

EPMA was employed for the detailed characterization of nitrogen and boron content within cBN particles. A JEOL JXA-8230 micro-analyzer (Tokyo, Japan) equipped with microprobe and WDS unit was used for this study. By doing so, different X-ray maps of nitrogen and boron were acquired in high-resolution mode, using a channel width of 1 eV. Electron currents were selected to ensure that counting rates were less than 10^4 counts per second.

3.2.3 Electron backscatter diffraction (EBSD)

EBSD detector/technique has been developed to characterize crystalline materials. It enables to identify the individual grain orientations, phase identification and distribution, point-to-point orientation correlation and local texture. EBSD signals are generated from a thin volume of the sample, normally a top layer of 20 - 50 nm depending on acceleration voltage.

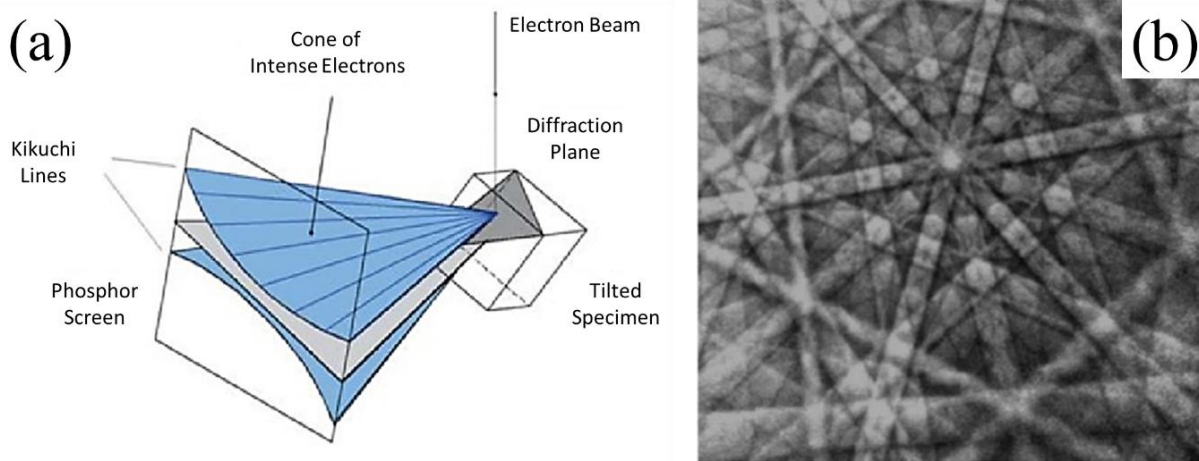


Figure 3.5. (a) Scheme of the formation of Kikuchi patterns. (b) Kikuchi pattern of Cadmium [207].

The technique is based on the generation and interpretation of Kikuchi patterns (from BSEs). **Figure 3.5a** presents the diffraction cones with respect to the reflecting plane, the specimen and the phosphor screen. The latter registers the BSEs from a stationary beam of high-energy electrons. **Figure 3.5b** displays an EBSD pattern made by the Kikuchi lines. The crystallographic structure and the orientation of the sample region are derived from these patterns formed by Kikuchi lines. The center of the projection (in the phosphor screen) is the point of incidence of the primary electron beam on the specimen surface. The lattice planes can be thought of as a pair of large angled cones stretched out to intersect the screen (seen in **Figure 3.5b**), and the plane between these cones is the projection of the diffracted plain in the screen [207].

In order to perform the EBSD analysis, polished samples were mounted inside the chamber of the JEOL JSM-7001F unit, and positioned at approximately 70° relative inclination to the normal incidence of the electron beam (as shown in **Figure 3.6**). The camera/detector is located on a horizontally mounted movable panel which is equipped with a phosphor screen combined with a digital frame receiver. In order to obtain more accurate results, the camera had to be as close as possible to the inclined sample, while the distance had to be adjusted in a safe position to prevent any collision between the delicate phosphor screen and the sample. Accordingly, the detector was positioned at about 20 mm distance from the inclined samples. EBSD maps were collected with a scanning step size of 250 nm for DSS samples. The step size was chosen considering the required accuracy and the grain size of the studied materials. The acceleration voltage and probe current were fixed at 20 kV and 9 nA, respectively.

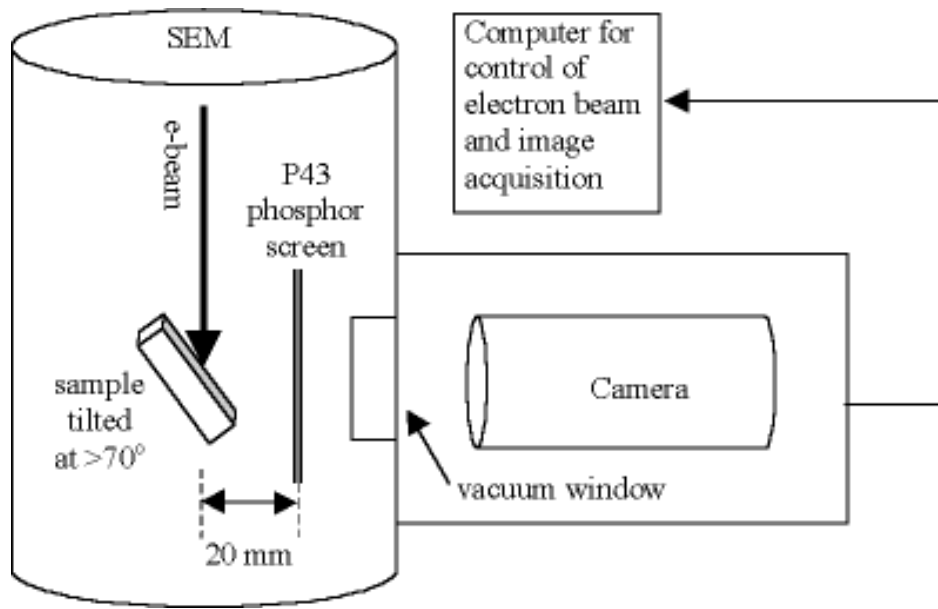


Figure 3.6. Schematic of the EBSD technique [208].

Obtained results were analyzed with Channel 5.0 software (Oxford instruments PLC, Abingdon, UK) which could convert the raw EBSD data to various visual features, as follows:

- *Quality image (QI) map*: is constructed from EBSD data, which can offer effective visualization of microstructure. This feature allows to observe the surface and clearly distinguish grain boundaries and their morphology as well as the surface damage (**Figure 3.7a**).
- *Phase map*: provides the different constitutive phases of studied materials with different colors (**Figure 3.7b**).
- *Inverse Pole Figures (IPF map)*: they allow to determine the crystallographic orientations of each grain within the analyzed region. The obtained map presents each grain with a particular color which corresponds to a given crystallographic orientation (**Figure 3.7c**).

This technique was mainly used to determine austenitic and ferritic phases and their surface fractions, as well as the crystallographic orientations of grains within the studied DSS samples. **Figure 3.7** shows some examples of obtained images by the EBSD technique for the DSSs studied.

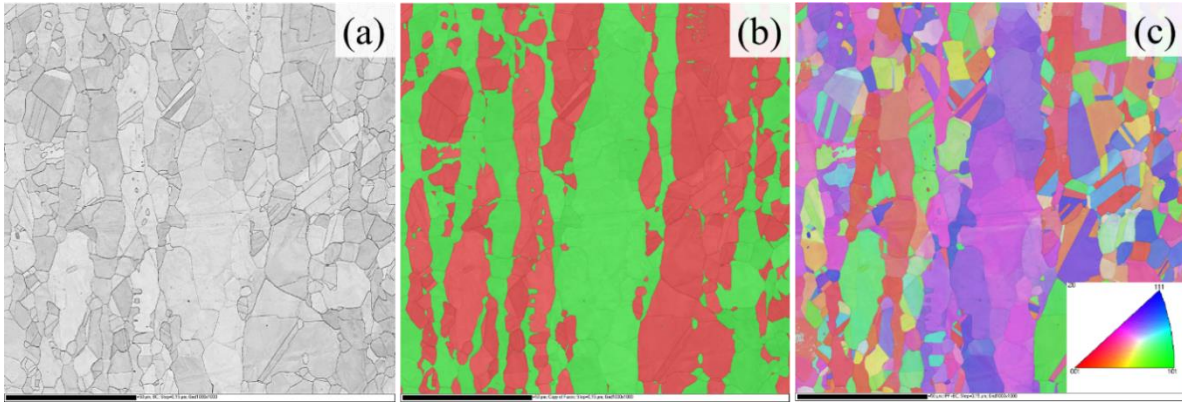


Figure 3.7. (a) Quality image, (b) phase map, and (c) IPF map of DSS, obtained by means of EBSD technique.

3.2.4 Focused ion beam (FIB)

Focused ion beam / Field emission scanning electron microscopy (FIB/FESEM) is a scientific instrument that resembles a scanning electron microscope. While SEM uses a focused beam of electrons to image the sample in the chamber, the FIB setup employs a focused beam of ions instead.

FIB systems have been manufactured commercially since three decades ago. However, the scientific implementation of FIB in material science did not take place until the early 90s. FIB is capable to be equipped with some additional tools in order to increase its functionality. Furthermore, it is quite useful for preparing Transmission Electron Microscopy (TEM) foils, micromachining of specimens, cross-section milling, atom probe post preparation, and 3D tomography [209].

The operation principle of the FIB microscope consists of sputtering atoms onto a target material, with a high energetic Gallium ion beam, Ga^+ (see **Figure 3.8**). The ions are generated from a Ga liquid metal ion source composed of a Ga reservoir mounted above a tungsten needle. Ga source is heated up to its melting point and then it flows to the tip of the needle. An intense electric field is produced at the source tip that ionizes the Ga, draws the liquid metal into the fine tip of about 2-5 nm in diameter, and extract ions from that narrow tip. The Ga^+ are accelerated down the column in an electrical field of about 30 KV and sputtered over the region of interest [209,210]. At low primary beam currents, very little material is sputtered and modern FIB systems can easily achieve 5 nm imaging resolution. At higher primary currents, a great deal of material can be removed by sputtering, allowing precision milling of the specimen down to sub-micrometer or even nanometric length scales [211,212].

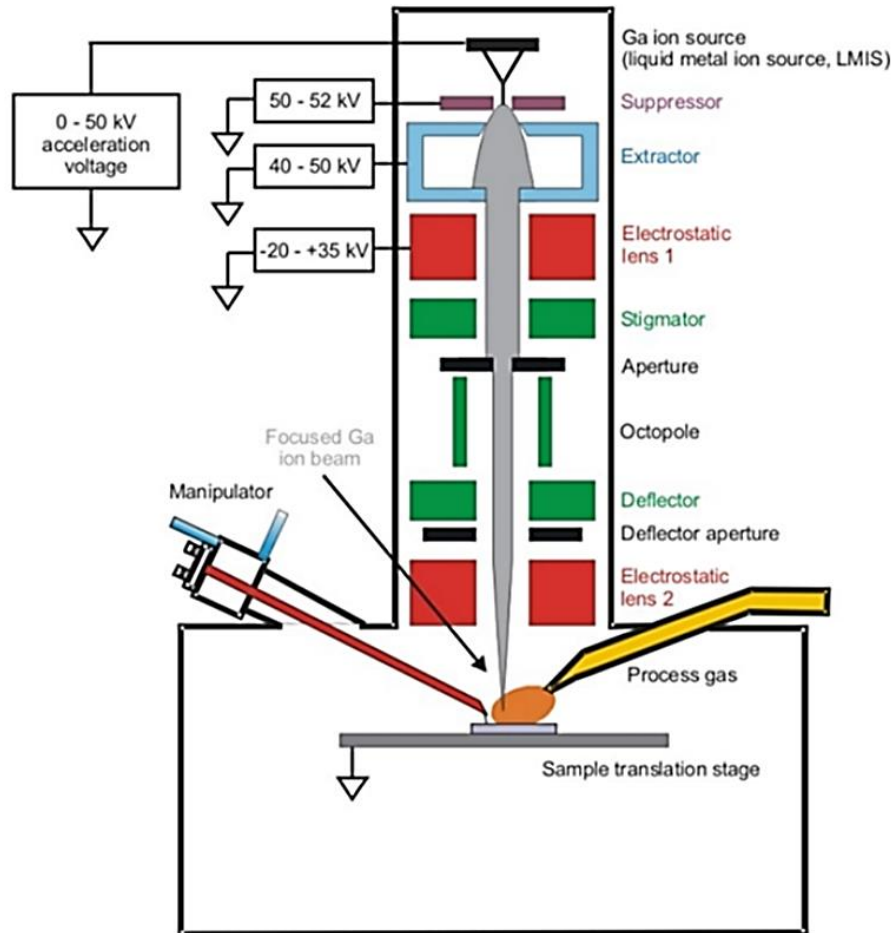


Figure 3.8. FIB scheme [213].

Gas injection system (GIS) consists of different elements such as platinum, tungsten, carbon, etc. GIS can be employed for different aims such as: to reduce the charging effect of electron and ion beams, to enhance etching, to improve the fine milling process, etc. Regarding the goal of this work, wherein performing the cross-sections were the main application of the FIB, GIS was used to enhance the quality of the obtained cross sections by reducing the curtaining effect on the cross-sections generated by FIB milling. In doing so, prior to milling, thin protective layers of platinum were deposited on the regions of interest to circumvent any waterfall effect, which could affect the quality of the images (see **Figure 3.9**) [129].

Initial FIB systems were equipped with a single beam that was used for both imaging and preparing microstructural cross-sections. However, such a system had several limitations, and nowadays a great number of FIB systems are equipped with an additional FESEM column (**Figure 3.9**). This permits an improved flexibility by using the FIB column preferentially to cross-section and the FESEM one for imaging [209].

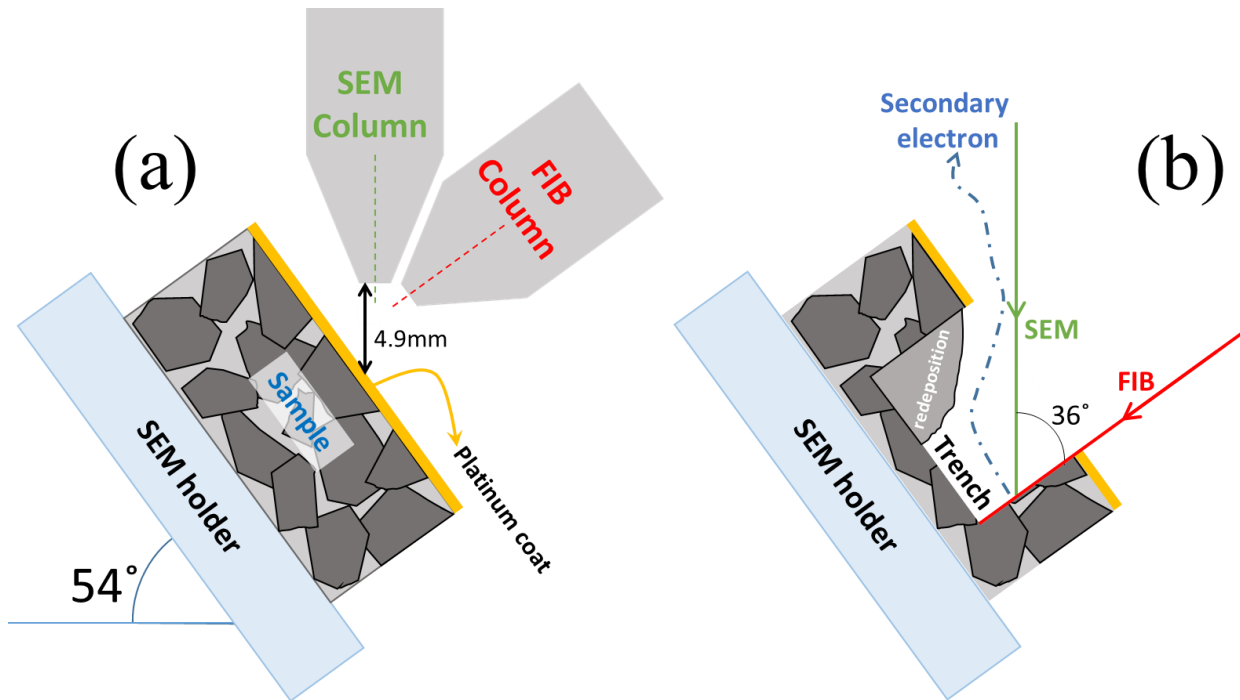


Figure 3.9. Scheme of cross-section milling by FIB.

A ZEISS NEON 40EsB Crossbeam unit was used in the current study. As it can be seen in **Figure 3.9**, SEM and FIB columns are positioned at 36° relative to each other, within the FIB/FESEM microscope. In order to mill the sample, the surface has to be perpendicular to the FIB column. Thus, the SEM holder was tilted by 54° (**Figure 3.9a**), and positioned at a working distance of around 4.9 mm from the columns, in order to be aligned with both detectors for milling. Moreover, this distance allows the sensors to detect more emitted electrons from the surface (**Figure 3.9b**), which aids to attain a better resolution of the obtained SEM images in a cross-section view.

In order to have the cross-section view, a trench had to be milled first. This initial step was achieved by fixing the aperture size to 3 nA. It allowed to get fast milling to open the trench, but the quality of the obtained cross-section surface was rather rough. The milling process was then followed by a fine milling step that had to be performed at 500 pA. By doing so, the process gets relatively slower than in the first step, while the final cross-section surface gets polished and consequently, a high-quality surface is finally attained. Some obtained cross sections for different studied samples are shown in **Figure 3.10**. They are quite useful to observe and analyze the deformations or defects induced by nanoindentation.

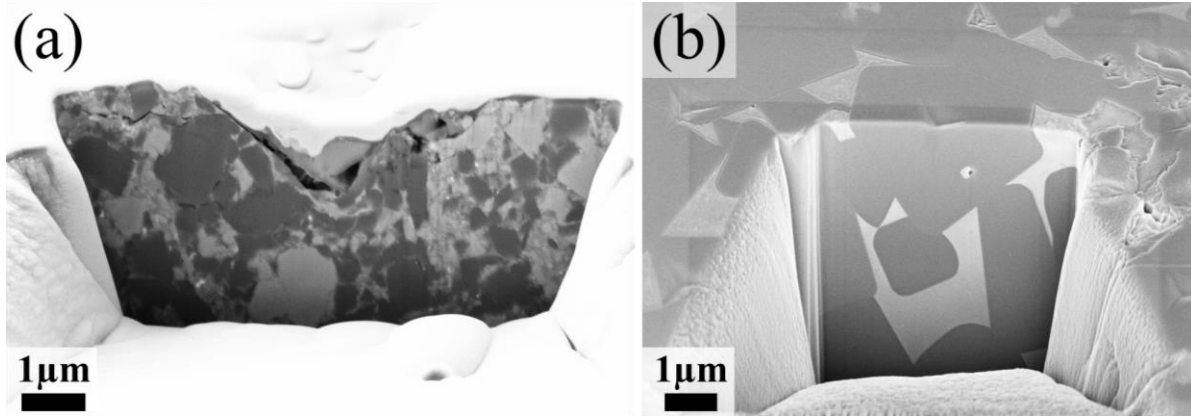


Figure 3.10. Cross-section view of different samples obtained by FIB technique: (a) PcBN composite, and (b) Ti(C,N)-FeNi cermet.

3.3 Mechanical characterization techniques

3.3.1 Nanoindentation: equipment and testing conditions

Nanoindentation testing procedure, including restrictions and critical variables of this technique, was discussed before. In this section different equipment, their features and functionality as well as the supplied variables in order to perform the tests to measure the mechanical properties of the composites and individual phases are explained. In this regard, two equipment were used to perform nanoindentations in this study, as follows:

- 1- Nanoindenter XP (MTS, Minnesota, USA): It can be used to obtain different properties and tests such as hardness, elastic modulus, scratch tests, and pillar compression, among others. In this work, it has been mainly used to perform indentations with different applied loads or penetration depths to obtain bulk and/or intrinsic H and E of the studied multiphase systems. Parameters of the tests performed using this nanoindenter are summarized in **Table 5.2**. All tests were conducted by using a sharp diamond Berkovich indenter which was calibrated with fused silica with known values of elastic modulus, $E = 72$ GPa, and Poisson's ratio of 0.17. H and E values were directly determined from the $P-h$ curves, following the Oliver and Pharr method (*Section 1.4*) [171,172]. Tests could be performed on penetration and/or load control mode (depending on the testing method). The performed tests by Nanoindenter XP were carried out under the penetration control mode. This nanoindenter is equipped with a continuous stiffness measurement (CSM) module. This feature yields different information such as stiffness, applied load, hardness and elastic modulus at each penetration depth for a single test. It is then very helpful to calculate the minimum penetration depth, by plotting P/S^2 values against penetration depth (*Section 1.5.1*), for which indentation size effects may be disregarded (*Section 1.4*). Moreover, this testing unit has the ability to perform both, single

and/or arrays of indentations at variable penetration depths. Different variables such as penetration depth, the number of indentations of each array and space between imprints can be adjusted. This feature permits to attain statistically enough data to evaluate hardness and elastic modulus at micro- and nanometric length scales by performing arrays of imprints at different penetration depths. It needs to be mentioned that Nanoindenter XP exhibits some testing limitations: 650 mN of maximum applied load and/or 2000 nm of maximum penetration depth. Performing each dynamic nanoindentation test takes around 7 minutes. Hence, to obtain thousands of indentations per sample was a protracted process, and another indentation system was needed to speed up the process.

- 2- iNano[®] nanoindenter (KLA-Tencor, Milpitas, CA, USA): It was mainly used for its high-speed indentation capability by means of the NanoBlitz technique. It makes iNano[®] capable to perform each test in a relatively short time. In high-speed mode (NanoBlitz 3D), positioning the indenter, reaching the surface, apply the load and retraction would take less than 1 second. Furthermore, this equipment can provide mechanical property (H and E) cartography maps of the indented area (**Figure 3.11**). NanoBlitz 3D technique performs the indentation (quasi-static) test just under load control mode. Thus, the applied load has to be somehow adjusted to achieve the desired penetration depth. In doing so, the required applied load may be attained from tests performed in the Nanoindenter XP unit at fixed penetration depth. Parameters of tests conducted by means of the iNano nanoindenter are summarized in **Table 5.3** (*Section 5.2*).

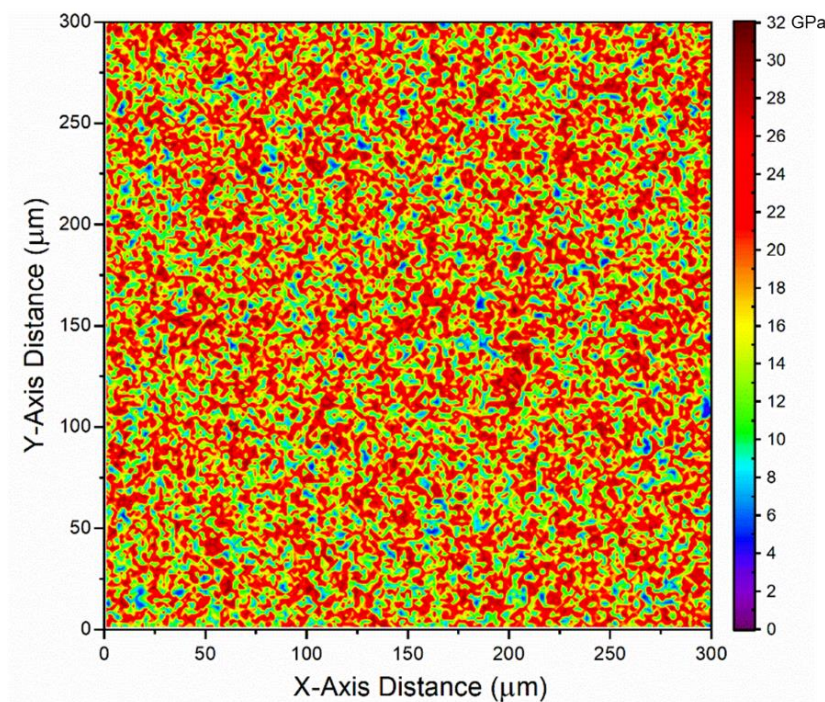


Figure 3.11. Hardness cartography map, obtained by NanoBlitz technique using iNano for a studied cermet.

3.3.2 Macroindentation: equipment and testing conditions

Indentation tests using relatively large applied forces were implemented on the different cermets studied aiming to understand the influence of microstructural parameters (ceramic/metal phase ratio) as well as carbon addition on macrohardness. In this regard, various indentations were performed at different applied loads, using a DuraScan 20 G5 unit (EMCO-TEST Prüfmaschinen GmbH, Kuchl, Austria). Testing conditions are summarized in **Table 3.6**:

Table 3.6. Micro-indentation testing conditions.

Applied load (kgf)	Indenter	Holding time (s)	Number of tests
10	Vickers	15	10
30			5

Vickers imprints performed at 30 kgf were additionally used to determine the indentation fracture toughness (Palmqvist toughness) for the different cermets under consideration. This is an established method to evaluate the indentation fracture toughness of brittle materials, based on the lengths of cracks emanating out of the imprint corners, resulting after indentations using relatively high loads. The corresponding critical stress intensity factor K_{Ic} (MPa \sqrt{m}) may be estimated using the equation proposed by Shetty *et al.* [214]:

$$K_{Ic} = \beta \left(\frac{HP}{4a} \right)^{\frac{1}{2}} \quad \text{Equation 3.1}$$

where β is a constant factor which is 0.0889 for Vickers indenter, H is Vickers hardness (MPa), P is the applied load (N), and a is the crack length (mm).

Chapter 4

Scientific articles presentation

Chapter 4.

Scientific articles presentation

This Ph.D. thesis can be partitioned into three sections, each one focused on the different composites studied. Microstructural characteristics and micromechanical properties of each composite system as well as of the corresponding constitutive phases were evaluated. Within this context, published articles are accordingly classified on the basis of the system under consideration:

- Metal-Metal (DSS) in article I;
- Ceramic-Ceramic (PcBN composite) in article II; and
- Ceramic-Metal (Ti(C,N)-FeNi cermet) in articles III and IV.

Article I:**Novel mechanical characterization of austenite and ferrite phases within a duplex stainless steel**

H. Besharatloo, M. Carpio, J.M. Cabrera, A. Mateo, G. Fargas, J.M. Wheeler, J.J. Roa and L. Llanes. *Metals* 10 (2020) 1352. <https://doi.org/10.3390/met10101352>.

Summary

The microstructure and micromechanical properties of the constitutive phases of a particular duplex stainless steel in various processing conditions have been characterized. Hardness (H), elastic modulus (E), and H/E cartography maps were obtained by using a high-speed nanoindentation mapping technique. Small-scale H and E evolution at different processing conditions have been investigated by statistical analysis of a large number of nanoindentations (10,000 imprints per sample). Two mechanically distinct phases, austenite (γ) and ferrite (α) were deconvoluted from this dataset (using the statistical method proposed by Ulm and Constantinides), with the remaining values assigned to a third mechanical phase linked to composite-like (containing γ/α interphase boundaries) regions. These mechanical property phase assessments were supplemented by overlaying the attained mechanical property (H , E , and H/E) maps and the crystallographic phase maps obtained by EBSD. An excellent correlation between microstructure and small-scale mechanical properties was achieved, especially when considering the ratio H/E .

Article

Novel Mechanical Characterization of Austenite and Ferrite Phases within Duplex Stainless Steel

Hossein Besharatloo ^{1,2}, Marcel Carpio ³, José-María Cabrera ^{3,4}, Antonio Manuel Mateo ^{1,2}, Gemma Fargas ^{1,2}, Jeffrey Martin Wheeler ⁵, Joan Josep Roa ^{1,2} and Luis Llanes ^{1,2,*}

¹ CIEFMA (Centro de Integridad Estructural, Fiabilidad y Micromecánica de los Materiales)-Department of Materials Science and Engineering, EEBE, Universitat Politècnica de Catalunya-BarcelonaTech, 08019 Barcelona, Spain; hossein.besharatloo@upc.edu (H.B.); antonio.manuel.mateo@upc.edu (A.M.M.); gemma.fargas@upc.edu (G.F.); joan.josep.roa@upc.edu (J.J.R.)

² Barcelona Research Centre in Multiscale Science and Engineering, Universitat Politècnica de Catalunya-BarcelonaTech, 08019 Barcelona, Spain

³ PROCOMAME - Department of Materials Science and Engineering, EEBE, Universitat Politècnica de Catalunya-BarcelonaTech, 08019 Barcelona, Spain; marcel.francisco.carpio@upc.edu (M.C.); jose.maria.cabrera@upc.edu (J.-M.C.)

⁴ Institute of Research in Metallurgy and Materials, Universidad Michoacana de San Nicolás de Hidalgo, 58030 Morelia, Mexico

⁵ Laboratory for Mechanics of Materials and Nanostructures, Department of Materials, ETH Zürich, 8093 Zürich, Switzerland; jeff.wheeler@mat.ethz.ch

* Correspondence: luis.miguel.llanes@upc.edu; Tel.: +34-934011083

Received: 5 September 2020; Accepted: 8 October 2020; Published: 10 October 2020

Abstract: The microstructure and micromechanical properties of the constitutive phases of a particular duplex stainless steel in various processing conditions have been characterized. Hardness (H), elastic modulus (E) and H/E cartography maps were obtained by using a high-speed nanoindentation mapping technique. Small-scale H and E evolution at different processing conditions has been investigated by statistical analysis of a large number of nanoindentations (10,000 imprints per sample). Two mechanically distinct phases, ferrite (α) and austenite (γ), were deconvoluted from this dataset using Ulm and Constantinides' method, with the remaining values assigned to a third mechanical phase linked to composite-like (containing α/γ interphase boundaries) regions. These mechanical property phase assessments were supplemented by overlaying crystallographic phase maps obtained by electron backscattered diffraction. An excellent correlation between microstructure and small-scale mechanical properties was achieved, especially when considering the ratio H/E .

Keywords: duplex stainless steel; cold work; mechanical and crystallographic phase mapping; high-speed nanoindentation; statistical analysis; H/E ratio

1. Introduction

Duplex stainless steel (DSS) is a two-phase alloy in which the proportion of constitutive elements (chemical composition) modifies the volume fraction and properties of austenite (γ phase) and ferrite (α phase). DSSs are typically twice as strong as single-phase austenitic or ferritic stainless steels. The combination of mechanical properties (high yield strength and ductility) and corrosion resistance of DSSs demonstrates better overall performance than expected from a simple average of the two phases and surpasses those exhibited by γ and α phases separately. It makes DSSs suitable for many industrial applications involving stringent service conditions, e.g. offshore, chemical, oil industries, etc. [1–5]. The content of individual elements, such as Cr, Mo and N, within DSSs results in an elevated pitting corrosion resistance. Nitrogen plays a similar role as carbon, i.e. an effective solid

solution strengthening agent. In this regard, it is intentionally added to DSSs, as it can significantly increase the strength of austenitic alloys [6–9].

It is well known that, for a given chemical composition, the mechanical properties of DSSs are primarily modified by microstructural parameters, such as the phase fraction and crystallographic texture of each phase. These microstructural parameters can be regulated by the processing conditions [10–18]. Due to the two-phase nature of these alloys and the distinct mechanical behaviour between austenite and ferrite, some damage and failure (edge cracks) may be induced during the processing of DSS components. Hence, studies of the plastic compatibility between the constitutive phases become necessary [19].

Although the mechanical properties of DSSs have been extensively studied from a macroscopic perspective, the number of works involving small-scale characterization is quite limited for these materials. In this regard, the reported results of micromechanical properties of constitutive phases (γ or α) are diverse. Austenitic phase could have higher, lower or equal hardness/elastic modulus compared with ferritic phase, depending on different variables such as specific processing route under consideration [20,21], chemical compositions (N content) [22–26], and microstructural/crystallographic texture of the individual phases [27–29].

It is evident that the mechanical behaviour of constitutive phases at the micro-scale is a key parameter for optimising the microstructural design of DSSs. In order to attain reliable values of the hardness and elastic modulus of each constitutive phase, massive nanoindentation combined with statistical analysis [30–33] is here proposed as a methodology for assessing small-scale mechanical properties. This method can assess the mechanical properties of predefined constitutive phases. Alternatively, it may provide information about the content and distribution of constitutive phases by linking different discerned responses exhibited by distinct mechanical phases [30–33]. Recently, this methodology has been validated for several multiphase systems [34–40], where indentations were performed to determine the mechanical properties of predefined phases [34,36,39], and/or constitutive phases were distinguished on the basis of obtained mechanical properties maps [37,38,40]. In both cases, mechanical properties of each phase were inherently constant and had significant difference with those assessed for the other phases. However, applying this methodology on DSS is challenging since, as mentioned before, mechanical properties (i.e. hardness (H) and elastic modulus (E)) of $-\alpha$ and $-\gamma$ phases within DSS) are not stable and can be tailored by different factors. Therefore, austenite or ferrite could not be defined by massive indentation technique, unless those phases were already determined by microstructural characterization techniques. On the other hand, in some cases, depending on alloying elements and processing conditions, austenite and ferrite show relatively similar mechanical properties (H and E) [21–29]; thus, assigning/correlating the obtained H or E to/with an austenite or ferrite phase would be complicated. Attempting to address satisfactorily this challenge for DSSs, a novel high-speed nanoindentation mapping technique in conjunction with microstructural characterization techniques were here employed. This led us to acquire a persistent correlation between microstructure and micromechanical properties (hardness H , elastic modulus E , and H/E) as a function of the processing conditions in a particular DSS.

2. Materials and Methods

2.1. Materials and Sample Preparation

The material used in this study is a commercial EN 1.4462 DSS, equivalent to AISI S31803, provided by UGINE and ALZ (ArcelorMittal Group, Luxembourg C, Luxembourg). Three different specimens were supplied after each industrial processing step (schematically illustrated in Figure 1). They are designated as: S1–hot rolled (HR), S2–cold rolled (CR) and S3–final product (FP). More information about the industrial processes employed and the resulting microstructures in terms of texture can be found elsewhere [23]. The chemical composition of the DSS studied is summarized in Table 1.

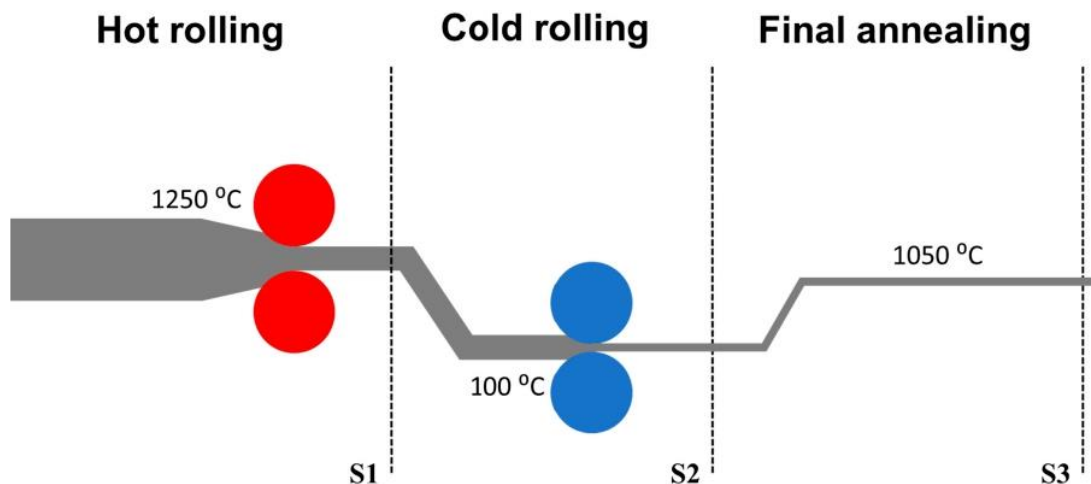


Figure 1. Schematic diagram of industrial processing steps associated with the duplex stainless steel (DSS) specimens investigated in this study.

Table 1. Chemical composition of the studied DSS (wt. %).

C	Mn	P	S	Si	Cr	Ni	Mo	N	Fe
0.023	2.55	0.026	0.006	0.45	22.62	5.92	3.02	0.158	Bal.

Prior to microstructural and micromechanical characterization, the different specimens were initially ground using silicon carbide paper, followed by sequential polishing with diamond suspensions, with decreasing particle size down to 1 μm . Finally, all the samples were polished for 4 hours with a 0.03 silica suspension using a vibratory polisher unit (VibroMet 2, Buehler, Lake Bluff, IL, USA). This last step was taken in order to achieve a high-quality polished surface and diminish the work hardening induced during the grinding and polishing process.

The microstructures of the processed samples were characterized using electron backscatter diffraction (EBSD) in a field emission scanning electron microscope (FESEM, 7100F model, JEOL, Tokyo, Japan). EBSD maps were collected with a 250 nm scanning step size at an acceleration voltage of 20 kV and probe current of 9 nA. Various parameters, such as image quality (IQ) (Figure 2), phase map, volume fraction and grain size of each phase were evaluated using Channel 5.0 software (Oxford instruments PLC, Abingdon, UK).

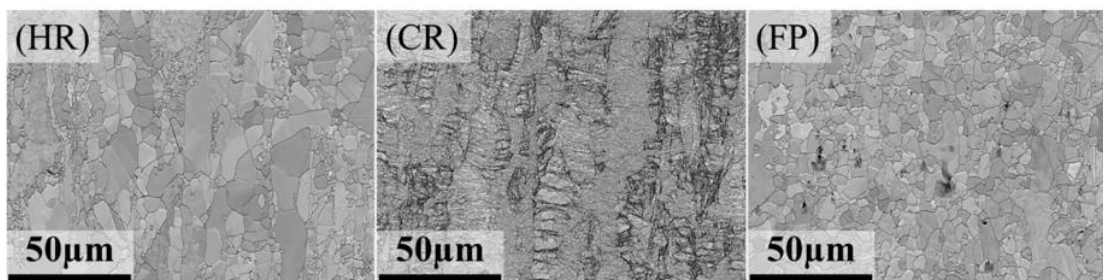


Figure 2. Image quality (IQ) of the different DSS samples studied.

2.2. Assessment of Small-Scale Mechanical Properties and Statistical Analysis

Hardness and indentation elastic modulus measurements were performed using an iNano® nanoindenter (KLA, Milpitas, CA, USA) equipped with a diamond, Berkovich indenter. H and E cartography maps were acquired using a high-speed mechanical property mapping technique called NanoBlitz. In doing so, each test can be accomplished in less than a second, which includes

positioning the testing region under the indenter, surface approach, loading, unloading and retracting process of the indenter. This relatively new technique can provide mechanical mapping over relatively large (within the micrometric range) areas by performing arrays of thousands of imprints, each evaluated by the Oliver and Pharr method [41,42]. Three large maps of 30,000 imprints (10,000 per specimen) were performed under load control mode at 4 mN, which corresponded to an indentation penetration depth ranging between 180 and 200 nm. This minimum required penetration depth was evaluated on the basis of the dependence of the ratio between the applied load and the stiffness squared on the penetration depth, by applying 16 imprints under an applied load of 45 mN (see Section 3.2.1). Indentations were spaced at an interval of 2 μm to avoid any overlapping effect from neighbouring indentations, according to the indentation depth/spacing ratio of 10 suggested by Phani and Oliver [43]. This margin allows each imprint to be treated as an independent statistical value to assess the micromechanical properties. The Poisson ratio was fixed at 0.3, which is representative of DSS and various other metals [44].

The statistically analysis proposed by Ulm and co-workers [30–33] was employed to evaluate the H and E response of each phase. In this statistical method, it is considered that the investigated samples contain different constitutive phases (i) with distinct mechanical properties. Furthermore, the Ulm method assumes that the distribution of mechanical properties of each constitutive phase (P_i) follows a Gaussian distribution:

$$P_i = \frac{1}{\sqrt{2\pi\sigma_i^2}} e^{-\frac{[P-P_i]^2}{2\sigma_i^2}} \quad (1)$$

where P_i is the arithmetic mean for number of indentations exerted on different constitutive phases (i), and σ_i is the standard deviation. The obtained H or E values (P) were plotted by cumulative distribution function (CDF), while density functions were fitted by Gaussian distributions. Consequently, the corresponding CDF using a sigmoidal shaped error function could be fitted by the following equation:

$$CDF = \sum_i^n \frac{1}{2} f_i \operatorname{erf} \left[\frac{P - P_i}{\sqrt{2}\sigma_i} \right] \quad (2)$$

where f_i is the relative volume fraction occupied by each individual phase. The total volume fraction of constitutive phases was fixed at 1. The fitting process was set to finalize when the χ^2 tolerance was less than $1 \cdot 10^{-15}$. Finally, experimental CDFs were deconvoluted, yielding then mean and standard deviation of hardness and elastic modulus for each mechanical phase. Details of the statistical method employed on different system may be found elsewhere [30–38].

3. Results and Discussions

3.1. Microstructural Characterization

The mean grain size and distribution of each constitutive phase (γ and α) were measured in each processing condition using the linear intercept method [45]. In doing so, four separate micrographs obtained by means of FESEM/EBSD were analysed per condition. Grain boundaries as well as both γ and α phases are shown in Figure 3a,b respectively. In addition, the volume fraction of each constitutive phase for all studied samples was measured—Figure 3c.

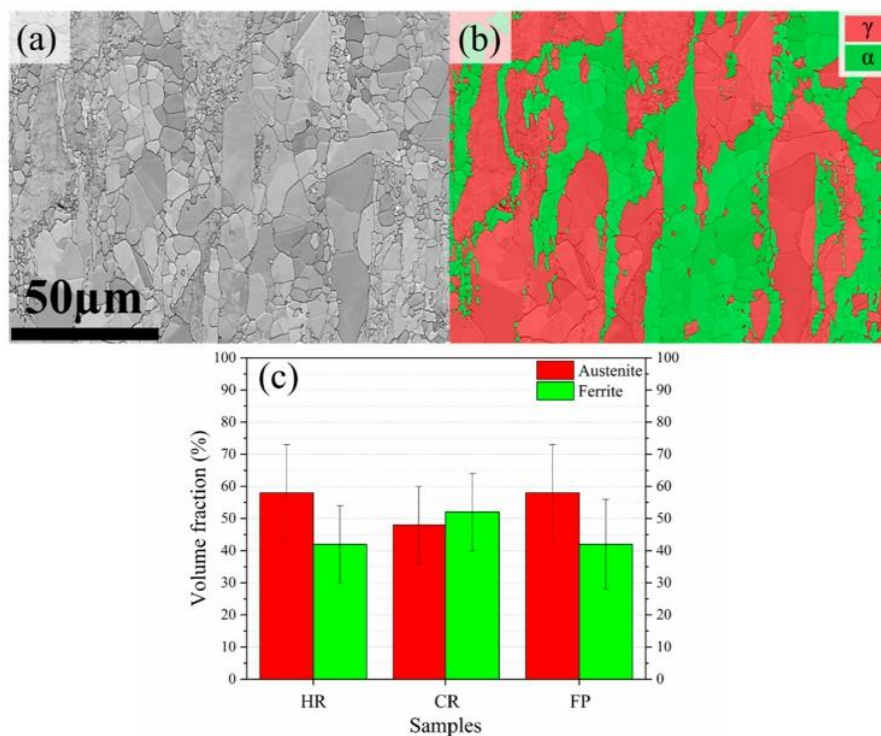


Figure 3. (a) Microstructure of the hot rolled (HR) sample illustrated by IQ; (b) phase map which illustrates the surface fraction of the γ and α phases; and (c) volume fractions of both constitutive phases for all the studied samples.

According to the general literature observation, for DSSs with medium and high N contents (i.e. above 0.15%), the γ phase is harder than the α phase [23,24,46–49]. It is clear that the overall hardness of the DSS depends on the volume fraction and intrinsic hardness of each constitutive phase within the bulk material. This work focuses on the evaluation of the intrinsic mechanical properties of each phase after each processing step. Hence, it may be expected that grain boundary strengthening would also play a relevant role. In this regard, grain sizes were measured for both constitutive phases. Figure 4a displays the histogram of the measured grain sizes with a constant bin size of 250 nm, obtained from an average of at least 2000 grains from the HR sample (Figure 2). Qualitatively similar histograms were obtained for the other studied samples and are not shown here. The measured grain sizes for both phases were found to be effectively the same, with no statistically significant differences. Therefore, the obtained histograms show the combined results from both phases. Three main distributions illustrate the accumulation of grains within the defined ranges (see Figure 4a), which relatively can be classified in low, medium and high ranges. The first peak corresponds to a relatively lower range (less than 2 μm), the second one corresponds to a medium-range (between 2 and 5 μm), and the final rectangular region represents the higher range (greater than 5 μm). The reason behind this classification is given in Section 3.2.1.

Despite the number of high-range (coarser) grains being relatively small compared with the measured low-range ones, the surface fraction occupied by the former is larger (see Figure 4b). Grain refinement occurred during the cold rolling process. It consequently raised the surface fraction of medium-sized grains dramatically. This resulted from the elongation and fragmentation of grains during cold work induced at room temperature [49–51]. Finally, significant grain growth took place after the final annealing process in the FP sample, as a result of the recrystallization and recovery of deformed grains of both phases in the CR sample [23,47,52–57].

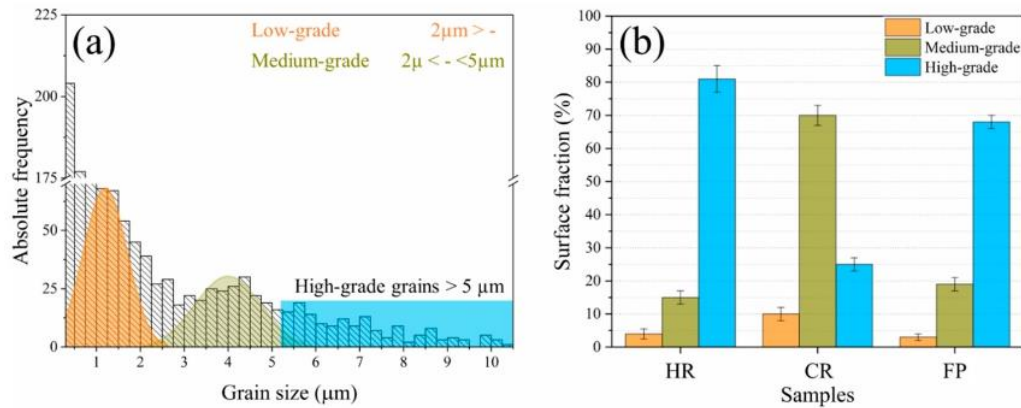


Figure 4. (a) Grain size histogram for HR sample, with 250 nm of bin size, computed from at least 2000 counted grains. (b) Surface fraction occupied by grains with different size ranges for all the studied samples.

3.2. Micromechanical Properties

3.2.1. Micromechanical Properties–Microstructure Correlation: Cartography Maps

Prior to performing the indentation mapping, testing conditions such as penetration depth and spacing parameters were assessed and analysed. These parameters were optimized to achieve nanoindentation results independent of both indentation size (ISE) and overlapping effects. In order to attain this, 16 imprints were performed under an applied load of 45 mN. Figure 5 displays the ratio between the applied load and the stiffness squared (P/S^2) as a function of penetration depth (h). It shows the minimum penetration depth, where the micromechanical properties will remain constant and unaffected by ISE, tip defect or scale effect. As evidenced in Figure 5, P/S^2 reaches a plateau as penetration depth reaches values greater than 175 nm. This implies that for $h \geq 175$ nm, it is possible to assess the intrinsic H and E for each constitutive phase. Thus, in the current study, the penetration depth was fixed at ≈ 200 nm. On the other hand, plastic flow induced by the indentation is known to be about 10 times the penetration depth [43]. Hence, for indentations performed on grains smaller than 2 μm , the plastic flow might not be confined within them, and it might be affected by the surrounding ones. However, as mentioned before, surface fractions occupied by grains finer than 2 μm are very small compared with those of grains whose size is within the medium and large ranges defined previously. Therefore, the effect of obtained hardness values from imprints performed in fine grains on the results are statistically negligible.

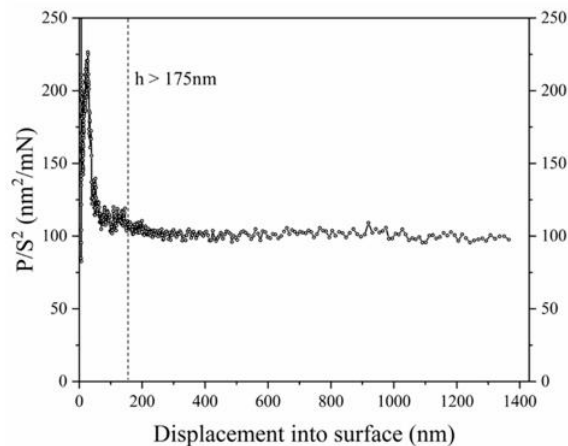


Figure 5. P/S^2 ratio versus displacement into the surface for indentations on cold rolled (CR) sample.

A high magnification EBSD micrograph of one indented area and the corresponding phase map is given in Figure 6. Similarly, another (at lower magnification) EBSD micrograph and the corresponding property maps: H , E and H/E ratio, obtained from the 10,000 (matrix of 100 by 100) imprints are shown in Figure 7 for HR and CR samples. Both γ (red) and α (green) phases are clearly differentiated in the EBSD maps of the indented regions. Meanwhile, within Figure 7, three distinct colour gradients (red, green and yellow) may be seen in the cartography maps. A qualitative visual comparison between EBSD and H -cartography maps demonstrates that red shades (ranges of 3.9–4.1 and 5.6–5.8 GPa for HR and CR respectively) correspond to the γ phase, while green tones (ranges of 3.5–3.7 GPa and 4.5–4.9 GPa for HR and CR respectively) are related to the α phase. From the obtained H -maps, it is evidenced that, as expected for the DSS studied, γ is harder than α . This might be related to the lower stacking fault energy (SFE) of γ phase, which in turn, promotes dislocation multiplication and more uniform dislocation distribution [22,23,49,58]. Moreover, it could be associated with the influence of the nitrogen on stabilizing the γ phase and promoting the deformation by planar glide, which strengthens γ grains [24,46].

This situation is different for elastic modulus. In Figure 7, α and γ are shown by red and green shades, respectively, in the E cartography map. It is observed that α phase has a higher elastic modulus than γ one. Moreover, yellow tinges (in both H and E maps) between γ and α phases can be considered as a composite response. It results from the indentations whose plastic zones include both α and γ phases; thus, α/γ interphase boundaries (see white dashed circles in Figure 6b).

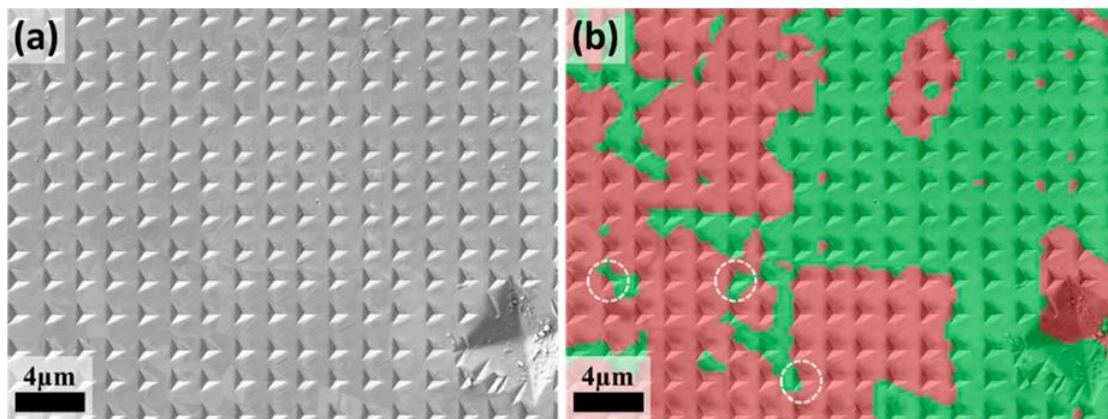


Figure 6. (a) Field emission scanning electron microscope (FESEM) micrograph of a region of the indented surface. (b) Phase map of the same region overlaid with the original micrograph.

As shown in Figure 7, limits between γ and α phases can only be faintly discerned from the H - and E -maps. On the other hand, phase contrast is more pronounced in the H/E ratio map. Although H and E represent different mechanical phenomena, the H and E values are interrelated in such a way that the corresponding H/E ratio demonstrates more consistent values. It highlights the differences of crystal structure and partition of chemical elements for each phase. Therefore, the H/E ratio yields a clearer map of γ and α phases [40], in which the austenitic phase manifests a higher plasticity ratio compared with the ferritic one.

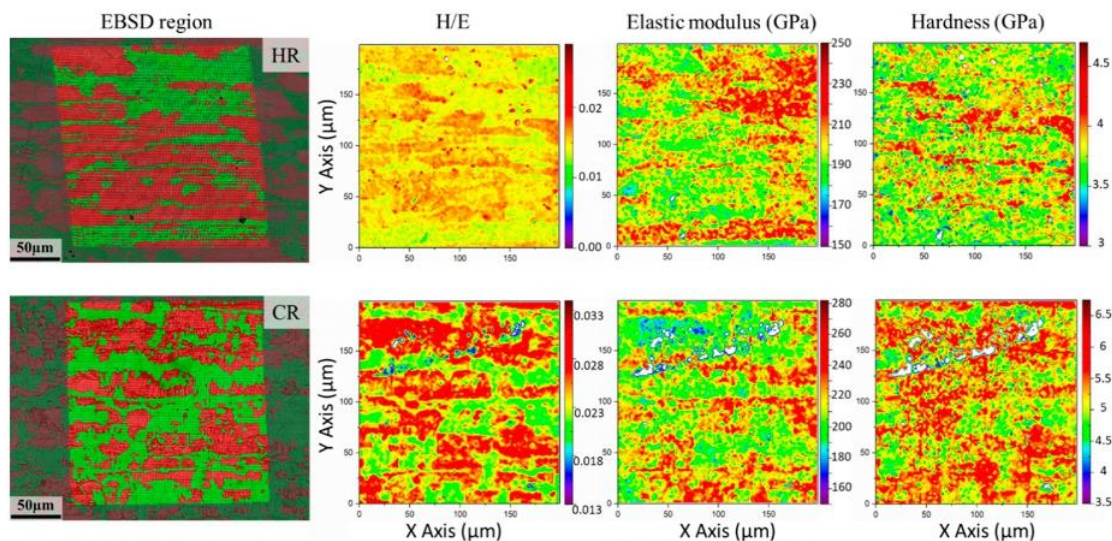


Figure 7. Electron backscatter diffraction (EBSD) maps of indented surfaces and corresponding cartography maps of indicated region for HR and CR samples.

3.2.2. Small-Scale Mechanical Properties of Each Constitutive Phase: Statistical Analysis

The evaluation of the mechanical properties of each constitutive phase in the studied DSS specimens under different processing conditions is quite challenging, since conventional nanoindentation results show only slight differences in hardness between the phases. Moreover, it has been reported that the hardness of each phase is anisotropic [29]. In order to overcome these challenges, statistical sampling was employed by the effective implementation of novel high-speed nanoindentation techniques. This allowed the collection of significant amounts of H and E data for each condition. Such a large amount of data enhances the accuracy of statistical analysis and enables one to discriminate relative differences for the mechanical properties of each phase.

As was indicated above, the H/E ratio offers higher accuracy for discrimination of mechanical response of the constitutive phases of DSSs, as shown in Figure 7. Aiming to sustain this statement, a novel data analysis graph where H and E values are simultaneously displayed as a 2D histogram [40] is shown in Figure 8. It includes the H and E values obtained from 10,000 imprints performed on each HR and CR sample (a similar trend is also observed in FP condition, not shown here). In this image, the colour of each pixel represents the number of indentations that are included within a range of H and E , which is defined as a 2D bin size. Particularly, for CR, two clear peaks can be immediately identified in these plots. They correspond to the two major phases: one located at $H \sim 5.5$ GPa and $E \sim 210$ GPa, and another at $H \sim 5.0$ GPa and $E \sim 240$ GPa. The tail of pixels below these main peaks corresponds to blue and white traces within the H/E cartography map (Figure 7). It resulted from indentations into surface contamination that effectively reduce the penetration depth of the indentation, yielding lower values along the same H/E ratio as the underlying material. As depicted in Figure 7, the γ phase has a higher H/E ratio than the α phase. Therefore, the peaks with higher H (~ 3.8 GPa for HR and 5.5 GPa for CR) and lower E (~ 190 and 210 GPa for HR and CR respectively) values are attributed to the γ phase (FCC peak within Figure 8). Meanwhile, the other peaks with lower H (~ 3.6 GPa for HR and ~ 5.0 GPa for CR) and higher E (~ 210 GPa for HR and 240 GPa for CR) are attributed to the α phase (BCC peak in Figure 8). These peaks have overlapping property distributions. If the distributions were Gaussian and sufficiently separated, it would be expected to produce a saddle between the two peaks in the 2D histogram. However, the intensity of values between the two peaks is higher than might be expected—producing rather a ridgeline between them. This additional intensity may be rationalised by considering the indentations performed on the phase boundaries, and whose plastic zones included both phases (Figure 6), then yielding a composite-like (containing α/γ interphase boundaries) response.

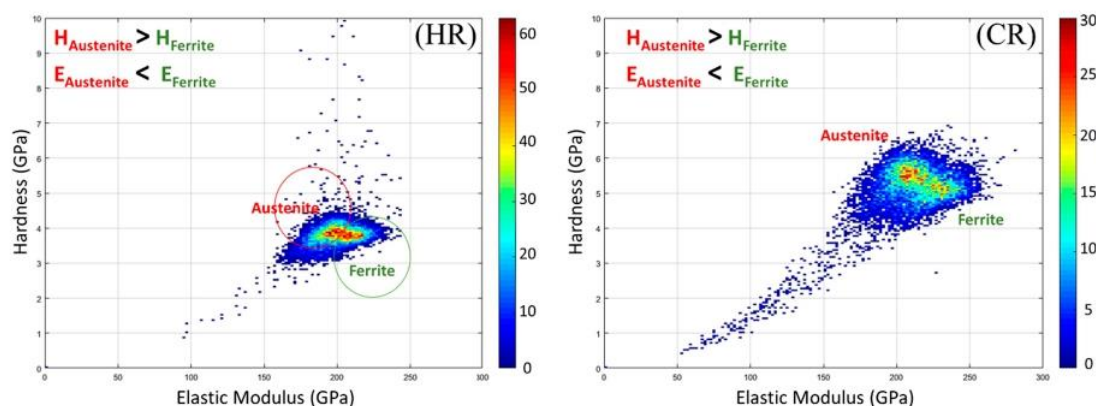


Figure 8. 2D histograms of Hardness (y-axis) vs. Elastic Modulus (x-axis) acquired from 10,000 indentations on each HR and CR sample.

In order to obtain the mean values of H and E for each constitutive phase, the statistical analysis proposed by Ulm and co-workers [30–33] was implemented. Figure 9 shows separate H and E histograms calculated from the experimental data from HR and CR samples. Three peaks were fitted on each histogram. They correspond to γ , α , and composite-like (interphase) phases. By using the phase information from EBSD mapping (Figure 7), the different peaks could be clearly assigned to their respective phases for each investigated sample. These findings were further supported by relative differences discerned among experimental p-h curves. Representative examples of them are given in Figure 10, corresponding to discrete imprints examined and located within individual phase grains (ferrite and austenite) and regions containing phase boundaries.

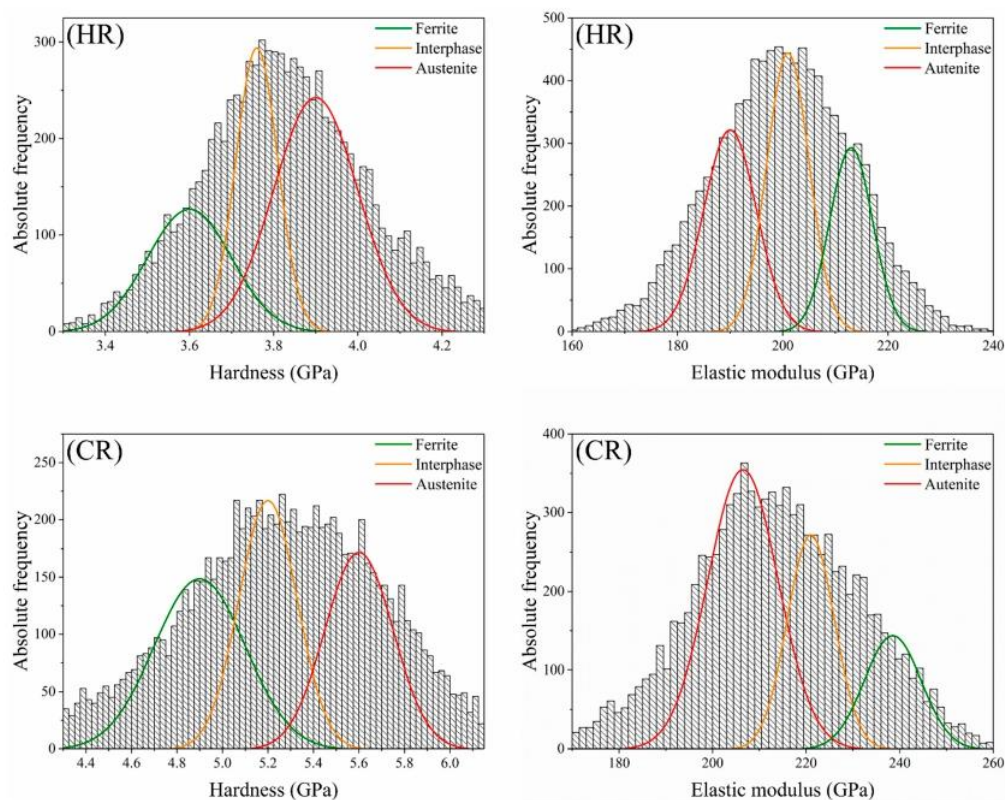


Figure 9. H and E histograms with bin sizes of 25 MPa and 1.5 GPa respectively, evaluated from 10,000 indentations for HR and CR samples studied.

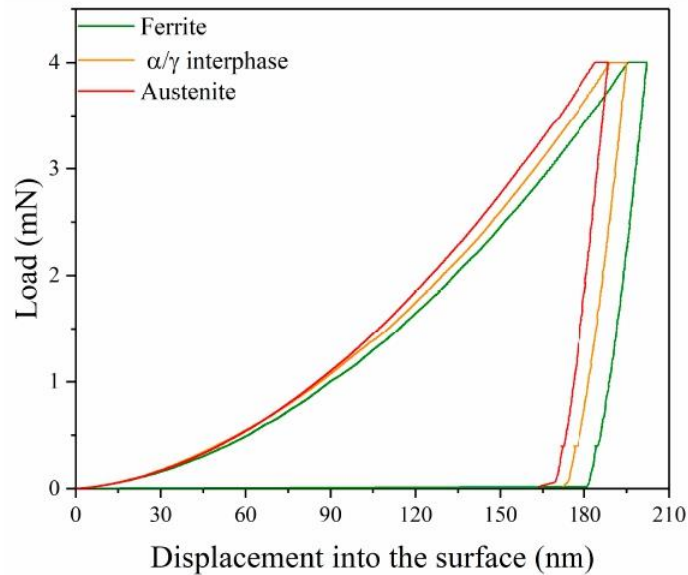


Figure 10. Load-displacement curves obtained from different imprints performed on austenite, ferrite and interphase.

These statistically derived results are in agreement with values previously reported in the literature, for DSSs with similar chemical compositions [22–24]. The obtained values for each constitutive phase for each processing condition are summarized in Table 2.

Table 2. Summary of H and E values of the defined phases in each processing condition of DSS determined from statistical analysis.

Samples	Hardness, H (GPa)			Elastic modulus, E (GPa)		
	α	α/γ Interphase	γ	α	α/γ Interphase	γ
HR	3.6 ± 0.2	3.8 ± 0.1	3.9 ± 0.2	213 ± 8	201 ± 8	190 ± 10
CR	4.9 ± 0.2	5.2 ± 0.2	5.6 ± 0.2	240 ± 8	220 ± 10	208 ± 15
FP	3.7 ± 0.2	3.9 ± 0.2	4.2 ± 0.2	215 ± 10	202 ± 7	190 ± 10

Figure 11a illustrates the influence of the processing conditions on the hardness of each constitutive phase, as well as on the surface fraction of coarse grains. As expected, H increased dramatically after cold working (CR) in both phases, due to dislocation glide, which in turn promoted an increment in the dislocation densities within the grains causing strain hardening [49,50]. Finally, after the annealing treatment (FP), the hardness value decreases as a consequence of the recovery and recrystallization mechanism within the deformed microstructure formed during the cold rolling step [59–61].

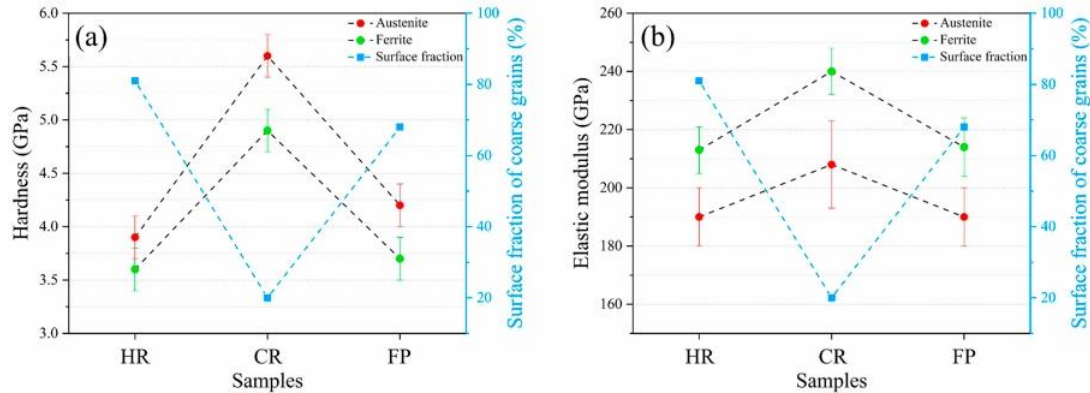


Figure 11. Intrinsic mechanical properties [(a)- H and (b)- E] evolution of both ferritic and austenitic phases and surface fraction of coarse grains during the DSS processing.

As shown in Table 2 and Figure 11b, the α phase exhibits a higher E (20 GPa) due to its BCC crystal structure, which has a lower interatomic distance (smaller lattice parameter) than the FCC crystal structure of the γ phase [22]. Hardness and elastic modulus differences must be taken into account to prevent crack appearance after intense plastic forming. More interestingly, and partially unexpected, the elastic modulus E of both phases changed after the cold-rolling step. Traditionally, the elastic modulus is considered a characteristic parameter, which remains constant irrespective of the grain size, phase morphology and chemical composition. For instance, the elastic modulus of plain carbon steels is assumed to be 210 GPa, while this value is 200 GPa in an AISI-304 (i.e. a highly alloyed steel). However, recent studies [62–66] carried out at macro-scale have shown that the elastic modulus has a minor but not irrelevant dependence on strain hardening. Account of this phenomenon allows having better predictions of the spring back character of most metallic alloys, which is indeed of enormous industrial interest. Although a detailed explanation of the observed response is out of the scope of this study, besides the strain hardening effect commented, crystallographic texture induced by the deformation itself could also be recalled as possible reason for explaining the above experimental findings. This hypothesis is supported by the fact that, once work hardening and deformation texture are removed by annealing (FP sample), elastic modulus values recover those assessed for the HR condition (Figure 11b).

4. Conclusions

The microstructure and micromechanical properties of each constitutive phase of a duplex stainless steel were investigated as a function of processing condition. According to the obtained results, the following conclusions may be drawn:

1. The surface fraction occupied by medium- and large-sized grains demonstrated a high sensitivity to cold work. Grains were significantly refined during cold work via the elongation and fragmentation of grains. Subsequent annealing treatment activated recovery and recrystallization of the grains, which caused a higher surface fraction of coarser grains.
2. Hardness and elastic modulus cartography maps provided a satisfactory correlation between micromechanical properties and constitutive phases (confirmed by EBSD analysis). The accuracy and definition of such a relationship were increased by using H/E maps. Therefore, the H/E ratio is proposed as an appropriated and reliable parameter for mechanically distinguishing between phases with relatively similar properties.
3. The different processing routes investigated here have similar effects on the mechanical properties of both phases. For the DSS here studied (with an intermediate N content of 0.15 in %wt), the austenitic phase demonstrated higher hardness and lower elastic modulus compared with the ferritic one.

- Cold work resulted in higher values of hardness and elastic modulus for both austenite and ferrite phases, as compared to the hot-rolled as well as the annealed (final product) ones. Such relative changes assessed in the small-scale properties are expected to be related to work hardening and deformation texture effects. Further research is here recalled for a deeper understanding of these correlations.

Author Contributions: H.B.: conceptualization, investigation, writing—original draft, writing—review and editing. M.C.: Investigation, writing—review and editing. J.M.C.: writing—review and editing. A.M.: writing—review and editing. G.F.: resources. J.M.W.: conceptualization, writing—review and editing. J.J.R.: writing—review and editing. L.L.: conceptualization, supervision, writing—review and editing. All authors have read and agreed to the published version of the manuscript.

Funding: This research was funded by the Spanish Ministerio de Economía y Competitividad through grant MAT2015-70780-C4-3-P (MINECO-FEDER).

Acknowledgments: Authors want to express their special thanks to Jose Antonio Benito for his time and scientific support. J.J.R acknowledges the Serra Hunter programme of the Generalitat de Catalunya. M.C. and J.M.C. acknowledge the CONACyT Mexico for his Ph.D. grant and the partial funding of his sabbatical leave, respectively.

Conflicts of Interest: The authors declare no conflict of interest.

References

- Solomon, H.D.; Devine Jr., T.M. Proc. Conf. on duplex stainless steels, Am. Soc. Met. Met. Park. **1983**, *1*, 693–756.
- Guha, P.; Clark, C. Properties and applications of high-chromium duplex stainless steels. In *Duplex Stainless Steels*; Lula, R.A., Ed.; American Society for Metals: Ceauga, OH, USA, 1983; pp. 355–369.
- Nilsson, J.-O. Super duplex stainless steels. *Mater. Sci. Technol.* **1992**, *8*, 685–700, doi:10.1179/mst.1992.8.8.685.
- Olsson, J.; Snis, M. Duplex—A new generation of stainless steels for desalination plants. *Desalination* **2007**, *205*, 104–113, doi:10.1016/j.desal.2006.02.051.
- Sotomayor, M.; De Kloe, R.; Levenfeld, B.; Varez, A. Microstructural study of duplex stainless steels obtained by powder injection molding. *J. Alloy. Compd.* **2014**, *589*, 314–321, doi:10.1016/j.jallcom.2013.11.144.
- Gunn, R.N. *Duplex Stainless Steels*; Elsevier: Amsterdam, The Netherlands, 1997.
- Tahchieva, A.B.; Llorca-Isem, N.; Cabrera-Marrero, J.-M. Duplex and Superduplex Stainless Steels: Microstructure and Property Evolution by Surface Modification Processes. *Metals* **2019**, *9*, 347, doi:10.3390/met9030347.
- Hertzman, S.; Charles, J. On the effect of nitrogen on duplex stainless steels. *Rev. De Métallurgie* **2011**, *108*, 413–425, doi:10.1051/metal/2011071.
- Horvath, W.; Prantl, W.; Stroišnigg, H.; Werner, E. Microhardness and microstructure of austenite and ferrite in nitrogen alloyed duplex steels between 20 and 500 °C. *Mater. Sci. Eng. A* **1998**, *256*, 227–236, doi:10.1016/s0921-5093(98)00839-9.
- Malta, P.O.; Dias, F.L.; De Souza, A.C.M.; Santos, D.B. Microstructure and texture evolution of duplex stainless steels with different molybdenum contents. *Mater. Charact.* **2018**, *142*, 406–421, doi:10.1016/j.matchar.2018.06.006.
- Song, J.; Bate, P. Plastic Anisotropy in A Superplastic Duplex Stainless Steel. *Acta Mater.* **1997**, *45*, 2747–2757, doi:10.1016/s1359-6454(96)00396-5.
- Sarkar, A.; Sanyal, S.; Bandyopadhyay, T.; Mandal, S. Influence of annealing parameters on phase evolution and recrystallization kinetics of a Mn-Al-Si alloyed duplex steel. *Mater. Charact.* **2017**, *134*, 213–224, doi:10.1016/j.matchar.2017.10.023.
- Fargas, G.; Anglada, M.; Mateo, A. Effect of the annealing temperature on the mechanical properties, formability and corrosion resistance of hot-rolled duplex stainless steel. *J. Mater. Process. Technol.* **2009**, *209*, 1770–1782, doi:10.1016/j.jmatprotec.2008.04.026.
- Martins, M.; Casteletti, L.C. Heat treatment temperature influence on ASTM A890 GR 6A super duplex stainless steel microstructure. *Mater. Charact.* **2005**, *55*, 225–233, doi:10.1016/j.matchar.2005.05.008.

15. Hutchinson, W.B.; Ushioda, K.; Runnsjö, G. Anisotropy of tensile behaviour in a duplex stainless steel sheet. *Mater. Sci. Technol.* **1985**, *1*, 728–736, doi:10.1179/mst.1985.1.9.728.
16. Rodrigues, D.G.; Maria, G.G.B.; Viana, N.A.L.; Santos, D. Effect of low cold-rolling strain on microstructure, texture, phase transformation, and mechanical properties of 2304 lean duplex stainless steel. *Mater. Charact.* **2019**, *150*, 138–149, doi:10.1016/j.matchar.2019.02.011.
17. Mateo, A. Anisotropy effects on the fatigue behaviour of rolled duplex stainless steels. *Int. J. Fatigue* **2003**, *25*, 481–488, doi:10.1016/s0142-1123(02)00173-1.
18. Ren, L.; Xiao, W.; Han, W.; Ma, C.; Zhou, L. Influence of duplex ageing on secondary α precipitates and mechanical properties of the near β -Ti alloy Ti-55531. *Mater. Charact.* **2018**, *144*, 1–8, doi:10.1016/j.matchar.2018.06.025.
19. Cabrera-Marrero, J.-M. Hot deformation of duplex stainless steels. *J. Mater. Process. Technol.* **2003**, *143*, 321–325, doi:10.1016/s0924-0136(03)00434-5.
20. Hosseini, A.; Karlsson, V.; Örnek, L.; Reccagni, C.; Wessman, P.; Engelberg, D.S. Microstructure and functionality of a uniquely graded super duplex stainless steel designed by a novel arc heat treatment method. *Mater. Charact.* **2018**, *139*, 390–400, doi:10.1016/j.matchar.2018.03.024.
21. Moallemi, M.; Zarei-Hanzaki, A.; Kim, S.J.; Alimadadi, H. On the microstructural-textural characterization and deformation analysis of a nano/ultrafine grained Fe-20Cr-8Mn-0.3N duplex alloy with superior mechanical properties. *Mater. Charact.* **2019**, *156*, 109878, doi:10.1016/j.matchar.2019.109878.
22. Wang, X.F.; Yang, X.P.; Guo, Z.D.; Zhou, Y.C.; Song, H.W. Nanoindentation Characterization of Mechanical Properties of Ferrite and Austenite in Duplex Stainless Steel. *Adv. Mater. Res.* **2007**, *26*, 1165–1170, doi:10.4028/www.scientific.net/amr.26-28.1165.
23. Fargas, G.; Akdut, N.; Anglada, M.; Mateo, A. Microstructural Evolution during Industrial Rolling of a Duplex Stainless Steel. *ISIJ Int.* **2008**, *48*, 1596–1602, doi:10.2355/isijinternational.48.1596.
24. Tao, P.; Gong, J.; Wang, Y.-F.; Jiang, Y.; Li, Y.; Cen, W.-W. Characterization on stress-strain behavior of ferrite and austenite in a 2205 duplex stainless steel based on nanoindentation and finite element method. *Results Phys.* **2018**, *11*, 377–384, doi:10.1016/j.rinp.2018.06.023.
25. Zhang, Q.; Singaravelu, A.S.S.; Zhao, Y.; Jing, T.; Chawla, N. Mechanical properties of a thermally-aged cast duplex stainless steel by nanoindentation and micropillar compression. *Mater. Sci. Eng. A* **2019**, *743*, 520–528, doi:10.1016/j.msea.2018.11.112.
26. Olanipekun, A.T.; Nthabiseng, M.; Ayodele, O.O.; Mphahlele, M.; Mampuya, B.M.; Olubambi, P.A. Datasets on the measurement of mechanical properties of ferrite and austenite constitutive phases using nanoindentation and micro hardness techniques. *Data Brief.* **2019**, *27*, 104551, doi:10.1016/j.dib.2019.104551.
27. Tromas, C.; Stinville, J.; Templier, C.; Vilechaise, P. Hardness and elastic modulus gradients in plasma-nitrided 316L polycrystalline stainless steel investigated by nanoindentation tomography. *Acta Mater.* **2012**, *60*, 1965–1973, doi:10.1016/j.actamat.2011.12.012.
28. Taylor, M.; Choi, K.; Sun, X.; Matlock, D.; Packard, C.E.; Xu, L.; Barlat, F. Correlations between nanoindentation hardness and macroscopic mechanical properties in DP980 steels. *Mater. Sci. Eng. A* **2014**, *597*, 431–439, doi:10.1016/j.msea.2013.12.084.
29. Roa, J.; Fargas, G.; Mateo, A.; Jimenez-Pique, E. Dependence of nanoindentation hardness with crystallographic orientation of austenite grains in metastable stainless steels. *Mater. Sci. Eng. A* **2015**, *645*, 188–195, doi:10.1016/j.msea.2015.07.096.
30. Constantinides, G.; Ulm, F.-J.; Van Vliet, K. On the use of nanoindentation for cementitious materials. *Mater. Struct.* **2003**, *36*, 191–196, doi:10.1007/bf02479557.
31. Constantinides, G.; Chandran, K.R.; Ulm, F.-J.; Van Vliet, K. Grid indentation analysis of composite microstructure and mechanics: Principles and validation. *Mater. Sci. Eng. A* **2006**, *430*, 189–202, doi:10.1016/j.msea.2006.05.125.
32. Constantinides, G.; Ulm, F.-J. The nanogranular nature of C–S–H. *J. Mech. Phys. Solids* **2007**, *55*, 64–90, doi:10.1016/j.jmps.2006.06.003.
33. Ulm, F.-J.; Vandamme, M.; Bobko, C.; Ortega, J.A.; Tai, K.; Ortiz, C. Statistical Indentation Techniques for Hydrated Nanocomposites: Concrete, Bone, and Shale. *J. Am. Ceram. Soc.* **2007**, *90*, 2677–2692, doi:10.1111/j.1551-2916.2007.02012.x.
34. Roa, J.; Jimenez-Pique, E.; Verge, C.; Tarragó, J.; Mateo, A.; Fair, J.; Llanes, L. Intrinsic hardness of constitutive phases in WC–Co composites: Nanoindentation testing, statistical analysis, WC crystal

- orientation effects and flow stress for the constrained metallic binder. *J. Eur. Ceram. Soc.* **2015**, *35*, 3419–3425, doi:10.1016/j.jeurceramsoc.2015.04.021.
35. De Bono, D.M.; London, T.; Baker, M.; Whiting, M. A robust inverse analysis method to estimate the local tensile properties of heterogeneous materials from nano-indentation data. *Int. J. Mech. Sci.* **2017**, *123*, 162–176, doi:10.1016/j.ijmecsci.2017.02.006.
 36. Besharatloo, H.; De Nicolas, M.; Roa, J.; Dios, M.; Mateo, A.; Ferrari, B.; Gordo, E.; Llanes, L. Assessment of mechanical properties at microstructural length scale of Ti(C,N)–FeNi ceramic-metal composites by means of massive nanoindentation and statistical analysis. *Ceram. Int.* **2019**, *45*, 20202–20210, doi:10.1016/j.ceramint.2019.06.292.
 37. Besharatloo, H.; Gordon, S.; Rodriguez-Suarez, T.; Can, A.; Oliver, W.; Llanes, L.; Roa, J. Small-scale mechanical properties of constitutive phases within a polycrystalline cubic boron nitride composite. *J. Eur. Ceram. Soc.* **2019**, *39*, 5181–5189, doi:10.1016/j.jeurceramsoc.2019.08.023.
 38. Besharatloo, H.; De Nicolas, M.; Wheeler, J.; Mateo, A.; Ferrari, B.; Gordo, E.; Llanes, L.; Roa, J. Carbon addition effects on microstructure and small-scale hardness for Ti(C,N)-FeNi cermets. *Int. J. Refract. Met. Hard Mater.* **2019**, *85*, 105064, doi:10.1016/j.ijrmhm.2019.105064.
 39. De Nicolás, M.; Besharatloo, H.; Wheeler, J.; De Dios, M.; Alvaredo, P.; Roa, J.; Ferrari, B.; Llanes, L.; Gordo, E. Influence of the processing route on the properties of Ti(C,N)-Fe15Ni cermets. *Int. J. Refract. Met. Hard Mater.* **2020**, *87*, 105046, doi:10.1016/j.ijrmhm.2019.105046.
 40. Xiao, Y.; Besharatloo, H.; Gan, B.; Maeder, X.; Spolenak, R.; Wheeler, J.M. Combinatorial investigation of Al-Cu intermetallics using small-scale mechanical testing. *J. Alloy. Compd.* **2020**, *822*, 153536, doi:10.1016/j.jallcom.2019.153536.
 41. Oliver, W.; Pharr, G. An improved technique for determining hardness and elastic modulus using load and displacement sensing indentation experiments. *J. Mater. Res.* **1992**, *7*, 1564–1583, doi:10.1557/jmr.1992.1564.
 42. Oliver, W.; Pharr, G. Measurement of hardness and elastic modulus by instrumented indentation: Advances in understanding and refinements to methodology. *J. Mater. Res.* **2004**, *19*, 3–20, doi:10.1557/jmr.2004.19.1.3.
 43. Phani, P.S.; Oliver, W. A critical assessment of the effect of indentation spacing on the measurement of hardness and modulus using instrumented indentation testing. *Mater. Des.* **2019**, *164*, 107563, doi:10.1016/j.matdes.2018.107563.
 44. Callister, W.D.; Rethwisch, D.G. *Materials Science and Engineering*; John Wiley & Sons: Hoboken, NY, USA, 2011.
 45. Metallographic determination of microstructure. Part 2: Measurement of WC grain size, in: ISO 4499-2 2008, *Hardmetals*, Geneva, 2008.
 46. Gadelrab, K.R.; Li, G.; Chiesa, M.; Souier, T. Local characterization of austenite and ferrite phases in duplex stainless steel using MFM and nanoindentation. *J. Mater. Res.* **2012**, *27*, 1573–1579, doi:10.1557/jmr.2012.99.
 47. Shamanth, V.; Kumar, P.; Ravishankar, K. Effect of Heat Treatment on the High Cycle Fatigue Behaviour of S2205 Duplex Stainless Steels. *Mater. Today: Proc.* **2017**, *4*, 10798–10802, doi:10.1016/j.matpr.2017.08.030.
 48. Schwarm, S.C.; Kolli, R.P.; Aydogan, E.; Mburu, S.; Ankem, S. Characterization of phase properties and deformation in ferritic-austenitic duplex stainless steels by nanoindentation and finite element method. *Mater. Sci. Eng. A* **2017**, *680*, 359–367, doi:10.1016/j.msea.2016.10.116.
 49. Malta, P.O.; Condé, B.L.; Assumpção, R.F.; Perasoli, D.B.; Sicupira, D.C.; Santos, D.B. Effect of Annealing Temperature on Mechanical Behavior, Pitting Resistance and Grain Boundary Character of a 2304 Lean Duplex Stainless Steel. *Met. Mater. Trans. A* **2019**, *50*, 2665–2677, doi:10.1007/s11661-019-05193-1.
 50. Breda, M.; Brunelli, K.; Grazi, F.; Scherillo, A.; Calliari, I. Effects of Cold Rolling and Strain-Induced Martensite Formation in a SAF 2205 Duplex Stainless Steel. *Met. Mater. Trans. A* **2014**, *46*, 577–586, doi:10.1007/s11661-014-2646-x.
 51. Zhou, T.; Xiong, Y.; Yue, Y.; Lu, Y.; Chen, Y.-N.; He, T.-T.; Ren, F.-Z.; Singh, H.; Kömi, J.; Huttula, M.; et al. Controlled cold rolling effect on microstructure and mechanical properties of Ce-modified SAF 2507 super duplex stainless steel. *Mater. Sci. Eng. A* **2019**, *766*, 138352, doi:10.1016/j.msea.2019.138352.
 52. Cooke, B.A.; Jones, A.R.; Ralph, B. Recrystallization of microduplex steels. *Met. Sci.* **1979**, *13*, 179–186, doi:10.1179/msc.1979.13.3-4.179.
 53. Blicharski, M. Structure of deformed ferrite–Austenite stainless steel. *Met. Sci.* **1984**, *18*, 92–98, doi:10.1179/030634584790420267.

54. Padilha, A.F.; Plaut, R.L.; Rios, P.R. Annealing of Cold-worked Austenitic Stainless Steels. *ISIJ Int.* **2003**, *43*, 135–143, doi:10.2355/isijinternational.43.135.
55. Johannsen, D.L.; Kyröläinen, A.; Ferreira, P. Influence of annealing treatment on the formation of nano/submicron grain size AISI 301 Austenitic stainless steels. *Met. Mater. Trans. A* **2006**, *37*, 2325–2338, doi:10.1007/bf02586207.
56. Ghosh, S.K.; Mahata, D.; Roychaudhuri, R.; Mondal, R. Effect of rolling deformation and solution treatment on microstructure and mechanical properties of a cast duplex stainless steel. *Bull. Mater. Sci.* **2012**, *35*, 839–846, doi:10.1007/s12034-012-0353-z.
57. Moura, A.; Favarato, L.; Filho, A.I.; Alcântara, C.M.; Cunha, M.; Oliveira, T.; Machado, M. Study of the recrystallization and crystallographic texture evolution during final annealing of UNS S32304 Lean Duplex stainless steel. *Mater. Charact.* **2017**, *130*, 39–49, doi:10.1016/j.matchar.2017.05.025.
58. Farnoush, H.; Momeni, A.; Dehghani, K.; Mohandesi, J.A.; Keshmiri, H. Hot deformation characteristics of 2205 duplex stainless steel based on the behavior of constituent phases. *Mater. Des.* **2010**, *31*, 220–226, doi:10.1016/j.matdes.2009.06.028.
59. Zhang, X.; Wen, Z.; Dou, R.; Zhou, G.; Li, Z. Evolution of microstructure and mechanical properties of cold-rolled SUS430 stainless steel during a continuous annealing process. *Mater. Sci. Eng. A* **2014**, *598*, 22–27, doi:10.1016/j.msea.2014.01.017.
60. Rezaei, H.; Ghazani, M.S.; Eghbali, B. Effect of post deformation annealing on the microstructure and mechanical properties of cold rolled AISI 321 austenitic stainless steel. *Mater. Sci. Eng. A* **2018**, *736*, 364–374, doi:10.1016/j.msea.2018.09.012.
61. Sun, G.; Du, L.; Hu, J.; Zhang, B.; Misra, R.D.K. On the influence of deformation mechanism during cold and warm rolling on annealing behavior of a 304 stainless steel. *Mater. Sci. Eng. A* **2019**, *746*, 341–355, doi:10.1016/j.msea.2019.01.020.
62. Fonseca, I.; Benito, J.; Mejía, I.; Jorba, J.; Roca, A. Variación del módulo de Young en el acero C45E (norma EN 10083) tratado térmicamente. *Rev. De Met.* **2002**, *38*, 249–255, doi:10.3989/revmetalm.2002.v38.i4.407.
63. Pérez, R.; Benito, J.; Prado, J.M. Study of the Inelastic Response of TRIP Steels after Plastic Deformation. *ISIJ Int.* **2005**, *45*, 1925–1933, doi:10.2355/isijinternational.45.1925.
64. Mejía, I.; Maldonado, C.; Benito, J.A.; Jorba-Peiro, J.; Vallmajor, A.R. Determination of the Work Hardening Exponent by the Hollomon and Differential Crussard-Jaoul Analyses of Cold Drawn Ferrite-Pearlite Steels. *Mater. Sci. Forum* **2006**, *509*, 37–42, doi:10.4028/www.scientific.net/msf.509.37.
65. Yamada, Y.; Kuwabara, T. *Materials for Springs*; Springer Science & Business Media: Berlin, Germany, 2007.
66. Kizu, T.; Okuda, K.; Nagataki, Y.; Urabe, T.; Seto, K. Influence of Tensile Strain on Young's Modulus in High-strength Cold-rolled Steel Sheets. *ISIJ Int.* **2015**, *55*, 1502–1511, doi:10.2355/isijinternational.55.1502.



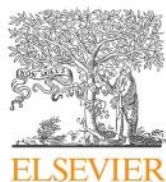
© 2020 by the authors. Licensee MDPI, Basel, Switzerland. This article is an open access article distributed under the terms and conditions of the Creative Commons Attribution (CC BY) license (<http://creativecommons.org/licenses/by/4.0/>).

Article II:**Small-scale mechanical properties of constitutive phases within a polycrystalline cubic boron nitride composite**

H. Besharatloo, S. Gordon, T. Rodriguez-Suarez, A. Can, W. C. Oliver, L. Llanes, and J. J. Roa. *Journal of the European Ceramic Society*. 39 (2019) 5181–5189. <https://doi.org/10.1016/J.JEURCERAMSOC.2019.08.023>.

Summary

Micromechanical properties of each constitutive phase of a polycrystalline cubic boron nitride (PcBN) composite have been assessed by statistical analysis of experimental data, gathered by using the massive nanoindentation technique. The mechanical study was complemented with electron probe X-ray microanalysis, aiming to correlate relative B/N ratio and local hardness for individual cBN particles. Best-fit of experimental and deconvoluted data is achieved by considering five mechanically different phases, defined on the basis of chemical nature, TiN/cBN interface presence, and phase stoichiometry. In-depth local micromechanical and chemical analysis permitted to propose and validate, for the first time, the existence of a correlation between intrinsic hardness and phase stoichiometry for cBN phase. Finally, based on experimental data measured by nanoindentation and analyzed in terms of plastic index, toughness for the PcBN composite studied is estimated to range between 4 and 6 MPa·√m.



Original article

Small-scale mechanical properties of constitutive phases within a polycrystalline cubic boron nitride composite



H. Besharatloo^{a,b}, S. Gordon^{a,b}, T. Rodriguez-Suarez^c, A. Can^c, W.C. Oliver^d, L. Llanes^{a,b,*}, J.J. Roa^{a,b}

^a CIEFMA - Department of Materials Science and Metallurgy, EEBE - Campus Diagonal Besòs, Universitat Politècnica de Catalunya - BarcelonaTech, 08019 Barcelona, Spain

^b Barcelona Research Center in Multiscale Science and Engineering, Campus Diagonal Besòs, Universitat Politècnica de Catalunya - BarcelonaTech, 08019 Barcelona, Spain

^c Element Six, Global Innovation Centre, Harwell Campus, Didcot OX11 0QR, UK

^d Nanomechanics Inc., Oak Ridge, TN 37830, USA

ARTICLE INFO

Keywords:

cBN-TiN
Super-hard multiphase material
Nanoindentation
Statistical method
Small-scale properties

ABSTRACT

Micromechanical properties of a polycrystalline cubic boron nitride (PcBN) composite have been assessed by statistical analysis of data gathered from experimental massive nanoindentation. The mechanical study was complemented with electron probe X-Ray microanalysis, aiming to correlate relative B/N ratio and local hardness for individual cBN particles. Best-fit of experimental and deconvoluted data is achieved by considering five mechanically different phases, defined on the basis of chemical nature, TiN/cBN interface presence, ratio between residual imprint dimension and microstructural length scale as well as phase stoichiometry. In-depth local micromechanical and chemical analysis permitted to propose and validate, for the first time, the existence of a correlation between intrinsic hardness and phase stoichiometry for cBN phase. Finally, based on experimental data measured by nanoindentation and analyzed in terms of plastic index, toughness for the PcBN composite studied is estimated to range between 4 and 6 MPa·√m.

1. Introduction

Polycrystalline cubic boron nitride (PcBN) is a super-hard multiphase material extensively used in highly demanding applications, such as tooling for high precision abrasive machining processes of alloys employed in the automotive and aerospace industries [1,2]. The success of PcBN mainly resides in its composite nature, consisting of hard micrometer-sized of cubic boron nitride (cBN) particles bound by a matrix of metal carbides, nitrides and/or oxides (e.g. Refs. [3,4]). On one hand, the intrinsic properties of cBN grains are solid attributes, as these provide PcBN with excellent hardness and wear resistance, high temperature stability as well as chemical inertness with respect to ferrous alloys and many other materials. On the other hand, the composite character allows assembling different microstructures by varying size and distribution of hard particles, together with chemical nature and content of the binder. It yields then a wide range of property combinations to satisfy distinct service-related requirements.

Literature information on PcBN cutting tools mainly focuses on machining performance and tool wear, as a function of workpiece and/

or cutting conditions (e.g. Refs. [5–15]). In general, in these studies, microstructures and properties of studied PcBN tools are rarely invoked as an experimental variable. Furthermore, research addressing the influence of microstructural parameters on basic mechanical or tribological properties of PcBN composite is also quite scarce [16–24]. Considering that an in-depth understanding of microstructure-property relationship has been a key parameter for enhancing functionality of other multiphase hard materials (e.g. cemented carbides [25–27] among others), the lack of this information clearly points out the need for research efforts in this direction for super-hard ceramic composites, and in particular for PcBN composites. Following the above ideas, this work aims to assess, document and analyze the small-scale mechanical properties (i.e. at the length scale of constitutive phases) of a PcBN composite. It is done by implementing systematic micromechanical testing protocols: experimental massive nanoindentation and statistical analysis of the gathered data, complemented with advanced characterization techniques of its microstructure. Such approach is expected to provide relevant knowledge towards microstructural design optimization of PcBN composites.

* Corresponding author at: CIEFMA - Department of Materials Science and Metallurgy, EEBE - Campus Diagonal Besòs, Universitat Politècnica de Catalunya - BarcelonaTech, 08019 Barcelona, Spain.

E-mail address: luis.miguel.llanes@upc.edu (L. Llanes).

<https://doi.org/10.1016/j.jeurceramsoc.2019.08.023>

Received 27 May 2019; Received in revised form 26 July 2019; Accepted 17 August 2019

Available online 18 August 2019

0955-2219/ © 2019 Elsevier Ltd. All rights reserved.

2. Experimental procedure

2.1. Material and microstructural characterization

A commercial ceramic/ceramic composite grade, cBN-TiN, was investigated. It was supplied as an insert brazed to a hardmetal (WC-Co) substrate. Prior to detailed microstructural and small-scale mechanical characterization, the specimen was chemo-mechanically polished by using diamond suspensions with gradually decreasing particle sizes, from 30 down to 1 μm . Afterwards, the sample was carefully polished with OPAN for 40 min; and thus, ultrasonically cleaned with acetone during 15 min and dried using pure air.

Field Emission Scanning Electron Microscopy (FESEM, JEOL 7100 F) was used to inspect the ceramic/ceramic microstructure. It was done by analyzing multiple micrographs in terms of phase content and cBN particle size. Volume fractions of cBN particles and ceramic binder were calculated from two-dimension data, attained by direct image correlation using the ImageJ software. Meanwhile, mean particle size of cBN grains was determined by means of the conventional linear intercept method [28]. This quantitative microstructural analysis was complemented by energy dispersive X-ray spectroscopy (EDS), in order to evaluate chemical nature of each constitutive phase.

Aiming for detailed characterization of nitrogen content within cBN particles, electron probe X-ray microanalysis (EPMA) was conducted. It was done by using a JEOL JXA-8230 microprobe and wavelength dispersive spectrometer (WDS) attached to this equipment. X-ray map for the nitrogen was recorded in high-resolution mode, using a channel width of 1 eV. Electron currents were selected to ensure that counting rates were less than 10^4 counts $\cdot\text{s}^{-1}$. More information about the protocol followed to conduct this analysis may be found in Refs. [29,30]. Two different nitrogen maps in the cBN-TiN specimen were attained, with counting times that ensured a statistical uncertainty lower than 1%.

2.2. Micromechanical properties: indentation testing

2.2.1. Hardness: Massive indentation and statistical analysis

Nanoindentation measurements were performed using two distinct nanoindentation units as well as following different protocols regarding testing conditions. First, reference values for hardness of each constitutive phase were assessed by carrying out three 10×10 indentation matrices working under displacement control mode. It was done by imposing a maximum displacement into surface of 200 nm and a distance between imprints of 5 μm . Matrices were conducted in at least three different (randomly selected) locations at the surface of the PcBN composite studied, yielding similar results in all the cases. These tests were conducted with a Nanoindenter XP (MTS) equipped with a continuous stiffness measurement (CSM) modulus and a Berkovich diamond tip. Calibration of the contact area of the tip was done with fused silica – known value of Young's modulus of 72 GPa and Poisson's ratio of 0.17 [31]. As a result of these tests, it was found that maximum values of applied load (corresponding to 200 nm indentation depth) were in the range of 25–30 mN. In order to document subsurface deformation and damage scenario associated with Berkovich nanoindentations confined within individual phases, cross-sections were prepared by means of Focused Ion Beam (FIB) coupled to a Zeiss Neon 40 FESEM. Prior to FIB milling, a protective thin platinum layer was deposited on the residual imprints to be studied. A Ga^+ source was used, and current as well as acceleration voltage were continuously decreased down to a final polishing stage at 500 pA at 30 kV.

Following the above study, two additional nanoindentation testing protocols were performed by implementation of novel high-speed and micromechanical mapping experimental upgrades. They were conducted under loading control using an iMicro® Nanoindenter (Nanomechanics Inc.). Load and depth data attained in all the above nanoindentation tests were analyzed by using the standard method

proposed by Oliver and Pharr, which leads to determine contact stiffness and hardness [31,32]. Different maximum applied loads and grid sizes were used, aiming to optimize data acquisition towards reliable determination of hardness values, within the framework of the statistical method proposed by Ulm and coworkers [33–36]. On one hand, 2,500 (50×50 grid) imprints at maximum applied load of 25 mN were done in an area of $50 \times 50 \mu\text{m}^2$. On the other hand, 12,500 imprints at maximum applied load of 10 mN were performed. The latter were divided into 2 matrices of 100×100 and 50×50 indentations in areas of $50 \times 50 \mu\text{m}^2$ and $25 \times 25 \mu\text{m}^2$, respectively. The indentation spacing was chosen as per the recommendation of Phani and Oliver [37]. For these tests, Nanoblitz software was used to attain a mechanical property mapping at high speed, each test being performed in less than 1 s. The fast testing capability enables mapping over large areas in a short amount of time as well as access to large data sets for statistical analysis. In all the cases, a sharp Berkovich tip (calibrated as indicated above) was used. Contact stiffness was continuously measured as a function of depth using a phase lock amplifier oscillating at 100 Hz frequency and 2 nm displacement amplitude.

Obtained hardness results were then statistically analyzed, according to the method proposed by Ulm and coworkers [33–36]. Such testing and data analysis protocol has been recently validated for other hard and microstructurally heterogeneous materials, such as WC- and Ti(C,N)-based cemented carbides, by the authors of this study [38–41]. Theoretical framework behind this approach is based on: (1) consideration of the heterogeneous system as composed by several distinct phases with different mechanical properties (H); (2) assumption of mechanical properties of each phase to follow Gaussian distributions (p_i), as given by:

$$p_i = \frac{1}{\sqrt{2\pi\sigma_i^2}} e^{-\frac{|H-H_i|^2}{2\sigma_i^2}} \quad (1)$$

where H_i is the arithmetic mean for all the indentations (N_i) probing each constitutive phase (i) and σ_i is the standard deviation; (3) generation of experimental cumulative distribution function (CDF) for each constitutive (Gaussian distributed) phase, written as follows:

$$CDF = \sum_i^n \frac{1}{2} f_i \text{erf}\left[\frac{H-H_i}{\sqrt{2}\sigma_i}\right] \quad (2)$$

where f_i is the volume fraction of a mechanically identifiable phase [33]; and (4) final deconvolution of experimental CDFs, yielding then mean and standard deviation of H for each mechanical phase. In this investigation, considering the ratio between residual imprint dimensions and microstructural length scales, three mechanically different phases were originally defined. Two of them correspond to the two microstructurally distinct constitutive phases, i.e. cBN particles and TiN matrix. The third one refers to a “composite-like” phase, and is related to events where imprints were indeed probing combined mechanical response of both constituents, i.e. cBN and TiN. Details of the statistical method followed may be found elsewhere [38].

Finally, aiming to evaluate relative H of cBN particles regarding nitrogen or boron amount diffused in the grains, an additional study was conducted in all three 10×10 indentation matrices performed following the first testing protocol described above. There, a correlation between intrinsic H and local chemical composition was attempted by comparison of micromechanical mapping data with results attained from EPMA analysis within a defined region, limited for easier identification by a FIB-marked square (see Fig. 5a).

2.2.2. Indentation fracture toughness: cube corner indentation

Indentation fracture toughness (K_{Ic}) in ceramic materials is commonly measured by means of indentation techniques, as follows [42,43]:

$$K_{Ic} = \alpha \left(\frac{E}{H} \right)^{\frac{1}{2}} \left(\frac{P}{c^2} \right) \quad (3)$$

where H is the hardness, E is the elastic modulus (assessed from nanoindentation tests described in previous section), P is the maximum indentation load, c is the radial crack length created in the residual imprint, and α is an empirical constant related to the indenter geometry.

In order to estimate K_{Ic} of the entire PcBN composite, six different loads (i.e. 5, 10, 20, 30, 40 and 50 gf) and five indentations per load were done, under load control mode and using a cube-corner indenter. This indenter was used, instead of a Berkovich one, because the higher sharpness of the former; hence, plasticity is induced earlier. Load (P) – displacement (h) data was also recorded in these tests. Corresponding P – h curves showed several pop-ins, i.e. plateaus at given load levels observed during loading part. This phenomenon is related with the onset of plasticity on the material. Within this context, pop-ins could be associated with nucleation of dislocations, crack formation, rupture and/or phase transformation. Data recording was complemented with high-resolution images of the residual imprints as well as transversal sections of them, obtained by means of FESEM/FIB. It was done to analyze the damage induced in the material and try to correlate it with microstructure and mechanical response.

3. Results and discussions

3.1. Microstructural characterization

The volume fraction (vol. %) of cBN particles is estimated to be 70%. Meanwhile, mean particle size of cBN grains and binder mean free path (λ) are discerned to be about 2.7 and 2.0 μm respectively. The main microstructural parameters are summarized in Table 2. These microstructural findings were complemented by an EDS analysis, which indicated presence of aluminum, besides other expected elements (Table 1). Addition of aluminum is a common practice during PcBN manufacturing for enhancing adhesion and wettability between cBN particles and TiN binder, as reported in Ref. [44].

3.2. Small-scale hardness

3.2.1. Reference hardness values of the constitutive phases

Fig. 1a shows a FESEM micrograph corresponding to a small array of indentations (performed at 200 nm of maximum penetration depth). From such image, it is evident that some residual imprints are completely allocated within one of the two constitutive phases. This is the case for imprints encircled with blue and yellow dashed lines for TiN and cBN particles, respectively. On the other hand, it is also clear that there are many other indentations which are indeed assessing the mechanical response of the composite itself, as residual imprints are probing regions including phase boundaries. In those cases, corresponding plastic flow would be expected to interact with both phases (imprints encircled with red dashed lines in Fig. 1a). Such a scenario, directly related to the ratio between residual imprint dimension and microstructural length scale for the material studied, supports the above definition of three mechanically different phases for the PcBN system under consideration: two microstructurally distinct constitutive phases, i.e. cBN particles and TiN matrix, and a third phase corresponding to one exhibiting the “composite-like” response.

Fig. 2 shows H evolution as a function of penetration depth until

Table 2

Microstructural parameters of PcBN composite studied.

cBN particle size (μm)	TiN binder mean free path, λ (μm)	Vol. % binder
2.7 ± 0.2	2.0 ± 0.1	30

reaching 200 nm, for each mechanically different phase. All the curves tend to get into plateau values for penetration depths higher than 100 nm. Under these conditions, reference values for the intrinsic H of each constitutive phase, i.e. independent of size or scale effects, may be estimated to be around 20 and 42 GPa for TiN binder and cBN particles, respectively. On the other hand, intermediate H values, in a range defined by those assessed for individual phases, could be expected for the third composite phase. These values are in satisfactory agreement with those reported by different research groups for bulk TiN (see Refs. [45–48]) and PcBN composites (see Refs. [17–19,23,24]).

In order to implement statistical method to obtain small-scale properties of each mechanical phase under consideration, plastic flow (affecting a region with dimensions about 10 times maximum penetration depth [37]) must be confined inside each phase. Fig. 1c and e shows FIB-milled cross-section images of subsurface scenario for individual imprints, pointed by arrows in Fig. 1a and detailed in Fig. 1b and d. It is clear in both cases that above condition (plastic flow region, defined by white dashed line, completely embedded within the individual phase) is satisfied for imprints performed within binder and particles. This validates the consideration of each nanoindentation test as an individual event regarding subsequent statistical analysis of the gathered data.

3.2.2. Massive nanoindentation and statistical analysis

Hardness histograms (with a constant bin size of 1 GPa) corresponding to experimental data attained out of the 15,000 indentations performed following the high-speed testing protocols are shown in Fig. 3. They are determined from data with different numbers of imprints and maximum applied load: 12,500 indentations at 10 mN (Fig. 3a) and 2,500 imprints at 25 mN (Fig. 3b). By applying the statistical method proposed by Ulm and co-workers [33–36], it is possible to further deconvolute the experimental data into three peaks with different mean values, as summarized in Table 3. Following the reference values assessed before, the higher and lower peaks can be attributed to cBN particles and TiN binder, whereas the intermediate one must be related to the composite-like phase defined by phase boundary regions. Statistical analysis of the data gathered using distinct maximum applied load levels do not yield relevant differences in mean and standard deviation of small-scale H values. However, data attained imposing a load of 25 mN (as compared to 10 mN) do yield a better screening among Gaussian distributions for each defined phase. Main reason behind it may be related to size-scale effects (e.g. surface roughness) or influence of indenter tip defects, these being more critical for shallower penetrations.

Very interesting, from direct observation of the obtained histograms (gray filled areas “marked by arrows” around the red Gaussian distribution curves in Fig. 3), it could be speculated that analysis of cBN data would be better-fitted by considering two additional populations, corresponding to harder and softer (with respect to the original main peak) cBN particles. These differences could be related to variations of chemical composition within cBN particles, and this aspect will be addressed later in this study.

3.2.3. Hardness cartography map

One of the advantages of implementing novel high-speed nanoindentation testing protocols is that they are inherently associated with gathering of large amounts of data, small penetration depths and close spacing of indents. This altogether allows enhancing accuracy and statistical significance of data attained, including assessment of values

Table 1

Chemical composition of constitutive phases for the composite investigated.

Position	Phase	B	N	Al	Ti
1	cBN	46.81	48.82	1.33	3.04
2	TiN	–	25.30	–	74.70

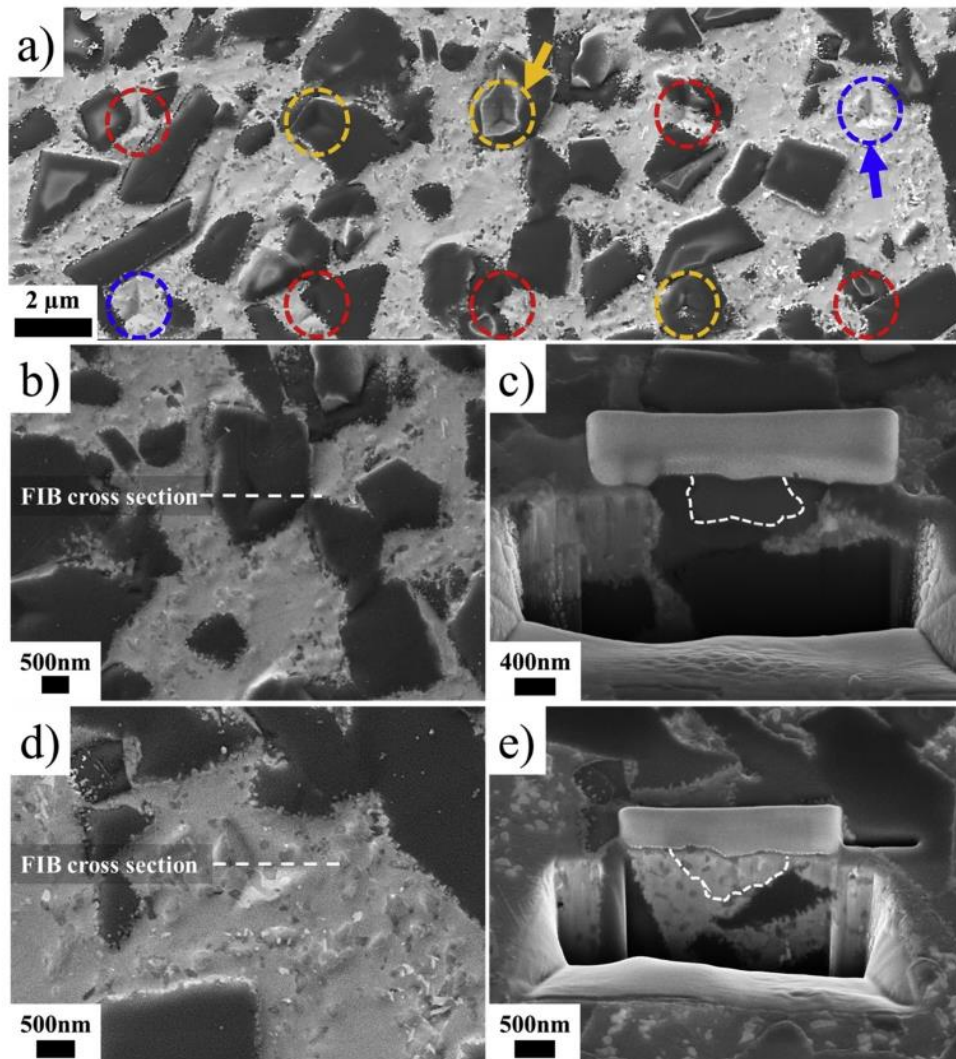


Fig. 1. (a) FESEM micrograph of a small array of imprints performed at 200 nm of maximum displacement into surface; (b) and (d) magnified FESEM micrograph of arrowed residual imprints (Fig. 1a) for cBN particle and TiN binder, respectively; and (c) and (e) FIB-milled cross sections of such imprints, showing estimated size and extension of plastic deformation region induced by nanoindentation.

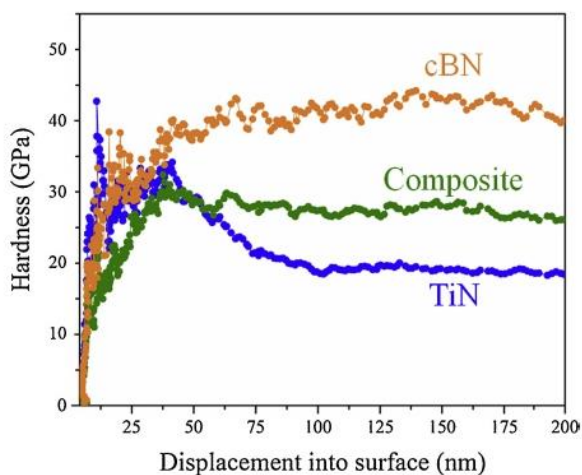


Fig. 2. Hardness against displacement into surface for imprints performed at 200 nm of maximum penetration depth and whose residual imprints are probing the three mechanically different phases defined for the PcBN composite studied.

corresponding to smaller length scale regions than individual phases themselves.

Fig. 4 presents H cartography maps for the PcBN composite studied. As before, they correspond to testing done using two different levels of maximum applied load. Maps have been obtained from bicubic interpolation using 12,500 and 2,500 indents performed at 10 and 25 mN of maximum applied load respectively (Fig. 4a and b, respectively). As already commented from results presented in Fig. 3 and Table 3, H for the TiN phase is observed to range between 15 and 25 GPa, in fair agreement with the data reported in the literature (e.g. Ref. [49]). On the other hand, cBN particles show not only higher H values, but also a much wider scatter, i.e. between 45 and 80 GPa. Finally, intermediate H values are discerned for regions containing phase boundaries, i.e. composite-like nature, where binder and particles are somehow interdispersed or clearly interacting with each other. Regarding property resolution, it is interesting to highlight the higher level attained when imposing lower applied loads (i.e. 10 mN as compared to 25 mN). This must be associated with the lower effective ratio existing between imprint size and microstructural length scale as applied load decreases. However, care should be taken here on the final data analysis, as size (either surface or just length-related) effects may not be neglected as penetration depth becomes extremely shallow.

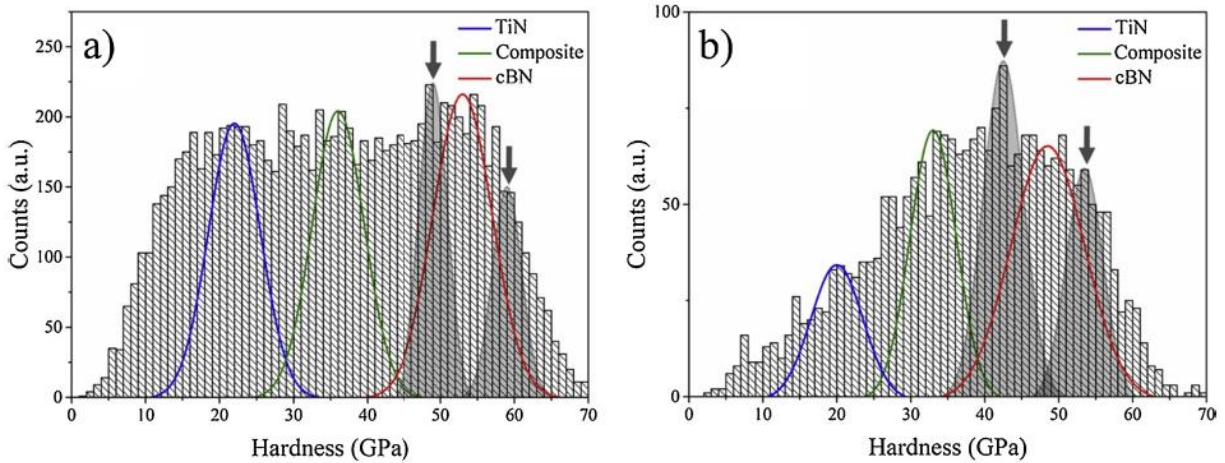


Fig. 3. Hardness histograms computed from (a) 12,500 indentations performed at 10 mN of maximum applied load, and (b) 2,500 indentations performed at 25 mN of maximum applied load.

Table 3

Hardness values for each mechanical phase, obtained from the fitting of the experimental values by using statistical analysis.

Phase	Hardness, H (GPa) (10 mN applied load)	Hardness, H (GPa) (25 mN applied load)
TiN	23 ± 5	21 ± 5
Composite	36 ± 5	33 ± 5
cBN	53 ± 5	49 ± 7

3.2.4. Chemical nature effects on the small-scale hardness of cBN particle

As it was commented in Section 3.2.2, deeper analysis of the histograms shown in Fig. 3 points out that better-fitting of the experimental data could be attained by considering three different small-scale H peaks (instead of just one) for cBN particles as related to chemical nature effects. This hypothesis was proposed on the basis of findings reported by Sachdev [50] who states that morphology and residual stresses of cBN crystals may be directly related to impurity effects as well as different N and B contents along the particle. In this regard, B rich (which implies particles deficient of N) cBN is prone to form B clusters in some specific crystalline planes, finally yielding octahedral/irregular shaped grains with their crystallographic packaging distorted. Within this context, the two extra peaks referred above (see grey arrows in Fig. 3) could then be rationalized on the basis of possible non-stoichiometry effects on measured H of cBN particles, as far as these differences could be discriminated by the massive indentation and statistical analysis protocol implemented in this study.

Attempting to shed some light on this matter, EPMA analysis was used to establish the composition of small areas of the material studied

where a homogeneous indentation array was subsequently performed, under displacement control mode at 200 nm of maximum penetration depth into surface. Main goal behind it was to evaluate possible correlation between N amount and small-scale H of individual cBN particles (where indentations were absolutely confined within the cBN phase, see black circles in Fig. 5b).

From the images shown in Fig. 6a, following EPMA analysis, cBN particles could be classified in three different groups, depending upon relative B/N content in atomic % (at. %): stoichiometric (50/50), and non-stoichiometric - either B-poor (B at. % content lower than 25, Fig. 6b) or B-rich (B at. % content higher than 75, Fig. 6c). Although specific reasons for non-stoichiometry of cBN particles is out of the scope of this investigation, it could be speculated to result, following recent findings by Dios et al. [51], from element diffusion between TiN binder and cBN particles during the sintering stage. Taking this into consideration, small-scale H data may then be assessed for cBN particles as a function of relative B/N content. Fig. 7a shows representative mechanical response, in terms of H against the displacement into surface, exhibited by three cBN particles with different chemical composition. From these results, it is discerned that B-poor particles are clearly harder than B-rich ones, yielding support to the consideration of three mechanically different cBN phases for reliable assessment of small-scale mechanical properties of the PcBN here studied (Fig. 7b and Table 4 with fitted small-scale H for 5 mechanically different phases).

3.3. Indentation fracture toughness

Fig. 8 shows a representative $P-h$ curve recorded when indenting, up to 50 gf, for the material studied. Different pop-ins are discerned in

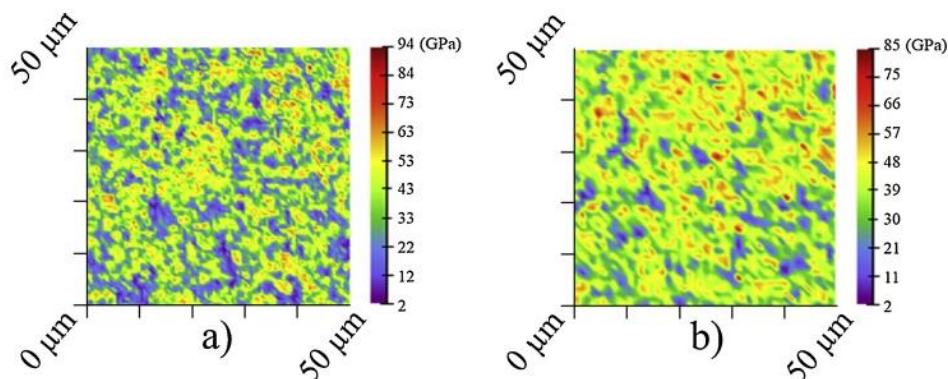


Fig. 4. Hardness map evaluated under loading control mode for studied sample with different applied loads: (a) 10 mN and (b) 25 mN.

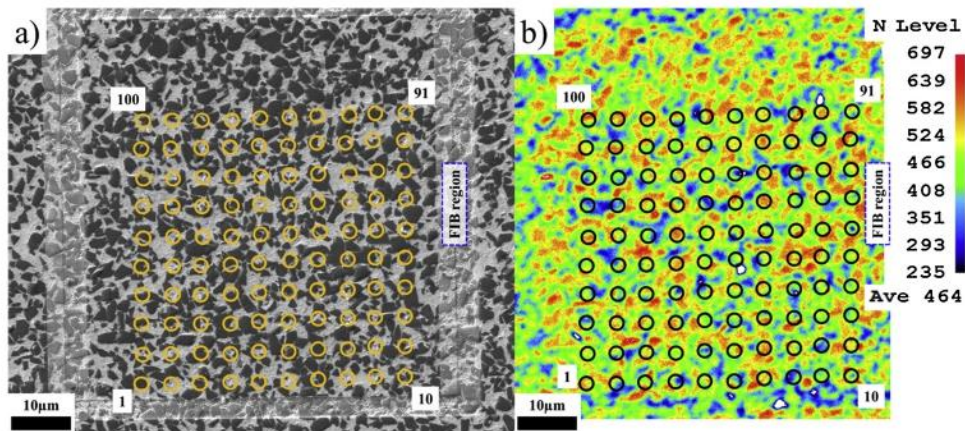


Fig. 5. Matrix of indentations (10 × 10) applied on specific area (framed by a FIB-milled square) of the sample: (a) FESEM micrograph of the region with the matrix of indentations, and (b) N map of corresponding zone, as detected by EPMA.

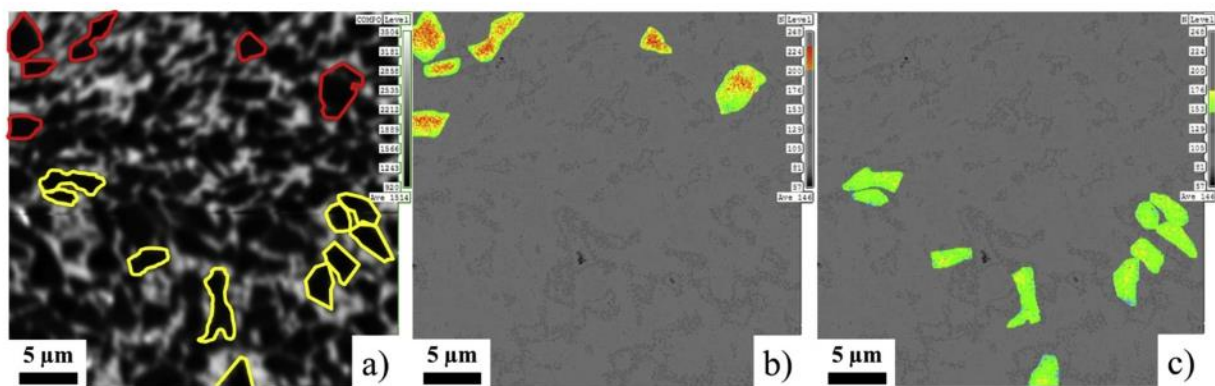


Fig. 6. Atomic chemical analysis performed by EPMA: (a) SEM micrograph, (b) N map for High N grains marked by red dashed lines in SEM image, and (c) N map for Low N grains marked by yellow dashed line in the SEM image, which implies low and high B content, respectively. (For interpretation of the references to colour in this figure legend, the reader is referred to the web version of this article).

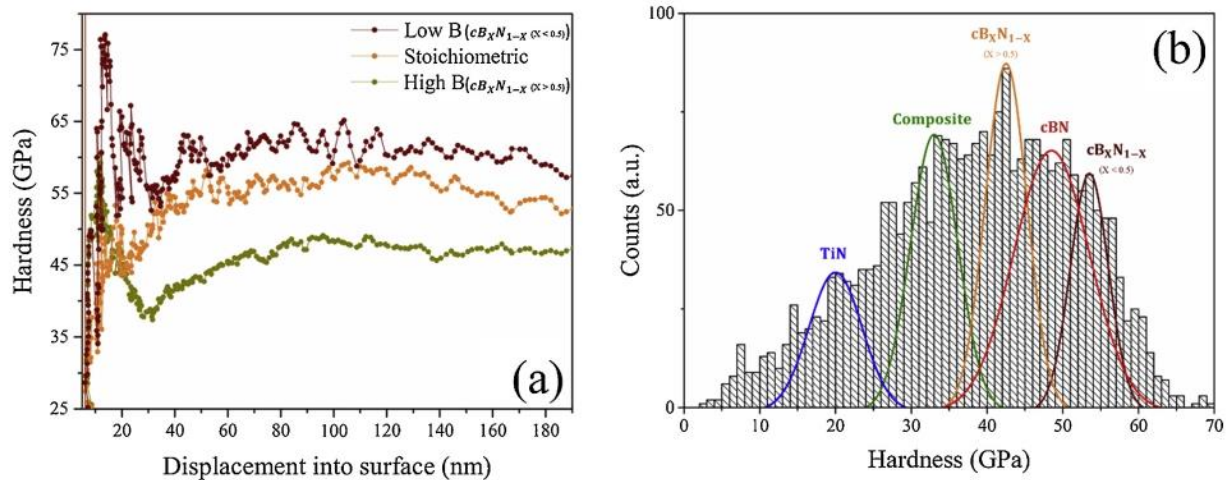


Fig. 7. (a) Hardness against penetration depth for cBN particles exhibiting different B (and N) content, assessed from indentations performed in the region observed by EPMA and within individual cBN particles. (b) Hardness histogram determined from 2,500 indentations performed at 25 mN. Five mechanically different phases were deconvoluted: TiN binder, composite and stoichiometric as well as non-stoichiometric (B-rich and B-poor) cBN particles are overlapped on the histogram.

Table 4
Small-scale *H* for five mechanically different phases of studied sample.

Phase	TiN	Composite	Low N cBN	Stoichiometric cBN	High N cBN
Hardness, <i>H</i> (GPa)	21 ± 5	33 ± 5	43 ± 3	49 ± 7	54 ± 3

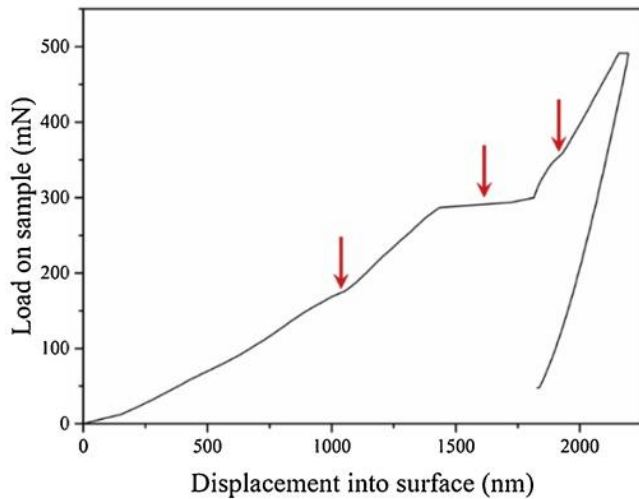


Fig. 8. $P-h$ curve for the indentation performed at 50 gf (red arrows indicate the pop-ins).

the loading curve, possibly in direct relation to irreversible deformation and damage phenomena induced on the material. Fig. 9 shows residual imprints resulting after cube-corner indentations conducted at different applied loads (from 5 to 50 gf). Independent of applied load, radial cracks emanating at the corners of the residual imprints are always absent. At applied load level of 10 gf, material pile-up comes out around the residual imprints (Fig. 9a and b). It is intensified as maximum applied load increases. As applied load gets higher than 20 gf, cracking and chipping are identified as additional damage-induced events (Fig. 9c–f).

FESEM/FIB inspection on transversal sections of residual imprint performed at 50 gf of maximum applied load (Fig. 10a) allows inspection of damage scenario and crack-microstructure interaction induced by the cube corner indentation. Very interesting, it is discerned that besides lateral cracking (white arrow in Fig. 10b), crack bridging (white dashed circle shown in Fig. 10c) also develops. In this regard, it is found that the former nucleates at the material subsurface and runs

parallel to the surface. However, as applied stress rises, the lateral cracks emerges into the surface and induces chipping. During this damage evolution, crack propagation seems to take place mostly through the ceramic binder or ceramic/ceramic interfaces, exhibiting local deflections as it meets the harder cBN particles.

Taking into account that well-developed radial cracks are not observed in the residual imprints (Fig. 9), conventional indentation microfracture method (i.e. through Eq. (3)) cannot be implemented for quantitative assessment of indentation fracture toughness. However, as illustrated in this equation, this parameter mainly depends on the ratio between H and elastic modulus (E) of the material. Within this context, a qualitatively estimation of the effective toughness of the composite studied may be done by invoking the plasticity index ($PI = H/E$ [52,53]). In general, lower plasticity index values are linked to higher effective toughness levels. From gathered data of nanoindentation testing (as referred in previous sections), mean values for macroscopic E and H for the PcBN composite may be taken as 650 GPa and 35 GPa, respectively. It results in a PI value around $5 \cdot 10^{-2}$. For comparison purposes, such value is close to PI levels exhibited by other hard ceramic materials such as WC (E and intrinsic H values in the ranges of 475–650 GPa and 25–33 GPa, respectively [38,39]). Hence, effective toughness for the PcBN composite system studied here may be estimated to range between 4 and 6 $\text{MPa}\cdot\sqrt{\text{m}}$ [54,55], in agreement with lower-bound results reported in the literature for those composites [17,23,24].

4. Conclusions

A systematic investigation, aiming to assess micromechanical properties of the constitutive phases of a PcBN composite has been conducted. The mechanical study has been complemented by the use of advanced characterization techniques such as FESEM/FIB and EPMA. Based on the obtained data the following conclusions may be drawn:

- A protocol based on massive nanoindentation and statistical analysis was successfully implemented for assessing small-scale mechanical properties of a PcBN composite. In doing so, the heterogeneous system was originally considered as constituted by three distinct

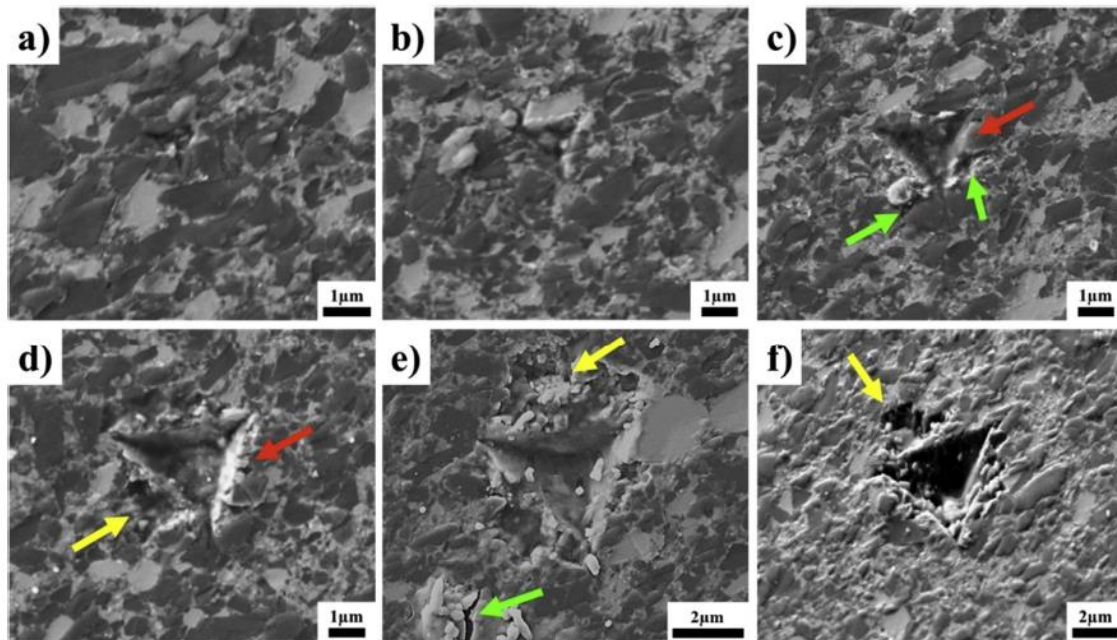


Fig. 9. FESEM micrographs of the residual imprints for cube-corner indentations performed at: a) 5, b) 10, c) 20, d) 30, e) 40, and f) 50 gf. (Red, green and yellow arrows indicate pile-up, cracks and chipping, respectively). (For interpretation of the references to colour in this figure legend, the reader is referred to the web version of this article).

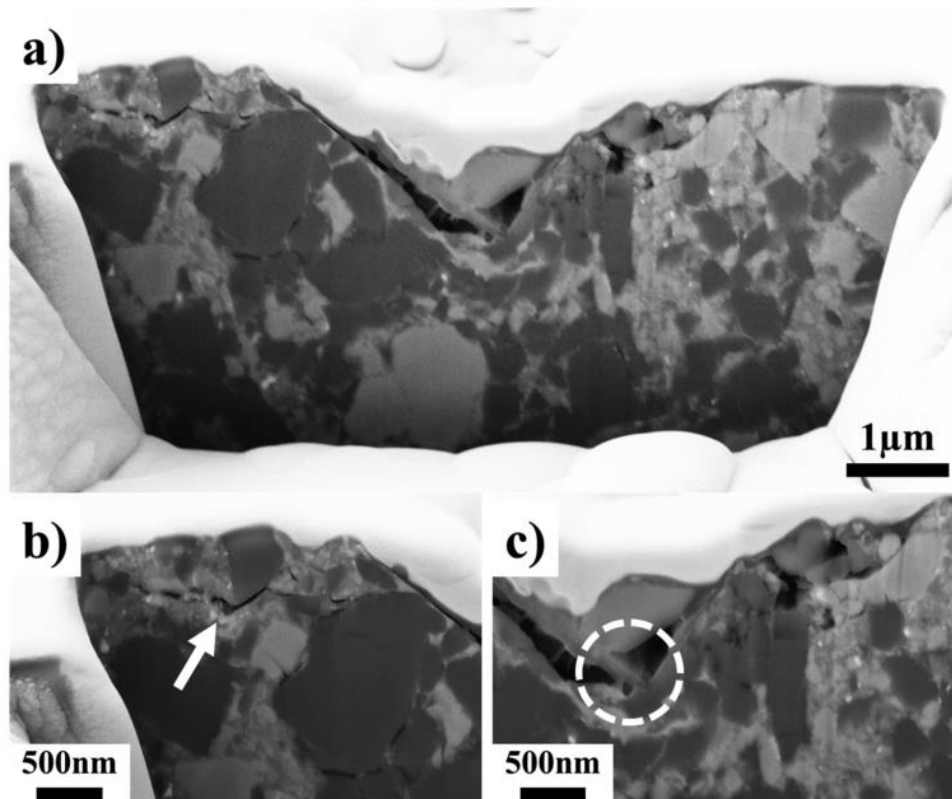


Fig. 10. FESEM micrograph of a) the transversal section of the residual imprint performed at 50 gf, b) magnified micrograph indicating lateral cracks with white arrow and c) crack bridging shown with white dashed circle.

phases with different mechanical properties: two of them microstructurally different, i.e. cBN particles and TiN matrix, and a third phase corresponding to one exhibiting the “composite-like” response. Within this context, intrinsic H values of about 20 and 50 GPa were assessed for TiN binder and cBN grains as lower and upper bounds to the hardness range determined for the composite-like phase, i.e. between 30 and 40 GPa.

- Mean and standard deviation of small-scale H values are independent, within the experimental set outs used in this study, of maximum applied load and number of experimental events (indentations) accounted. However, data attained imposing different load levels, i.e. 25 mN or 10 mN, yielded either better screening among Gaussian distributions for each defined phase or higher microstructure-property resolution within hardness mapping, respectively. Such differences are related to distinct relevance of size-scale effects (e.g. surface roughness) or indenter tip defects depending upon penetration depth.
- An in-depth statistical analysis of the upper-level H data complemented with implementation of advanced characterization techniques (i.e. combined EPMA, instrumented nanoindentation and FESEM) pointed out and validated the consideration of additional mechanically different cBN-related phases on the basis of relative B/N content. To the best knowledge of the authors, it is the first time that different intrinsic H values are reported for cBN particles as a function of phase (B/N ratio) stoichiometry.
- Direct quantitative measurement of K_{Ic} for the composite was not possible because absence of radial cracks emanating from corners of residual imprints. However, PI assessment and subsequent comparison with literature data for WC ceramics, points out that toughness for TiN-cBN composite investigated ranges between 4 and $6 \text{ MPa m}^{1/2}$.

Acknowledgments

The current study was supported by the Spanish Ministerios de Economía y Competitividad MINECO and Ciencia, Innovación y Universidades MICINN - FEDER through grants MAT2015-70780-C4-3-P and PGC2018-096855-B-C41 respectively, and by the industry-university collaborative program between Element Six and UPC. J.J. Roa acknowledges the Serra Hunter program of the Generalitat de Catalunya.

References

- [1] M. Cook, P. Bossom, Trends and recent developments in the material manufacture and cutting tool application of polycrystalline diamond and polycrystalline cubic boron nitride, *Int. J. Refract. Met. Hard. Mater.* 18 (2000) 147–152, [https://doi.org/10.1016/S0263-4368\(00\)00015-9](https://doi.org/10.1016/S0263-4368(00)00015-9).
- [2] R. M'Saoubi, D. Axinte, S.L. Soo, C. Nobel, H. Attia, G. Kappmeyer, S. Engin, W.-M. Sim, High performance cutting of advanced aerospace alloys and composite materials, *CIRP Ann. Manuf. Technol.* 64 (2015) 557–580, <https://doi.org/10.1016/j.cirp.2015.05.002>.
- [3] J. Angseryd, M. Elfving, E. Olsson, H.-O. Andrén, Detailed microstructure of a cBN based cutting tool material, *Int. J. Refract. Met. Hard. Mater.* 27 (2009) 249–255, <https://doi.org/10.1016/j.ijrmhm.2008.09.008>.
- [4] S. Fang, L. Llanes, D. Bähre, F. Mücklich, 3D characterization of cubic boron nitride (cBN) composites used as tool material for high precision abrasive machining processes, *Ceram. Int.* 43 (2017) 14693–14700, <https://doi.org/10.1016/j.ceramint.2017.07.198>.
- [5] J. Arsecularatne, L. Zhang, C. Montross, Wear and tool life of tungsten carbide, PCBN and PCD cutting tools, *Int. J. Mach. Tool Manu.* 46 (2006) 482–491, <https://doi.org/10.1016/j.ijmactools.2005.07.015>.
- [6] C. Lahiff, S. Gordon, P. Phelan, PCBN tool wear modes and mechanisms in finish hard turning, *Robot. Comput. Manuf.* 23 (2007) 638–644, <https://doi.org/10.1016/j.rcim.2007.02.008>.
- [7] K. Katuku, A. Koursaris, I. Sigalas, Wear mechanisms of PcBN cutting tools when dry turning ASTM Grade 2 austempered ductile iron under finishing conditions, *Wear* 268 (2010) 294–301, <https://doi.org/10.1016/j.wear.2009.08.027>.
- [8] M. Okada, A. Hosokawa, R. Tanaka, T. Ueda, Cutting performance of PVD-coated carbide and CBN tools in hardmilling, *Int. J. Mach. Tool Manu.* 51 (2011) 127–132, <https://doi.org/10.1016/j.ijmactools.2010.10.007>.

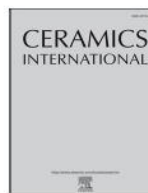
- [9] V. Bushlya, J. Zhou, J.-E. Ståhl, Effect of cutting conditions on machinability of superalloy Inconel 718 during high speed turning with coated and uncoated PCBN tools, *Proc. CIRP*. 3 (2012) 370–375, <https://doi.org/10.1016/j.procir.2012.07.064>.
- [10] R. M'Saoubi, M.P. Johansson, J.M. Andersson, Wear mechanisms of PVD-coated PCBN cutting tools, *Wear* 302 (2013) 1219–1229, <https://doi.org/10.1016/j.wear.2013.01.074>.
- [11] M.A. Shalaby, M.A. El Hakim, M.M. Abdelhameed, J.E. Krzanowski, S.C. Veldhuis, G.K. Dosbaeva, Wear mechanisms of several cutting tool materials in hard turning of high carbon–chromium tool steel, *Tribol. Int.* 70 (2014) 148–154, <https://doi.org/10.1016/j.triboint.2013.10.011>.
- [12] S. Saketi, S. Sveen, S. Gunnarsson, R. M'Saoubi, M. Olsson, Wear of a high cBN content PCBN cutting tool during hard milling of powder metallurgy cold work tool steels, *Wear*. 332 (2015) 752–761, <https://doi.org/10.1016/j.wear.2015.01.073>.
- [13] G.K. Dosbaeva, M.A. El Hakim, M.A. Shalaby, J.E. Krzanowski, S.C. Veldhuis, Cutting temperature effect on PCBN and CVD coated carbide tools in hard turning of D2 tool steel, *Int. J. Refract. Met. Hard. Mater.* 50 (2015) 1–8, <https://doi.org/10.1016/j.jirmhm.2014.11.001>.
- [14] O. Gutnichenko, V. Bushlya, J. Zhou, J.-E. Ståhl, Tool wear and machining dynamics when turning high chromium white cast iron with pcBN tools, *Wear* 390 (2017) 253–269, <https://doi.org/10.1016/j.wear.2017.08.005>.
- [15] L. Chen, J.-E. Stahl, W. Zhao, J. Zhou, Assessment on abrasiveness of high chromium cast iron material on the wear performance of PCBN cutting tools in dry machining, *J. Mater. Process. Technol.* 255 (2018) 110–120, <https://doi.org/10.1016/j.jmatprotec.2017.11.054>.
- [16] R.M. Erasmus, J.D. Comins, M.L. Fish, Raman and photoluminescence spectra of indented cubic boron nitride and polycrystalline cubic boron nitride, *Diam. Relat. Mater.* 9 (2000) 600–604, [https://doi.org/10.1016/S0925-9635\(00\)00241-7](https://doi.org/10.1016/S0925-9635(00)00241-7).
- [17] A. McKie, J. Winzer, I. Sigalas, M. Herrmann, L. Weiler, J. Rödel, N. Can, Mechanical properties of cBN–Al composite materials, *Ceram. Int.* 37 (2011) 1–8, <https://doi.org/10.1016/j.ceramint.2010.07.034>.
- [18] M.A. Umer, P.H. Sub, D.J. Lee, H.J. Ryu, S.H. Hong, Polycrystalline cubic boron nitride sintered compacts prepared from nanocrystalline TiN coated cBN powder, *Mater. Sci. Eng. A*. 552 (2012) 151–156, <https://doi.org/10.1016/j.msea.2012.05.024>.
- [19] K. Mawęja, L. Cornish, N. Can, Polycrystalline cubic boron nitride sintered with Ti (C, N)–W–Al mechanically alloyed binders, *J. Eur. Ceram. Soc.* 32 (2012) 3593–3601, <https://doi.org/10.1016/j.jeurceramsoc.2012.05.011>.
- [20] D. Carolan, A. Ivanković, N. Murphy, A combined experimental–numerical investigation of fracture of polycrystalline cubic boron nitride, *Eng. Fract. Mech.* 99 (2013) 101–117, <https://doi.org/10.1016/j.engfracmech.2012.09.008>.
- [21] P. Alveen, D. McNamara, D. Carolan, N. Murphy, A. Ivanković, The influence of microstructure on the fracture properties of polycrystalline cubic boron nitride, *Comp. Mater. Sci.* 109 (2015) 115–123, <https://doi.org/10.1016/j.commatsci.2015.06.036>.
- [22] Y. Ichida, H. Ohfui, T. Irifune, Y. Kojima, T. Shinmei, Synthesis of ultrafine nanocrystalline cubic boron nitride by direct transformation under ultrahigh pressure, *J. Eur. Ceram. Soc.* 38 (2018) 2815–2822, <https://doi.org/10.1016/j.jeurceramsoc.2018.02.023>.
- [23] L. Li, Y. Zhao, K. Sun, H. Ji, D. Feng, Z. Li, Composition, microstructure and mechanical properties of cBN-based composites sintered with AlN–Al–Ni binder, *Ceram. Int.* 44 (2018) 16915–16922, <https://doi.org/10.1016/j.ceramint.2018.06.130>.
- [24] K. Slipchenko, V. Turkevich, I. Petrusha, V. Bushlya, J.-E. Ståhl, Superhard pcBN materials with chromium compounds as a binder, *Procedia Manuf.* 25 (2018) 322–329, <https://doi.org/10.1016/j.promfg.2018.06.090>.
- [25] H.E. Exner, Physical and chemical nature of cemented carbides, *Int. Mater. Rev.* 24 (1979) 149–173, <https://doi.org/10.1179/imtr.1979.24.1.149>.
- [26] B. Roebuck, E. Almond, Deformation and fracture processes and the physical metallurgy of WC–Co hardmetals, *Int. Mater. Rev.* 33 (1988) 90–112, <https://doi.org/10.1179/imr.1988.33.1.90>.
- [27] L. Prakash, Fundamentals and general applications of hardmetals, in: V.K. Sarin, D. Mari, L. Llanes (Eds.), *Comprehensive Hard Materials*, Elsevier Ltd, Oxford, 2014, pp. 29–90.
- [28] Metallographic Determination of Microstructure. Part 2: Measurement of WC Grain Size, in: ISO 4499-2: 2008, (2008) Hardmetals, Geneva.
- [29] C. Merlet, X. Llovet, F. Salvat, Measurements of the surface ionization in multi-layered specimens, X-ray spectrum. 33 (2004) 376–386, <https://doi.org/10.1002/xrs.757>.
- [30] C. Merlet, X. Llovet, O. Dugne, S. Brémier, W. Van Renterghem, R. Restani, Virtual standard for wavelength-dispersive electron-probe microanalysis, *Microchim. Acta*. 161 (2008) 427–432, <https://doi.org/10.1007/s00604-007-0856-2>.
- [31] W.C. Oliver, G.M. Pharr, An improved technique for determining hardness and elastic modulus using load and displacement sensing indentation experiments, *J. Mater. Res.* 7 (1992) 1564–1583, <https://doi.org/10.1557/JMR.1992.1564>.
- [32] W.C. Oliver, G.M. Pharr, Measurement of hardness and elastic modulus by instrumented indentation: advances in understanding and refinements to methodology, *J. Mater. Res.* 19 (2004) 3–20, <https://doi.org/10.1557/jmr.2004.19.1.3>.
- [33] G. Constantinides, F.-J. Ulm, K. Van Vliet, On the use of nanoindentation for cementitious materials, *Mater. Struct.* 36 (2003) 191–196, <https://doi.org/10.1007/BF02479557>.
- [34] G. Constantinides, K.S. Ravi Chandran, F.J. Ulm, K.J. Van Vliet, Grid indentation analysis of composite microstructure and mechanics: principles and validation, *Mater. Sci. Eng. A*. 430 (2006) 189–202, <https://doi.org/10.1016/j.msea.2006.05.125>.
- [35] G. Constantinides, F.-J. Ulm, The nanogranular nature of C–S–H, *J. Mech. Phys. Solids* 55 (2007) 64–90, <https://doi.org/10.1016/j.jmps.2006.06.003>.
- [36] F.-J. Ulm, M. Vandamme, C. Bobko, J. Alberto Ortega, K. Tai, C. Ortiz, Statistical indentation techniques for hydrated nanocomposites: concrete, bone, and shale, *J. Am. Ceram. Soc.* 90 (2007) 2677–2692, <https://doi.org/10.1111/j.1551-2916.2007.02012.x>.
- [37] P.S. Phani, W.C. Oliver, A critical assessment of the effect of indentation spacing on the measurement of hardness and modulus using instrumented indentation testing, *Mater. Des.* 64 (2019) 107563, <https://doi.org/10.1016/j.matdes.2018.107563>.
- [38] J.J. Roa, E. Jiménez-Piqué, C. Verge, J.M. Tarragó, A. Mateo, J. Fair, L. Llanes, Intrinsic hardness of constitutive phases in WC–Co composites: Nanoindentation testing, statistical analysis, WC crystal orientation effects and flow stress for the constrained metallic binder, *J. Eur. Ceram. Soc.* 35 (2015) 3419–3425, <https://doi.org/10.1016/j.jeurceramsoc.2015.04.021>.
- [39] J.J. Roa, P.S. Phani, W.C. Oliver, L. Llanes, Mapping of mechanical properties at microstructural length scale in WC–Co cemented carbides: Assessment of hardness and elastic modulus by means of high speed massive nanoindentation and statistical analysis, *Int. J. Refract. Met. Hard. Mater.* 75 (2018) 211–217, <https://doi.org/10.1016/j.jirmhm.2018.04.019>.
- [40] D.A. Sandoval, J.J. Roa, O. Ther, E. Tarrés, L. Llanes, Micromechanical properties of WC–(W, Ti, Ta, Nb) C–Co composites, *J. Alloys. Compd.* 777 (2019) 593–601, <https://doi.org/10.1016/j.jallcom.2018.11.001>.
- [41] H. Besharatloo, M. de Nicolás, J.J. Roa, M. Dios, A. Mateo, B. Ferrari, E. Gordo, L. Llanes, Assessment of mechanical properties at microstructural length scale of Ti (C,N)–FeNi ceramic-metal composites by means of massive nanoindentation and statistical analysis, *Ceram. Int.* (2019), <https://doi.org/10.1016/j.ceramint.2019.06.292> in press.
- [42] B.R. Lawn, A. Evans, D. Marshall, Elastic/plastic indentation damage in ceramics: the median/radial crack system, *J. Am. Ceram. Soc.* 63 (1980) 574–581, <https://doi.org/10.1111/j.1151-2916.1980.tb10768.x>.
- [43] G. Pharr, Measurement of mechanical properties by ultra-low load indentation, *Mater. Sci. Eng. A* 253 (1998) 151–159, [https://doi.org/10.1016/S0921-5093\(98\)00724-2](https://doi.org/10.1016/S0921-5093(98)00724-2).
- [44] Y. Yuan, X. Cheng, R. Chang, T. Li, J. Zang, Y. Wang, Y. Yu, J. Lu, X. Xu, Reactive sintering cBN–Ti–Al composites by spark plasma sintering, *Diam. Relat. Mater.* 69 (2016) 138–143, <https://doi.org/10.1016/j.diamond.2016.08.009>.
- [45] H. Kuwahara, N. Mazaki, M. Takahashi, T. Watanabe, X. Yang, T. Aizawa, Mechanical properties of bulk sintered titanium nitride ceramics, *Mater. Sci. Eng. A* 319 (2001) 687–691, [https://doi.org/10.1016/S0921-5093\(01\)00936-4](https://doi.org/10.1016/S0921-5093(01)00936-4).
- [46] D. Demirskyi, D. Agrawal, A. Ragulya, Comparisons of grain size-density trajectory during microwave and conventional sintering of titanium nitride, *J. Alloys. Compd.* 581 (2013) 498–501, <https://doi.org/10.1016/j.jallcom.2013.07.159>.
- [47] S. Suarez-Vazquez, M. Nanko, Preparation of dense TiN1 – X (X = 0–0.4) by pulsed electric current sintering: Densification and mechanical behavior, *Int. J. Refract. Met. Hard. Mater.* 44 (2014) 54–59, <https://doi.org/10.1016/j.jirmhm.2014.01.008>.
- [48] B.M. Moshtaghion, D. Gómez-García, A. Domínguez-Rodríguez, Spark plasma sintering of titanium nitride in nitrogen: Does it affect the sinterability and the mechanical properties? *J. Eur. Ceram. Soc.* 38 (2018) 1190–1196, <https://doi.org/10.1016/j.jeurceramsoc.2017.12.029>.
- [49] D. Stone, K. Yoder, W. Sproul, Hardness and elastic modulus of TiN based on continuous indentation technique and new correlation, *J. Vac. Sci. Technol. A* 9 (1991) 2543–2547, <https://doi.org/10.1116/1.577270>.
- [50] H. Sachdev, Influence of impurities on the morphology and Raman spectra of cubic boron nitride, *Diam. Relat. Mater.* 12 (2003) 1275–1286, [https://doi.org/10.1016/S0925-9635\(03\)00072-4](https://doi.org/10.1016/S0925-9635(03)00072-4).
- [51] M. Dios, Z. Gonzalez, E. Gordo, B. Ferrari, Chemical precipitation of nickel nanoparticles on Ti (C, N) suspensions focused on cermet processing, *Int. J. Refract. Met. Hard. Mater.* 63 (2017) 2–8, <https://doi.org/10.1016/j.jirmhm.2016.08.009>.
- [52] A. Leyland, A. Matthews, On the significance of the H/E ratio in wear control: a nanocomposite coating approach to optimised tribological behaviour, *Wear* 246 (2000) 1–11, [https://doi.org/10.1016/S0043-1648\(00\)00488-9](https://doi.org/10.1016/S0043-1648(00)00488-9).
- [53] A. Leyland, A. Matthews, Design criteria for wear-resistant nanostructured and glassy-metal coatings, *Surf. Coat. Technol.* 177 (2004) 317–324, <https://doi.org/10.1016/j.surfcoat.2003.09.011>.
- [54] R. Warren, Measurement of the fracture properties of brittle solids by Hertzian indentation, *Acta. Metall.* 26 (1978) 1759–1769, [https://doi.org/10.1016/0001-6160\(78\)90087-1](https://doi.org/10.1016/0001-6160(78)90087-1).
- [55] J.M. Tarragó, J.J. Roa, V. Valle, J. Marshall, L. Llanes, Fracture and fatigue behavior of WC–Co and WC–CoNi cemented carbides, *Int. J. Refract. Met. Hard. Mater.* 49 (2015) 184–191, <https://doi.org/10.1016/j.jirmhm.2014.07.027>.

Article III:**Assessment of mechanical properties at microstructural length scale of Ti(C,N)–FeNi ceramic-metal composites by means of massive nanoindentation and statistical analysis**

H. Besharatloo, M. de Nicolás, J.J. Roa, M. Dios, A. Mateo, B. Ferrari, E. Gordo and L. Llanes. *Ceramics International* 45 (2019) 20202–20210. <https://doi.org/10.1016/j.ceramint.2019.06.292>.

Summary

It is well known the interest of the scientific community in substituting the traditional cemented carbides (WC-Co) by alternative ceramic-metal systems. In this regard, Ti(C,N)-based cermets arise as excellent candidates due to their exceptional mechanical, tribological and thermal properties. In this work, microstructurally different Ti(C,N)-FeNi cermets were processed using a combination of colloidal and powder metallurgy techniques. Three distinct ceramic/metal phase ratios were used: 85/15, 80/20, and 70/30 (volume fraction) of Ti(C,N) and FeNi, respectively. Microstructural parameters and micromechanical properties (hardness and stiffness) of the three composite systems and their constitutive phases were assessed. Small-scale hardness was evaluated by means of massive nanoindentation testing and statistical analysis of the gathered data, under the consideration of three mechanically different phases: Ti(C,N) particles, metallic binder, and a composite-like one, corresponding to probing regions containing both constitutive phases. It is found that values of local hardness for both composite-like and metallic phases increase as the ceramic/metal phase ratio rises. In particular, local hardness values are determined to be significantly distinct for the metallic binder in the three cermets investigated. Results are discussed and rationalized on the basis of the constrained deformation imposed for the harder phase to the softer and more ductile one. Estimated effective flow stress values for the metallic binder as well as detailed inspection of crack-microstructure interaction and fractographic features point out the effectiveness of FeNi as reinforcement phase and toughening agent for Ti(C,N)-based cermets.



Assessment of mechanical properties at microstructural length scale of Ti(C, N)–FeNi ceramic-metal composites by means of massive nanoindentation and statistical analysis

H. Besharatloo^{a,b,*}, M. de Nicolás^c, J.J. Roa^{a,b}, M. Dios^c, A. Mateo^{a,b}, B. Ferrari^d, E. Gordo^c, L. Llanes^{a,c}

^a CIEFMA - Department of Materials Science and Metallurgical Engineering, EEBE, Universitat Politècnica de Catalunya-BarcelonaTech, 08019, Barcelona, Spain

^b Barcelona Research Centre in Multiscale Science and Engineering, Universitat Politècnica de Catalunya-BarcelonaTech, 08019, Barcelona, Spain

^c GTP - Department of Materials Science and Engineering, Universidad Carlos III Madrid, Avda. De la Universidad, 30, 28911, Leganés, Spain

^d Institute of Ceramic and Glass, CSIC, 28049, Madrid, Spain

ARTICLE INFO

Keywords:

Cermet
Nanoindentation
Massive indentation
Statistical analysis

ABSTRACT

It is well known the interest of the scientific community in substituting the traditional cemented carbides (WC–Co) by alternative ceramic-metal systems. In this regard, Ti(C,N)-based cermets arise as excellent candidates due to their exceptional mechanical, tribological and thermal properties. In this work, microstructurally different Ti(C,N)–FeNi cermets were processed using a combination of colloidal and powder metallurgy techniques. Three distinct ceramic/metal phase ratios were used: 85/15, 80/20 and 70/30 (volume fraction) of Ti (C,N) and FeNi respectively. Microstructural parameters and micromechanical properties (hardness and stiffness) of the three composite systems and their constitutive phases were assessed. Small-scale hardness was evaluated by means of massive nanoindentation testing and statistical analysis of the gathered data, under the consideration of three mechanically different phases: Ti(C,N) particles, metallic binder and a composite-like one, corresponding to probing regions containing both constitutive phases. It is found that values of local hardness for both composite-like and metallic phases increase as the ceramic/metal phase ratio rises. In particular, local hardness values are determined to be significantly distinct for the metallic binder in the three cermets investigated. Results are discussed and rationalized on the basis of the constrained deformation imposed for the harder phase to the softer and more ductile one. Estimated effective flow stress values for the metallic binder as well as detailed inspection of crack-microstructure interaction and fractographic features point out the effectiveness of FeNi as reinforcement phase and toughening agent for Ti(C,N)-base cermets.

1. Introduction

Cemented carbides are a group of ceramic-metal composite materials with exceptional combinations of hardness, strength and toughness together with unique wear and abrasion resistance [1,2]. Main reasons behind it are the wide range of microstructural assemblages available for these composites, all of them consisting of interpenetrating networks of two phases with completely different properties: hard/brittle ceramic particles and soft/ductile metallic binder [3–5]. Among these materials, WC–Co alloys, also referred to as hardmetals, are one of the most successful “tailor-made” composites. As a result, they are nowadays preminent material choices for extremely demanding applications, such as metal cutting/forming or mining tools, where high

performance and reliability levels are required [6]. However, in recent years both scientific and industrial sectors have been struggling to find substitution materials for these reference WC–Co cemented carbides. This is mainly because the classification of cobalt and tungsten as critical raw materials by the European Union (i.e. besides being considered as raw materials of a high importance to the economy of the EU, there exists a high risk of a disruption in their supply), as well as their consideration as hazardous substances for human health [7–9].

Following above ideas, Ti(C,N)-based ceramic-metal systems (cermets) have been proposed as competitive alternative systems to plain WC–Co alloys, owing to their outstanding hardness, oxidation and wear resistance, as well as thermal and chemical stability [10–13]. With respect to the metallic constituent, Fe and Ni alloys are both considered to

* Corresponding author. CIEFMA - Department of Materials Science and Metallurgical Engineering, EEBE, Universitat Politècnica de Catalunya-BarcelonaTech, 08019, Barcelona, Spain.

E-mail address: luis.miguel.llanes@upc.edu (H. Besharatloo).

<https://doi.org/10.1016/j.ceramint.2019.06.292>

Received 17 May 2019; Received in revised form 24 June 2019; Accepted 27 June 2019

Available online 28 June 2019

0272-8842/ © 2019 Elsevier Ltd and Techna Group S.r.l. All rights reserved.

substitute Co. The lower price and non-toxicity state of Fe compared to Co, make it a proper option as a metallic binder. Furthermore, Fe is an abundant raw material and has the ability to be hardened by thermal treatments [14–16]. Meanwhile, Ni becomes an optimal alloying element, as previous studies have demonstrated that it improves the wettability between Fe and Ti(C,N), a behaviour directly related to the densification of the samples during the sintering stage [17]. Nevertheless, high functional performance levels exhibited by hardmetal tools and components require, besides achievable processing, similar exceptional hardness-toughness correlations. Thus, both intrinsic hardness of ceramic particles and effective toughening by the metallic binder become key microstructural design parameters for designing and developing new ceramic-metal systems.

Although there exist a large amount of studies on mechanical properties of ceramic-metal systems (either WC- or Ti(C,N)-based), they have been mainly addressed to evaluate basic and macroscopic parameters, i.e. Vickers hardness and/or Palmqvist indentation fracture toughness [18–22]. On the other hand, research focused on small-scale hardness/toughness, i.e. at the level of microstructural dimensions, has been rather limited and mainly focused on WC-based systems [23–32]. In this regard, as it has been recently validated by the authors, massive nanoindentation together with statistical analysis of the gathered data have shown to be a quite effective micromechanical testing protocol for experimental assessment and understanding intrinsic mechanical properties of main constitutive phases, especially those of the constrained binder [25,27,32]. Within this framework, it is the objective of the present study to evaluate the small-scale mechanical properties for the main constitutive phases present on Ti(C,N)–FeNi composites exhibiting different ceramic/metal phase ratio. Results are expected to provide microstructural design guidelines for novel cemented carbides aiming to satisfy mechanical and tribological requirements associated with increasingly demanding applications.

2. Experimental procedure

2.1. Sample preparation

Titanium carbonitride (Ti(C,N), Ti(C_{0.5}N_{0.5})) and iron (Fe, Fe SM) submicron powders were supplied by H.C Starck (Germany). On the other hand, submicron powder of nickel (Ni, Ni 210H) was provided by INCO (Canada). Particle size and specific surface area were characterized by means of laser analyser (Mastersizer S, Malvern instruments Ltd., UK) and one-point N₂ absorption (Monosorb Surface Area, Quantachrome Corporation, USA), respectively. Moreover, Monosorb Multipycnometer (Quantachrome Corporation, USA) set was used to measure the density of the as-received powders. All the mentioned parameters are summarized in Table 1.

Powders were processed using a combination of colloidal and powder metallurgy techniques. High solid content suspensions were formulated for submicron powders of Ti(C,N), Fe and the mixture of Fe and Ni, using deionized water as dispersion medium [33,34]. In all cases, the slurries were prepared in deionized water and pH was adjusted up to 10–11 adding Tetra methyl ammonium hydroxide (TMAH), where surfaces of the powder particles are chemically stable. Then the

Table 1
Physical characteristics for the as-received submicron powders.

Characteristics	Powder		
	Ti(C,N)	Fe	Ni
Density ^a (g·cm ⁻³)	5.1	7.8	8.9
D _{v50} (μm)	2.1	3.5	1.7
Surface area ^b (m ² /g)	3.0	0.6	4.0

^a ± 0.1 Standard deviation in density measurements.

^b ± 0.1 Standard deviation in specific surface area measurements.

Table 2
Chemical formulation of suspensions.

Sample	Vol. %	wt. %		Composition metal matrix, wt. %	
		Ti(C,N)	Fe/Ni	Fe	Ni
85Ti(C,N)–15FeNi	85	15	78.4	21.6	85
80Ti(C,N)–20FeNi	80	20	71.9	28.1	85
70Ti(C,N)–30FeNi	70	30	59.9	40.1	85

necessary amount of Polyethylenimine (PEI) to completely cover the particle surface in each case, was added as dispersant. Slurries of Ti (C,N) and the mixture of Fe and Ni powders were prepared and milled separately in a ball mill for 1 h, using Si₃N₄ and nylon balls, respectively.

Milling process was followed by the mixture of the Ti(C,N) and Fe/Ni slurries in order to get the desired powder compositions. The volume ratio of Ti(CN)/FeNi were 85/15, 80/20 and 70/30 vol/vol for each mixture. Table 2 summarizes the volume and weight ratio of considered powder composition as well as the composition of the formulated metallic binder (85/15 wt/wt Fe/Ni) which was maintained in all cases. Then, 2 wt% of Polyvinyl alcohol (PVA) was added as the processing polymer binder, and afterwards the slurry was kept for 20 min under mechanical stirring, before the spray-drying step.

Spray-dry method was implemented using stable aqueous suspensions of the mixture of powders to provide granules able to be pressed. This processing step allows the fabrication of a feedstock for pressing where ceramic and metal powders are homogeneously dispersed and mixed. In doing so, LabPlant SD-05 atomizer (North Yorkshire, UK) was used with the main controlled operating parameters being inlet and exhaust temperatures: 190 °C and 100 °C respectively. The slurry pump rate (2 L/h) and the atomizing nozzle design were set to attain spherical agglomerates with high compressibility, capable to be formed by uniaxial pressing [34]. Finally, a uniaxial die was used to press the granules into disks (16 mm in diameter) at 600 MPa. Compressed samples were sintered in a high-vacuum furnace (10⁻⁵ bar) for 2 h at 1450 °C, with a dwell time of 30 min at 800 °C.

In order to correctly prepare sample surfaces for microstructural and micromechanical characterization, cross sections of the sintered materials were polished precisely with diamond paste down to 3 μm. Polishing by colloidal alumina was conducted as final step, in order to release any work-hardening effect induced in the metallic binder during previous sample preparation stages.

2.2. Microstructural characterization

Microstructural characterization included the evaluation of grain size of the carbonitride phase ($d_{Ti(C,N)}$), mean free path (λ) of the metallic binder and porosity. The former two parameters were assessed on images obtained in a field emission scanning electron microscopy (FESEM) unit (JSM-7100F, JEOL Ltd., Japan) at the acceleration voltage of 20 kV. Five micrographs per specimen were used and values were determined by means of the linear interception method (LIM) [35]. On the other hand, amount of porosity was determined, as a function of volume fraction of the metallic binder, by means of ImageJ software.

2.3. Small-scale mechanical characterization

Nanoindentation technique was implemented to evaluate the composite hardness (H) and elastic modulus (E) of Ti(C,N)–FeNi systems as well as the intrinsic hardness for each constitutive phase at both micro- and nanometric length scales, respectively. Nanoindentation tests were performed using a testing unit (Nanoindenter XP, MTS Systems Corporation, USA) coupled with a continuous stiffness measurement

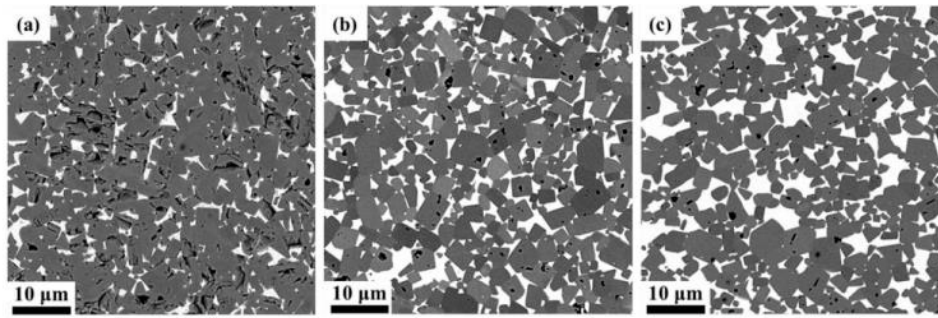


Fig. 1. FESEM images of microstructure for Ti(C,N)-FeNi with different vol% of the metallic binder: a) 85Ti(C,N)-15FeNi, b) 80Ti(C,N)-20FeNi and c) 70Ti(C,N)-30FeNi.

(CSM) modulus. The set was equipped with a diamond Berkovich indenter, which was precisely calibrated by using a fused silica standard sample with a known Young's modulus, 72 GPa [36]. The micro-mechanical properties were extracted directly by using the Oliver and Pharr method [36,37].

In order to determine H and E of the composite system (Ti(C,N)-FeNi), an homogeneous array of 16 indentations (4 by 4) was performed at 2 μm of maximum penetration depth or until reaching the maximum applied load of the loading cell, 650 mN. On the other hand, aiming to evaluate the intrinsic hardness of each constitutive phase, 2000 indentations per sample (five matrices of 20 by 20) were done at a maximum displacement into surface of 200 nm. In this testing protocol, residual imprints and plastic flow need to be confined inside each phase, in order to guarantee that each single indentation could be considered as an individual statistical outcome. Furthermore, the distance between imprints was required to be set adequately to avoid any overlapping effect of neighbouring imprints. Taking these testing requirements into consideration, distances between applied imprints at 2000 and 200 nm penetration depths were kept constant at 50 and 5 μm , respectively [25].

2.4. Statistical analysis

Intrinsic hardness of each constitutive phase was evaluated by using the statistical analysis of the gathered H data, as proposed by Ulm and co-workers [25,38–41]. In doing so, investigated specimens were considered to contain several (i) mechanically distinct phases. In this regard, three main phases were contemplated for the studied system: Ti(C,N) particles, metallic binder and a third one representative of the case where plastic flows of ceramic and metal phases are interacting, i.e. composite-like response. This statistical analysis assumes that distribution (p_i) of interested mechanical properties (in this case hardness) of each constitutive phase follows a Gaussian distribution:

$$p_i = \frac{1}{\sqrt{2\pi\sigma_i^2}} \exp\left[-\frac{(H - H_i)^2}{2\sigma_i^2}\right] \quad (1)$$

where H_i is the arithmetic mean of all individual indentations (N_i) performed on each phase (i) and σ_i is the standard deviation. Then, the cumulative distribution function (CDF) using sigmoid shape error function, may be fit by the following expression:

$$CDF = \sum_i \frac{1}{2} f_i \operatorname{erf}\left[\frac{H - H_i}{\sqrt{2}\sigma_i}\right] \quad (2)$$

Table 3
Microstructural parameters of studied samples.

Sample name	Binder content, vol %	Mean Ti(C,N) grain size, $d_{Ti(C,N)}$ (μm)	Mean free path, λ (μm)	Porosity %
85Ti(C,N)-15FeNi	15	2.2 \pm 0.3	0.5 \pm 0.1	2.7 \pm 1.1
80Ti(C,N)-20FeNi	20	2.2 \pm 0.3	0.6 \pm 0.1	0.5 \pm 0.1
70Ti(C,N)-30FeNi	30	2.3 \pm 0.3	1.0 \pm 0.2	1.2 \pm 0.9

where f_i is defined as the relative fraction occupied by each constitutive phase. In order to acquire reliable values, several restrictions were programmed during the deconvolution process. In this regard, the total volume fraction of constitutive phase was fixed at 1, while the fitting process was set to finalize when the chi-square (χ^2) tolerance was less than 10^{-15} , with an ultimate coefficient of determination (R^2) of 0.9998. Additional and detailed information about the statistical method followed can be found in Refs. [25,38–41].

In order to implement this protocol, three main critical parameters must be taken into account: (I) indentation size, (II) relative difference in hardness values between the constitutive phase, and (III) grid size. These three main parameters will be recalled as results are presented and discussed in the following sections.

2.5. Damage and fracture micromechanisms

Deformation, subsurface damage and fracture-related (crack-microstructure interaction) scenario induced by residual imprints were evaluated by scrutinizing contact surfaces through a dual beam FESEM/Focused Ion Beam (FIB) unit (Neon40 Crossbeam, Carl Zeiss MicroImaging GmbH, Germany). Regarding cross-section examination, prior to milling, a thin protective layer of platinum was deposited on the region of interest to circumvent any waterfall effect, which could affect the quality of the images. Current and acceleration voltage of Ga^+ source were subsequently reduced down to a final polishing stage at 500 pA and 30 kV respectively. Finally, special attention was paid to discern fractographic features of the metallic binder on intentionally (and abruptly) broken sections of previously indented samples.

3. Results and discussions

3.1. Microstructural parameters

FESEM micrographs of studied samples are shown in Fig. 1. The corresponding microstructural parameters are summarized in Table 3. Grain size for the ceramic phase followed bimodal distributions, although mean value was quite similar for all the samples. Fig. 2 shows a typical grain size histogram for the Ti(C,N) particles with a constant bin size of 100 nm. It was plotted from data measured for 675 different grains in the sample 85Ti(C,N)-15FeNi. Qualitative similar histograms were attained for the rest of the specimens studied. Two distributions are overlapped to the experimental values, corresponding to coarse and fine Ti(C,N) particles, in agreement with microstructural scenarios

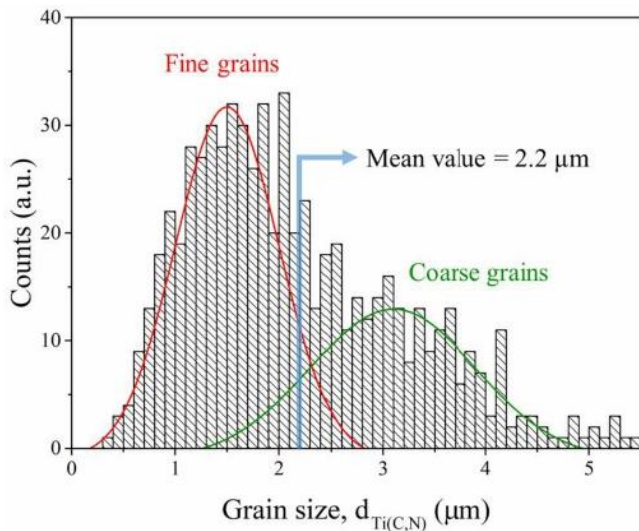


Fig. 2. Grain size histogram for sample 85Ti(C,N)–15FeNi, with 100 nm of bin size. Two simulated distributions were fitted over the experimental values, as related to fine and coarse grains.

discerned in images shown in Fig. 1.

As it can be appreciated in Fig. 1 and Table 3, porosity was between 0.5 and 2.7% for all the specimens. It was reduced and density reached values close to 99% for specimens with the highest volume fraction of metallic phase studied. Considering that all the specimens were sintered using same temperature and time conditions, lack of binder for embedding all the ceramic particles when the liquid phase is formed seems to be a plausible reason for the higher porosity levels attained for 85/15 and 80/20 ceramic/metal phase ratios [17,34]. Nevertheless, it should be highlighted that, besides sintering temperature and time, there are additional processing variables that could affect final density of specimens. Achievement of full density for every composition studied was out of the scope of this investigation, although it is a topic being addressed in ongoing research carried out by the authors.

3.2. Small-scale mechanical properties

3.2.1. Mechanical properties of the composite: hardness and elastic modulus

Representative curves of measured hardness (H) and elastic modulus (E) values as a function of the displacement into the surface for the different Ti(C,N)–FeNi systems are shown in Fig. 3a and Fig. 3b, respectively. Possible indentation size effect (ISE) or tip defect interactions were evaluated by plotting the ratio between applied load and stiffness squared (P/S^2) as a function of the displacement into surface (e.g. Fig. 4 for cermet 80Ti(C,N)–20FeNi). As it may be seen, P/S^2

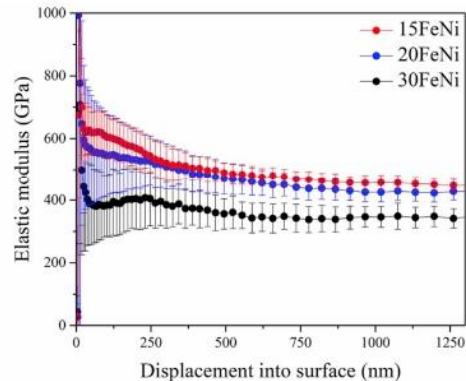
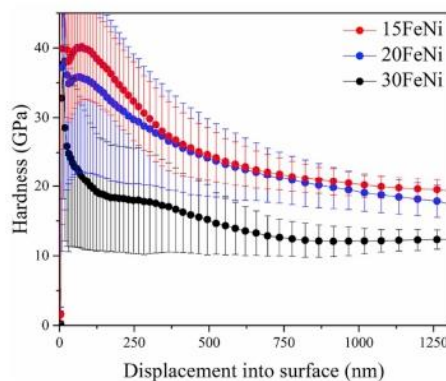


Fig. 3. (a) H and (b) E evolution as a function of the maximum displacement into the surface for all the investigated samples.

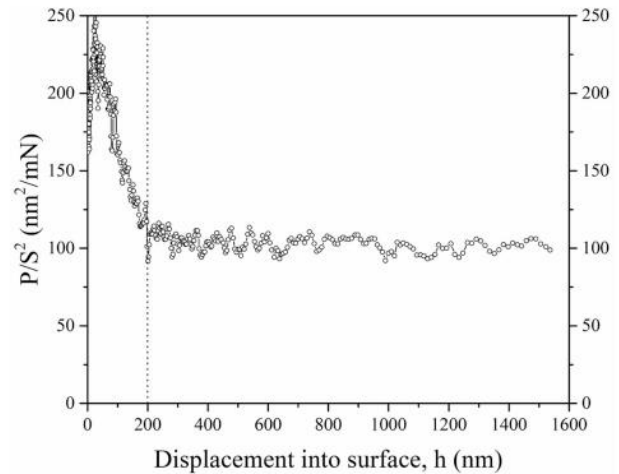


Fig. 4. P/S^2 ratio versus displacement into surface for indentations performed at maximum applied load for sample 80Ti(C,N)–20FeNi.

becomes independent of indenter penetration after 200 nm of displacement into surface. Therefore, values for H and E assessed for $h \geq 200$ nm may be considered as intrinsic ones for the three cermets studied (see Refs. [23,42]). Small-scale mechanical properties evolution shown in Fig. 3 and data for H and E summarized in Table 4 highlights an expected inverse correlation between mean free path of the metallic binder (directly related to ceramic/metal phase ratio) and both parameters. This is in accordance with trends observed for microstructural effects on macro hardness (i.e. evaluated at much higher applied load levels, i.e. 10 and 30 Kgf) for the cermets here studied (Table 4, which are in agreement with the Vickers hardness values reported in Ref. [34]). Relative differences in hardness values listed in Table 4 may be accounted recalling the mechanistic models proposed by Nix & Gao [43], on the basis of geometrically necessary dislocation concepts, for rationalizing hardness-penetration depth correlation according to:

$$\frac{H}{H_0} = \sqrt{1 + \frac{h^*}{h}} \quad (3)$$

where H is the hardness for a given depth of indentation (h), H_0 is the hardness in the limit of the infinite depth and h^* is a characteristic length that depends on the shear modulus, H_0 and the shape of the indenter [43]. In this regard, implementation of Nix & Gao model was found to fit satisfactorily the experimental data for hardness values of studied systems, measured under different levels of applied load.

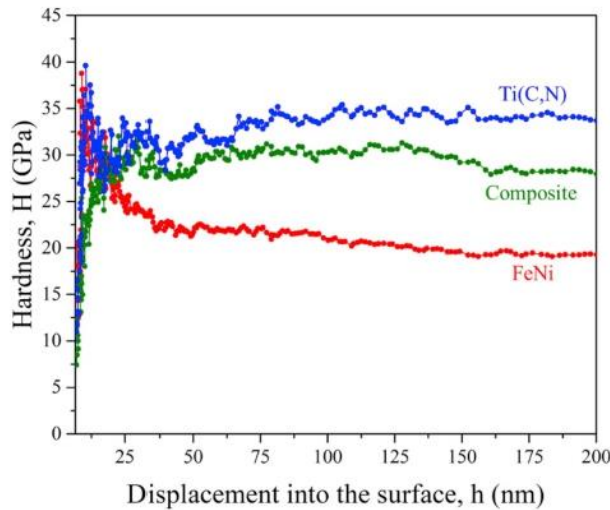
3.2.2. Intrinsic hardness

Prior to perform massive indentation testing, it is necessary to do a discrete evaluation of the intrinsic H for each phase. In this regard;

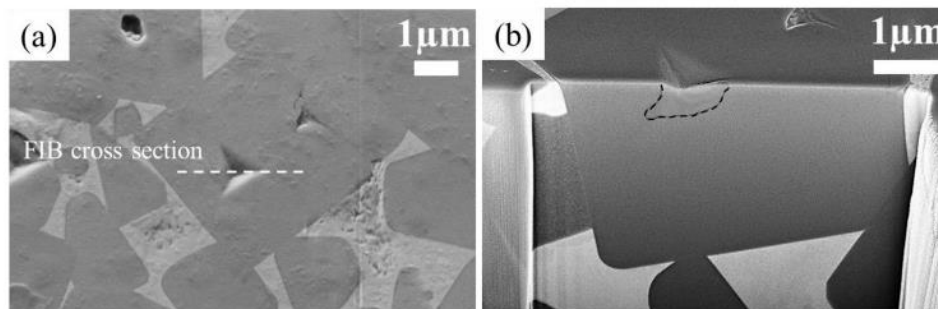
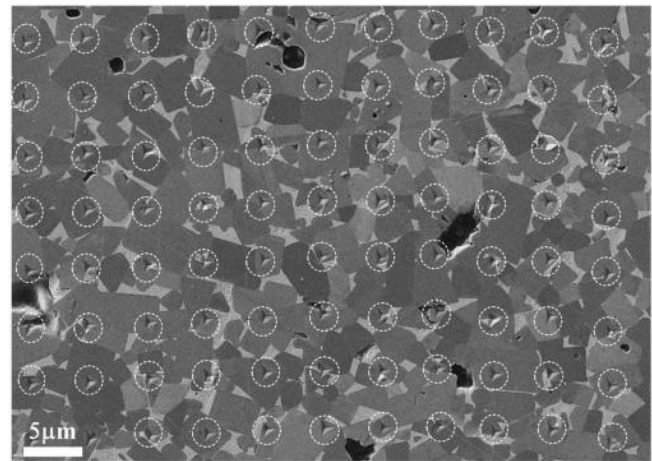
Table 4

Mechanical properties data for the three different Ti(C,N)–FeNi composites studied in different length scale.

Sample	Nanoindentation data, performed by Berkovich indenter at 650 mN		HV10 (GPa)	HV30 (GPa)
	Elastic modulus, E (GPa)	Hardness, H (GPa)		
85Ti(C,N)–15FeNi	455 ± 20	20.2 ± 2.0	13.0 ± 0.4	12.8 ± 0.1
80Ti(C,N)–20FeNi	420 ± 18	18.5 ± 2.0	11.3 ± 0.3	11.0 ± 0.1
70Ti(C,N)–30FeNi	346 ± 22	12.3 ± 1.5	9.5 ± 0.4	9.1 ± 0.2

**Fig. 5.** Hardness evolution as a function of the maximum displacement into the surface for each constitutive phase for the 80Ti(C,N)–20FeNi specimen.

typical curves of hardness evolution as a function of maximum displacement into the surface are presented in Fig. 5 for the 80Ti(C,N)–20FeNi composite system. They correspond to indentations whose residual imprints were either completely confined in a constitutive phase or probing both phases (including interfaces) simultaneously. There, H values for both individual phases and the composite itself are not only distinguishable, but also discerned to follow trends towards plateau levels as penetration depth gets deeper than 100 nm. This supports above finding that mechanical response is not affected by any ISE for $h \geq 200$ nm (see Fig. 4 [25,27]). Furthermore, additional inspection was done to assess imprint scenario at the subsurface level. Fig. 6a and Fig. 6b shows surface and FIB-milled cross-section views of a residual imprint in a Ti(C,N) particle respectively. It is evidenced that it is absolutely embedded within the ceramic phase. This will also apply for plastic field dimensions, estimated to range between 1.4 and 2.0 μm (i.e. between 7 and 10 times maximum displacement into the surface); thus, slightly smaller than the mean grain size determined experimentally by using the LIM (see Table 3) for the Ti(C,N) particles. These facts then point out the data gathered from 200 nm in-depth indentations as

**Fig. 6.** (a) FESEM micrographs of a residual imprint performed at 200 nm of maximum displacement into surface performed inside the ceramic phase of sample 80Ti(C,N)–20FeNi; and (b) FIB-milled cross section of the same imprint, where plastic flow induced during the indentation process is marked with a black dash line.**Fig. 7.** FESEM micrograph image of small part of indentation array performed at 200 nm of maximum displacement into surface for sample 80Ti(C,N)–20FeNi.

valid for implementing the statistical method to be used for extracting intrinsic hardness values of individual phases for cermets here investigated.

3.2.3. Massive nanoindentation testing and statistical analysis

Fig. 7 shows a small-cropped region of the indentation arrays of 2000 imprints performed at 200 nm of maximum penetration depth, as observed by FESEM. The related hardness histogram, with a constant bin size of 1 GPa, for sample 85Ti(C,N)–15FeNi is presented in Fig. 8. Three discrete peaks with mean values of 19, 27 and 34 were determined. The highest and lowest peaks are attributed to the intrinsic hardness of ceramic and metallic phases respectively. Meanwhile, the middle peak should be linked to the composite hardness (i.e. imprints probing effective two-phase regions). Qualitatively similar histograms have been obtained for the other two cermets. Mean as well as standard deviation values for small-scale hardness for the three defined mechanically phases, determined by implementing the statistical method proposed by Ulm and co-workers [25,38–41], are listed in Table 5.

Two interesting observations may be done regarding the data

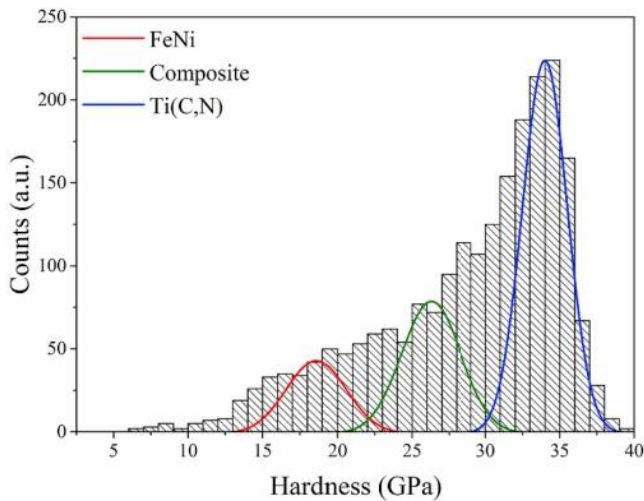


Fig. 8. Histogram of hardness values with constant bin size of 1 GPa, extracted from 2000 indentations for sample 85Ti(C,N)–15FeNi.

Table 5

Intrinsic hardness values (GPa) for each constitutive phase of Ti(C,N)–FeNi composite systems.

Sample	FeNi	Composite	Ti(C,N)
85Ti(C,N)–15FeNi	19.0 ± 0.5	26.3 ± 0.1	34.0 ± 1.0
80Ti(C,N)–20FeNi	15.5 ± 0.3	25.7 ± 0.2	34.0 ± 0.3
70Ti(C,N)–30FeNi	9.0 ± 0.1	22.3 ± 0.3	34.0 ± 0.3

presented in Table 5. First, and as expected, mean value of hardness for Ti(C,N) particles is determined to be about 34 GPa for the three materials, pointing out it is independent of microstructure and volume fraction of the ceramic phase. Second, opposite to this finding, values of local hardness for both composite-like and metallic phases are found to increase as the ceramic/metal phase ration rises. Here, differences are relatively minor for the former, and possibly linked to the variable amount of ceramic particles. However, small-scale hardness values are significantly distinct for the metallic binder, indicating the relevance of the constrained deformation imposed for the harder phase to the softer and more ductile one, as it will be discussed now.

Details of binder peaks and data gathered in the lower-side range of the histograms are given in Fig. 9. It is evidenced that small-scale hardness of the metallic phase rises about twice (from 9 to 19 GPa) as its mean free path reduces about half (from 1 to 0.5 μm). This is similar to the trend reported by Roa et al. [27] on WC-Co grades, and must be associated with the constraining effect of the ceramic phase over the metallic ones. However, before further discussing microstructure-mechanical property correlations, special care should be taken on the reliability of the absolute values listed in Table 5. As it may be seen in Fig. 10a and Fig. 10b, for samples with 15 and 20 vol% of FeNi, most of

the imprints probing the metallic phase could not be completely confined in the corresponding binder mean free path. This was not the usual case for samples with 30 vol% of metallic binder (Fig. 10c). Consequently, the plastic flow associated with binder-related nanoindentations could be expected to interact with the surrounding ceramic particles. Under these conditions, assessed hardness values for the binder may be overestimated. As proposed and validated by Roa et al. [25], a more realistic value of intrinsic hardness for the constrained FeNi binder may be deconvoluted from the experimental values by implementing established thin film models. The use of thin films model is expected to yield reasonable values of hardness as the lateral stiffness is considered low in comparison to the normal stiffness, due to the large opening angle of the Berkovick tip. In this work Korsunsky et al.'s method [44] was implemented, resulting in hardness reductions of about 22% for 85Ti(C,N)–15FeNi and 80Ti(C,N)–20FeNi samples, and 12% for 70Ti(C,N)–30FeNi ones (Table 6).

The binder mean free path is a normalizing microstructural parameter in two-phase alloys. From a mechanical viewpoint, considering systems containing different phases (i.e. one hard and another soft) bound by a strong interface, it usually translates into constrained deformation of the soft phase due to the surrounding hard one. As a result, effective flow stress of the ductile phase is significantly enhanced. An estimation of this parameter for the FeNi binder may be done through simple conversion of previously estimated intrinsic hardness data, i.e. using Tabor's equation. In doing so, both a constraint factor ranging between 3 and 4 (as reported for cemented carbides [45]), as well as a correction one of 0.9, related to the Berkovick indenter geometry instead of Vickers tip for measurement of mechanical properties [46], are considered. Resulting flow stress values for the three composites studied are also listed in Table 6. In general, they are within the range of values (from 1.8 to 4.5 GPa) reported for WC-Co cemented carbides [25,27,28,32,47,48], highlighting the potential of FeNi binder as effective reinforcement for Ti(C,N)-base cermets.

3.3. Deformation, damage and fracture mechanisms

Cermets demonstrate brittle fracture behaviour at macroscale, while both brittle features in the ceramic phase and ductile ones in the metallic binder phase can be distinguished at the microscale [49]. Fig. 11a displays a FESEM micrograph of an imprint left after indentation down to high penetration depth in a 85Ti(C,N)–15FeNi specimen. Under these conditions, deformation/damage scenario is clearly involving the whole composite system. As it is shown in Fig. 11b, damage within the residual imprint is mainly localized in Ti(C,N) ceramic particles (labelled with white arrows in Fig. 11b). On the other hand, plastic deformation is evidenced within the binder, particularly in regions close to Ti(C,N)–FeNi interfaces. A more detailed inspection of fracture phenomena induced under the residual imprint during the indentation process was performed by cross-sectional analysis, by using FESEM/FIB, through the white dash line presented in Fig. 11c. A general view of the trench of the region of interest under the residual imprint is

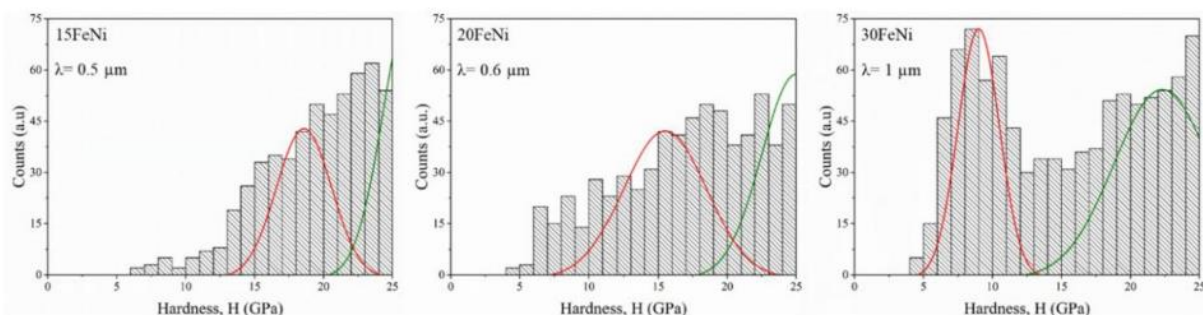


Fig. 9. Histogram of hardness values for the metallic binder for all studied samples.

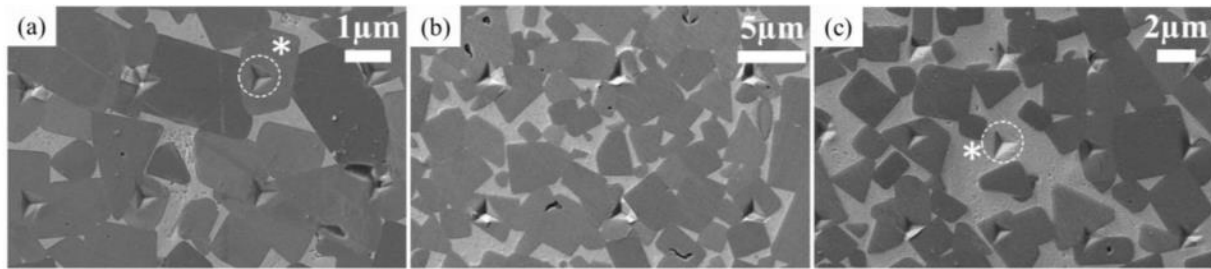


Fig. 10. FESEM images of performed imprints on samples with different vol% of metallic binder. (a) Sample 85Ti(C,N)–15FeNi, (b) sample 80Ti(C,N)–20FeNi, and (c) sample 70Ti(C,N)–30FeNi. The imprints, labelled by (*) in Fig. 10a/c, have been performed and confined in a Ti(C,N) particle and the metallic binder respectively. The white dash circle for Fig. 10a/c represents the plastic field created during the indentation process.

Table 6

Corrected hardness values and flow stress (estimated by using Tabor's equation) of the metallic binder within Ti(C,N)–FeNi composites.

Sample	Binder Hardness (GPa)	Flow stress (GPa)
85Ti(C,N)–15FeNi	14.8 ± 0.4	3.4–4.5
80Ti(C,N)–20FeNi	12.1 ± 0.2	2.7–3.6
70Ti(C,N)–30FeNi	7.9 ± 0.1	1.8–2.4

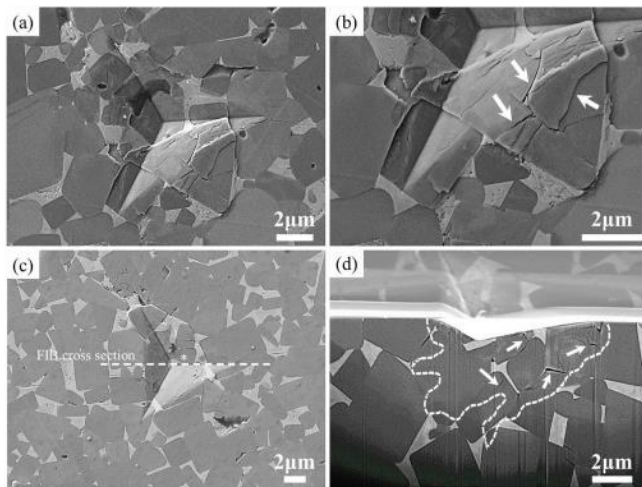


Figure 11. (a) and (c): FESEM images of residual indentation imprints performed on the 80Ti(C,N)–20FeNi specimen. (b): Higher magnification image of residual imprint shown in (a), highlighting some fracture mechanisms activated during the indentation process (mainly within ceramic particles). (d): FIB-milled cross-section of residual imprint shown in (c), under the region of interest indicated by the white dash line.

shown in Fig. 11d, which exhibits a highly deformed zone (underlined with a white dash line). Cracking induced is mainly located at ceramic/ceramic interfaces (indicated by white arrows).

As it can be appreciated in Fig. 12a and Fig. 12b, corresponding to imprints performed at a shallow penetration depth, same fracture mechanisms may be discerned inside the ceramic particles. Very interesting, cracks are found to propagate through the hard phase, but they often get arrested at the interface between Ti(C,N) particles and the metallic binder. This could be described as clear indication of the toughening role played by the ductile metallic binder, in terms of increasing crack-growth resistance in these ceramic-metal composites.

Evidence of similar toughening mechanisms as those reported for WC-Co grades is key for effective consideration of any alternative ceramic-metal systems as candidates to substitute hardmetals. In this regard, crack-microstructure interaction must be examined aiming to assess whether ductile reinforcement indeed takes place. Fig. 13a shows typical cracking phenomena resulting at corners of residual imprints after Vickers indentation (in this case under applied load of 30 Kgf) on the hardest grade here studied. It can be seen that interaction of cracks induced by sharp indentation with microstructure is complex, combining transgranular, intergranular and through binder paths. Regarding the latter, the effectiveness of the metallic binder as a toughening agent is clearly discerned in terms of: smaller crack opening (red dashed circles in Fig. 13b) and crack arrest in metallic binder pools, the latter sometimes inducing crack bifurcation (yellow dashed circles in Fig. 13b). Above statement is further supported by fractographic inspection of broken surfaces of previously indented specimens. As it is shown in Fig. 14, as cracks go through the metallic phase and rupture takes place, well-developed ductile dimple features are left behind. This is by itself a clear proof of ligament reinforcement being operative, by reducing the driving force for crack propagation, towards effective toughening of the composite. Nevertheless, the area fraction of the metallic phase on fracture surfaces seems to be lower than expected, considering as a reference the metal/ceramic phase content defined during processing and later quantified by microstructural

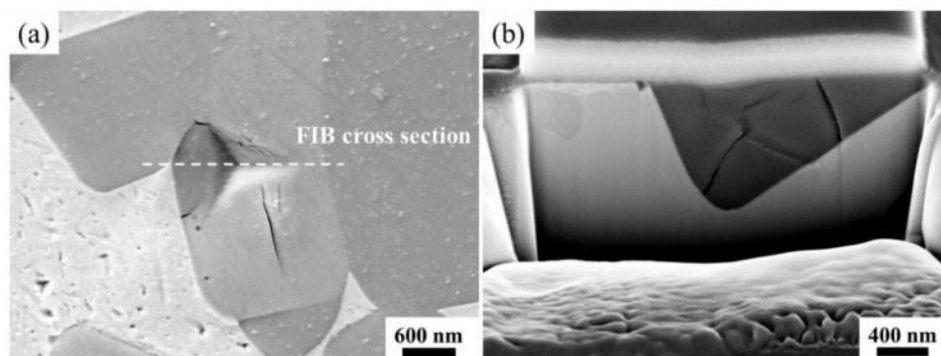


Fig. 12. (a) General view of a residual imprint performed at 200 nm of maximum displacement into surface; and (b) FIB-milled cross-section view, under the region of interest indicated by the white dash line in (a), for the 70Ti(C,N)–30FeNi specimen.

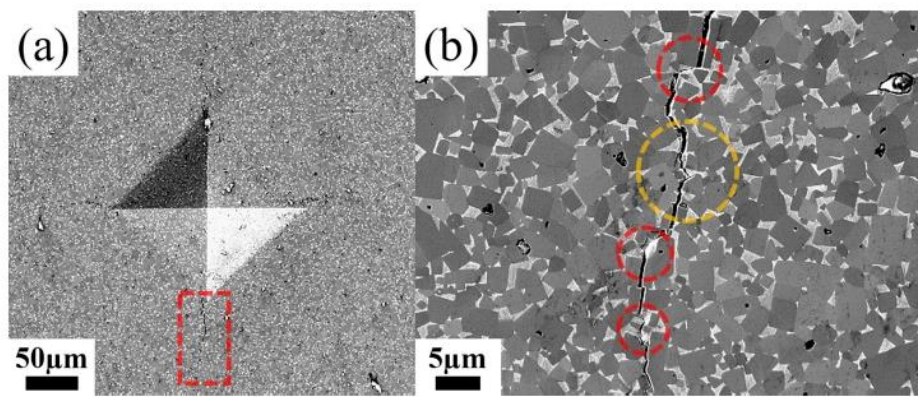


Fig. 13. Cracking induced by sharp indentation in sample 85Ti(C,N)–15FeNi: a) imprint corresponding to Vickers indentation under 30kgf of applied load; and b) crack-microstructure interaction (enlarged view of red dashed area in (a)), highlighting toughening action linked to metallic phase in this composite system. (For interpretation of the references to colour in this figure legend, the reader is referred to the Web version of this article.)

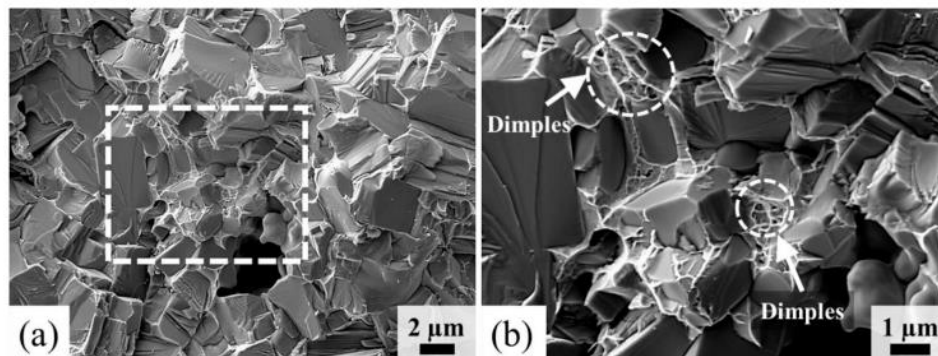


Fig. 14. FESEM images from the fractured surface of sample 80Ti(C,N)–20FeNi. (a) ductile fracture within metallic binder, as evidenced by dimples clearly discerned in enlarged image (b).

characterization. This would point out the need for microstructural design optimization in the studied systems, if the interaction between propagating cracks and the interdispersed metallic network acting as reinforcement phase wants to be enhanced.

4. Conclusions

The mechanical properties at microstructural length scale of Ti(C,N)–FeNi ceramic-metal composites have been assessed. Based on the obtained data, the following conclusions may be drawn:

1. Combination of massive nanoindentation and statistical analysis of the gathered data has proven to be a successful testing protocol for determining small-scale hardness and stiffness of Ti(C,N)–FeNi ceramic-metal composites. Nevertheless, successful implementation requires careful consideration of testing parameters used, on the basis of microstructural, residual imprint and plastic flow length scales.
2. The implemented testing protocol has allowed to document an inverse relationship between the mechanical parameters evaluated and the volume fraction of the metallic phase. For the particular case of the small-scale hardness of the metallic binder, such correlation has been analysed and rationalized in terms of strengthening of ductile ligaments due to constrained deformation by the surrounding ceramic particles.
3. The effective flow stress for the constrained metallic binder have been estimated from small-scale hardness values experimentally determined. It has yielded values ranging from 1.8 to 4.5 GPa, i.e. similar to those usually reported for cobalt ligaments in WC-Co systems. This points out the effectiveness of FeNi as reinforcement phase for Ti(C,N)-base cermets, towards optimization of hardness-toughness relationships for these ceramic-metal systems.
4. Toughening action of FeNi phase in the Ti(C,N)-base cermets

studied has been validated by detailed characterization of deformation, damage and fracture mechanisms. In particular, enhanced crack growth resistance has been discerned in terms of smaller opening, arrest and bifurcation of propagating cracks as they intersect metallic regions.

Acknowledgment

The current study was supported by the Spanish Ministerio de Economía y Competitividad through Grant MAT2015-70780-C4-P (MINECO/FEDER). J.J.Roa acknowledges the Serra Hunter programme of the Generalitat de Catalunya.

References

- [1] H.E. Exner, Physical and chemical nature of cemented carbides, *Int. Met. Rev.* 24 (1979) 149–173, <https://doi.org/10.1179/imtr.1979.24.1.149>.
- [2] G.S. Upadhyaya, *Cemented Tungsten Carbides: Production, Properties and Testing*, William Andrew, 1998.
- [3] J. Gurland, New scientific approaches to development of tool materials, *Int. Mater. Rev.* 33 (1988) 151–166, <https://doi.org/10.1179/imr.1988.33.1.151>.
- [4] E. Jiménez-Piqué, M. Turon-Vinas, H. Chen, T. Trifonov, J. Fair, E. Tarrés, L. Llanes, Focused ion beam tomography of WC-Co cemented carbides, *Int. J. Refract. Metals Hard Mater.* 67 (2017) 9–17 <https://doi.org/10.1016/j.ijrmhm.2017.04.007>.
- [5] J. García, V.C. Ciprés, A. Blomqvist, B. Kaplan, Cemented carbide microstructures: a review, *Int. J. Refract. Metals Hard Mater.* 80 (2019) 40–68 <https://doi.org/10.1016/j.ijrmhm.2018.12.004>.
- [6] L. Prakash, Fundamentals and general applications of hardmetals, in: V.K. Sarin, D. Mari, L. Llanes (Eds.), *Compr. Hard Mater.* Elsevier Ltd, Oxford, UK, 2014, pp. 29–90 <https://doi.org/10.1016/B978-0-08-096527-7.00002-7>.
- [7] B. Gries, L.J. Prakash, Hard materials 1: acute inhalation toxicity by contact corrosion-the case of WC-Co, *Eur. Congr. Exhib. Powder Metall. Eur. PM Conf. Proc. The European Powder Metallurgy Association*, 2007, p. 189.
- [8] National Toxicology Program, Department of health and human service (n.d.), <http://ntp.niehs.nih.gov/?objectid=03C9AF75-E1BF-FF40-DBA9EC0928DF8B15> (USA).
- [9] M. Grilli, T. Bellezze, E. Gamsjäger, A. Rinaldi, P. Novak, S. Balos, R. Piticescu, M. Ruello, Solutions for critical raw materials under extreme conditions: a review, *Materials* 10 (2017) 285 <https://doi.org/10.3390/ma10030285>.

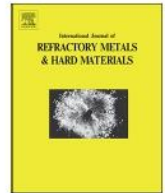
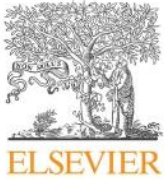
- [10] P. Ettmayer, H. Kolaska, W. Lengauer, K. Dreyer, Ti(C,N) cermets - metallurgy and properties, *Int. J. Refract. Metals Hard Mater* 13 (1995) 343–351 [https://doi.org/10.1016/0263-4368\(95\)00027-G](https://doi.org/10.1016/0263-4368(95)00027-G).
- [11] A. Bellosi, R. Calzavari, M.G. Faga, F. Monteverde, C. Zancolò, G.E. D'Errico, Characterisation and application of titanium carbonitride-based cutting tools, *J. Mater. Process. Technol.* 143–144 (2003) 527–532 [https://doi.org/10.1016/S0924-0136\(03\)00339-X](https://doi.org/10.1016/S0924-0136(03)00339-X).
- [12] Y. Peng, H. Miao, Z. Peng, Development of TiCN-based cermets: mechanical properties and wear mechanism, *Int. J. Refract. Metals Hard Mater.* 39 (2013) 78–89 <https://doi.org/10.1016/j.jrmhm.2012.07.001>.
- [13] Q. Xu, J. Zhao, X. Ai, Fabrication and cutting performance of Ti (C, N)-based cermet tools used for machining of high-strength steels, *Ceram. Int.* 43 (2017) 6286–6294 <https://doi.org/10.1016/j.ceramint.2017.02.034>.
- [14] B. Wittmann, W.-D. Schubert, B. Lux, WC grain growth and grain growth inhibition in nickel and iron binder hardmetals, *Int. J. Refract. Metals Hard Mater.* 20 (2002) 51–60 [https://doi.org/10.1016/S0263-4368\(01\)00070-1](https://doi.org/10.1016/S0263-4368(01)00070-1).
- [15] E. Gordo, B. Gómez, E.M. Ruiz-Navas, J.M. Torralba, Influence of milling parameters on the manufacturing of Fe–TiCN composite powders, *J. Mater. Process. Technol.* 162–163 (2005) 59–64 <https://doi.org/10.1016/j.jmatprotec.2005.02.154>.
- [16] B. Gries, L. Prakash, WC hardmetals with Iron based binders, in: P. Rödhammer, L. Sigl, H. Wildner (Eds.), *Proceedings of 17th Plansee Seminar, Reutte, Austria, 2009 HM 5/1-HM 5/13*.
- [17] P. Alvaredo, M. Dios, B. Ferrari, E. Gordo, Understanding of wetting and solubility behavior of Fe binder on Ti (C, N) cermets, *J. Alloy. Comp.* 770 (2019) 17–25 <https://doi.org/10.1016/j.jallcom.2018.07.243>.
- [18] A. V. Shatov, S.S. Ponomarev, S.A. Firstov, Hardness and deformation of hardmetals at room temperature, in: V.K. Sarin, D. Mari, L. Llanes (Eds.), *Compr. Hard Mater*, Elsevier Ltd, Oxford, UK, 2014, pp. 267–299 <https://doi.org/10.1016/B978-0-08-096527-7.00009-X>.
- [19] A. V. Shatov, S.S. Ponomarev, S.A. Firstov, Fracture and strength of hardmetals at room temperature, in: V.K. Sarin, D. Mari, L. Llanes (Eds.), *Compr. Hard Mater*, Elsevier Ltd, Oxford, UK, 2014, pp. 301–343 <https://doi.org/10.1016/B978-0-08-096527-7.00010-6>.
- [20] W. Lengauer, F. Scagnetto, Ti (C, N)-Based Cermets: critical review of achievements and recent developments, *Solid State Phenom*, Trans Tech Publ, 2018, pp. 53–100 <https://doi.org/10.4028/www.scientific.net/SSP.274.53>.
- [21] J.-H. Kim, Y. Kim, Influence of Mo contents on microstructures and mechanical properties of (Ti, W, Mo)(CN)–Ni cermets, *Ceram. Int.* 45 (2019) 5361–5366 <https://doi.org/10.1016/j.ceramint.2018.11.236>.
- [22] C. Chen, Z. Guo, S. Li, Y. Xiao, B. Chai, J. Liu, Microstructure and properties of WC-17Co cermets prepared using different processing routes, *Ceram. Int.* 45 (2019) 9203–9210 <https://doi.org/10.1016/j.ceramint.2019.01.265>.
- [23] A. Duszová, R. Halgaš, M. Bfanda, P. Hvizdoš, F. Lofaj, J. Dusza, J. Morgiel, Nanoindentation of WC–Co hardmetals, *J. Eur. Ceram. Soc.* 33 (2013) 2227–2232 <https://doi.org/10.1016/j.jeurceramsoc.2012.12.018>.
- [24] M. Trueba, A. Aramburu, N. Rodríguez, I. Iparraguirre, M.R. Elizalde, I. Ocaña, J.M. Sánchez, J.M. Martínez-Esnaola, “In-situ” mechanical characterisation of WC–Co hardmetals using microbeam testing, *Int. J. Refract. Metals Hard Mater.* 43 (2014) 236–240 <https://doi.org/10.1016/j.jrmhm.2013.12.005>.
- [25] J.J. Roa, E. Jiménez-Piqué, C. Verge, J.M. Tarragó, A. Mateo, J. Fair, L. Llanes, Intrinsic hardness of constitutive phases in WC–Co composites: nanoindentation testing, statistical analysis, WC crystal orientation effects and flow stress for the constrained metallic binder, *J. Eur. Ceram. Soc.* 35 (2015) 3419–3425 <https://doi.org/10.1016/j.jeurceramsoc.2015.04.021>.
- [26] T. Csanádi, M. Bl'anda, N.Q. Chinh, P. Hvizdoš, J. Dusza, Orientation-dependent hardness and nanoindentation-induced deformation mechanisms of WC crystals, *Acta Mater.* 83 (2015) 397–407 <https://doi.org/10.1016/j.actamat.2014.09.048>.
- [27] J.J. Roa, E. Jiménez-Piqué, J.M. Tarragó, D.A. Sandoval, A. Mateo, J. Fair, L. Llanes, Hall-Petch strengthening of the constrained metallic binder in WC–Co cemented carbides: experimental assessment by means of massive nanoindentation and statistical analysis, *Mater. Sci. Eng. A* 676 (2016) 487–491 <https://doi.org/10.1016/j.msea.2016.09.020>.
- [28] J.M. Tarragó, J.J. Roa, E. Jiménez-Piqué, E. Keown, J. Fair, L. Llanes, Mechanical deformation of WC–Co composite micropillars under uniaxial compression, *Int. J. Refract. Metals Hard Mater.* 54 (2016) 70–74 <https://doi.org/10.1016/j.jrmhm.2015.07.015>.
- [29] M.R. Elizalde, I. Ocaña, J. Alkorta, J.M. Sánchez-Moreno, Mechanical strength assessment of single WC–WC interfaces present in WC–Co hardmetals through microbeam bending experiments, *Int. J. Refract. Metals Hard Mater.* 72 (2018) 39–44 <https://doi.org/10.1016/j.jrmhm.2017.12.009>.
- [30] D.A. Sandoval, A. Rinaldi, J.M. Tarragó, J.J. Roa, J. Fair, L. Llanes, Scale effect in mechanical characterization of WC–Co composites, *Int. J. Refract. Metals Hard Mater.* 72 (2018) 157–162 <https://doi.org/10.1016/j.jrmhm.2017.12.029>.
- [31] J.J. Roa, P.S. Phani, W.C. Oliver, L. Llanes, Mapping of mechanical properties at microstructural length scale in WC–Co cemented carbides: assessment of hardness and elastic modulus by means of high speed massive nanoindentation and statistical analysis, *Int. J. Refract. Metals Hard Mater.* 75 (2018) 211–217 <https://doi.org/10.1016/j.jrmhm.2018.04.019>.
- [32] D.A. Sandoval, J.J. Roa, O. Ther, E. Tarrés, L. Llanes, Micromechanical properties of WC–(W, Ti, Ta, Nb) C–Co composites, *J. Alloy. Comp.* 777 (2019) 593–601 <https://doi.org/10.1016/j.jallcom.2018.11.001>.
- [33] J.A. Escribano, J.L. García, P. Alvaredo, B. Ferrari, E. Gordo, A.J. Sanchez-Herencia, FGM stainless steel–Ti (C, N) cermets through colloidal processing, *Int. J. Refract. Metals Hard Mater.* 49 (2015) 143–152 <https://doi.org/10.1016/j.jrmhm.2014.05.008>.
- [34] M. Dios, Z. Gonzalez, P. Alvaredo, R. Bermejo, E. Gordo, B. Ferrari, Novel colloidal approach for the microstructural improvement in Ti (C, N)/FeNi cermets, *J. Alloy. Comp.* 724 (2017) 327–338 <https://doi.org/10.1016/j.jallcom.2017.07.034>.
- [35] *Metallographic Determination of Microstructure. Part 2: Measurement of WC Grain Size, Hardmetals*, Geneva, 2008 ISO 4499-2 2008.
- [36] W.C. Oliver, G.M. Pharr, An improved technique for determining hardness and elastic modulus using load and displacement sensing indentation experiments, *J. Mater. Res.* 7 (1992) 1564–1583, <https://doi.org/10.1557/JMR.1992.1564>.
- [37] W.C. Oliver, G.M. Pharr, Measurement of hardness and elastic modulus by instrumented indentation: advances in understanding and refinements to methodology, *J. Mater. Res.* 19 (2004) 3–20 <https://doi.org/10.1557/jmr.2004.19.1.3>.
- [38] G. Constantinides, F.-J. Ulm, K. Van Vliet, On the use of nanoindentation for cementitious materials, *Mater. Struct.* 36 (2003) 191–196, <https://doi.org/10.1007/bf02479557>.
- [39] G. Constantinides, K.S. Ravi Chandran, F.J. Ulm, K.J. Van Vliet, Grid indentation analysis of composite microstructure and mechanics: principles and validation, *Mater. Sci. Eng. A* 430 (2006) 189–202 <https://doi.org/10.1016/j.msea.2006.05.125>.
- [40] G. Constantinides, F.-J. Ulm, The nanogranular nature of C–S–H, *J. Mech. Phys. Solids* 55 (2007) 64–90 <https://doi.org/10.1016/j.jmps.2006.06.003>.
- [41] F.-J. Ulm, M. Vandamme, C. Bobko, J. Alberto Ortega, K. Tai, C. Ortiz, Statistical indentation techniques for hydrated nanocomposites: concrete, bone, and shale, *J. Am. Ceram. Soc.* 90 (2007) 2677–2692, <https://doi.org/10.1111/j.1551-2916.2007.02012.x>.
- [42] B. Roebuck, P. Klose, K.P. Mingard, Hardness of hexagonal tungsten carbide crystals as a function of orientation, *Acta Mater.* 60 (2012) 6131–6143 <https://doi.org/10.1016/j.actamat.2012.07.056>.
- [43] W.D. Nix, H. Gao, Indentation size effects in crystalline materials: a law for strain gradient plasticity, *J. Mech. Phys. Solids* 46 (1998) 411–425 [https://doi.org/10.1016/S0022-5096\(97\)00086-0](https://doi.org/10.1016/S0022-5096(97)00086-0).
- [44] A.M. Korsunsky, M.R. McGurk, S.J. Bull, T.F. Page, On the hardness of coated systems, *Surf. Coating Technol.* 99 (1998) 171–183 [https://doi.org/10.1016/S0257-8972\(97\)00522-7](https://doi.org/10.1016/S0257-8972(97)00522-7).
- [45] H. Doi, Y. Fujiwara, K. Miyake, Mechanism of plastic deformation and dislocation damping of cemented carbides, *Trans. Met. Soc. AIME* 245 (1969) 1457–1470.
- [46] O. Casals, J. Alcalá, The duality in mechanical property extractions from Vickers and Berkovich instrumented indentation experiments, *Acta Mater.* 53 (2005) 3545–3561 <https://doi.org/10.1016/j.actamat.2005.03.051>.
- [47] L.S. Sigl, H.F. Fischmeister, On the fracture toughness of cemented carbides, *Acta Metall.* 36 (1988) 887–897 [https://doi.org/10.1016/0001-6160\(88\)90143-5](https://doi.org/10.1016/0001-6160(88)90143-5).
- [48] H.F. Fischmeister, S. Schmauder, L.S. Sigl, Finite element modelling of crack propagation in WC–Co hard metals, *Mater. Sci. Eng. A* 105 (1988) 305–311 [https://doi.org/10.1016/0025-5416\(88\)90711-2](https://doi.org/10.1016/0025-5416(88)90711-2).
- [49] M. Dios, I. Kraveva, Z. González, P. Alvaredo, B. Ferrari, E. Gordo, R. Bermejo, Mechanical characterization of Ti (C, N)-based cermets fabricated through different colloidal processing routes, *J. Alloy. Comp.* 732 (2018) 806–817 <https://doi.org/10.1016/j.jallcom.2017.07.034>.

Article IV:**Carbon addition effects on microstructure and small-scale hardness for Ti(C,N)-FeNi cermets**

H. Besharatloo, M. de Nicolás, J.M. Wheeler, A. Mateo, B. Ferrari, E. Gordo, L. Llanes and J.J. Roa. International Journal of Refractory Metals and Hard Materials 85 (2019) 105064. <https://doi.org/10.1016/j.ijrmhm.2019.105064>.

Summary

This study investigated the influence of carbon addition on the microstructural and micromechanical properties of Ti(C,N)-FeNi cermets with different ceramic/metal phase ratios. Evaluation of small-scale hardness was conducted by using high-speed nanoindentation in conjunction with statistical analysis. It allows to gather extremely large data sets (40,000 imprints per grade and condition); and thus, detailed hardness mapping at the microstructure length scale. Subsequent statistical analysis was done by considering three mechanically distinct phases: Ti(C,N) particles, the metallic binder, and one exhibiting the composite behavior (i.e. imprints probing two-phase regions). In general, it is found that porosity amount is reduced as ceramic/metal phase ratio decreases and carbon is added. Carbon addition is also observed to rise small-scale hardness, but only for two of the defined phases: metallic binder and the composite one. Similar trends were observed regarding the influence of ceramic/metal phase ratio and carbon addition on the inverse hardness-fracture toughness correlation measured under high applied loads.



Carbon addition effects on microstructure and small-scale hardness for Ti(C,N)-FeNi cermets

H. Besharatloo^{a,b,*}, M. de Nicolás^c, J.M. Wheeler^d, A. Mateo^{a,b}, B. Ferrari^e, E. Gordo^c, L. Llanes^{a,b}, J.J. Roa^{a,b}

^a CIEFMA – Department of Materials Science and Metallurgical Engineering, EEBE, Universitat Politècnica de Catalunya-BarcelonaTech, 08019 Barcelona, Spain

^b Barcelona Research Centre in Multiscale Science and Engineering, Universitat Politècnica de Catalunya-BarcelonaTech, 08019 Barcelona, Spain

^c GTP – Department of Materials Science and Engineering, Universidad Carlos III Madrid, Avda. De la Universidad, 30, 28911 Leganes, Spain

^d Laboratory for Mechanics of Materials and Nanostructures, Department of Materials, ETH Zürich, Vladimir-Prelog-Weg 5, 8093 Zürich, Switzerland

^e Institute of Ceramic and Glass, CSIC, 28049 Madrid, Spain

ARTICLE INFO

Keywords:

Cermet
High speed indentation
Hardness
Mechanical mapping
Massive indentation
Statistical analysis

ABSTRACT

The current study investigates the influence of carbon addition on the microstructural and micromechanical properties of Ti(C,N)-FeNi cermets with different ceramic/metal phase ratios. Evaluation of small-scale hardness is conducted by using high speed nanoindentation in conjunction with statistical analysis. It allows to gather extremely large data sets (40,000 imprints per grade and condition); and thus, detailed hardness mapping at the microstructure length scale. Subsequent statistical analysis was done by considering three mechanically distinct phases: Ti(C,N) particles, the metallic binder, and one exhibiting the composite behaviour (i.e. imprints probing two-phase regions). In general, it is found that porosity amount is reduced as ceramic/metal phase ratio decreases and carbon is added. Carbon addition is also observed to rise small-scale hardness, but only for two of the defined phases: metallic binder and the composite one. Similar trends are observed regarding the influence of ceramic/metal phase ratio and carbon addition on the inverse hardness-fracture toughness correlation measured under high applied loads.

1. Introduction

Substitution of traditional WC-Co hardmetals have become a tough challenge for academic and industrial sectors. Main reasons behind it are related to health (toxicity), economic (fluctuating price) and strategic (critical raw materials) considerations [1–3]. In this regard, Ti (C,N)-based cermets have emerged as a competitive alternative system due to their exceptional combination of physical and mechanical properties [4,5]. Regarding the metallic binder, iron (Fe) alloys have been considered as natural substitutes for Co, because their lower price and non-toxicity. Furthermore, Fe is an abundant raw material and has the ability to be hardened by heat treatments [1,6,7]. On the other hand, for an Fe binder phase, nickel (Ni) becomes an optimal alloying element, as previous studies have demonstrated that it improves the wettability between Fe and Ti(C,N). This is essential for achieving full densification of the cermets during the sintering stage [8]. Accordingly, Ti(C,N)-FeNi system have been proposed as a promising competitive alternative for WC-Co for applications where hard materials are

required.

The mechanical properties of Ti(C,N)-FeNi cermets at the macroscopic length scale have been reported previously [9,10]. However, little information is available on the micro-scale behaviour of these materials, which is crucial for microstructural design optimization. In this regard, a recent study by the authors have shown that testing protocols based on massive nanoindentation and statistical analysis, previously proposed for characterizing WC-base alloys [11–14], may also be valid for evaluation of small-scale properties of Ti(C,N)-based cermets [15]. Furthermore, such investigation pointed out the effectiveness of FeNi as reinforcement phase for these materials, towards optimization of hardness-toughness relationships of ceramic-metal systems. In this study, such approach is extended by addressing the influence of carbon addition on microstructure and mechanical properties of Ti(C,N)-FeNi cermets with three different ceramic/metal phase ratios. In doing so, a relatively new high speed nanoindentation mapping technique is employed to analyse and correlate the microstructural and hardness of the constitutive phases at the microstructural length

* Corresponding author at: CIEFMA – Department of Materials Science and Metallurgical Engineering, EEBE, Universitat Politècnica de Catalunya-BarcelonaTech, 08019 Barcelona, Spain.

E-mail address: hossein.besharatloo@upc.edu (H. Besharatloo).

<https://doi.org/10.1016/j.ijrmhm.2019.105064>

Received 4 July 2019; Received in revised form 12 August 2019; Accepted 19 August 2019

Available online 20 August 2019

0263-4368/ © 2019 Elsevier Ltd. All rights reserved.

Table 1
Main characteristics of the as-received commercial powders.

Powder	Type/Supplier	Density (g/cm ³) ^a	Particle size distribution			SSA (m ² /g) ^b
			D _{V50} (μm)	D _{BET} (μm)	F _{ag} (-)	
Ti(C,N)	Ti(C _{0.5} N _{0.5})/H.C.Starck (Germany)	5.1	2.1	0.4	5.0	3.0
Fe	Fe SM/H.C.Starck (Germany)	7.8	3.5	1.2	3.0	0.6
Ni	Ni 210H/INCO (Canada)	8.9	1.7	0.2	10	4.0

^a ± 0.1 Standard deviation in density measurements.

^b ± 0.1 Standard deviation in specific surface area measurements.

scale. This is achieved by means of massive nanoindentation in conjunction with statistical analysis [16–19].

2. Experimental procedure

2.1. Sample preparation

The main characteristics of the Ti(C,N), Fe and Ni as-received commercial powders used in this investigation are summarized in Table 1. The density of the powders was calculated employing a Helium Monosorb Multipycnometer (Quantachrome Corporation, USA). Particle size distribution (average particle size in volume (D_{V50}), Brunauer-Emmett-Taller diameter (D_{BET}) and the agglomeration factor ($F_{ag} = D_{V50}/D_{BET}$) was measured with a laser analyser (Mastersizer S, Malvern instruments Ltd., UK) and the specific surface area (SSA) was characterized by means of one-point nitrogen absorption (Monosorb Surface Area, Quantachrome Corporation, USA).

A combination of powder metallurgy and colloidal processing was used to manufacture the powder compacts, following the procedure described in [9]. Water-suspensions of high solid content of ceramic and metallic powders were separately prepared. The medium pH was modified to 10–11 with tetra-methyl-ammonium hydroxide (TMAH) to stabilize the particle surfaces, and polyethyleneimine (PEI) was added in a 0.4 wt% to act as dispersant. Ti(C,N) and Fe15Ni slurries were separately milled for 1 h at 50 rpm for homogenization using Si₃N₄ and nylon balls, respectively. For the extra C addition, a 10 g/L graphite suspension was prepared in another vessel, mixing ethanol and Black Carbon (ISTA, Germany), with a mean particle size of 18 μm and density of 2.24 g/cm³. The ceramic, metallic and graphitic suspensions were blended according to the formulations collected in Table 2. In all of them, the composition of the metal matrix was 85–15 Fe–Ni wt%. Before spray-drying, a 2 wt% of polyvinyl alcohol (PVA) was added to the mixture slurries to enable the formation of agglomerates. An Atomizer LabPlant SD-05 (North Yorkshire, UK) was used, with a modified nozzle design to obtain easy-to-press spherical granules, with inlet and exhaust temperatures held constant at 190 and 100 °C, respectively, a slurry pump rate of 2 L/h, and an airflow rate of 29 m³/h. After atomization, the mixed agglomerates were uniaxially pressed at 600 MPa into 16 mm-diameter disks. The green bodies were sintered in a high-vacuum furnace (10⁻⁵ mbar) using the following heating cycle: 800 °C – 30 min, 1450 °C – 2 h (5 °C/min).

For metallographic and micromechanical characterization, the sintered samples were transversally cut, embedded in conductive resin, and polished with successively smaller diamond pastes down to 3 μm,

Table 2
Formulations of the different materials prepared.

Specimen	Volume (Vol%)		Weight (wt%)	
	Ti(C,N)	FeNi	Ti(C,N)	FeNi
15FeNi	85	15	78.2	21.8
20FeNi	80	20	71.7	28.3
30FeNi	70	30	59.7	40.3

finishing with a colloidal Al₂O₃ final polish.

2.2. Microstructural characterization

Microstructures of processed and manufactured cermets were analysed using field emission gun scanning electron microscopy (FEG-SEM) to evaluate several parameters of interest: grain size of the Ti(C,N) phase, porosity, and the mean free path of the metallic binder. The carbo-nitride grain size ($d_{Ti(C,N)}$) and mean free path (λ) of the metallic binder were measured by means of the linear interception method (LIM) [20], measured on a minimum of five micrographs per sample. These images were taken using a 7100F FEG-SEM unit (JEOL, Tokyo, Japan) at an acceleration voltage of 20 kV. In addition, the amount of porosity was determined, by means of ImageJ software, as a function of volume fraction and/or carbon content of the metallic binder.

2.3. Macro-mechanical characterization: Vickers hardness and indentation fracture toughness

Vickers hardness (HV) and indentation fracture toughness (K_{Ic}) were evaluated at the macro-metric length scale. HV was determined using a diamond Vickers indenter and applied loads 10 and 30 kgf (15 s hold time) using a DuraScan 20 G5 unit (EMCO-TEST Prüfmaschinen GmbH, Kuchl, Austria). K_{Ic} was assessed using Shetty et al.'s equation [21], on the basis of length of cracks emanating out of the corner of imprints, resulting after applying a 30 kgf load. Residual imprint dimensions and cracks' length were measured using a Phenom XL SEM unit (Thermo-Fisher Scientific, Waltham, MA, USA).

2.4. Massive nanoindentation and hardness mapping

Hardness cartography maps were obtained by implementing NanoBlitz technique using an iNano® nanoindenter (Nanomechanics Inc., Oak Ridge, USA) with a diamond Berkovich indenter tip. This technique can offer relatively fast testing speeds, wherein positioning of the specimen under the indenter, surface approach, loading, unloading and retracting can be completed in < 1 s. This novel technique allows H - and E -mapping over a relatively large region via indentation grids of thousands of indentations and immediate evaluation following Oliver and Pharr method [22,23]. It provides a large data set that may then be statistically analysed, following the methodology proposed by Ulm and co-workers [16–19], aiming to extract the intrinsic mechanical properties of each constitutive phase, see Table 2. In this study, large grids of 40,000 (matrix of 200 by 200) imprints were performed at a maximum load of 10 mN on each sample. The distance between indentations was held constant at 1.5 μm, to prevent significant overlap or effect from neighbouring imprints. It permits to treat each imprint as an independent statistical value. Such spacing value was chosen as it represents 10× the average indentation depth at 10 mN within the majority hard phase, using the spacing criterion suggested by Phani and Oliver [24].

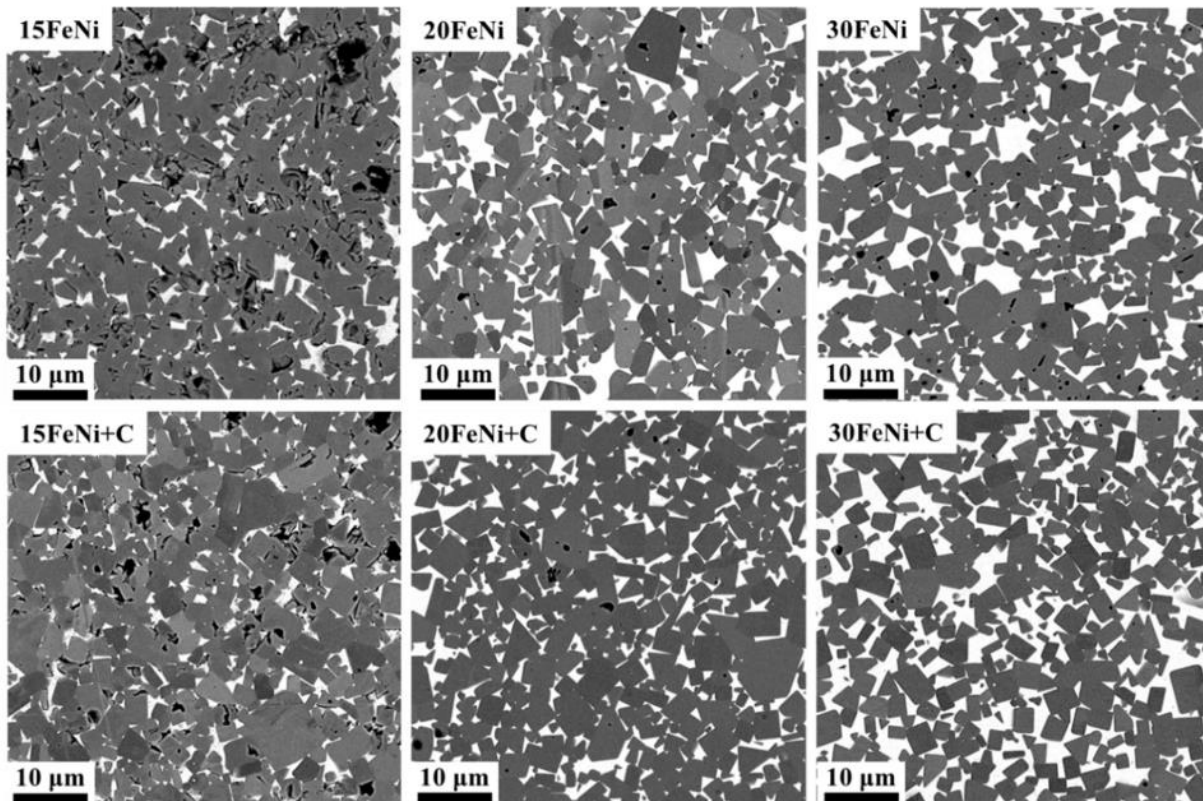


Fig. 1. SEM images of Ti(C,N)-FeNi cermets with different vol% and carbon addition of the metallic binder.

3. Results and discussion

3.1. Microstructural parameters

Secondary electron micrographs for the studied samples are shown in Fig. 1. Two different phases can be clearly distinguished: Ti(C,N) particles (grey particles) heterogeneously embedded in the FeNi binder (white region). Furthermore, porosity is also discerned as black spots, spread over the samples in both phases. The corresponding microstructural parameters are summarized in Table 3.

Porosity was highest in specimens containing 15% Vol. of the metallic binder (Fig. 1 and Table 3). In higher binder content samples, porosity was significantly reduced. Within this context, porosity content may be attributed to insufficient binder to fully wet/enclose all the ceramic particles during the liquid phase sintering. Previous results suggest that the poor sintering of Fe binder cermets reinforced with Ti(C,N) attributes to the low wettability of Fe on TiN. Nevertheless, the addition of small amount of Ni (15 wt%) to the Fe binder reduces the contact angle of the liquid phase ($> 90^\circ$) to values close to the Ni ones (25°). Consequently, wettability of the binder on TiN is the responsible of the sintering of FeNi binder cermets reinforced with Ti(C,N).

Table 3
Summary of the microstructural parameters of studied samples.

Sample name	Binder content %	Carbon content %wt	Mean Ti(C,N) grain size, $d_{Ti(C,N)}$ (μm)	Mean free path, λ (μm)	Porosity %
15FeNi	15	0	2.2 ± 0.3	0.5 ± 0.1	2.7 ± 1.1
15FeNi+C		0.5	2.3 ± 0.2		2.3 ± 0.2
20FeNi	20	0	2.2 ± 0.3	0.6 ± 0.1	0.5 ± 0.1
20FeNi+C		0.5	2.2 ± 0.3		0.2 ± 0.1
30FeNi	30	0	2.3 ± 0.3	1.0 ± 0.2	0.8 ± 0.2
30FeNi+C		0.5	2.3 ± 0.3		0.1 ± 0.1

Moreover, the calculated phase diagram reveals the evolution of Fe15Ni with respect the carbon content, which demonstrates that an increase in the C content decreases the liquidus temperature. Consequently, the presence of C from the Ti(C,N) substrate is the responsible of the temperature of liquid phase formation, improving the cermet sintering. In this sense, the addition of C, reduced porosity in all cases and enhanced the hardness [25]. Furthermore, addition of C was observed to reduce porosity in all cases. This C addition effect was more pronounced with increasing binder content – Fig. 2.

In some samples porosity was observed to exhibit a bimodal distribution, as shown in Fig. 2 for the 30FeNi (sample without carbon).

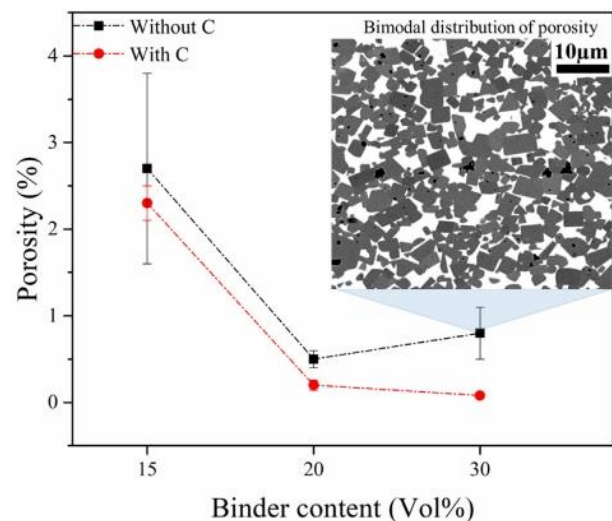


Fig. 2. Porosity versus binder content for samples with (red) and without (black) carbon content. (For interpretation of the references to colour in this figure legend, the reader is referred to the web version of this article.)

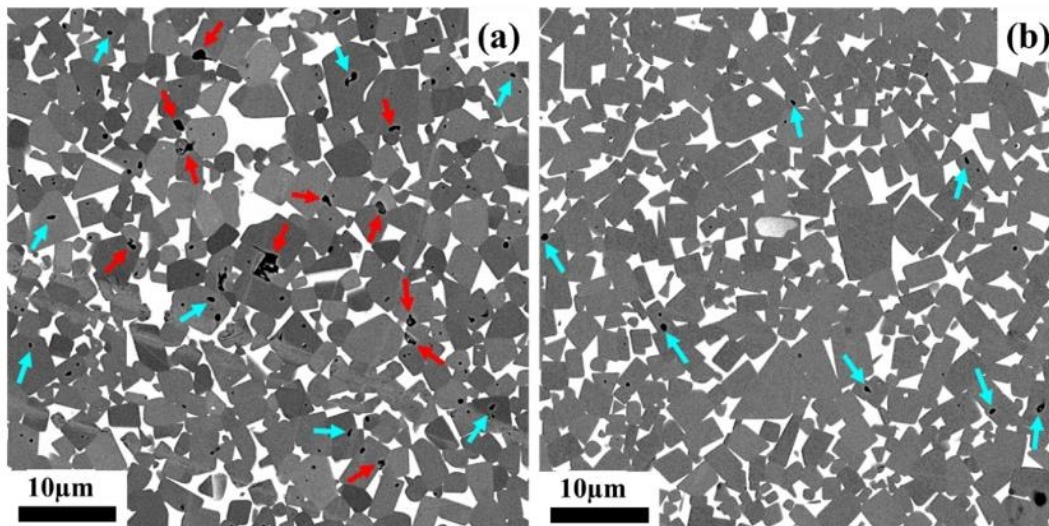


Fig. 3. Porosities of the samples with 20 vol% of the metallic binder, (a) without carbon addition and (b) with carbon addition.

This suggests that large cavities were left unfilled at interfaces or inside agglomerated particles, in addition to small voids inside individual Ti (C,N) particles. It could be rationalized on the basis of incomplete sintering and may be responsible for the relatively large scatter in porosity of these samples. This bimodal distribution of porosity was also seen in the 20FeNi (without carbon addition) - Fig. 3.

Porosity related to incomplete sintering was observed to disappear with the addition of 0.5 wt% of carbon (see Fig. 3). Addition of carbon is known to decrease solidus and liquidus temperatures of the metallic matrix, as well as to increase the temperature range between them. Consequently, a more homogeneous and less porous microstructure is achieved [26–29]. This is confirmed by thermal simulation and differential thermal analysis (DTA) measurements - Fig. 4. Such phenomenon enhances liquid phase sintering and densification of the material, yielding lower final porosity levels. Moreover, optimization of the carbon addition may improve the wettability of the ceramic phase by the metallic one. Further information on the effect of carbon addition

on the microstructural parameters of the studied materials may be found in Refs. [25, 30–32].

3.2. Macro hardness assessment

Macro-scale Vickers hardness is one of the standard parameters used for industry for immediate quality control purposes. Table 4 summarizes the assessed Vickers hardness values performed at different applied loads. Fig. 5 illustrates the influence of both binder content and carbon addition on Vickers hardness (HV10) of investigated cermets. In general, and as expected, Vickers hardness decreases as the binder content increases. Addition of carbon yields similar hardness increase effect. The influence of carbon addition is more evident for samples with higher binder content. Since carbon addition is expected to promote hardening of the metallic binder, its influence is expected to be relatively higher in the grades containing a relatively higher amount of metallic phase. Nevertheless, changes in mechanical properties of the investigated samples should be described as the combined effect of carbon addition on both metallic binder hardening and effective amount of porosity [27,32].

3.3. Indentation fracture toughness

Indentation fracture toughness, or Palmqvist toughness [21], is an established method for evaluating the fracture toughness of cermet materials on the basis of lengths of cracks emanating out of imprint corners, obtained after indentation applying relatively high loads. Fig. 6a shows a residual imprint of a Vickers indenter together with the induced radial crack system (measuring lines also indicated in Fig. 6a). Table 5 and Fig. 6b demonstrate the influence of binder content and carbon addition on the indentation fracture toughness of investigated Ti (C,N)-FeNi systems. As expected, it increases dramatically with binder content, highlighting the influence of this variable due to the ductile

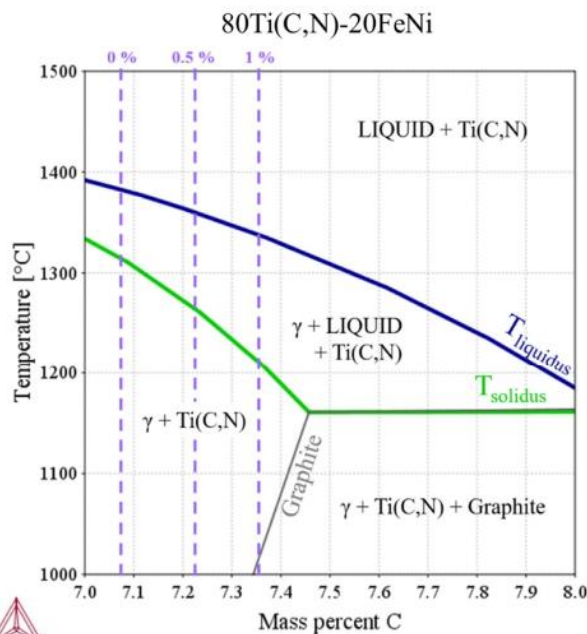


Fig. 4. Equilibrium phase diagram (simulated by Thermo-Calc) for sample with 20 Vol% of the metallic binder.

Table 4
Summary of the HV values obtained at 10 and 30 kgf of maximum applied load.

Sample	HV10 (GPa)	HV 30 (GPa)
15FeNi	13.0 ± 0.4	12.8 ± 0.1
15FeNi+C	13.3 ± 0.3	13 ± 0.1
20FeNi	11.3 ± 0.3	11 ± 0.1
20FeNi+C	12.2 ± 0.2	11.7 ± 0.1
30FeNi	9.5 ± 0.4	9.1 ± 0.2
30FeNi+C	10.5 ± 0.2	9.9 ± 0.2

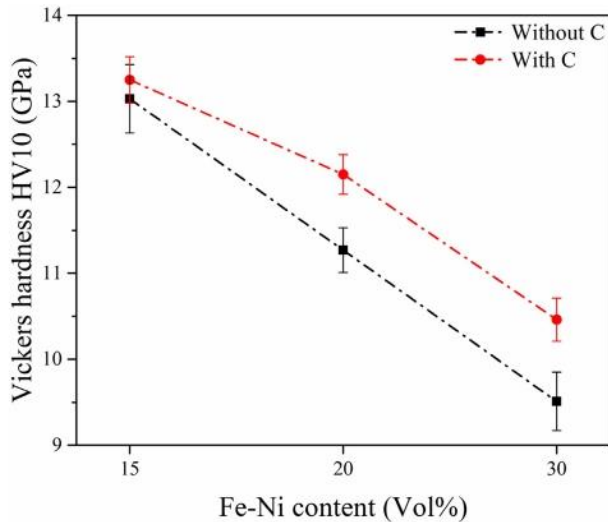


Fig. 5. Influence of binder content and carbon (C) addition on HV for all the different samples.

nature of the metallic phase. The Fig. 6b also reveals that carbon addition slightly diminishes the indentation fracture toughness, whereas it improves hardness due to the hardening effect in the metallic binder.

3.4. Hardness mapping

Modern high speed nanoindentation techniques allow the performance of large grids of nanoindentations to statistically extract the properties of individual phases and composite behaviour. Fig. 7 illustrates a cropped region of an indentation matrix carried out on the 20FeNi + C sample, in which three kinds of indentation, depending on probing zone, are marked: Ti(C,N) particles (dash-dot circle), metallic binder (solid line circle) and two-phase regions including ceramic/metal interfaces (dashed circle). Since these indentations were performed in load-control mode (load kept constant at 10 mN), it can be evidenced that indentations performed on the hard phase are smaller than the ones within the metallic binder. Moreover, some fractures can be observed around Ti(C,N) particles (white arrows), in agreement with brittle response expected for the ceramic phase. Imprints within the

Table 5 Indentation fracture toughness of studied samples.

Sample	Indentation fracture toughness (MPa·√m)
15FeNi	10.8 ± 2.7
15FeNi + C	10.5 ± 1.7
20FeNi	12.4 ± 2.2
20FeNi + C	11.6 ± 2.9
30FeNi	20.8 ± 2.0
30FeNi + C	17.6 ± 3.0

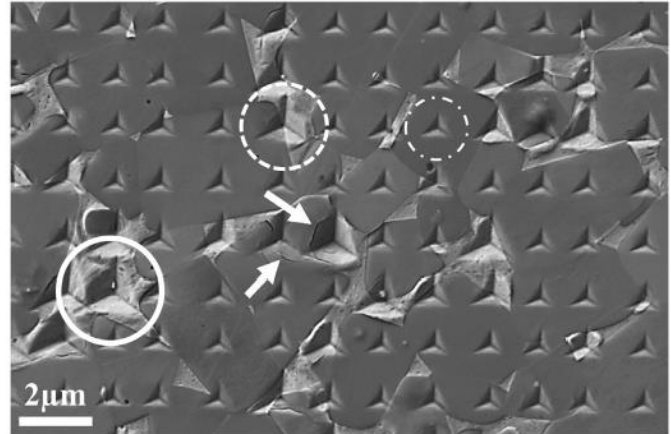


Fig. 7. FESEM micrograph of magnified region of indentation array applied at 10 mN applied force on the 20FeNi + C sample.

metallic binder (solid line circle) show pile-up characteristic of confined plastic deformation, further supporting the intrinsic ductility exhibited by the metallic binder.

Furthermore, Fig. 7 illustrates that spacing between indentations appears sufficient to prevent significant overlap for the majority of impressions, following the criterion of spacing the indentations 10× larger than the indentation depth [24]. There are some exceptions in the softer phase, which were anticipated due to the significant differences in the hardness of the constituent phases. Load chosen for the indentation grid was selected to keep the majority of indentations within the spacing = 10× indent depth criterion, while still

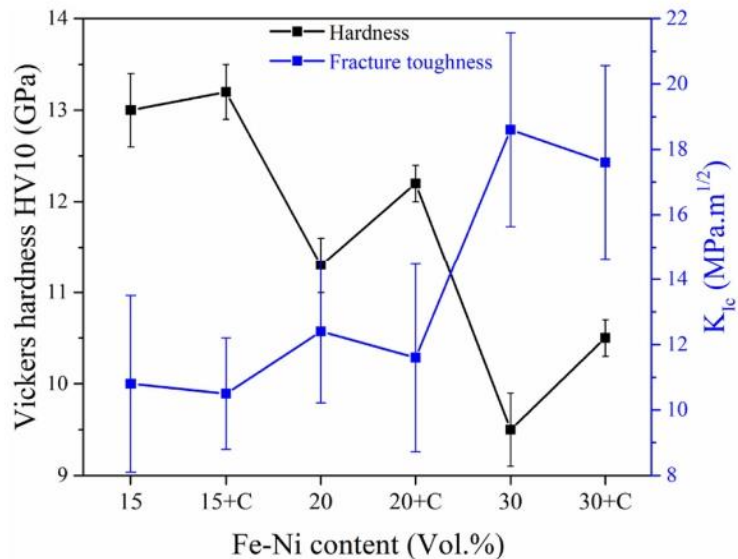
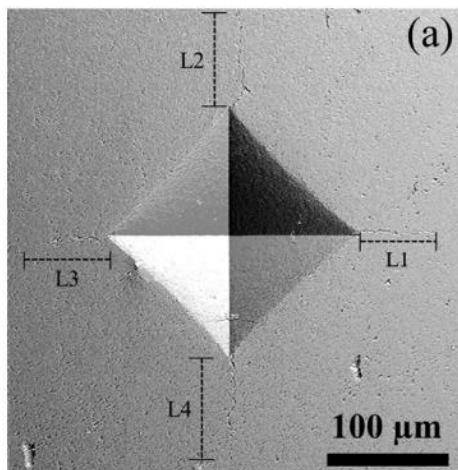


Fig. 6. (a) Residual Vickers imprint applied on 20FeNi + C sample at 30 kgf, (b) Influence of binder content and carbon addition on the Vickers hardness and indentation fracture toughness of studied samples.

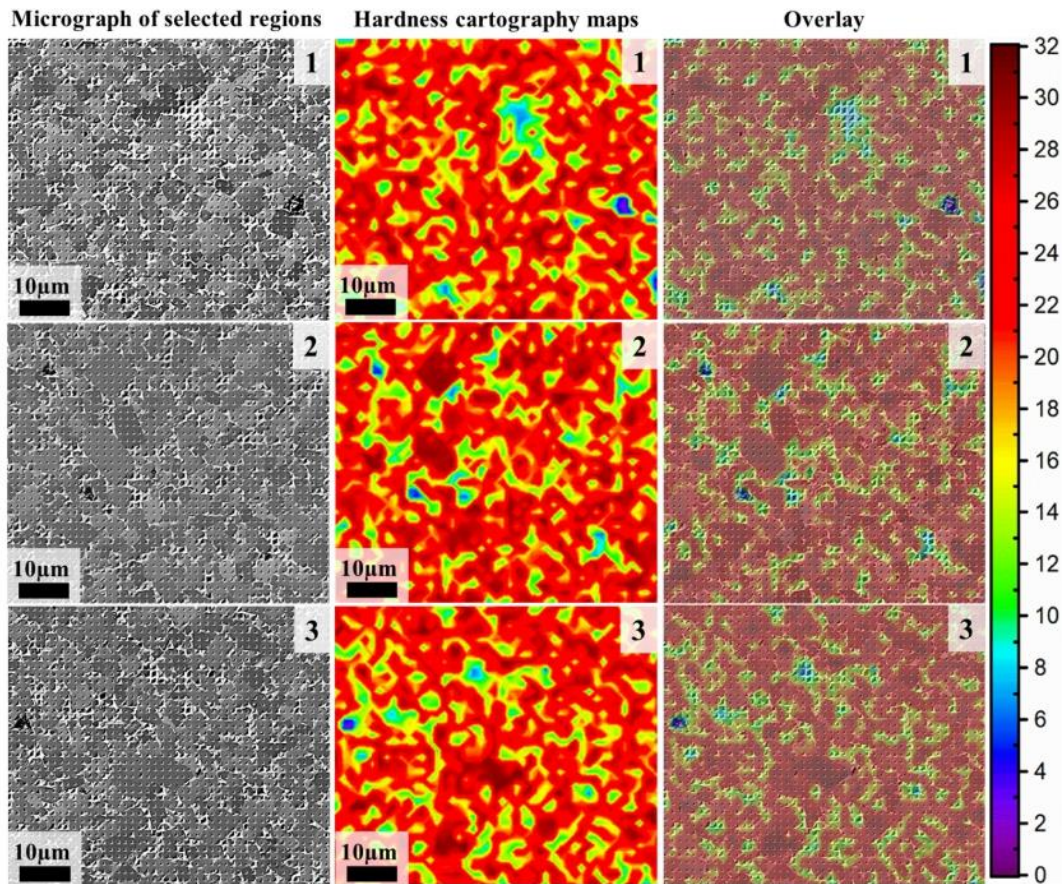


Fig. 8. FESEM micrographs and hardness cartography maps of different selected regions of applied matrix of indentations on 20FeNi + C sample are shown in the left and middle columns, respectively. Combined images showing the hardness maps overlaid on the electron micrographs are shown in the right column.

maintaining a sufficient depth in the hard phase to yield a representative value.

Hardness maps of three different regions in comparison with corresponding FESEM micrographs are shown in Fig. 8. Additionally, obtained micrographs and hardness maps were overlaid to offer an illustration of the correlation between the microstructure and micromechanical properties. Several gradient responses, even within individually defined phases, can be distinguished in the hardness maps due to their distinct ranges of colours (Fig. 8). First, Ti(C,N) particles are tinted with red shades, ranging from 23 up to 30 GPa. Second, metallic binder is manifested in a range from light blue to light green (ranging between 8 up to 15 GPa). Here, higher hardness values are indicative of more constraining (by the surrounding hard phase) of the binder. Third, a composite-like response (defined here as a third mechanically distinct phase) is linked to yellow/orange tones. It describes the interaction of the plastic flow (induced by imprints probing regions including phase boundaries) of both ceramic and metallic constitutive phases. Finally, some dark blue spots can also be observed in direct relation to assessed hardness values below 4 GPa. Such extremely low values are attributed to porosity, as it is sustained by observation of overlaid maps in Fig. 8.

Fig. 9 demonstrates the hardness cartography maps which are attained from 40,000 indentations (matrices of 200×200) performed at 10 mN applied load on different samples with carbon addition. Obtained maps manifest the inverse relationship between the evaluated mechanical property and the volume fraction of metallic phase, which attributes to the constraining effect imposed on metallic binder by the harder phase. More information can be found in Ref [15].

3.5. Statistical analysis of hardness cartography maps

Previously, the data extracted from the massive nanoindentation grids was qualitatively compared to the sample morphology. In order to extract the hardness of each individual phase, a statistical analysis (proposed by Ulm and co-workers [16–19]) was performed on the data. Fig. 10 shows a representative histogram of hardness values with a constant bin size of 0.5 GPa gathered from 40,000 indentations performed on the 20FeNi + C sample. As can be seen in Fig. 8, three discrete peaks were fitted, corresponding to the two constitutive phases and a third composite-like one, where probing regions contain ceramic/metal interfaces. The highest peak, mean value of ~ 27 GPa, relates to Ti(C,N) ceramic phase, while the lowest peak, with a mean value of 12.5 GPa, is attributed to the FeNi metallic binder. The intermediate peak, with a mean value of 19.6 GPa, can be considered as the hardness response of the combined interaction of Ti(C,N) and FeNi binder. A similar histogram analysis was performed on every sample in the study. The mean and standard deviation values of small-scale hardness for each of the three defined phases, in all samples studied, are summarized in Table 6.

On the basis of data listed in Table 6, several observations may be done. First, hardness values of the ceramic particles are observed to remain constant for all samples, regardless of microstructure, volume fraction of ceramic phase (as reported in Ref [15]), and/or carbon addition. Second, and opposite to previous statement, hardness values assessed for both metallic binder and composite-like phases increase as ceramic/metal phase ratio rises. This can be rationalized by the direct effect of increasing ceramic contribution on load-bearing action on one hand, and the indirect influence linked to higher constraint on the effective deformation of the metallic binder (smaller binder mean free

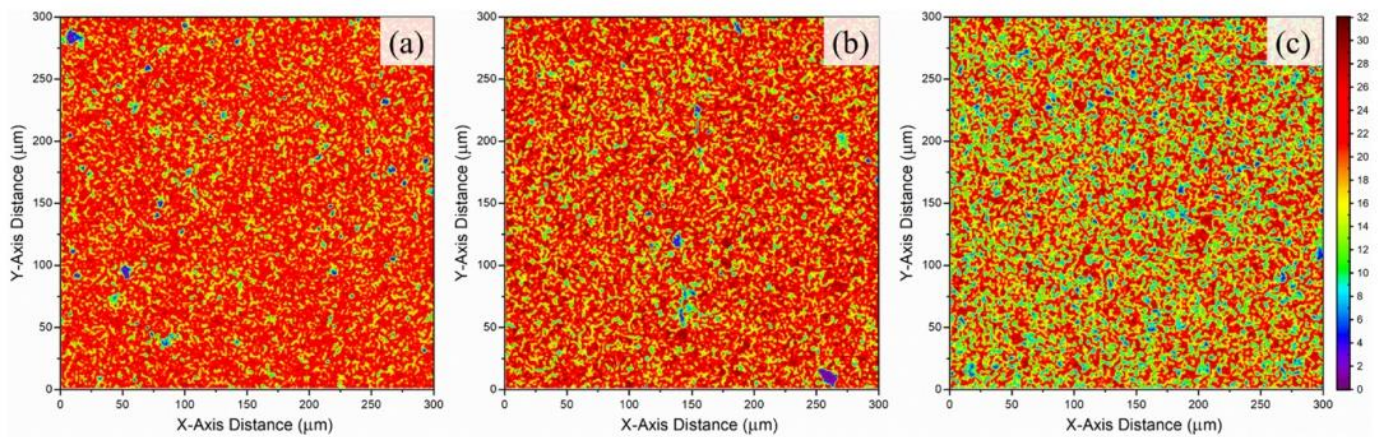


Fig. 9. Hardness cartography map obtained from three different matrices of indentations (200×200) performed at 10 mN on (a) 15FeNi + C, (b) 20FeNi + C and (c) 30FeNi + C samples.

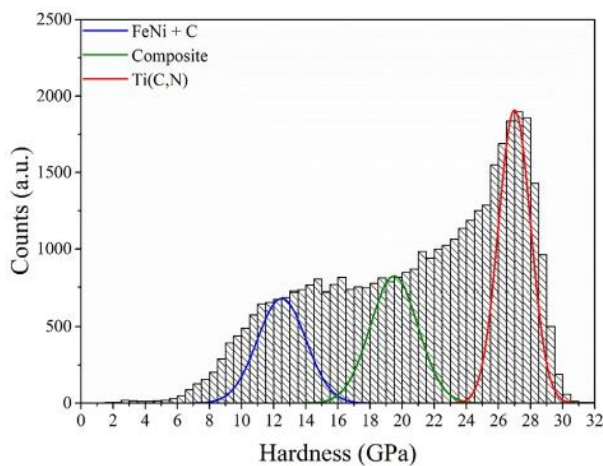


Fig. 10. Hardness histogram determined from 40,000 indentations performed at a maximum applied load of 10 mN on sample 20FeNi + C.

Table 6

Summary of the hardness mean values for each phase of the investigated samples obtained through the statistical analysis.

Sample	Hardness (GPa)		
	FeNi	Composite	Ti(C,N)
15FeNi	13.7 ± 0.3	20.4 ± 0.2	26.8 ± 0.2
15FeNi + C	14.1 ± 0.3	21.5 ± 0.2	26.9 ± 0.2
20FeNi	11.7 ± 0.2	19.1 ± 0.2	26.7 ± 0.2
20FeNi + C	12.5 ± 0.2	19.6 ± 0.1	26.9 ± 0.2
30FeNi	8.3 ± 0.3	15.0 ± 0.3	26.6 ± 0.3
30FeNi + C	9.6 ± 0.2	17.1 ± 0.2	26.7 ± 0.3

path) on the other one.

Moreover, carbon addition is discerned to enhance local hardness of the binder for samples with given ceramic/metal phase ratio. It will then point out carbon-activated hardening mechanisms in the metallic binder. This scenario can be also extended to the composite phase, where hardness values also increased with carbon addition. However, in this case, besides the referred intrinsic hardening effect for the metallic phase, effective reduction of porosity amount within the cermet should also be recalled for explaining such finding, as it will be now discussed.

Carbon addition effects on the hardness of cermets studied, through effective reduction of porosity amount, can be illustrated in Fig. 11. It shows lower-hardness regions of histograms for samples which

displayed greater porosity. Hardness values < 4 GPa are assumed to correspond to indentations performed in areas with porosity (dark blue spots in Fig. 8). In both cases, it is clear that carbon addition reduces the number of indentations which encountered weak porosity-related areas. A similar trend is also observed with increasing the relative amount of binder within the cermet, in agreement with our previous microstructural observations (Fig. 2).

4. Conclusions

The influence of carbon addition on the microstructural and micromechanical characteristics of Ti(C,N)-FeNi cermets has been investigated. Based on the obtained data, the following conclusions may be drawn:

- Higher volume fraction of metallic phase as well as carbon addition yield more homogeneous and less porous microstructure for the same ceramic/metal ratio. It results in significant changes in hardness and indentation fracture toughness (following the well-established inverse correlation between both mechanical properties), these being more pronounced in the softer grades.
- The addition of carbon results in higher hardness values at macro- and micro- length scales. Such changes are directly related to an intrinsic (small-scale) hardening effect of the metallic phase as well as to an effective reduction of porosity amount affecting the two-phase composite-like hardness.
- Hardness cartography at the microstructural length scale showed an excellent qualitative correlation between micromechanical characteristics (measured from massive nanoindentation) and microstructural assemblage (as evidenced from FESEM inspection).
- Massive nanoindentation and statistical analysis has proven to be a successful tool for analysing small-scale properties of different constitutive phases. It includes not only assessment of intrinsic hardness values but also evaluation of change in these properties for individual or mechanically distinct phases, as related to specific influence of microstructural/processing variables, e.g. carbon addition or ceramic/metal phase ratio.

Acknowledgements

This investigation was supported by the Spanish Ministerios de Economía y Competitividad MINECO through grant MAT2015-70780-C4-P. J.J. Roa acknowledges the Serra Hunter programme of the Generalitat de Catalunya.

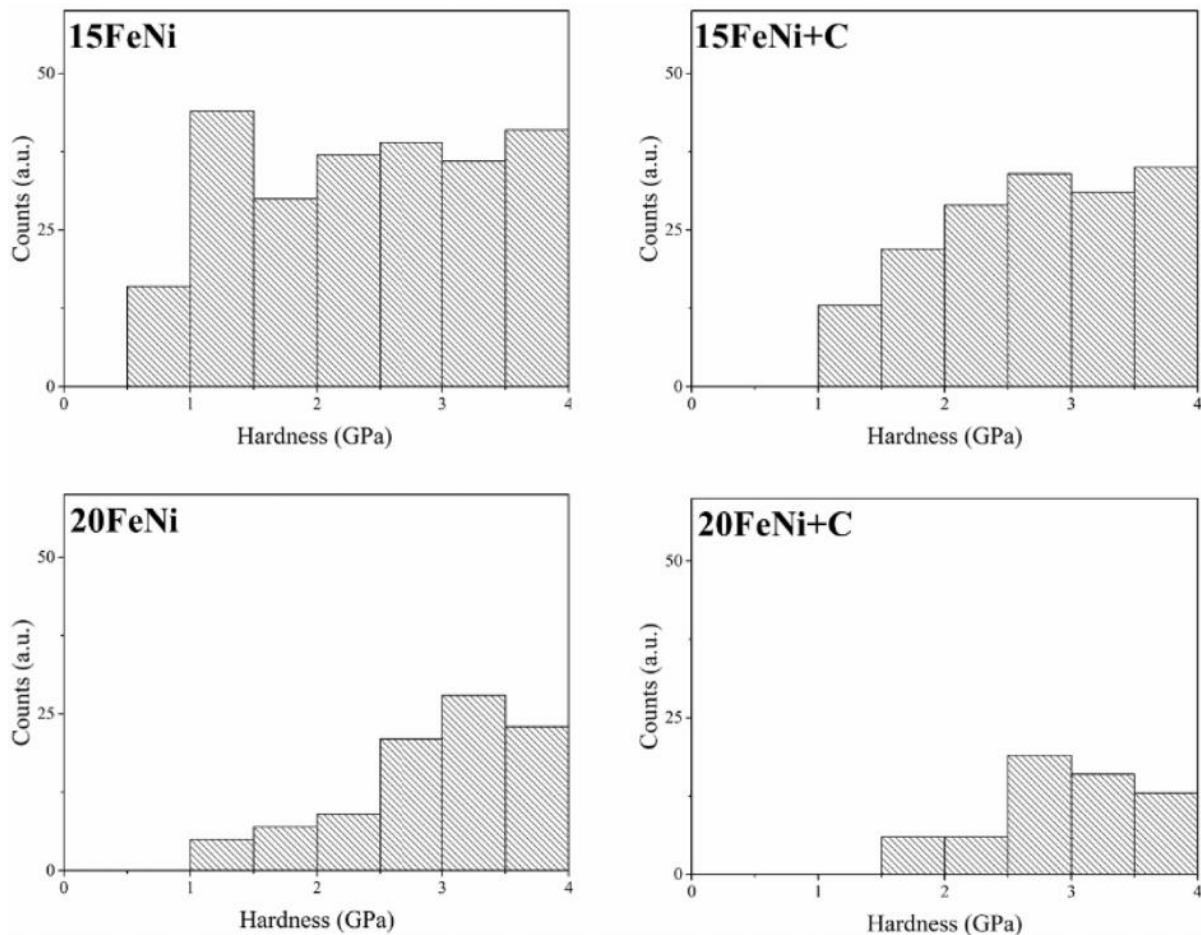


Fig. 11. Hardness histograms for studied samples exhibiting relatively high porosity levels, magnified on the regions corresponding to hardness values lower than 4 GPa.

References

- [1] B. Gries, L. Prakash, WC hardmetals with Iron based binders, in: P. Rödhammer, L. Sigl, H. Wildner (Eds.), Proceedings of 17th Plansee Seminar, Reutte, Austria, 2009, pp. HM 5/1–HM 5/13.
- [2] National Toxicology Program, Department of Health and Human Service in USA, 2019. <http://ntp.niehs.nih.gov/?objectid=03C9AF75-E1BF-FF40-DBA9EC0928DF8B15>.
- [3] M. Grilli, T. Bellezze, E. Gamsjäger, A. Rinaldi, P. Novak, S. Balos, R. Piticescu, M. Ruello, Solutions for critical raw materials under extreme conditions: a review, Materials (Basel). 10 (2017) 285, <https://doi.org/10.3390/ma10030285>.
- [4] P. Ettmayer, H. Kolaska, W. Lengauer, K. Dreyer, Ti(C,N) Cermets – metallurgy and properties, Int. J. Refract. Met. Hard Mater. 13 (1995), [https://doi.org/10.1016/0263-4368\(95\)00027-G](https://doi.org/10.1016/0263-4368(95)00027-G).
- [5] A. Bellosi, R. Calzavarini, M.G. Faga, F. Monteverde, C. Zancolò, G.E. D'Errico, Characterisation and application of titanium carbonitride-based cutting tools, J. Mater. Process. Technol. 143–144 (2003) 527–532 [https://doi.org/10.1016/S0924-0136\(03\)00339-X](https://doi.org/10.1016/S0924-0136(03)00339-X).
- [6] B. Wittmann, W.-D. Schubert, B. Lux, WC grain growth and grain growth inhibition in nickel and iron binder hardmetals, Int. J. Refract. Met. Hard Mater. 20 (2002) 51–60 [https://doi.org/10.1016/S0263-4368\(01\)00070-1](https://doi.org/10.1016/S0263-4368(01)00070-1).
- [7] E. Gordo, B. Gómez, E.M. Ruiz-Navas, J.M. Torralba, Influence of milling parameters on the manufacturing of Fe-TiCN composite powders, J. Mater. Process. Technol. 162–163 (2005) 59–64 <https://doi.org/10.1016/j.jmatprotec.2005.02.154>.
- [8] P. Alvaredo, B. Ferrari, E. Gordo, Interface study for the design of alternative matrixes in cermets. In EuroPM2015 International Powder Metallurgy Congress & Exhibition Reims (France), EPMA European Powder Metallurgy Association (2015).
- [9] M. Dios, Z. Gonzalez, P. Alvaredo, R. Bermejo, E. Gordo, B. Ferrari, Novel colloidal approach for the microstructural improvement in Ti (C, N)/FeNi cermets, J. Alloys Compd. 724 (2017) 327–338, <https://doi.org/10.1016/j.jallcom.2017.07.034>.
- [10] M. Dios, I. Kraveva, Z. González, P. Alvaredo, B. Ferrari, E. Gordo, R. Bermejo, Mechanical characterization of Ti (C, N)-based cermets fabricated through different colloidal processing routes, J. Alloys Compd. 732 (2018) 806–817, <https://doi.org/10.1016/j.jallcom.2017.10.274>.
- [11] J.J. Roa, E. Jimenez-Pique, C. Verge, J.M. Tarragó, A. Mateo, J. Fair, L. Llanes, Intrinsic hardness of constitutive phases in WC-Co composites: Nanoindentation testing, statistical analysis, WC crystal orientation effects and flow stress for the constrained metallic binder, J. Eur. Ceram. Soc. 35 (2015) 3419–3425, <https://doi.org/10.1016/j.jeurceramsoc.2015.04.021>.
- [12] J.J. Roa, E. Jiménez-Piqué, J.M. Tarragó, D.A. Sandoval, A. Mateo, J. Fair, L. Llanes, Hall-Petch strengthening of the constrained metallic binder in WC-Co cemented carbides: experimental assessment by means of massive nanoindentation and statistical analysis, Mater. Sci. Eng. A 676 (2016) 487–491, <https://doi.org/10.1016/j.msea.2016.09.020>.
- [13] J.J. Roa, P.S. Phani, W.C. Oliver, L. Llanes, Mapping of mechanical properties at microstructural length scale in WC-Co cemented carbides: assessment of hardness and elastic modulus by means of high speed massive nanoindentation and statistical analysis, Int. J. Refract. Met. Hard Mater. 75 (2018) 211–217, <https://doi.org/10.1016/j.jrmhm.2018.04.019>.
- [14] D.A. Sandoval, J.J. Roa, O. Ther, E. Tarrés, L. Llanes, Micromechanical properties of WC-(W, Ti, Ta, Nb) C-Co composites, J. Alloys Compd. 777 (2019) 593–601, <https://doi.org/10.1016/j.jallcom.2018.11.001>.
- [15] H. Besharatloo, M. de Nicolás, J.J. Roa, M. Dios, A. Mateo, B. Ferrari, E. Gordo, L. Llanes, Assessment of mechanical properties at microstructural length scale of Ti (C,N)-FeNi ceramic-metal composites by means of massive nanoindentation and statistical analysis, Ceram. Int. (2019), <https://doi.org/10.1016/j.ceramint.2019.06.292>.
- [16] G. Constantinides, F.-J. Ulm, K. Van Vliet, On the use of nanoindentation for cementitious materials, Mater. Struct. 36 (2003) 191–196, <https://doi.org/10.1007/BF02479557>.
- [17] G. Constantinides, K.S. Ravi Chandran, F.J. Ulm, K.J. Van Vliet, Grid indentation analysis of composite microstructure and mechanics: principles and validation, Mater. Sci. Eng. A 430 (2006) 189–202 <https://doi.org/10.1016/j.msea.2006.05.125>.
- [18] G. Constantinides, F.-J. Ulm, The nanogranular nature of C-S-H, J. Mech. Phys. Solids. 55 (2007) 64–90, <https://doi.org/10.1016/j.jmps.2006.06.003>.
- [19] F.-J. Ulm, M. Vandamme, C. Bobko, J. Alberto Ortega, K. Tai, C. Ortiz, Statistical indentation techniques for hydrated nanocomposites: concrete, bone, and shale, J. Am. Ceram. Soc. 90 (2007) 2677–2692, <https://doi.org/10.1111/j.1551-2916.2007.02012.x>.
- [20] Metallographic Determination of Microstructure, Part 2: Measurement of WC Grain Size, ISO 4499-2 2008, Hardmetals, Geneva (2008).

- [21] D.K. Shetty, I.G. Wright, P.N. Mincer, A.H. Clauer, Indentation fracture of WC-Co cermets, *J. Mater. Sci.* 20 (1985) 1873–1882, <https://doi.org/10.1007/BF00555296>.
- [22] W.C. Oliver, G.M. Pharr, An improved technique for determining hardness and elastic modulus using load and displacement sensing indentation experiments, *J. Mater. Res.* 7 (1992) 1564–1583, <https://doi.org/10.1557/JMR.1992.1564>.
- [23] W.C. Oliver, G.M. Pharr, Measurement of hardness and elastic modulus by instrumented indentation: advances in understanding and refinements to methodology, *J. Mater. Res.* 19 (2004) 3–20, <https://doi.org/10.1557/jmr.2004.19.1.3>.
- [24] P. Sudharshan Phani, W.C. Oliver, A critical assessment of the effect of indentation spacing on the measurement of hardness and modulus using instrumented indentation testing, *Mater. Des.* 164 (2019) 107563, <https://doi.org/10.1016/j.matdes.2018.107563>.
- [25] P. Alvaredo, M. Dios, B. Ferrari, E. Gordo, Understanding of wetting and solubility behavior of Fe binder on Ti (C, N) cermets, *J. Alloys Compd.* 770 (2019) 17–25, <https://doi.org/10.1016/j.jallcom.2018.07.243>.
- [26] M. Seo, J. Kim, S. Kang, Effect of carbon content on the microstructure and properties of (Ti_{0.7}W_{0.3})C-Ni cermet, *Int. J. Refract. Met. Hard Mater.* 29 (2011) 424–428, <https://doi.org/10.1016/j.ijrmhm.2011.01.004>.
- [27] P. Alvaredo, S.A. Tsipas, E. Gordo, Influence of carbon content on the sinterability of an FeCr matrix cermet reinforced with TiCN, *Int. J. Refract. Met. Hard Mater.* 36 (2013) 283–288, <https://doi.org/10.1016/j.ijrmhm.2012.10.007>.
- [28] Y. Zhao, Y. Zheng, W. Zhou, J. Zhang, Q. Huang, W. Xiong, Effect of carbon addition on the densification behavior, microstructure evolution and mechanical properties of Ti (C, N)-based cermets, *Ceram. Int.* 42 (2016) 5487–5496, <https://doi.org/10.1016/j.ceramint.2015.12.097>.
- [29] M. Chen, Q. Zhuang, N. Lin, Y. He, Improvement in microstructure and mechanical properties of Ti (C, N)-Fe cermets with the carbon additions, *J. Alloys Compd.* 701 (2017) 408–415, <https://doi.org/10.1016/j.jallcom.2017.01.119>.
- [30] P. Alvaredo, C. Abajo, S.A. Tsipas, E. Gordo, Influence of heat treatment on the high temperature oxidation mechanisms of an Fe–TiCN cermet, *J. Alloys Compd.* 591 (2014) 72–79, <https://doi.org/10.1016/j.jallcom.2013.12.009>.
- [31] E. Chicardi, Y. Torres, M.J. Sayagués, V. Medri, C. Melandri, J.M. Córdoba, F.J. Gotor, Toughening of complete solid solution cermets by graphite addition, *Chem. Eng. J.* 267 (2015) 297–305, <https://doi.org/10.1016/j.cej.2015.01.022>.
- [32] P. Alvaredo, P. Bruna, D. Crespo, E. Gordo, Influence of carbon content on microstructure and properties of a steel matrix cermet, *Int. J. Refract. Met. Hard Mater.* 75 (2018) 78–84, <https://doi.org/10.1016/j.ijrmhm.2018.04.006>.

Chapter 5

Summary of main results

Chapter 5.

Summary of main results

As it has been detailed in *Chapter 2*, the goal of this work is to evaluate the small-scale mechanical properties of constitutive phases of different inorganic multiphase systems by means of the massive nanoindentation technique in conjunction with statistical analysis. The strategy to achieve it satisfactorily is based on following a three-step protocol:

- (i) Comprehensive microstructural characterization;
- (ii) Assessment of micromechanical properties of unidentified individual phases; and
- (iii) Tagging of all the mechanically distinct phases on the basis of physically-based correlations between microstructure features and small-scale properties that are experimentally determined.

In this section, the main results obtained in this investigation, within each of the above research stages, are summarized and discussed individually for each of the systems studied.

5.1 Microstructural characterization

5.1.1 Duplex stainless steel (Metal-Metal system)

Microstructural characterization of DSSs was conducted aiming to evaluate the characteristic size of each phase (grain size) as well as the influence of the processing route on the microstructural assemblage of the studied material. The former is critical for determining testing parameters to be used when implementing massive indentation, particularly penetration depth; and consequently, applied load and grid spacing. Regarding the latter, EBSD is recalled as a quite appropriated complementary tool for documenting and understanding changes in the grain size of the two constitutive phases after each processing step studied.

Figure 5.1 shows the phase map and its corresponding quality image (cropped region) attained for all DSS samples. The 150 nm step size was chosen to achieve high-resolution images. Obtained data were analyzed by the Channel 5 program, and the grain size of both austenitic and ferritic phases was measured by means of linear interception method, for all processing routes considered.

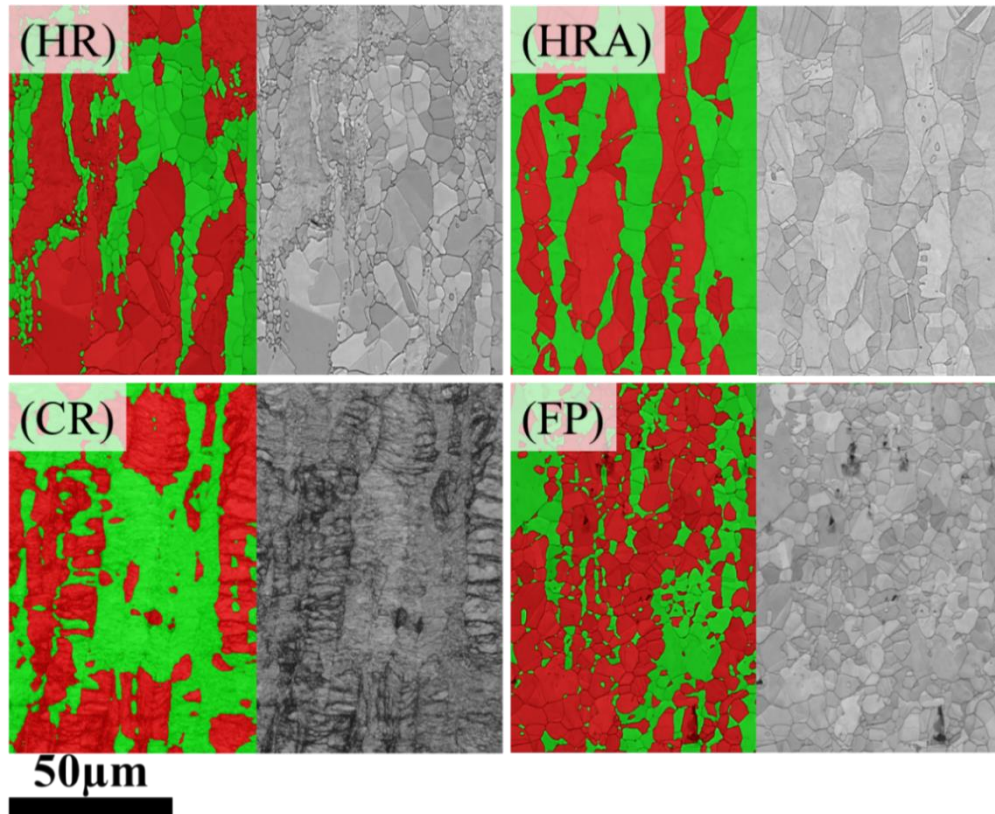


Figure 5.1. Phase map and corresponding quality images for studied DSS samples.

Experimental findings are plotted in **Figure 5.2**. The volume fractions of austenite and ferrite phases are shown in **Figure 5.2a** for all studied samples. The histogram of measured grain size for the HR sample is plotted in **Figure 5.2b**. It includes measurements of grain size for both phases since they were within the same range of values. Qualitative similar measurements were obtained for the other DSS samples. Histograms contain data measured on ~2000 grains and they were plotted with a constant bin size of 250 nm. As it is shown in **Figure 5.2b**, grains are distributed within three defined ranges: fine (less than 2 μm), medium (between 2 and 5 μm), and coarse (higher than 5 μm), illustrated with orange, green, and blue colors, respectively. **Figure 5.2c** displays surface fraction occupied by different grain size ranges of each phase for all the studied samples. From **Figures 5.2b** and **5.2c** it is clear that, although the number of medium and coarse grains are relatively small compared with fine-sized grains, the surface fraction occupied by the former is much higher (for both phases). A direct consequence of this experimental fact is that size of medium and coarse grains is indeed representative of the grain size of the DSS samples. Accordingly, the characteristic size of both constitutive phases (mean grain size) may be effectively assumed as higher than 2 μm ; and thus, the maximum penetration depth must be less than 200 nm ($h < D/10$). Presented results in **Figure 5.2** are proving that some processing routes (CR) may significantly affect the phase content and grain size distribution of the DSSs studied.

The influence of the processing route on the microstructure of DSS is documented and discussed in **Article I**.

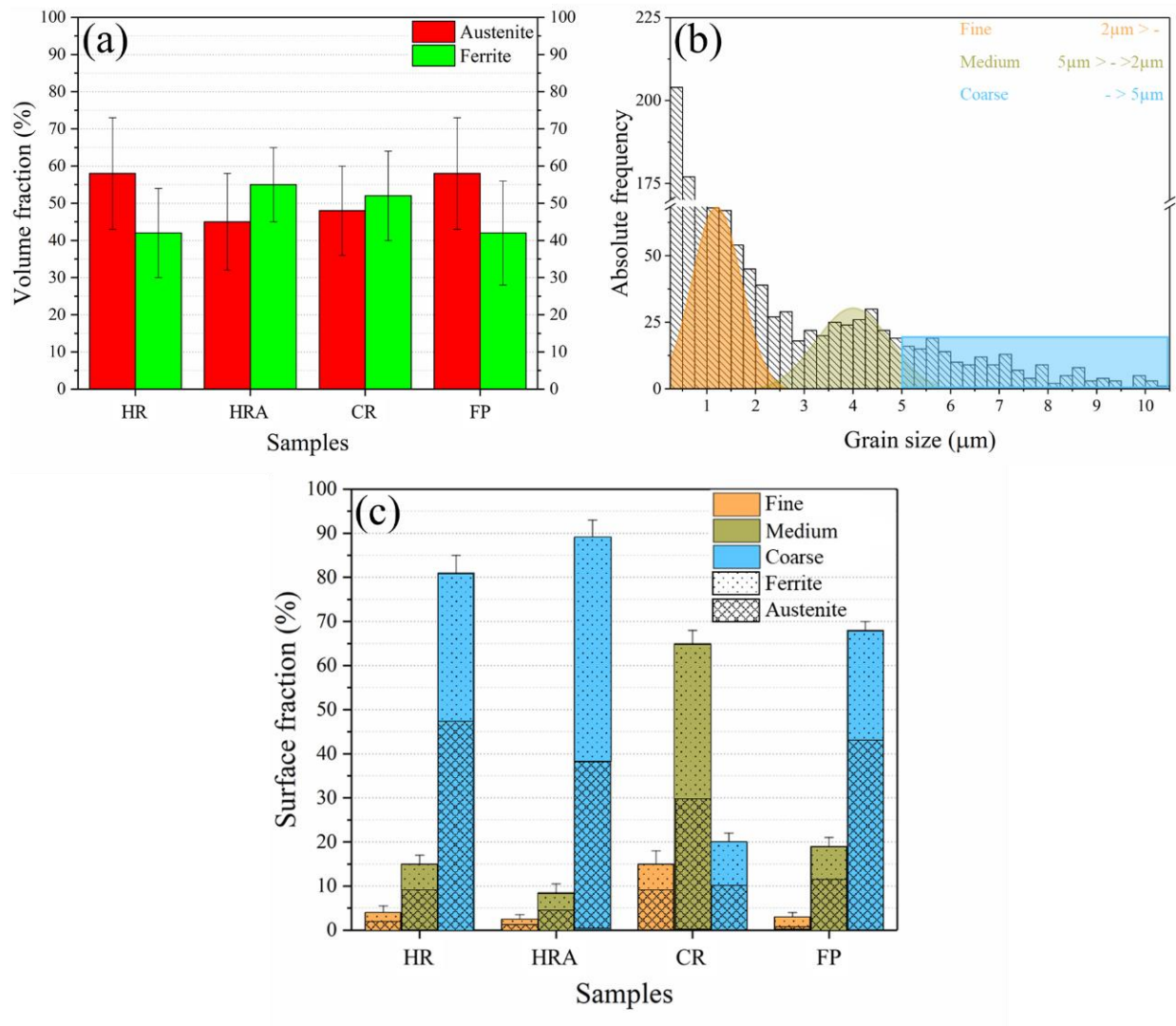


Figure 5.2. (a) Volume fractions of both constitutive phases for all the studied samples. (b) Grain size histogram for the HR sample, with 250 nm of bin size, computed from at least 2000 counted grains. (c) Surface fraction occupied by different grain size ranges of each phase for all the studied samples.

5.1.2 Polycrystalline cubic boron nitride composite (Ceramic-Ceramic system)

The microstructure of the ceramic-ceramic system studied material consists of cBN particles embedded in a TiN matrix. Within this context, the grain size of the cBN particles and the mean free path of the TiN binder (λ_{TiN}) represent the characteristic sizes of these materials.

Figure 5.3a displays the microstructure of the PcBN grade studied. The dark and light grey phases correspond to cBN particles and TiN binder respectively. Mean values of cBN particle size and length of TiN binder free path (**Figure 5.3b**) were determined to be 2.7 and 2.0 μm , respectively. They were measured by means of the linear interception method on 5 different micrographs obtained by FESEM. Accordingly, the maximum penetration depth for this material was defined to be $h_{max} \leq 200 \text{ nm}$, i.e. lower than 1/10 of the smaller characteristic length. This penetration depth guarantees that the plastic flow induced by residual imprint will be confined inside both phases.

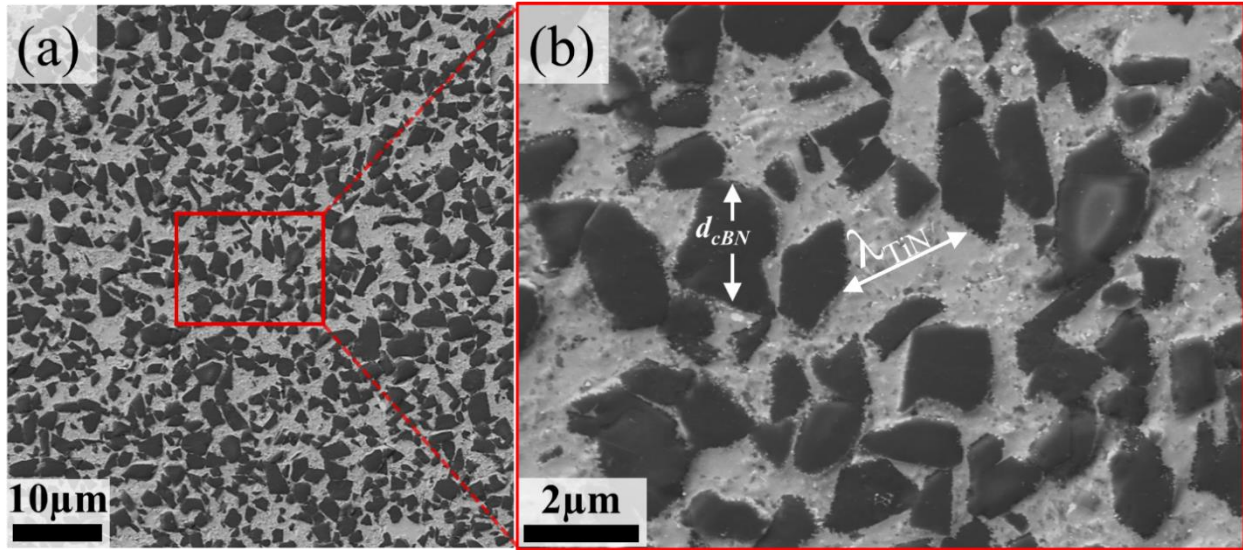


Figure 5.3. (a) FESEM micrograph of PcBN microstructure. (b) Magnified micrograph of the red marked region where microstructural parameters of PcBN composite are indicated.

5.1.3 Ti(C,N)-FeNi cermets (Ceramic-Metal system)

The main objective of the work conducted on Ti(C,N)-FeNi cermets included the evaluation of the influence of ceramic/metal phase ratio and carbon addition on microstructure and small-scale mechanical properties of the composite as well as of each of the constitutive phases. In this regard, the volume fraction of both phases, porosity, ceramic particle size and mean free path of the metallic binder (λ_{FeNi}) were assessed to accomplish the defined aims.

Figure 5.4 displays the microstructure of the studied samples. At least 5 images were taken in each case. The linear interception method was used to measure the size of the ceramic particles and the λ_{FeNi} . Meanwhile, picture analysis by means of ImageJ software was used to determine the area fraction of each phase and porosity. The obtained microstructural parameters of each studied sample are summarized in **Table 5.1**.

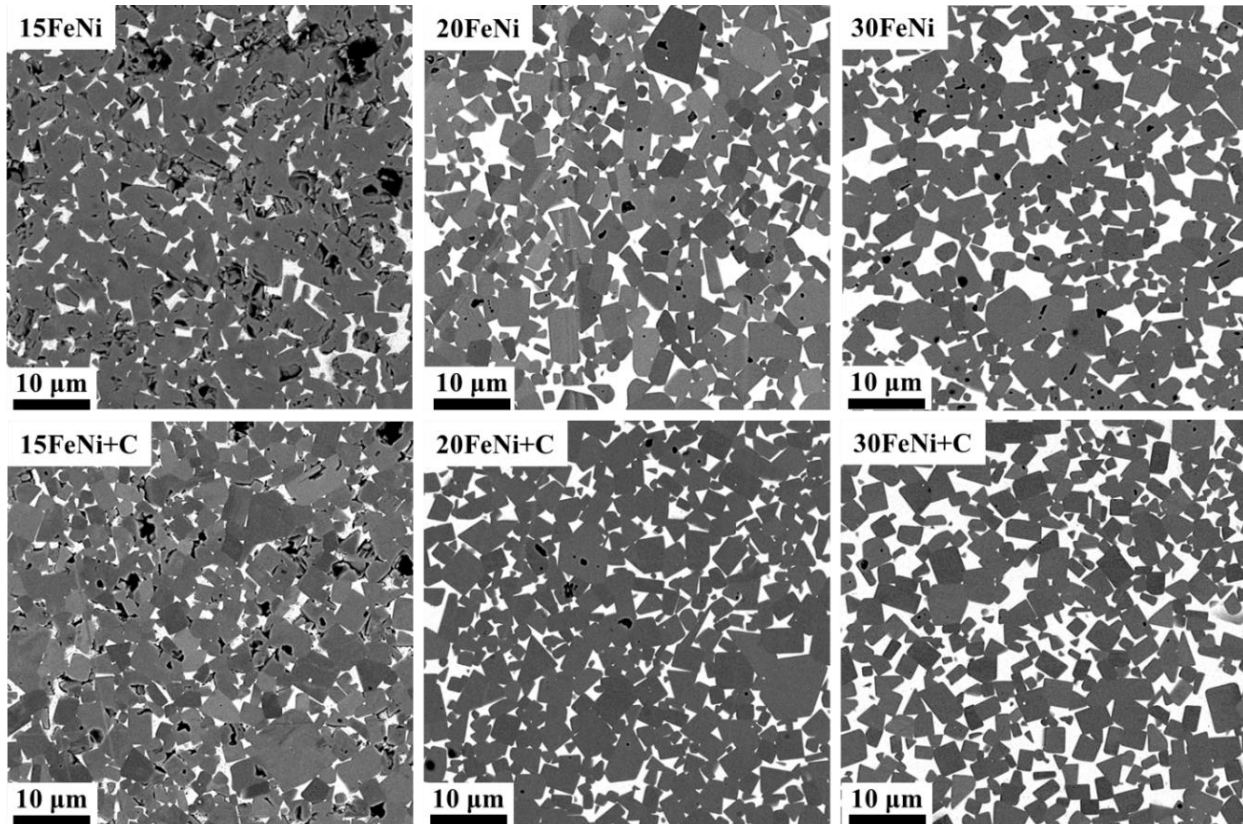


Figure 5.4. Micrographs of Ti(C,N)-FeNi cermets with different *vol. %* and carbon addition of the metallic binder.

Table 5.1. Microstructural parameters of studied cermets.

Sample	Ceramic/metal phase ratio	Carbon content (wt. %)	Porosity (vol. %)	Ti(C,N) mean grain size (μm)	λ_{FeNi} (μm)
15FeNi	85/15	0	2.7 ± 1.1	2.2 ± 0.3	0.5 ± 0.1
15FeNi+C	85/15	0.5	2.3 ± 0.2	2.3 ± 0.2	
20FeNi+C	80/20	0	0.5 ± 0.1	2.2 ± 0.3	0.6 ± 0.1
20FeNi+C	80/20	0.5	0.2 ± 0.1	2.2 ± 0.3	
30FeNi	70/30	0	0.8 ± 0.2	2.3 ± 0.3	1.0 ± 0.2
30FeNi+C	70/30	0.5	0.1 ± 0.1	2.3 ± 0.3	

It was found that the size of Ti(C,N) particles was similar, about $2.2 \mu\text{m}$, for all the specimens studied. Thus, it was concluded that ceramic/metal phase ratio and carbon addition did not modify the grain size of the ceramic particles, at least within the experimental ranges studied in this investigation. On the other hand, a higher volume fraction of metallic phase (higher λ_{FeNi}) yielded

a more homogeneous microstructure with lower porosity. A similar effect was induced by carbon addition, for a given ceramic/metal phase ratio. More information about these correlations can be found in **Article IV**.

Similar to the case of the PcBN composite, the size of the ceramic particles and the λ_{FeNi} (here metallic) are defined as the characteristic length parameters for cermet. In all the ceramic-metal systems investigated, the latter was smaller than the former; and thus, λ_{FeNi} should be considered as the representative characteristic size to determine the h_{max} . However, it would require h_{max} values (lower than 50 - 100 nm) for which ISE may not be disregarded, i.e. $h_{min} \geq 150$ nm (see *Chapter 1, Section 1.4*). Under these considerations, h_{max} was set at 200 nm, based on the mean grain size of the ceramic particles. Such compromising value implies that plastic flow induced by the indentation performed on the metallic binder could not be confined within the binder, and this interaction with the surrounded ceramic particles should be considered in the corresponding analysis (more information in *Section 5.2.3*).

5.2 Micromechanical characterization

Micromechanical properties measured by means of nanoindentation will be presented here. In the previous section, the appropriate penetration depth (h) values to evaluate the small-scale mechanical properties of the constitutive phases for each multiphase system were determined, on the basis of the microstructural characterization conducted. Consequently, indentation spacing was determined for performing the gedanken experiments.

As it was mentioned before (*Section 3.3.1*), in order to expedite the massive indentation process, tests were carried out using iNano[®] nanoindenter. However, it has to be taken into account that the NanoBlitz 3D technique implies tests performed under load control mode and quasi-static indentations. Hence, before conducting tests using the iNano[®] nanoindenter, some indentations were performed by means of the Nanoindenter XP, which could perform dynamic indentations under penetration control mode. This was done in order to assess the load needed for achieving the desired penetrations for different systems, as well as to obtain mechanical properties that could then be used to compare with the H and E determined out of quasi-static indentations.

Testing conditions and the corresponding goals for each test are summarized in **Tables 5.2** and **5.3** for Nanoindenter XP and iNano[®] indenter, respectively. The process and calculations to acquire these parameters for each multiphase system will be explained in detail in the following sections. Moreover, it has to be indicated that tests run using the nanoindenter XP sometimes stopped before reaching the aimed values, because such testing unit is limited to maximum applied load and maximum penetration depth values of 650 mN and 2000 nm, respectively.

Table 5.2. Testing conditions and achievements of each set of indentation tests performed by Nanoindenter XP.

System	h_{max} (nm)	AS per sample	IS (μm)	Achievements
DSS	200	1200	5	-Detect the related applied load of h_{max} - H and E of γ - and α - phases
	2000	16	50	Determining the h_{min}
PcBN	200	1400	5	- Detect the related applied load of h_{max} - H and E of cBN grains and TiN binder
	2000	16	50	Determining the h_{min}
Cermet	200	2000	5	- Detect the related applied load of h_{max} - H and E of Ti(C,N) particles and FeNi binder
	2000	16	50	-Determining the h_{min} - H and E of Ti(C,N)-FeNi system

AS (Array size): The number of indentations performed on each sample.

h_{max} : Maximum penetration depth.

IS: Space between each imprint.

Table 5.3. Testing conditions and achievements of each set of indentation tests performed by iNano[®] nanoindenter.

System	AS per sample	P_{max} (mN)	IS (μm)	Achievements
DSS	10,000	4	2	H and E of γ - and α - phases
PcBN	12,500	10-25	2-3	H and E of cBN grains and TiN binder
Cermet	40,000	10	1.5-2	H and E of Ti(C,N) particles and FeNi binder

AS (Array size): The number of indentations performed on each sample.

P_{max} : Maximum applied load.

IS: Space between each imprint.

5.2.1 Duplex stainless steel (Metal-Metal system)

Prior to performing the test by iNano[®] nanoindenter, two sets of tests were conducted using Nanoindenter XP, at 2000 and 200 nm, in order to determine the h_{min} and corresponding load for h_{max} , respectively. On the one hand, **Figure 5.5** shows the obtained h_{min} by plotting P/S^2 against the penetration depth. On the other hand, performed indentations at 200 nm illustrated that the corresponding load (P_{max}) to reach the desired penetration depth is around 4 mN. **Figure 5.6** displays the obtained h_{max} in different phases by fixing the P_{max} at 4 mN. Therefore, for the massive indentation tests performed at 4 mN on DSS samples, the penetration depth (h_{final}) was kept in the appropriate range for all the constitutive phases. i.e. $h_{min} < h_{final} < h_{max}$.

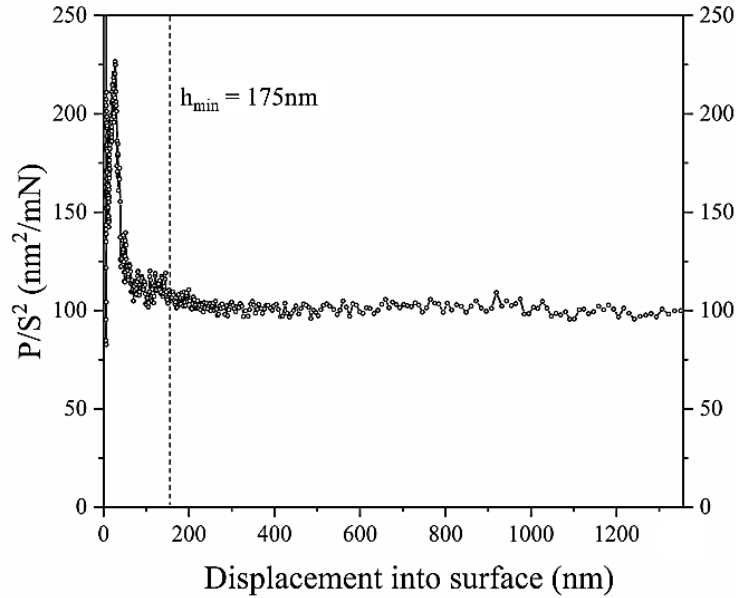


Figure 5.5. P/S^2 ratio versus penetration depth for indentations on CR DSS sample.

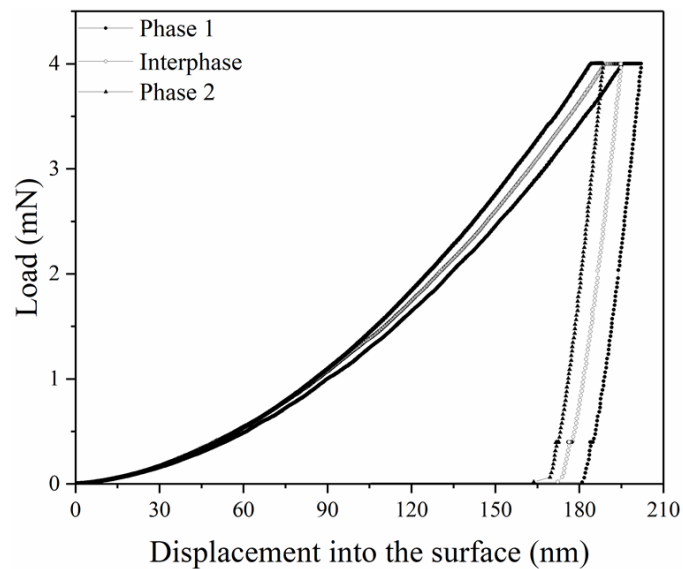


Figure 5.6. P - h curves, obtained from different imprints performed on different phases, performed at 4 mN.

Figure 5.7 displays a phase map of an indented area, conducted on CR sample. There it can be seen that most of the imprints were totally confined inside individual phases. However, it is also evidenced that there is another group of imprints that are probing both austenitic and ferritic phases. The fact that plastic flow induced by these imprints interact with both phases would imply that obtained mechanical properties represent those of a composite-like behavior. Hence, statistical analysis of the data gathered out of the massive indentation tests requires consideration of three mechanically distinct phases.

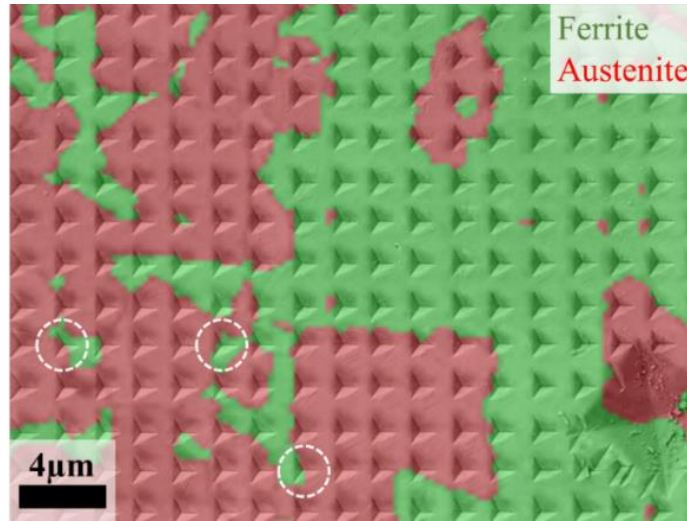


Figure 5.7. Phase map of an indented area in a DSS sample.

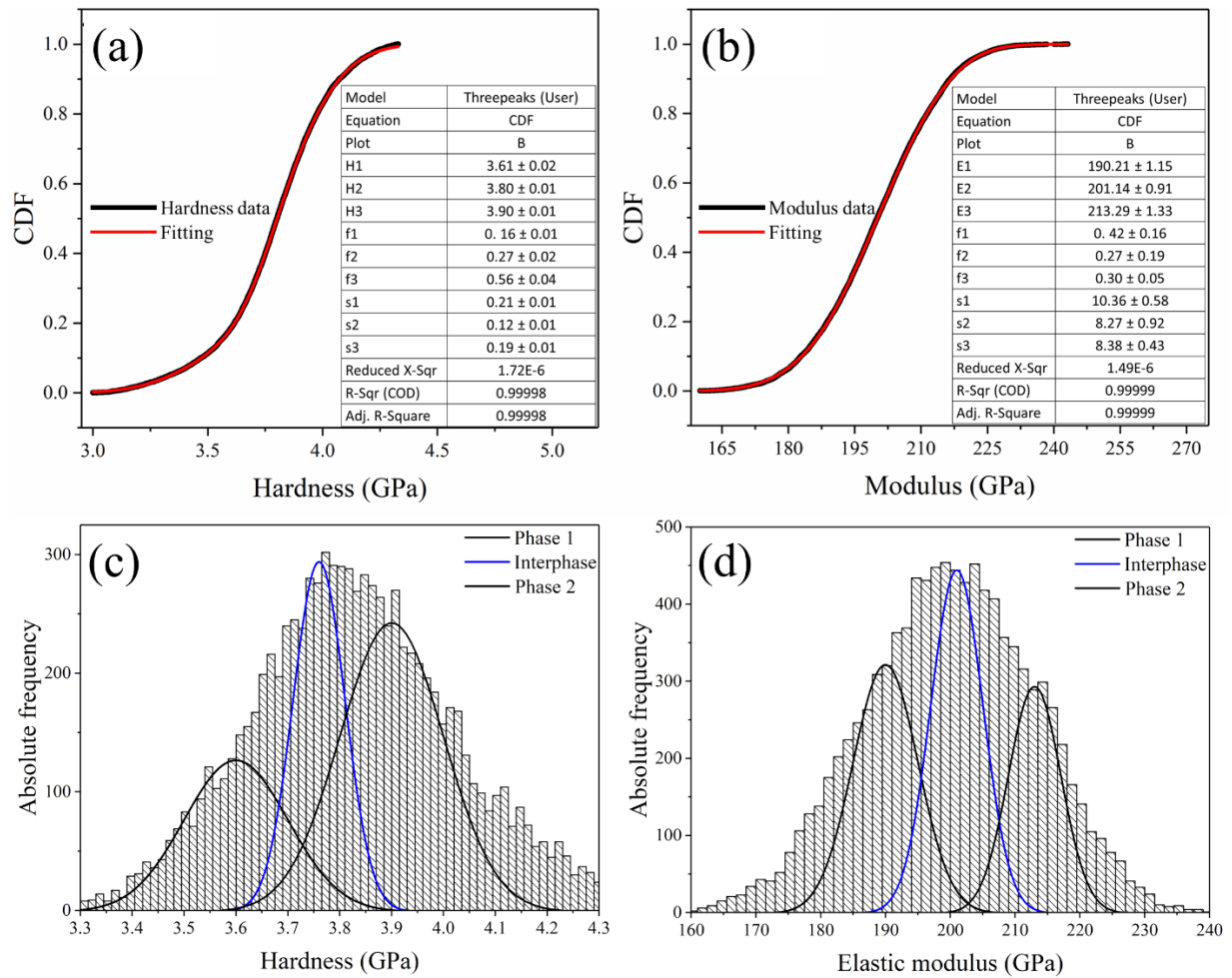


Figure 5.8. (a) and (b) CDF fittings for obtained experimental H and E of the HR DSS sample, respectively. (c) and (d) Fitted Gaussian distributions (obtained from CDF plot) on hardness and elastic modulus histogram, respectively.

Following the above ideas, the obtained massive indentation data (H and E) were statistically analyzed by the methodology proposed by Ulm and co-workers [10,181,182,190]. **Figures 5.8a** and **5.8b** show best-fit *CDFs* of H and E values, using the sigmoid shape error function. By doing so, the mean H and E values of each constitutive phase (p_i) and their corresponding standard deviation (σ_i) were determined (see the fitting information in the insets presented in **Figures 5.8a** and **5.8b**, wherein “s” values demonstrate the standard deviation).

By assessing p_i and σ_i for each phase, three different density functions (Gaussian distributions) could be fitted on each H and E histogram (**Figures 5.8c** and **5.8d**). Qualitative similar measurements were obtained for other studied DSS samples (not presented here). The acquired results are summarized in **Table 5.4**. As can be seen, the obtained H and E values for each phase are relatively close and barely distinguishable. Meanwhile, it is well known that the content of individual elements can modify the microstructure and micromechanical properties of DSS. For instance, N and C content as solid solution strengthening agents may affect the strength of the austenitic phase [29,150–152]. Accordingly, it is not straightforward to define austenite or ferrite as the hardest or stiffest phase. Aiming to solve this issue, the obtained mechanical properties of the unidentified phases were correlated with the microstructure of the studied samples by means of advanced characterization techniques (see *Section 5.3.1*). Nevertheless, the effect of the processing route could be evaluated at this stage, regardless of the fact that attained local mechanical properties (of γ - and α - phases) are still unidentified for the studied samples. In this regard, preliminary results point out that the cold working process increased the small-scale properties of both austenite and ferrite phases. By correlating the microstructural (*Section 5.1.1*) and micromechanical results, it can be derived that the influence of the cold work process on mechanical response is related to work hardening and deformation texture effects [215,216].

Table 5.4. Summary of H and E values of the unidentified phases in each processing condition of DSS, determined from statistical analysis.

Sample	Hardness, H (GPa)			Elastic modulus, E (GPa)		
	Phase 1	Interphase	Phase 2	Phase 1	Interphase	Phase 2
HR	3.6 ± 0.2	3.8 ± 0.1	3.9 ± 0.2	190 ± 10	201 ± 8	213 ± 8
HRA	3.5 ± 0.2	3.7 ± 0.1	3.9 ± 0.2	189 ± 15	200 ± 10	212 ± 10
CR	4.9 ± 0.2	5.2 ± 0.2	5.6 ± 0.2	208 ± 15	220 ± 10	240 ± 8
FP	3.7 ± 0.2	3.9 ± 0.2	4.2 ± 0.2	190 ± 10	202 ± 7	215 ± 10

5.2.2 Polycrystalline cubic boron nitride composite (Ceramic-Ceramic system)

Similar to DSS samples, maximum applied load and h_{min} were calculated by performing nanoindentations at 200 and 2000 nm, respectively, using nanoindenter XP. Obtained results pointed out that, performed indentation at the maximum applied load within a range of 10 - 25 mN reached the adequate penetration depth where $h_{min} < h_{final} < h_{max}$.

Figure 5.9 depicts a FESEM micrograph of a cropped region of an indented area on the PcBN sample. Three different types of imprints, in terms of the probed phase, are evidenced. Blue and red circles highlight imprints performed on TiN binder and cBN grains, respectively. Moreover, green circles correspond to imprints in which the induced plastic flow interact with both cBN and TiN phases. **Figures 5.9c** and **5.9e** show cross-section views of residual imprints performed on a cBN grain and TiN binder. They demonstrate that estimated plastic flow underneath the residual imprints is confined within each phase. As a final result, three mechanically distinct phases were identified for further consideration in the subsequent statistical analysis.

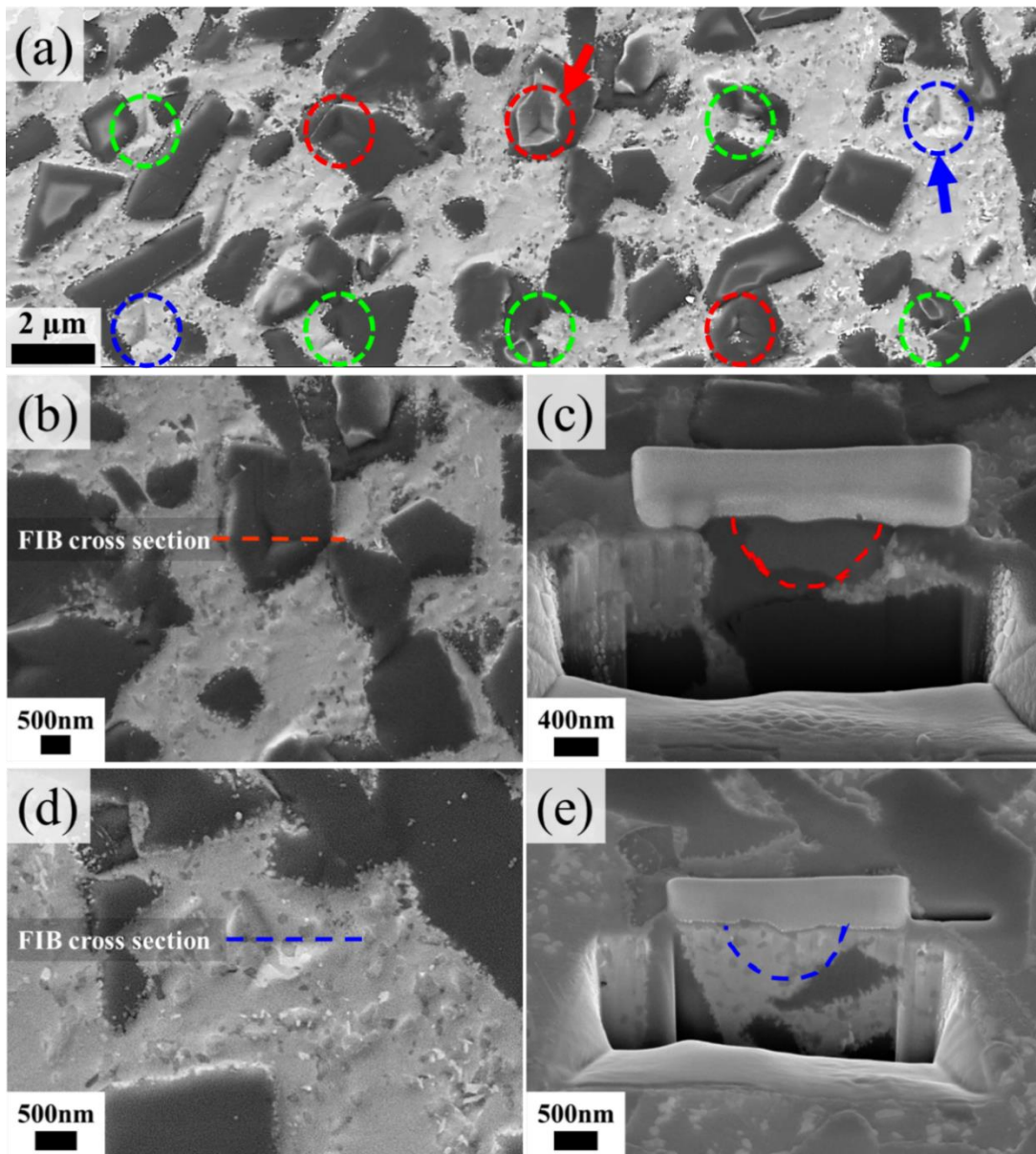


Figure 5.9. (a) FESEM micrograph of performed imprints on different phases of PcBN composite. (b),(d) Residual imprints performed on cBN and TiN binder, respectively. (c) and (d) cross-section view of figures (b) and (d), respectively, in which the estimated plastic flows for both phases are shown.

After implementing the statistical analysis on high-speed nanoindentation data (similar process as explained in the previous section, **Figures 5.8a** and **5.8b**), three mechanically distinct phases were fitted on the hardness histogram (with a constant bin size fixed at 1.85 GPa). There, cBN particles show the highest values around 50 GPa, whereas TiN binder displays a mean value close to 22 GPa. An intermediate peak – at values around 35 GPa – was considered as the response of a composite-like region, i.e. one combining both cBN and TiN phases (**Figure 5.10a**). Assessed mechanical properties for different phases are in excellent agreement with those measured from individual dynamic indentations, performed at 200 nm on each phase by means of Nanoindenter XP. Moreover, **Figure 5.10b** shows the hardness evolution of the different phases against the penetration depth. It proves that hardness reaches a constant value, in all the cases, after 100 nm. This sustains the statement that measured hardness values are not affected by ISE after 100 nm. Intrinsic hardness measured for each constative phase of the PcBN composite are summarized in **Table 5.5**.

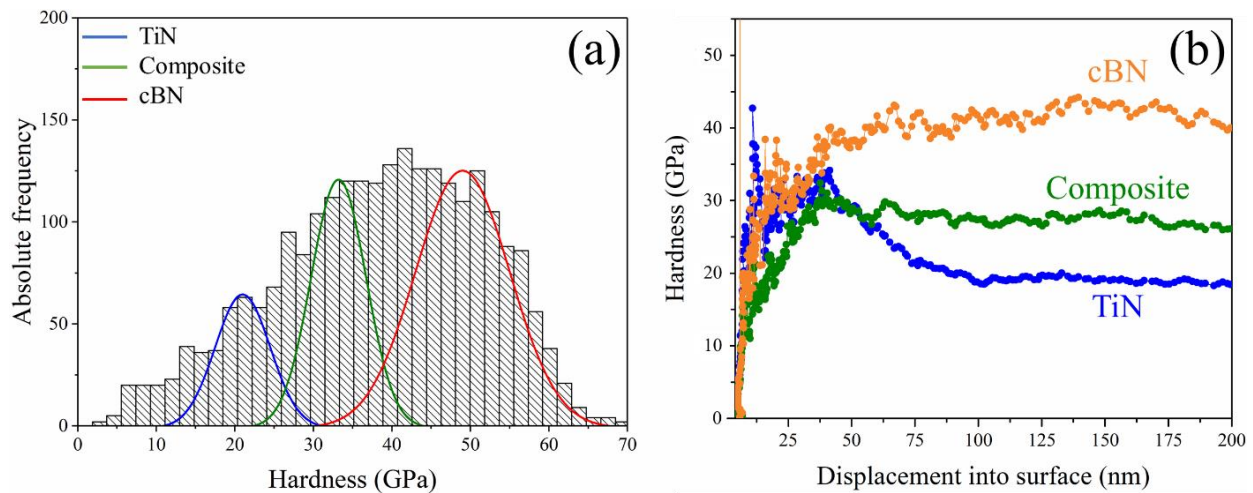


Figure 5.10. (a) Hardness histogram with a constant bin size of 1.8 GPa computed from imprints performed by high-speed indentation technique. (b) Hardness evolution against displacement into surface, obtained from dynamic indentations performed on different phases.

Table 5.5. Hardness values for each mechanically distinct phase of PcBN composite, obtained from statistical analysis.

Phase	TiN binder	Composite	cBN
Hardness (GPa)	21 ± 5	33 ± 5	49 ± 7

Considering the fact that the probability density function is dependent on the bin size [217], the hardness histogram (of the same results) was plotted with a smaller bin size, fixed at 1 GPa. By doing so, two additional peaks are identified in the obtained histogram (grey filled areas around the red Gaussian distribution curves in **Figure 5.11**). Accordingly, it could be claimed that statistical analysis of experimental data could be better fitted by considering two additional

populations, corresponding to harder and softer (with respect to the original main peak) cBN particles. Such a finding may be related to variations of chemical composition within cBN particles. This hypothesis might be assessed and rationalized by means of advanced characterization techniques (more information in *Section 5.3.2*).

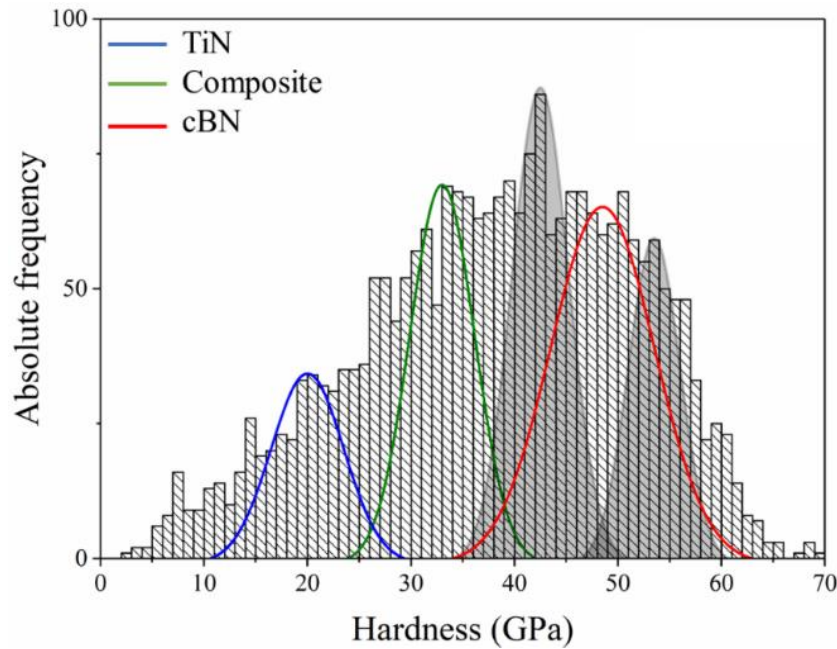


Figure 5.11. Hardness histogram obtained from the same data as shown in **Figure 5.10**, plotted with a constant bin size of 1 GPa.

5.2.3 Ti(C,N)-FeNi cermets (Ceramic-Metal system)

Similar to the cases of DSSs and PcBN composite, aiming to assess the applied load value required for reaching the appropriate penetration depth in the cermets under consideration, two sets of indentation tests at 2000 and 200 nm were performed on studied samples using nanoindenter XP. As a result, it was found that the maximum applied load was about 10 mN for the ceramic-metal system studied.

Moreover, performed imprints at 2000 nm penetration depth could provide information about the influence of ceramic/metal phase ratio and carbon addition on hardness and elastic modulus of the composite systems. As it can be seen in **Figures 5.12a** and **5.12c**, the residual imprints are probing both ceramic particles and metallic binder on the surface. Some fracture mechanisms are activated on the surface during the indentation process (mainly within ceramic particles), as highlighted by the white arrows in **Figure 5.12b**. Similar fracture mechanisms were detected underneath the residual imprint, as indicated by the white arrows in the cross-section view of the imprints shown in **Figure 5.12d**. It can elucidate how the plastic flow interact with each phase at both surface and subsurface levels.

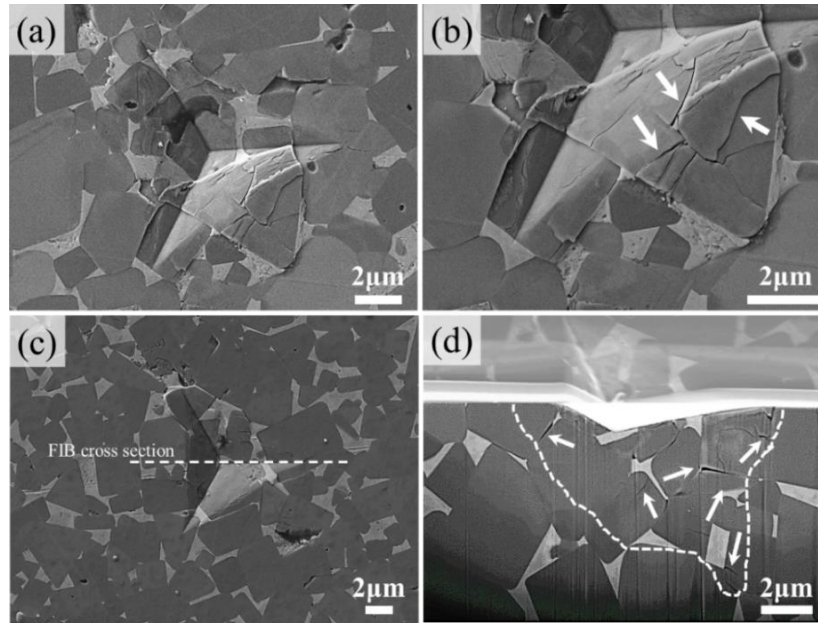


Figure 5.12. (a) and (c) FESEM micrographs of residual imprints performed at 2000 nm. (b) Magnified image of residual imprint shown in (a). (d) FIB-milled cross-section of residual imprint shown in (c), under the region of interest indicated by the white dash line.

Hardness and elastic modulus evolution against the penetration depth for all studied samples are shown in **Figure 5.13**. It can be seen that both composite hardness and elastic modulus of cermets are inversely related to the ceramic/metal phase ratio. Moreover, it is discerned that carbon addition has a direct relationship with hardness and elastic modulus of the studied cermets. The influence of carbon addition is more evident for samples with higher metallic binder content. Such a finding was expected as carbon addition is expected to promote hardening of the metallic binder. Similar trends were observed in the results attained from Vickers hardness tests performed at 10 and 30 kgf. All these experimental results are summarized in **Table 5.6**.

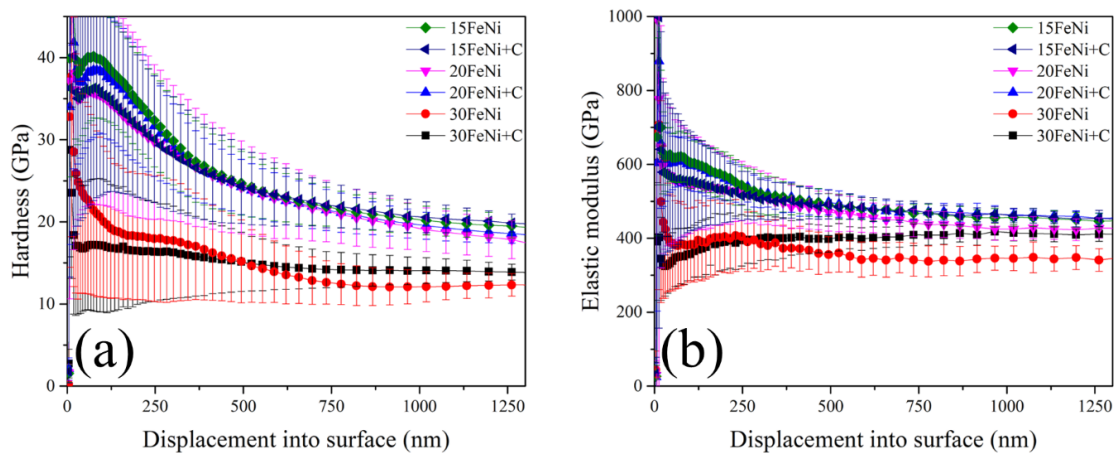


Figure 5.13. (a) Hardness and (b) Elastic modulus evolution against penetration depth for all the investigated cermets.

Table 5.6. Mechanical properties data assessed at different length scales for the studied Ti(C,N)–FeNi composites.

Sample	Nanoindentation data, performed by Berkovich indenter at 650 mN applied load or 2000 nm depth		<i>HV</i> 10 (GPa)	<i>HV</i> 30 (GPa)
	Hardness, <i>H</i> (GPa)	Elastic modulus, <i>E</i> (GPa)		
15FeNi	20.2 ± 2.0	455 ± 20	13.0 ± 0.4	12.8 ± 0.1
15FeNi+C	20.3 ± 2.0	459 ± 15	13.3 ± 0.3	13 ± 0.1
20FeNi	18.5 ± 2.0	420 ± 18	11.3 ± 0.3	11.0 ± 0.1
20FeNi+C	19.5 ± 1.5	460 ± 14	12.2 ± 0.2	11.7 ± 0.1
30FeNi	12.3 ± 1.5	346 ± 22	9.5 ± 0.4	9.1 ± 0.2
30FeNi+C	14.5 ± 0.5	414 ± 15	10.5 ± 0.2	9.9 ± 0.2

The influence of ceramic/metal phase ratio and carbon addition on the small-scale properties of each constitutive phase of studied cermets was attempted by performing nanoindentations at smaller penetration depths, where the plastic flow could be confined within each phase. In this regard, 40,000 indentations were performed at 10 mN of maximum applied load using the high-speed nanoindentation technique. Afterwards, obtained experimental data were statistically analyzed by implementing the methodology proposed by Ulm and co-workers (similar to analyses done for the other multiphase systems).

Figure 5.14a displays an example of the indented surface of a cermet sample. Since the applied load is constant, imprints performed on the softer phase penetrates more (reaching a higher depth) than the ones probing the harder one. Therefore, as can be seen in **Figure 5.14a** the residual imprints in the metallic binder (blue circle) are bigger/deeper than the ones performed on Ti(C,N) particles (red circles) and/or regions containing interphase boundaries (green circles). **Figure 5.14b** shows a hardness histogram with a constant bin size of 0.5 GPa. Three Gaussian distributions are fitted on the experimental results. The smallest and highest peaks (blue and red), with mean values around 12 and 27 GPa, are related to the metallic binder and the Ti(C,N) phase, respectively. The intermediate peak (green) with a mean value close to 19 GPa represents the mechanical response of the combined interaction of the hard ceramic and the soft metallic phases. Same mechanical property histograms were obtained for all studied samples and extracted hardness values for each individual phase are summarized in **Table 5.7**.

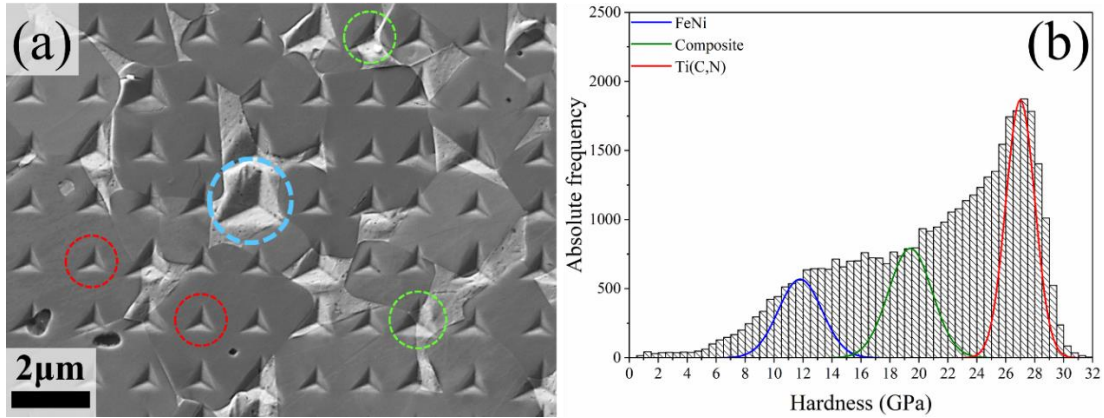


Figure 5.14. (a) SEM micrograph of a cropped region of the indented area on a cermet sample. (b) Hardness histogram of 15FeNi+C samples with a constant bin size of 0.5 GPa and fitted Gaussian distribution, corresponding to the mechanical properties of each phase.

Table 5.7. Hardness mean values for each phase of the investigated samples, obtained through statistical analysis.

Sample	Hardness (GPa)		
	FeNi	Composite	Ti(C,N)
15FeNi	13.7 ± 0.3	20.4 ± 0.2	26.8 ± 0.2
15FeNi+C	14.1 ± 0.3	21.5 ± 0.2	26.9 ± 0.2
20FeNi	11.7 ± 0.2	19.1 ± 0.2	26.7 ± 0.2
20FeNi+C	12.5 ± 0.2	19.6 ± 0.1	26.9 ± 0.2
30FeNi	8.3 ± 0.3	15.0 ± 0.3	26.6 ± 0.3
30FeNi+C	9.6 ± 0.2	17.1 ± 0.2	26.7 ± 0.3

Considering the extracted mechanical properties of each phase reported in **Table 5.7**, the first noticeable point is that intrinsic hardness of Ti(C,N) particles remain constant, in spite of microstructure, ceramic/metal phase ratio, and/or carbon addition. Meanwhile, the small-scale hardness of metallic binder and composite hardness rise with increasing ceramic/metal phase ratio. This can be rationalized by the direct influence of a higher ceramic contribution on load-bearing capability (for lower binder content). Moreover, it might also be indirectly related to the higher constraint on the effective deformation of the metallic binder (smaller binder mean free path). Regarding the influence of carbon, it is discerned that the addition of this element enhances the hardness of the metallic binder for a given ceramic/metal phase ratio. As a consequence, the composite hardness value is also positively affected by carbon addition.

As it was commented in *Section 5.3.1*, for the penetration depth defined in this study for the cermets under consideration, the plastic flow induced by the indentation performed on the metallic binder (at 4 mN) is also affected by the interaction with the surrounding ceramic particles. Therefore, the intrinsic hardness for the metallic binder directly extracted by statistical analysis may be overestimated. This must be related to the constraining effect of the ceramic phase over the metallic one. In this regard, in order to assess more rational hardness values for the constrained

metallic binder, a thin-film model might be implemented on the obtained data. The implementation of a thin-film model is expected to yield reasonable values of hardness as the lateral stiffness is considered low in comparison to the normal stiffness, due to the large opening angle of the Berkovich tip. Within this context Korsunsky *et al.*'s method [218] was implemented, to deconvolute the hardness of the metallic binder which were considered as a thin-film, using **Equation 5.1**:

$$H_c = H_s + \frac{(H_f - H_s)}{1 + k_k \left(\frac{h}{t}\right)^2}; k_k > 0 \quad \text{Equation 5.1}$$

where H_c , H_s and H_f are the hardness of composite, substrate, and film, respectively; h/t is the relative indentation depth, and k_k is a fitting parameter of film thickness. Deconvoluted hardness values for the metallic binder for different samples are summarized in **Table 5.8**.

Table 5.8. Corrected hardness values of metallic binder assessed by thin-film method (Korsunsky *et al.* [218]).

Sample	Corrected hardness values of metallic binder (GPa)
15FeNi	10.6 ± 0.2
15FeNi+C	10.9 ± 0.1
20FeNi	9.2 ± 0.1
20FeNi+C	9.8 ± 0.2
30FeNi	7.3 ± 0.1
30FeNi+C	8.5 ± 0.1

5.3 Correlation between microstructure and micromechanical properties

Depending on the studied multiphase materials and related objectives, correlating the unidentified mechanical properties (extracted from statistical analysis) with the microstructure of the multiphase systems could be either intricate (as in the case of the investigated DSS and PcBN composite) or rather simple (as the case of studied cermets). In this section, different techniques are implemented to shed light on the effective linking between the individual (mechanically distinct) phases and their small-scale mechanical properties for each of the multiphase systems under consideration.

5.3.1 Duplex stainless steel (Metal-Metal system)

As discussed in *Section 5.2.1*, three mechanically distinct peaks were extracted from statistical analysis (**Figure 5.8**). It was explained that the intermediate peak should be linked to the mechanical response of regions containing austenite/ferrite interphase boundaries. However, clear identification of local properties for the two remaining unidentified phases requires the use of

complementary advanced characterization techniques. For the DSSs under consideration, it may be attempted through a correlation between phase maps obtained by means of the EBSD technique (as those shown in **Figure 5.15**) with cartography maps of different mechanical parameters: H , E , and H/E (obtained from massive indentation technique).

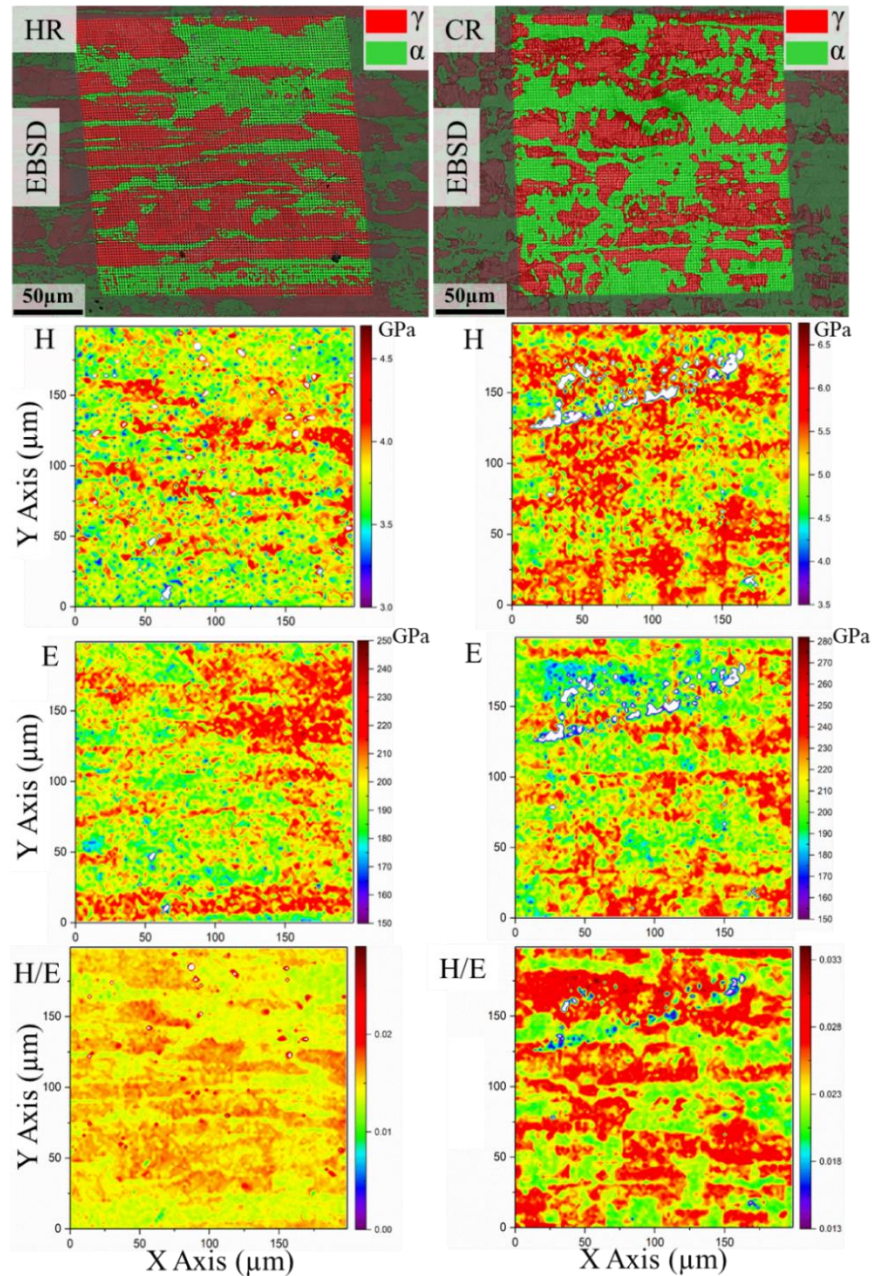


Figure 5.15. EBSD maps of indented surfaces and corresponding mechanical cartography maps of the indicated region for HR and CR samples.

Austenite (red) and ferrite (green) phases can be clearly distinguished in the obtained EBSD maps shown in **Figure 5.15**. Meanwhile, three tones of red, green and yellow can be observed in all

obtained mechanical cartography maps. By visualizing the H and E maps in **Figure 5.15**, the boundaries between austenite and ferrite can be falteringly distinguished. On the other hand, the H/E ratio map yields an excellent disparity (contrast) between both phases (especially for the CR sample). Furthermore, from H and E cartography maps it may be discerned that there is an inverse relationship between obtained hardness and modulus for each individual phase (harder phase has lower elastic modulus and vice versa). Therefore, it can be derived that although H and E represent different mechanical phenomena, H and E values are interrelated in such a way that the corresponding H/E ratio for each phase reveals more reliable and comparable values. As a result, it may be stated that the H/E ratio is a better discriminating parameter to identify the correlation between individual phases and their small-scale properties for DSSs. In this regard, it is found that the austenitic phase exhibits a higher plasticity ratio compared with the ferritic one.

Attempting to sustain the above-mentioned ideas, a novel data analysis is suggested wherein a $2D$ histogram graph manifest obtained H and E values simultaneously. **Figure 5.16** displays the proposed $2D$ histogram for HR and CR samples. The color of each pixel represents the number of indentations that are included within a range of H and E , which is defined as a $2D$ bin size. Thus, warm color tones indicate the accumulation of data related to each phase. As can be seen in **Figure 5.16**, two populations can be distinguished in both $2D$ histograms of HR and CR samples. Although the same analysis has been done for all studied samples, the CR sample will be discussed here due to the better visualization of its $2D$ histogram. In this regard, two clusters of data can be easily distinguished in the case of the CR sample: one peak with hardness ~ 5.5 GPa and modulus $E \sim 210$ GPa ($H/E = 0.026$) and another one with $H \sim 5.0$ GPa and $E \sim 240$ GPa ($H/E = 0.021$). It has already been discussed that the austenitic phase has higher H/E than the ferritic one. Accordingly, the unidentified hardness and elastic modulus values can be linked with austenite and ferrite. **Figure 5.17** is the updated version of **Figures 5.8c** and **5.8d**, in which the extracted mechanical peaks are associated with γ - and α - phases. **Table 5.9** summarizes the extracted mechanical properties for austenitic and ferritic phases for all the DSS samples studied.

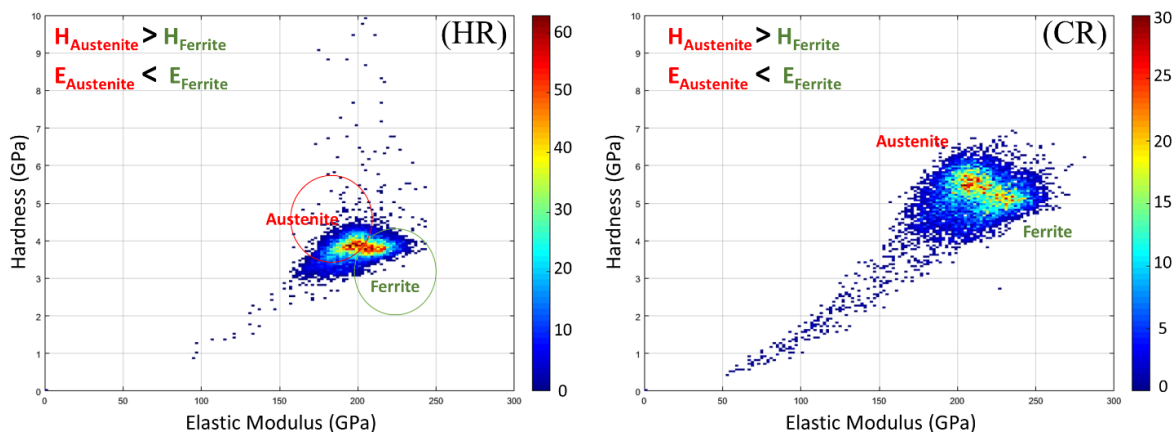


Figure 5.16. $2D$ histograms of Hardness (y-axis) vs Elastic Modulus (x-axis) acquired from 10,000 indentations on each HR and CR sample.

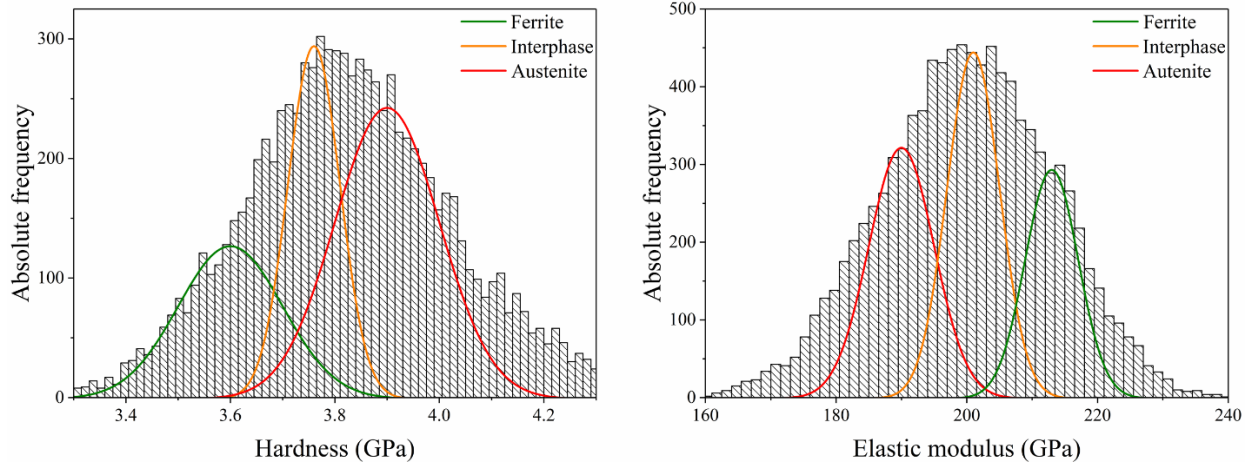


Figure 5.17. Final hardness and elastic modulus histogram of HR sample.

Table 5.9. Summary of hardness and elastic modulus values for defined phases of studied duplex steels computed by statistical analysis.

Sample	Hardness (GPa)			Elastic modulus (GPa)		
	Ferrite	Interphase	Austenite	Ferrite	Interphase	Austenite
HR	3.6 ± 0.2	3.75 ± 0.1	3.9 ± 0.2	213 ± 8	201 ± 8	190 ± 10
HRA	3.5 ± 0.2	3.7 ± 0.1	3.9 ± 0.2	212 ± 10	200 ± 10	189 ± 15
CR	4.9 ± 0.2	5.2 ± 0.2	5.6 ± 0.2	240 ± 8	220 ± 10	208 ± 15
FP	3.7 ± 0.2	3.9 ± 0.2	4.2 ± 0.2	215 ± 10	202 ± 7	190 ± 10

As it was explained before, the cold working process raises the hardness and elastic modulus of both austenite and ferrite. Hardness changes may be associated with finer grains and higher density of dislocations caused by this condition which leads to work hardening [215,216]. For elastic modulus, deformation texture effects might cause the difference. However, further study is required for a deeper understanding of these correlations. Both phases (γ - and α -) exhibited quite similar values for the mechanical properties studied, for the other processing conditions. The influence of processing route on micromechanical properties of each phase within DSS samples has been discussed in detail in **Article I**.

5.3.2 Polycrystalline cubic boron nitride composite (Ceramic-Ceramic system)

As it was presented in *Section 5.2.2*, assessment of local mechanical properties of TiN binder and cBN particles was already accomplished. However, the histogram plotted with a smaller bin size yielded two additional mechanically distinct phases around the cBN peak (**Figure 5.11**). In this

regard, a hypothesis was postulated by recalling non-stoichiometry effects (different B/N ratio) on the measured H for cBN particles. This idea emerged on the basis of the investigation reported by Sachdev [219], in which it was stated that morphology and residual stresses of cBN crystals may be directly related to impurity effects as well as different N and B contents within the cBN particle. Therefore, such a hypothesis was addressed and details are given in this section.

First of all, the distinct mechanical response exhibited by two different groups of cBN particles was validated through the hardness cartography map resulting from nanoindentation testing of the PcBN composite investigated. As it is depicted in **Figure 5.18**, blue and green shades correspond to TiN binder and composite phases respectively, while tones of warm colors are linked to cBN particles. The latter exhibits a wide range of hardness values, with deviations as high as 20 GPa. Therefore, the two unidentified peaks must be related to cBN phase since the hardness mean values of those peaks (grey peaks in **Figure 5.11**) are within the hardness range of cBN determined by the hardness cartography map.

Aiming to get further and more detailed information, EPMA was used as a complementary advanced characterization technique. The analysis was done on a marked region of the PcBN sample to determine local chemical composition, specifically N and B content in cBN particles. **Figure 5.19** displays the outcomes of the EPMA analysis. In such a figure, cBN particles may be classified in three different groups, depending upon relative B/N content in atomic % (at. %): stoichiometric (50/50), and non-stoichiometric, which are marked in **Figure 5.19a** by red and yellow lines. **Figures 5.19b** and **5.19c** show N-rich (N at. % content higher than 75,) and N-poor (N at. % content lower than 25) particles, respectively.

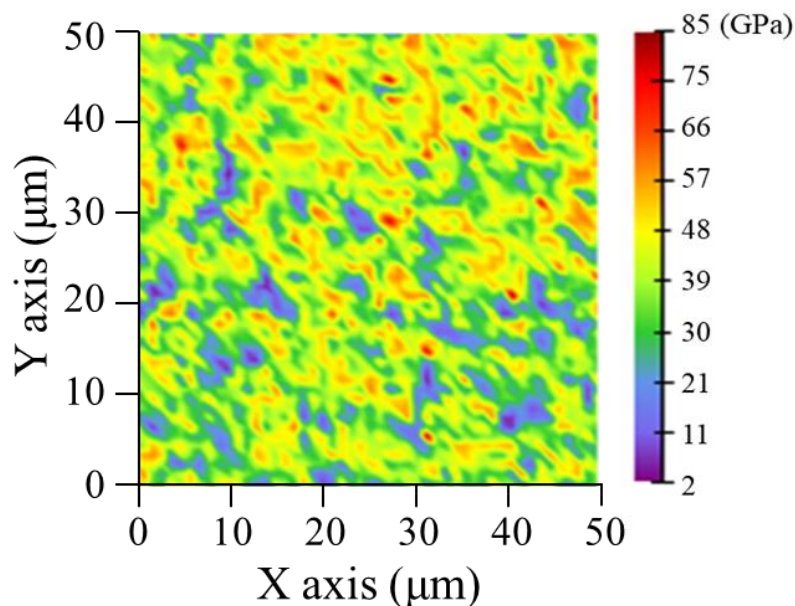


Figure 5.18. Hardness cartography map of PcBN composite obtained from nanoindentations performed at 25 mN.

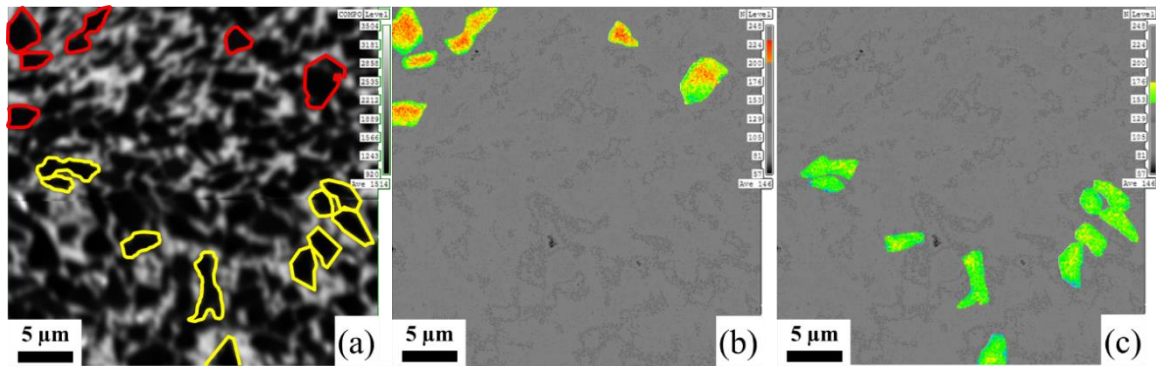


Figure 5.19. EPMA analysis performed on PcBN sample: (a) SEM micrograph of the analyzed region, (b) N map for high N grains marked by red lines in SEM image, and (c) N map for low N grains marked by yellow lines in the SEM image.

Subsequently, an array of indentation was performed on the mentioned region to determine the possible correlation between the small-scale hardness of individual cBN grains and its corresponding B/N ratio. Three grids of indentation matrices were performed (on different regions) under displacement control mode, while maximum penetration was fixed at 200 nm. This would guarantee that plastic flow will be confined within the cBN grains. **Figure 5.20a** shows a FESEM micrograph of the performed matrix of indentations, while **Figure 5.20b** displays the N map of the corresponding zone, as assessed by EPMA. Positions of individual imprints are marked and numbered in both FESEM and EPMA maps (yellow and black circles in FESEM image and EPMA map, respectively). It permitted to compare the local hardness values measured for cBN grains with high and low N amount (EPMA map). The results of hardness for cBN grains with different B/N are shown in **Figure 5.21a**, and they validate the postulated hypothesis. As a consequence, a hardness histogram for the PcBN composite, considering five mechanically distinct phases was attained by statistical analysis (**Figure 5.21a**). Results are summarized in **Table 5.10**.

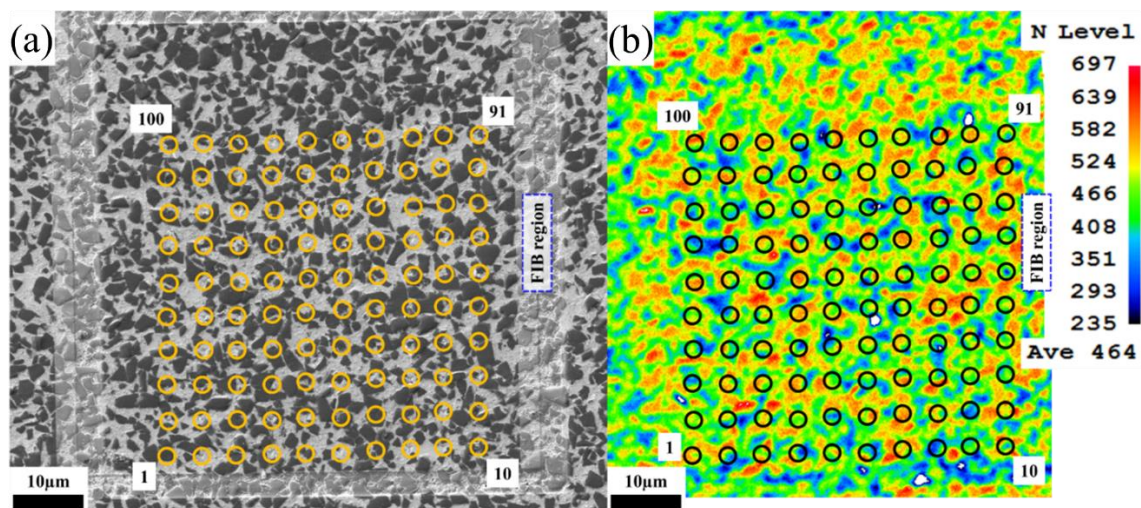


Figure 5.20. (a) FESEM micrograph of performed indentation matrix at 200 nm on the marked region of PcBN sample. (b) N map of microstructure, and corresponding indentations, attained by EPMA analysis.

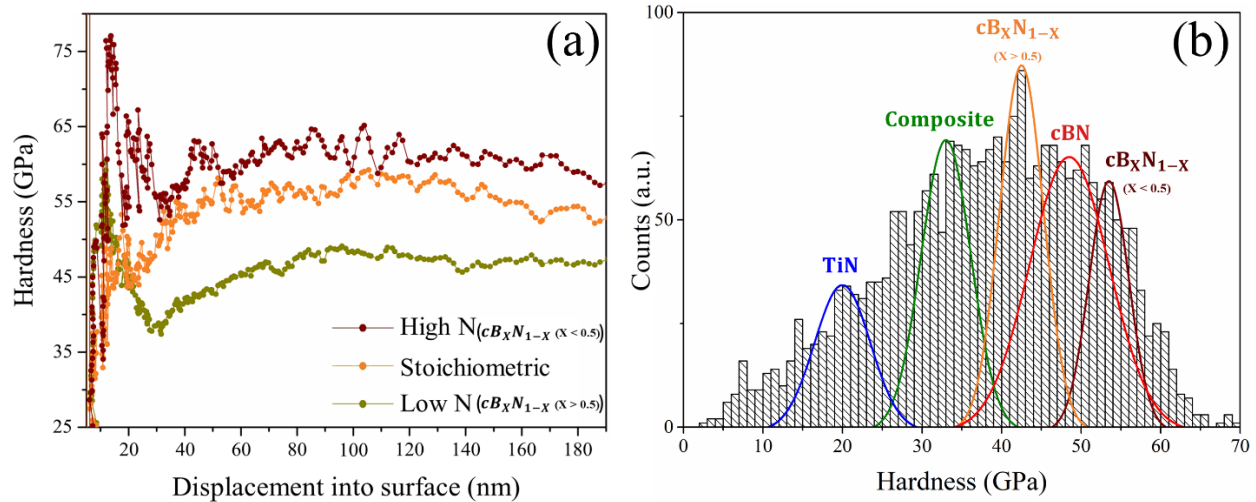


Figure 5.21. (a) Hardness evolution against penetration depth for cBN grains with different N (and B) content. (b) Hardness histogram of PcBN composite with five fitted mechanically distinct phases (the updated version of **Figure 5.11**).

Table 5.10. Intrinsic hardness values for five mechanically different phases of the studied PcBN composite.

Phase	TiN	Composite	Low N cBN	Stoichiometric cBN	High N cBN
Hardness (GPa)	21 ± 5	33 ± 5	43 ± 3	49 ± 7	54 ± 3

5.3.3 Ti(C,N)-FeNi cermets (Ceramic-Metal system)

Figure 5.22 shows an indented surface and the overlay of the hardness cartography map on the corresponding area. Red shades are related to the ceramic particles wherein the hardness mean value is about 26 GPa (as shown in the hardness value gauge, next to the cartography maps). This value is in complete agreement with the results obtained by the statistical analysis (**Figure 5.14**). The scenario is not as clear for the binder, where two tints of colors are identified. On the one hand, there are green tones spread all around the indented surface. The corresponding hardness is around 12 GPa. This value sustains the constrained H values extracted from the statistical analysis for the metallic binder of the 20FeNi+C sample (**Table 5.7**). On the other hand, there is a light blue tint which can be just seen in some regions (e.g. bottom right of **Figure 5.22b**). The overlay picture of the hardness map and FESEM micrograph (**Figure 5.22c**) allows to discern that indentations performed in this blue region are absolutely confined within the binder; and thus, they are not affected by the surrounding ceramic particles. The corresponding hardness of the metallic binder for this blue region is around 9 GPa. This value is in satisfactory agreement with the corrected hardness values estimated for the metallic binder of the 20FeNi+C sample, after implementation of the thin-film models for deconvolution of such intrinsic hardness (**Table 5.8**).

Moreover, a tinge of orange colors can be seen in the boundaries between the ceramic and metallic phases. The corresponding hardness value for these regions containing interphase boundaries is

around 19 GPa. Such a value nicely falls within the range of extracted hardness values for the composite-like phase for the 20FeNi+C sample.

Finally, as it can be seen in **Figure 5.22a**, it should be noticed the existence of some porosity on the indented surface. It is initially presented in navy blue and/or indigo, and continues to violet color, in hardness cartography maps. The corresponding hardness for this “porosity phase” can be considered to be less than 4 GPa. Although the surface fraction occupied by porosity is relatively small, the proper and small space between indentations (no neighboring effect) could provide a good resolution to detect it. **Figure 5.23** is showing the same hardness histograms for studied samples (**Figure 5.14b**) which are now magnified on the regions corresponding to hardness values lower than 4 GPa. These histograms are somehow indicating the porosity levels of the studied samples, as identified by the massive indentation technique. For a given ceramic/metal phase ratio, it can be discerned that carbon addition significantly reduces the number of indentations where weak porosity-related areas were proven. Moreover, it is evident that the porosity level decreases when the relative amount of binder increases. These findings are also in satisfactory agreement with the results obtained from the microstructural characterization conducted in *Section 5.1.3*.

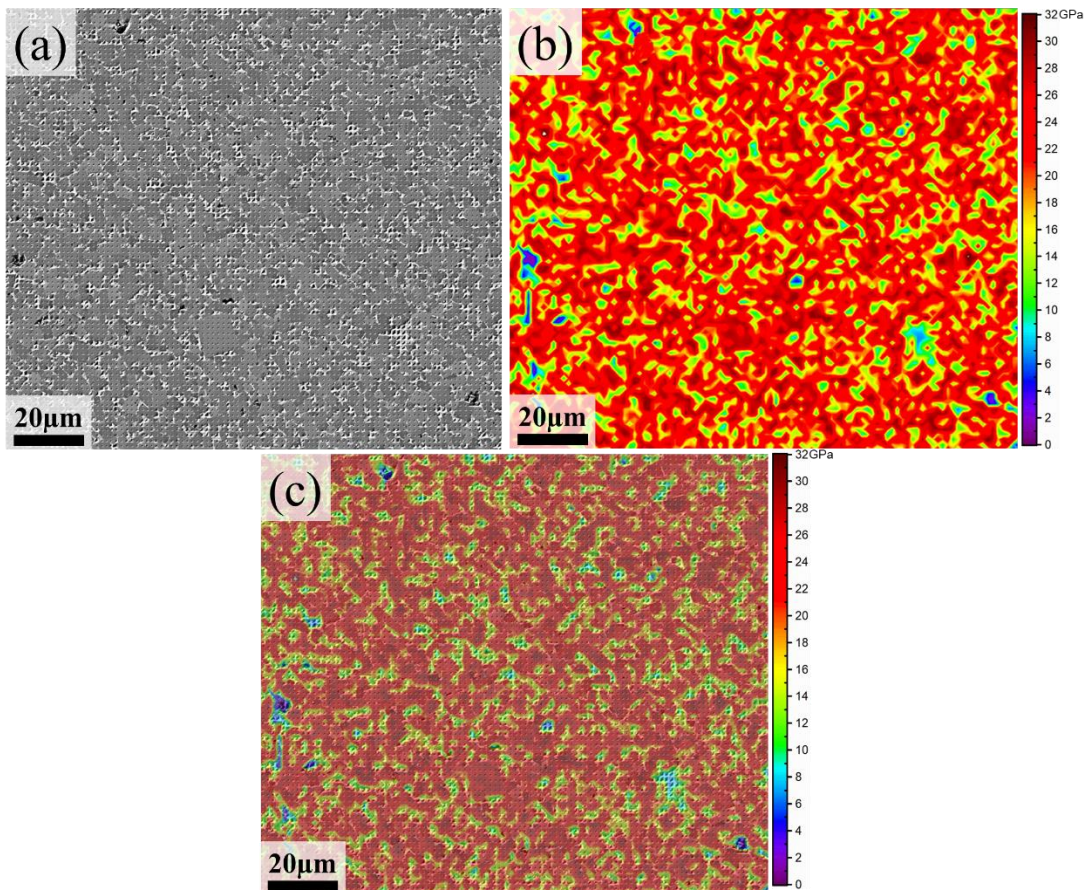


Figure 5.22. (a) FESEM micrograph on an indented surface of 20FeNi+C cermet. (b) Corresponding H cartography map of the indented surface. (c) Overlay of FESEM micrograph and H cartography maps.

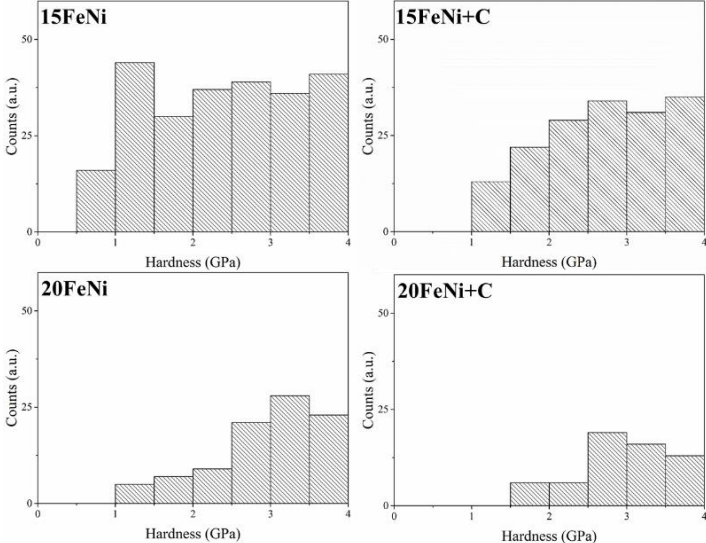


Figure 5.23. Magnified region of hardness histograms of studied samples for $H < 4$ GPa, corresponding to the porosity level.

Chapter 6

General conclusions and future work

Chapter 6:

General conclusions and future work

6.1 General conclusions

This Ph.D. thesis focused on the assessment of a methodology that can measure the small-scale properties of mechanically distinct phases within different metal-metal, ceramic-ceramic and ceramic-metal systems. In this regard, massive indentation technique and subsequent statistical analysis of the gathered data, complemented by advanced characterization techniques of microstructural features, are proposed, implemented and validated as a reliable protocol to satisfy the above objective. The chosen multiphase systems – DSSs, PcBN composite, and Ti(C,N)-FeNi cermets - yielded different challenging scenarios: unidentified mechanical phases with relatively similar properties (metal-metal), the effect of local chemical nature of cBN particles on their intrinsic hardness (ceramic-ceramic), and constrained deformation of the metallic binder by the surrounding hard ceramic particles (ceramic-metal). All those issues had to be addressed to attain reliable results. In this regard, independent microstructural and micromechanical characterization are first conducted, and the determined parameters are correlated through specific information supplied by the use of complementary techniques and models.

Through the whole work, it has been highlighted that maximum penetration depth (h_{max}) of performed indentations plays a key role in the effective length scale of the measured mechanical properties (p). This parameter is completely linked to the characteristic size of the constitutive phases (D), where:

$$h_{max} \gg D \rightarrow p_{composite}$$

$$h_{max} < 10D \rightarrow p_{individual\ phase}$$

Thus, initial microstructural characterization of the studied system through systematic and detailed FESEM inspection becomes critical, as its outcomes define the maximum penetration depth in the subsequent nanoindentation test. h_{max} indirectly defines indentation spacing too, another critical testing parameter of the indentation test. The proper space between indentations not only prevents any overlapping/neighborhood effect of residual imprints but also aids to optimize the resolution of cartography maps.

Regarding data analysis, bin size becomes a relevant parameter to determine the mean value of constitutive phases on obtained mechanical properties histograms. Setting an appropriate bin size is quite important for the effective identification of the number of mechanically distinct phases (p_i). Meanwhile, analysis of cumulative distribution functions (*CDF*) is crucial to calculate the mean values of the measured properties, independent of the bin size, i.e. just based on the number of phases. Therefore, by proper selection and identification of bin size and the number of phases, respectively, better *CDF* fitting and more accurate data may be attained.

Since the massive indentation tests are performed in the form of gedanken experiment, some imprints will inevitably probe different phases concomitantly. Accordingly, the plastic flow induced by these indentations yields a composite-like response by probing regions containing interphase boundaries. The probability of this event to take place is higher as the characteristic size of the involved phase decreases. In these cases, additional composite-like phases must be taken into account for the statistical analysis.

Within the above general framework, the following conclusions may be drawn from the studies conducted in this work:

DSSs (Metal-Metal system):

1. The surface fraction occupied by medium- and large-sized grains demonstrated a high sensitivity to cold work. Grains were significantly refined during cold work via elongation and fragmentation of grains. Subsequent annealing treatment activated recovery and recrystallization of the grains, which caused a higher surface fraction of coarser grains.
2. Hardness and elastic modulus cartography maps provided a satisfactory correlation between micromechanical properties and constitutive phases (confirmed by EBSD analysis). Accuracy and definition of such a relationship were increased by using *H/E* maps. Therefore, the *H/E* ratio is proposed as an appropriate and reliable parameter for mechanically distinguishing between phases with relatively similar properties.
3. The different processing routes investigated have similar effects on the mechanical properties of both phases. For the DSSs here studied (with an intermediate N content of 0.15 in *wt. %*), the austenitic phase demonstrated higher hardness and lower elastic modulus compared with the ferritic one.
4. Cold work resulted in higher values of hardness and elastic modulus for both austenite and ferrite phases, as compared to other samples studied. Such relative changes assessed in the small-scale properties are expected to be related to work hardening and deformation texture effects. Further research is here recalled for a deeper understanding of these correlations.

PcBN composite (Ceramic-Ceramic system):

5. A protocol based on massive nanoindentation and statistical analysis was successfully implemented for assessing small-scale mechanical properties of a PcBN composite. In doing so, the heterogeneous system was originally considered as constituted by three distinct phases with different mechanical properties: two of them microstructurally different, i.e. cBN particles and TiN matrix, and a third phase corresponding to one exhibiting the “composite-like” response. Within this context, intrinsic H values of about 20 and 50 GPa were assessed for TiN binder and cBN grains as lower and upper bounds to the hardness range determined for the composite like phase, i.e. between 30 and 40 GPa.
6. Mean and standard deviation of small-scale H values are independent, within the experimental set outs used in this study, of maximum applied load and number of experimental events (indentations) accounted. However, data attained imposing different load levels, i.e. 25 mN or 10 mN, yielded either better screening among Gaussian distributions for each defined phase or higher microstructure-property resolution within hardness mapping, respectively. Such differences are related to the distinct relevance of size-scale effects (e.g. surface roughness) or indenter tip defects depending upon penetration depth.
7. An in-depth statistical analysis of the upper-level H data complemented with the implementation of advanced characterization techniques (i.e. combined EPMA, instrumented nanoindentation, and FESEM) pointed out and validated the consideration of additional mechanically different cBN-related phases on the basis of relative B/ N content. To the best knowledge of the author, it is the first time that different intrinsic H values are reported for cBN particles as a function of phase (B/N ratio) stoichiometry.
8. Direct quantitative measurement of K_{Ic} for the composite was not possible because of the absence of radial cracks emanating from corners of residual imprints. However, plasticity index assessment and subsequent comparison with literature data for WC ceramics, points out that toughness for TiN-cBN composite investigated ranges between 4 and 6 MPa m^{1/2}.

Ti(C,N)–FeNi cermets (Ceramic-Metal system):

9. The combination of massive nanoindentation and statistical analysis of the gathered data has proven to be a successful testing protocol for determining small-scale hardness and stiffness of Ti(C,N)-FeNi ceramic-metal composites. Nevertheless, successful implementation requires careful consideration of testing parameters used, on the basis of microstructural, residual imprint, and plastic flow length scales.

10. The implemented testing protocol has allowed to document an inverse relationship between the mechanical parameters evaluated and the volume fraction of the metallic phase. For the particular case of the small-scale hardness of the metallic binder, such correlation has been analyzed and rationalized in terms of strengthening of ductile ligaments due to constrained deformation by the surrounding ceramic particles.
11. The effective flow stress for the constrained metallic binder has been estimated from small-scale hardness values experimentally determined. It has yielded values ranging from 1.8 to 4.5 GPa, i.e. similar to those usually reported for cobalt ligaments in WC-Co systems. This points out the effectiveness of FeNi as reinforcement phase for Ti(C,N)-based cermets, towards optimization of hardness-toughness relationships for these ceramic-metal systems.
12. Toughening action of FeNi phase in the Ti(C,N)-based cermets studied has been validated by detailed characterization of deformation, damage and fracture mechanisms. In particular, enhanced crack growth resistance has been discerned in terms of smaller opening, as well as arrest and bifurcation of propagating cracks as they intersect metallic regions.
13. The higher volume fraction of the metallic phase as well as carbon addition yield a more homogeneous and less porous microstructure for the same ceramic/metal ratio. It results in significant changes in hardness and indentation fracture toughness (following the well-established inverse correlation between both mechanical properties), these being more pronounced in the softer grades.
14. The addition of carbon results in higher hardness values at macro- and micro- length scales. Such changes are directly related to an intrinsic (small-scale) hardening effect of the metallic phase as well as to an effective reduction of porosity amount affecting the two-phase composite-like hardness.
15. Hardness cartography map at the microstructural length scale showed an excellent qualitative correlation between micromechanical characteristics (measured from massive nanoindentation) and microstructural assemblage (as evidenced from FESEM inspection).
16. Massive nanoindentation and statistical analysis have proven to be a successful tool for analyzing small-scale properties of different constitutive phases in the cermets studied. It includes not only assessment of intrinsic hardness values but also evaluation of change in these properties for individual or mechanically distinct phases, as related to the specific influence of microstructural/processing variables, e.g. carbon addition or ceramic/metal phase ratio.

6.2 Future work

Suggesting the future works and perspectives could improve the current study in different aspects that were not considered due to the lack of time, facilities, or specific knowledge of a certain technique or subject. In this regard, some future plans are listed below, which could enhance the knowledge about microstructural and micromechanical properties of inorganic multiphase systems.

- The number of performed imprints has to be high enough for the implementation of the statistical analysis. However, a high number of indentations may cause some difficulties and limitations such as: increasing the risk of damaging/blunting the tip, more time and energy consumption (mainly for processors of computers), and the testing price. In this regard, finding the optimized number of performed imprints that could satisfy both statistical analysis and testing limitations is essential.
- Within the DSS study, obtained hardness for cold-rolled samples presented higher values as compared to the other samples. Such relative changes in the small-scale properties are expected to be related to work hardening and deformation texture effects. Therefore, studying the correlation between hardness and crystallographic orientation for both austenite and ferrite phases within the DSS may provide a deeper understanding of the optimized microstructural design of these materials.
- This Ph.D. thesis has proposed a solid methodology to evaluate the local mechanical properties of each constitutive phase and find the correlations among such intrinsic parameters and the effective microstructural assemblage of different multiphase systems. As a result, it has been satisfactorily validated for DSSs and intermetallics [220,221], cermets [124,129,192,222] and PcBN composite [223]. However, all these works have been conducted on “pristine” specimens. Meanwhile, in the case that damage or microstructural changes are induced during service (e.g. by occasional hard body impacts or continuous contact-related degradation), similar information on the remnant small-scale mechanical properties of structural materials does not exist. Therefore, extending the approach here proposed and validated, by including damage-level as an additional variable, could be considered as an effective target. Accordingly, the main objective of future work might be to assess hardness – at the small-scale length where damage is concentrated on real tools and components (i.e. cutting edge, critical profile, etc.) – and use the corresponding maps as “index of merit” for selecting materials on the basis of the effective performance of tools and components after being exposed to real service conditions

- As it was mentioned before, nanoindentation testing has been recently combined and equipped with different high-speed and high-temperature accessories. The former was addressed and discussed in this Ph.D. thesis. However, the high-temperature nanoindentation technique may open new doors for evaluating the mechanical properties of ceramic-metal and ceramic-ceramic systems, as working conditions for such materials are mainly at elevated temperatures. This also applies to other complementary micro- and nanomechanical testing techniques, such as micro-compression as well as cantilever deflection – at both room and high temperatures – which may then provide information about the influence of microstructural and processing parameters on the overall mechanical response, plastic deformation phenomena and failure mechanisms, fracture toughness and even creep behavior [224–233].
- Obtaining a *3D* reconstruction of the ceramic-ceramic and ceramic-metal systems will allow to visualize and understand the real shape of ceramic particles, phase contiguity, and porosity features. *3D* image reconstruction of microstructural assemblage in conjunction with small-scale mechanical properties determined by means of massive nanoindentation, micropillar compression and/or cantilever deflection - at ambient and elevated temperatures – become key inputs for reliable and effective simulation of the mechanical response of these multiphase systems through finite element modeling.

Acknowledgments

During my Ph.D. I had a life replete with excitement and challenges. I am reviewing all the memories and experiences of these phenomenal and unforgettable years. Those are forming an unwritten life handbook full of amazing experiences and instructive lessons that will be my guide for life's journey. I would consider this part of the thesis as the hardest one to write, as I can not count all those stars who were shining my path. Therefore, I would mention some of those great people here, and I will keep the rest always in my heart even if I am not mentioning them in the following paragraphs.

First I would like to express my great appreciation to my supervisor Prof. *Luis Llanes* who had a great impact on my both professional and personal life. His great leadership was my motivation to work harder to reach my goals. I always received open-ended supports from him. There has been never a “NO” if I provide a good plan to make something work. He taught me how to have a comprehensive view, how to become a professional scientist, how to plan the future, etc. Although I have been far from my family, his manner made me feel I have another family which is CIEFMA. Thank you, *Luis*. You are simply the best.

I would like to thank Dr. *Joan Josep Roa*, for all that he has done for me. He taught me the base of science, he took my hand and taught me how to walk in the scientific world. He was so patient to teach me various things, I learned how to write, how to present good, how to be ambitious. He gave me some amazing advice and credits which have changed my professional life, i.e. recommending me to have a stage in ETH Zurich. I remember all his amazing effort during these years and I owe a great part of my professional career to him.

Some parts of my work were done in ETH Zurich in the Laboratory for Nanometallurgy. Here I would like to commend all members of that group, Prof. *Ralph Spolenak*, and a special thanks to Dr. *Jeffery Wheeler* who was supervising me during my stage. He was a great host, supportive, with innovative ideas. We have had great collaborations and hopefully, we will have more projects in the future.

As a member of the CIEFMA group, I would like to extend my great appreciation to professors *Gemma Fargas* and *Antonio Mateo*, as well as *Fernando Garcia* for the fruitful collaborations and their help. Special thanks to Prof. *Emilio Jiménez-Piqué* for offering his best in some critical situations, his advice, supports, and his trust. I will never forget his words when he offered me to

be the reviewer of an article in a Q1 journal for the first time. Those words gave me great confidence and made me believe in my abilities and knowledge. His first answer to any suggestion is “why?”. It made me always to think smartly and take each step in the most efficient way.

Many thanks to Barcelona Research Center in Multiscale Science and Engineering, and the staff for their supports. My special appreciation goes to Dr. *Trifon Trifonov*. Thanks to his efforts I could professionally learn how to use FESEM and FIB. I owe a great part of my Ph.D. to him, he made the impossible possible. He was the one who convinced Prof. *Jordi Llorca* to provide me full access (24 hours) to the center. He (literally) gave me the keys and let me be the first/only person who worked with FIB at 3:00 AM. He is one of my favorites characters in UPC. Although he is very serious and professional in his field, he is so funny (with another level of jokes) and supportive when it comes to friendship.

Here I would like to mention *Maria de Nicolas (Hermonia)* as I consider her as the best college, one of the best friends and my siblings. She is the best person to collaborate with (statistically obvious with the number of our published works) as she is so accurate, trustable and intelligent. As a friend she made me feel how reliable is she. And as a sister, she was next to me in very tough days of life. Thanks a lot, *Hermonia*.

Sometimes it is very hard to appreciate someone by words (as in the case of *Luis* and *Maria*), here I would like to mention two more persons who I don't know how to express my profound gratitude for accompanying me during these years. *Marcel Carpio (Mase-Mase)* and *Sandra Gordon (Sandlita)*, you made my Ph.D. life great with your presence. I would never forget all those uncountable coffee times and long lunches in which we were sharing our happiness, stresses, sadness and life stories. If there was a touchy subject we knew that we had to go to *Alex* bar and ask for “Sanmige”, after the second one we had been already plunged into the topic, and we were sure that we will solve/be calm after some more beers (even we get drunk). Some sentences are simple but are priceless, whenever I had a text which ends with “... just let me know” I felt your great supports. Thank you my BMFW.

I would like to extend my thanks to all Ph.D. and master students who were always kind and help me during these years. I would like to mention *Yafeng, Joaquim, Victor, Antoine, Xavi, Laia, Sandra (Garcia)* and *Ferran*. Special thanks to *Laura* and *Marc* for being professional colleagues and wonderful friends. I admire them for their super high capacity of making jokes, they are incredibly nice. I enjoyed our times, especially during that memorable trip to Turkey, having amazing and funny times, that “Mehreba Kebab” expression always brings a big smile to my face. Thanks for everything.

Having nice officemates was a great fortune during these years. I would like to thanks *Erica, Miquel, Yago, Mar, Joanna(s), Ines, Violetta, Anna, Junhui, Mona, Luis, Francesco, Irene,* and *Jonathan*. The great atmosphere of the offices was definitely because of these awesome people.

Last but foremost, I owe all my success to my parents. They have been always there absolutely and unconditionally, from the first day of my life and I hope until the last day. I wish the same for my wife Julia, who is a fabulous person with a pure soul. Her presence and extraordinary energy have been giving me hope, happiness and love (even from thousands of kilometers distance). I have learned lots of amazing life lessons during these years. I hope these lessons help me to be a better son, husband, and human.

Hossein Besharatloo
January 2021

Bibliography

- [1] W.D. Callister, D.G. Rethwisch, *Materials Science and Engineering*, 10th ed., John Wiley & Sons, New York, USA, 2011.
- [2] H. Clemens, S. Mayer, C. Scheu, *Microstructure and properties of engineering materials*, in: S. Peter, S. Andreas, H. Clemens, M. Svea (Eds.), *Neutrons and Synchrotron Radiation in Engineering Materials Science: From Fundamentals to Applications*, John Wiley & Sons, New York, USA, 2017: pp. 1–20. <https://doi.org/10.1002/9783527684489.ch1>.
- [3] G. Thomas, *Microstructural design and tailoring of advanced materials*, in: D. Rickerby, G. Valdre, U. Valdre (Eds.), *Impact of Electron and Scanning Probe Microscopy on Materials Research*, Springer, Dordrecht, Netherlands, 1999: pp. 25–40. <https://doi.org/10.1007/978-94-011-4451-3>.
- [4] D.R. Clarke, *Interpenetrating phase composites*, *Journal of the American Ceramic Society* 75 (1992) 739–758. <https://doi.org/10.1111/j.1151-2916.1992.tb04138.x>.
- [5] M.P. Harmer, H.M. Chan, G.A. Miller, *Unique opportunities for microstructural engineering with duplex and laminar ceramic composites*, *Journal of the American Ceramic Society* 75 (1992) 1715–1728. <https://doi.org/10.1111/j.1151-2916.1992.tb07188.x>.
- [6] A. Misra, R. Gibala, R.D. Noebe, *Optimization of toughness and strength in multiphase intermetallics*, *Intermetallics* 9 (2001) 971–978. [https://doi.org/10.1016/S0966-9795\(01\)00098-X](https://doi.org/10.1016/S0966-9795(01)00098-X).
- [7] H.X. Peng, Z. Fan, J.R.G. Evans, *Bi-continuous metal matrix composites*, *Materials Science and Engineering A* 303 (2001) 37–45. [https://doi.org/10.1016/S0921-5093\(00\)01879-7](https://doi.org/10.1016/S0921-5093(00)01879-7).
- [8] P. Palmero, V. Naglieri, G. Spina, M. Lombardi, *Microstructural design and elaboration of multiphase ultra-fine ceramics*, *Ceramics International* 37 (2011) 139–144. <https://doi.org/10.1016/j.ceramint.2010.08.031>.
- [9] G. Requena, H.P. Degischer, *Three-dimensional architecture of engineering multiphase metals*, *Annual Review of Materials Research* 42 (2012) 145–161. <https://doi.org/10.1146/annurev-matsci-070511-155109>.
- [10] F.-J. Ulm, M. Vandamme, C. Bobko, J. Alberto Ortega, K. Tai, C. Ortiz, *Statistical*

- indentation techniques for hydrated nanocomposites: concrete, bone, and shale, *Journal of the American Ceramic Society* 90 (2007) 2677–2692. <https://doi.org/10.1111/j.1551-2916.2007.02012.x>.
- [11] I. de Diego-Calderón, M.J. Santofimia, J.M. Molina-Aldareguia, M.A. Monclús, I. Sabirov, Deformation behavior of a high strength multiphase steel at macro-and micro-scales, *Materials Science and Engineering A* 611 (2014) 201–211. <https://doi.org/10.1016/j.msea.2014.05.068>.
- [12] H. ur Rehman, K. Durst, S. Neumeier, A.B. Parsa, A. Kostka, G. Eggeler, M. Göken, Nanoindentation studies of the mechanical properties of the μ phase in a creep deformed Re containing nickel-based superalloy, *Materials Science and Engineering A* 634 (2015) 202–208. <https://doi.org/10.1016/j.msea.2015.03.045>.
- [13] C.-M. Sanchez-Camargo, A. Hor, M. Salem, C. Mabru, A robust method for mechanical characterization of heterogeneous materials by nanoindentation grid analysis, *Materials & Design* 194 (2020) 108908. <https://doi.org/10.1016/j.matdes.2020.108908>.
- [14] J.D. French, M.P. Harmer, H.M. Chan, G.A. Miller, Coarsening-resistant dual-phase interpenetrating microstructures, *Journal of the American Ceramic Society* 73 (1990) 2508–2510. <https://doi.org/10.1111/j.1151-2916.1990.tb07621.x>.
- [15] X.-Q. Feng, Z. Tian, Y.-H. Liu, S.-W. Yu, Effective elastic and plastic properties of interpenetrating multiphase composites, *Applied Composite Materials* 11 (2004) 33–55. <https://doi.org/10.1023/B:ACMA.0000003972.32599.0c>.
- [16] M. Wang, N. Pan, Predictions of effective physical properties of complex multiphase materials, *Materials Science and Engineering R Reports* 63 (2008) 1–30. <https://doi.org/10.1016/j.mser.2008.07.001>.
- [17] C.C. Tasan, M. Diehl, D. Yan, C. Zambaldi, P. Shanthraj, F. Roters, D. Raabe, Integrated experimental–simulation analysis of stress and strain partitioning in multiphase alloys, *Acta Materialia* 81 (2014) 386–400. <https://doi.org/10.1016/j.actamat.2014.07.071>.
- [18] E. Werner, R. Wesenjak, A. Fillafer, F. Meier, C. Krempaszky, Microstructure-based modelling of multiphase materials and complex structures, *Continuum Mechanics and Thermodynamics* 28 (2016) 1325–1346. <https://doi.org/10.1007/s00161-015-0477-7>.
- [19] Z. Li, C. Wang, C. Chen, Effective electromechanical properties of transversely isotropic piezoelectric ceramics with microvoids, *Computational Materials Science* 27 (2003) 381–392. [https://doi.org/https://doi.org/10.1016/S0927-0256\(03\)00044-2](https://doi.org/https://doi.org/10.1016/S0927-0256(03)00044-2).
- [20] A. Borbély, P. Kenesei, H. Biermann, Estimation of the effective properties of particle-

- reinforced metal–matrix composites from microtomographic reconstructions, *Acta Materialia* 54 (2006) 2735–2744. <https://doi.org/10.1016/j.actamat.2006.02.012>.
- [21] C. Yan, Y. Shi, J. Yang, J. Liu, Multiphase polymeric materials for rapid prototyping and tooling technologies and their applications, *Composite Interfaces* 17 (2010) 257–271. <https://doi.org/10.1163/092764410X490680>.
- [22] C.C. Tasan, M. Diehl, D. Yan, M. Bechtold, F. Roters, L. Schemmann, C. Zheng, N. Peranio, D. Ponge, M. Koyama, An overview of dual-phase steels: advances in microstructure-oriented processing and micromechanically guided design, *Annual Review of Materials Research* 45 (2015) 391–431. <https://doi.org/10.1146/annurev-matsci-070214-021103>.
- [23] R. Rajasekar, C. Sivasenapathy, C. Moganapriya, A. Sivakumar, Multiphase materials for tire applications, in: J. Kim, S. Thomas, P. Saha (Eds.), *Multicomponent Polymeric Materials*, Springer, Dordrecht, Netherland, 2016: pp. 349–367. https://doi.org/10.1007/978-94-017-7324-9_13.
- [24] M. Kühne, F. Paolucci, J. Popovic, P.M. Ostrovsky, J. Maier, J.H. Smet, Ultrafast lithium diffusion in bilayer graphene, *Nature Nanotechnology* 12 (2017) 895. <https://doi.org/10.1038/nnano.2017.108>.
- [25] H.D. Solomon, T.M. Devine Jr, Duplex stainless steels: A tale of two phases, in: R.A. Lula (Ed.), *Conference of the Duplex Stainless Steels*, ASM, Materials Park, Ohio, USA, 1983: pp. 693–756.
- [26] W.B. Hutchinson, K. Ushioda, G. Runnsjö, Anisotropy of tensile behaviour in a duplex stainless steel sheet, *Materials Science and Technology* 1 (1985) 728–736. <https://doi.org/10.1179/mst.1985.1.9.728>.
- [27] J. Charles, Super duplex stainless steels: structure and properties, in: J. Charles, S. Bernardsson (Eds.), *Proceeding of the DSS '91 Conference*, Les Editions de Physique, Beaune, Bourgogne, France, 1991: pp. 3–48.
- [28] J.-O. Nilsson, Super duplex stainless steels, *Materials Science and Technology* 8 (1992) 685–700. <https://doi.org/10.1179/mst.1992.8.8.685>.
- [29] R.N. Gunn, *Duplex Stainless Steels: Microstructure, Properties and Applications*, 1st ed., Woodhead Publishing, Cambridge, England, 1997.
- [30] I. Alvarez-Armas, Duplex stainless steels: brief history and some recent alloys, *Recent Patents on Mechanical Engineering* 1 (2008) 51–57. <https://doi.org/10.2174/2212797610801010051>.

- [31] I. Alvarez-Armas, S. Degallaix-Moreuil, Duplex Stainless Steels, John Wiley & Sons, Hoboken, New Jersey, USA, 2013.
- [32] J. Charles, Duplex families and applications: A review. Part 1: From duplex pioneers up to 1991, *Stainless Steel World Magazine*, July-August (2015) 1–5.
- [33] J. Charles, Duplex families and applications: A review. Part 2: From 1991 to nowadays, *Stainless Steel World Magazine*, September (2015) 67–70.
- [34] J. Charles, Duplex families and applications: A review. Part 3: The lean duplex grades, *Stainless Steel World Magazine*, October (2015) 1–4.
- [35] T.F.A. Santos, R.R. Marinho, M.T.P. Paes, A.J. Ramirez, Microstructure evaluation of UNS S32205 duplex stainless steel friction stir welds, *Rem: Revista Escola de Minas* 66 (2013) 187–191. <https://doi.org/10.1590/S0370-44672013000200008>.
- [36] D.S. Bergstrom, J.J. Dunn, D. Hasek, Benchmarking of duplex stainless steels versus conventional stainless steel grades, in: AIM (Ed.), Duplex, Duplex 2007 International Conference and Expo., Associazione Italiana di Metallurgia, Grado, Italy, 2007: pp. 1–18.
- [37] M. Knyazeva, M. Pohl, Duplex steels-Part I: genesis, formation, and structure, *Metallography, Microstructure and Analysis* 2 (2013) 113–121. <https://doi.org/10.1007/s13632-013-0066-8>.
- [38] P. Guha, C. Clark, Properties and applications of high-chromium duplex stainless steels, in: R.A. Lula (Ed.), Conference of the Duplex Stainless Steels, ASM, Materials Park, Ohio, USA, 1983: pp. 355–369.
- [39] B. Messer, V. Oprea, A. Wright, Duplex stainless steel welding: best practices, *Stainless Steel World Magazine*, December (2007) 53–63.
- [40] API Technical Report 938-C, Use of duplex stainless steels in the oil refining industry, American Petroleum Institute, Washington DC, USA, 2015.
- [41] V.A. Hosseini, K. Hurtig, D. Eyzop, A. Östberg, P. Janiak, L. Karlsson, Ferrite content measurement in super duplex stainless steel welds, *Welding in the World* 63 (2019) 551–563. <https://doi.org/10.1007/s40194-018-00681-1>.
- [42] B. Holmes, M. Gittos, M. Dodge, K. Sotoudeh, Ferrite measurement in duplex stainless steels, in: Proceeding of the CORROSION Conference and Expo.2019, NACE International, Nashville, Tennessee, USA, 2019.
- [43] A. Putz, M. Althuber, A. Zelić, E.M. Westin, T. Willidal, N. Enzinger, Methods for the

- measurement of ferrite content in multipass duplex stainless steel welds, *Welding in the World* 63 (2019) 1075–1086. <https://doi.org/10.1007/s40194-019-00721-4>.
- [44] H.-Y. Liou, W.-T. Tsai, Y.-T. Pan, R.-I. Hsieh, Effects of alloying elements on the mechanical properties and corrosion behaviors of 2205 duplex stainless steels, *Journal of Materials Engineering and Performance* 10 (2001) 231–241. <https://doi.org/10.1361/105994901770345268>.
- [45] L.F. Garfias-Mesias, J.M. Sykes, C.D.S. Tuck, The effect of phase compositions on the pitting corrosion of 25 Cr duplex stainless steel in chloride solutions, *Corrosion Science* 38 (1996) 1319–1330. [https://doi.org/10.1016/0010-938X\(96\)00022-4](https://doi.org/10.1016/0010-938X(96)00022-4).
- [46] B. Walden, J.M. Nicholls, The Sandvik duplex family of stainless steel. Summary of data, in: *Proceeding of the VI Korrosyon Sempozyumu Bildiriler Kitabi*, Izmir, Turkey, 1998: pp. 100–122.
- [47] R. Sánchez, I. Moreno, J. Almagro, J. Botella, X. Llovet, Effects of composition and thermal history on the phase balance and elements distribution of standard and modified duplex stainless, in: *Proceeding Fourth Stainless Steel Science and Market Congress*, Paris, France, 2002.
- [48] J.M. Cabrera, A. Mateo, L. Llanes, J. Prado, M. Anglada, Hot deformation of duplex stainless steels, *Journal of Materials Processing Technology* 143–144 (2003) 321–325. [https://doi.org/10.1016/S0924-0136\(03\)00434-5](https://doi.org/10.1016/S0924-0136(03)00434-5).
- [49] J. Lippol, J.K. Damian, *Welding Metallurgy and Weldability of Stainless Steels*, John Wiley & Sons, New York, USA, 2005.
- [50] G. Fargas, N. Akdut, M. Anglada, A. Mateo, Microstructural evolution during industrial rolling of a duplex stainless steel, *ISIJ International* 48 (2008) 1596–1602. <https://doi.org/10.2355/isijinternational.48.1596>.
- [51] IMA Technical Report, Practical guidelines for the fabrication of duplex stainless steels, International Molybdenum Association, Bristol, UK, 2009.
- [52] D.R. Askeland, W.J. Wright, *Essentials of Materials Science & Engineering*, Cengage Learning, Boston, Massachusetts, USA, 2013.
- [53] I.-D. Utu, I. Mitelea, S.D. Urgan, C.M. Crăciunescu, Transformation and precipitation reactions by metal active gas pulsed welded joints from X2CrNiMoN22-5-3 duplex stainless steels, *Materials* 9 (2016) 606. <https://doi.org/10.3390/MA9070606>.
- [54] K. Ogawa, M. Miura, Y.-I. Komizo, Study on welding of high silicon containing stainless

- steels. II. HAZ toughness of high silicon containing duplex stainless steel, *Quarterly Journal of the Japan Welding Society* 9 (1991) 61–67.
- [55] C.-O.A. Olsson, The influence of nitrogen and molybdenum on passive films formed on the austenoferritic stainless steel 2205 studied by AES and XPS, *Corrosion Science* 37 (1995) 467–479. [https://doi.org/10.1016/0010-938X\(94\)00148-Y](https://doi.org/10.1016/0010-938X(94)00148-Y).
- [56] M.W. Cook, P.K. Bossom, Trends and recent developments in the material manufacture and cutting tool application of polycrystalline diamond and polycrystalline cubic boron nitride, *International Journal of Refractory Metals and Hard Materials* 18 (2000) 147–152. [https://doi.org/10.1016/S0263-4368\(00\)00015-9](https://doi.org/10.1016/S0263-4368(00)00015-9).
- [57] R. M'Saoubi, D. Axinte, S.L. Soo, C. Nobel, H. Attia, G. Kappmeyer, S. Engin, W.-M. Sim, High performance cutting of advanced aerospace alloys and composite materials, *CIRP Annals* 64 (2015) 557–580. <https://doi.org/10.1016/j.cirp.2015.05.002>.
- [58] R.H. Wentorf, R.C. DeVries, F.P. Bundy, Sintered superhard materials, *Science* 208 (1980) 873–880. <https://doi.org/10.1126/science.208.4446.873>.
- [59] R. Riedel, *Handbook of Ceramic Hard Materials*, Wiley-VCH, Weinheim, Germany, 2000. <https://doi.org/10.1002/9783527618217>.
- [60] A.S. More, W. Jiang, W.D. Brown, A.P. Malshe, Tool wear and machining performance of cBN–TiN coated carbide inserts and PcBN compact inserts in turning AISI 4340 hardened steel, *Journal of Materials Processing Technology* 180 (2006) 253–262. <https://doi.org/10.1016/j.jmatprotec.2006.06.013>.
- [61] S.N. Monteiro, A.L.D. Skury, M.G. de Azevedo, G.S. Bobrovnitchii, Cubic boron nitride competing with diamond as a superhard engineering material—an overview, *Journal of Materials Research and Technology* 2 (2013) 68–74. <https://doi.org/10.1016/j.jmrt.2013.03.004>.
- [62] Y. Pauleau, *Materials Surface Processing by Directed Energy Techniques*, Elsevier, Oxford, UK, 2006. <https://doi.org/10.1016/B978-0-08-044496-3.X5000-X>.
- [63] L. Vel, G. Demazeau, J. Etourneau, Cubic boron nitride: synthesis, physicochemical properties and applications, *Materials Science and Engineering B* 10 (1991) 149–164. [https://doi.org/10.1016/0921-5107\(91\)90121-B](https://doi.org/10.1016/0921-5107(91)90121-B).
- [64] J. Eichler, C. Lesniak, Boron nitride (BN) and BN composites for high-temperature applications, *Journal of the European Ceramic Society* 28 (2008) 1105–1109. <https://doi.org/10.1016/j.jeurceramsoc.2007.09.005>.

- [65] R.H. Wentorf Jr, Cubic form of boron nitride, *The Journal of Chemical Physics* 26 (1957) 956. <https://doi.org/10.1063/1.1745964>.
- [66] P.J. Heath, Ultrahard tool materials, *European Journal of Engineering Education* 12 (1987) 5–20. <https://doi.org/10.31399/asm.hb.v16.a0002127>.
- [67] T. Taniguchi, Synthesis and properties of single crystalline cBN and its sintered body, in: V.K. Sarin, D. Mari, L. Llanes, C. Nobel (Eds.), *Comprehensive Hard Materials*, Elsevier, Oxford, UK, 2014: pp. 587–604. <https://doi.org/10.1016/B978-0-08-096527-7.00060-X>.
- [68] L.N.L. de Lacalle, A. Lamikiz, J.F. de Larrinoa, I. Azkona, Advanced cutting tools, in: *Machining of Hard Materials*, Springer, London, UK, 2011: pp. 33–86. https://doi.org/10.1007/978-1-84996-450-0_2.
- [69] P. Ettmayer, H. Kolaska, H.M. Ortner, History of hardmetals, in: V.K. Sarin, D. Mari, L. Llanes, C. Nobel (Eds.), *Comprehensive Hard Materials*, Elsevier, Oxford, UK, 2014: pp. 3–27. <https://doi.org/10.1016/B978-0-08-096527-7.00001-5>.
- [70] E. Benko, J. Morgiel, T. Czeppe, T. Barr, Microstructure and hardness of cBN–Zr composite, *Journal of the European Ceramic Society* 18 (1998) 389–393. [https://doi.org/10.1016/S0955-2219\(97\)00147-7](https://doi.org/10.1016/S0955-2219(97)00147-7).
- [71] H.S.L. Sithebe, The preparation and characteristics of cBN ceramics with Al-based binder phases, Ph.D. Thesis, University of Witwatersrand, Johannesburg, South Africa, 2007.
- [72] H.S.L. Sithebe, D. McLachlan, I. Sigalas, M. Herrmann, Pressure infiltration of boron nitride preforms with molten aluminum, *Ceramics International* 34 (2008) 1367–1371. <https://doi.org/10.1016/j.ceramint.2007.03.033>.
- [73] R.M. Hooper, C. Brookes, Microstructure and wear of cubic boron nitride aggregate tools, *Institute of Physics Conference Series* 75 (1986) 907–917.
- [74] K. Shintani, M. Ueki, Y. Fujimura, Microstructure and mechanical properties of sintered cubic boron nitride, *Journal of Materials Science Letters* 6 (1987) 987–989. <https://doi.org/10.1007/BF01729893>.
- [75] R.M. Hooper, M.-O. Guillou, J.L. Henshall, Indentation studies of cBN–TiC composites, *Journal of Hard Materials* 2 (1991) 223–231.
- [76] H. Sumiya, S. Uesaka, S. Satoh, Mechanical properties of high purity polycrystalline cBN synthesized by direct conversion sintering method, *Journal of Materials Science* 35 (2000) 1181–1186. <https://doi.org/10.1023/A:1004780218732>.

- [77] S.N. Dub, I.A. Petrusha, Mechanical properties of polycrystalline cBN obtained from pyrolytic gBN by direct transformation technique, *High Pressure Research* 26 (2006) 71–77. <https://doi.org/10.1080/08957950600764239>.
- [78] Y. Li, S. Li, R. Lv, J. Qin, J. Zhang, J. Wang, F. Wang, Z. Kou, D. He, Study of high-pressure sintering behavior of cBN composites starting with cBN–Al mixtures, *Journal of Materials Research* 23 (2008) 2366–2372. <https://doi.org/10.1557/jmr.2008.0316>.
- [79] A. McKie, J. Winzer, I. Sigalas, M. Herrmann, L. Weiler, J. Rödel, N. Can, Mechanical properties of cBN–Al composite materials, *Ceramics International* 37 (2011) 1–8. <https://doi.org/10.1016/j.ceramint.2010.07.034>.
- [80] Q. Li, W. Zhang, S. Liu, S. Zhang, Comparative research on cutting boron-cast iron with PcBN, Diamond and Abrasive Engineering 35 (2015) 63–68. <https://doi.org/10.13394/j.cnki.jgszz.2015.2.0013>.
- [81] T.K. Harris, E.J. Brookes, C.J. Taylor, The effect of temperature on the hardness of polycrystalline cubic boron nitride cutting tool materials, *International Journal of Refractory Metals and Hard Materials* 22 (2004) 105–110. <https://doi.org/10.1016/j.ijrmhm.2004.01.004>.
- [82] C. Lahiff, S. Gordon, P. Phelan, PcBN tool wear modes and mechanisms in finish hard turning, *Robotics and Computer-Integrated Manufacturing* 23 (2007) 638–644. <https://doi.org/10.1016/j.rcim.2007.02.008>.
- [83] Y. Huang, Y.K. Chou, S.Y. Liang, CBN tool wear in hard turning: a survey on research progresses, *The International Journal of Advanced Manufacturing Technology* 35 (2007) 443–453. <https://doi.org/10.1007/s00170-006-0737-6>.
- [84] V.A.A. De Godoy, A.E. Diniz, Turning of interrupted and continuous hardened steel surfaces using ceramic and CBN cutting tools, *Journal of Materials Processing Technology* 211 (2011) 1014–1025. <https://doi.org/10.1016/j.jmatprotec.2011.01.002>.
- [85] A. Hara, S. Yatsu, Sintered compact for cutting tool and manufacture thereof, Patent Number JPS54149308A, Japan, 1979.
- [86] A. Hara, S. Yazu, Sintered body for use in a cutting tool and the method for producing the same, Patent Number US4442180A, USA, 1984.
- [87] S. Yazu, Y. Kohno, S. Sato, A. Hara, New CBN/TiN composite sintered under ultra-high pressure, *Modern Developments in Powder Metallurgy* 14 (1981) 363–371.
- [88] J. Morgiel, E. Benko, Microstructure of boron nitride sintered with titanium, *Materials*

- Letters 25 (1995) 49–52. [https://doi.org/10.1016/0167-577X\(95\)00138-7](https://doi.org/10.1016/0167-577X(95)00138-7).
- [89] X.-Z. Rong, T. Tsurumi, O. Fukunaga, T. Yano, High-pressure sintering of cBN-TiN-Al composite for cutting tool application, *Diamond and Related Materials* 11 (2002) 280–286. [https://doi.org/10.1016/S0925-9635\(01\)00692-6](https://doi.org/10.1016/S0925-9635(01)00692-6).
- [90] Sandvik's Technical Report, Hard part turning with CBN-PcBN cutting tools brochure, <https://www.sandvik.coromant.com/sitecollectiondocuments/downloads/global/catalogues/en-gb/c-2940-137.pdf> (accessed December 6, 2020).
- [91] P. Alveen, D. McNamara, D. Carolan, N. Murphy, A. Ivanković, The influence of microstructure on the fracture properties of polycrystalline cubic boron nitride, *Computational Materials Science* 109 (2015) 115–123. <https://doi.org/10.1016/j.commatsci.2015.06.036>.
- [92] K. Sobiya, I. Sigalas, G. Akdogan, Y. Turan, Performance of mixed ceramics and CBN tools during hard turning of martensitic stainless steel, *The International Journal of Advanced Manufacturing Technology* 77 (2015) 861–871. <https://doi.org/10.1007/s00170-014-6506-z>.
- [93] K. Sobiya, I. Sigalas, High-speed machining of martensitic stainless steel using PcBN, *Journal of Superhard Materials* 38 (2016) 34–39. <https://doi.org/10.3103/S1063457616010056>.
- [94] R.W. Rice, C.C. Wu, F. Boichelt, Hardness–grain-size relations in ceramics, *Journal of the American Ceramic Society* 77 (1994) 2539–2553. <https://doi.org/10.1111/j.1151-2916.1994.tb04641.x>.
- [95] W. König, M. Klinger, R. Link, Machining hard materials with geometrically defined cutting edges—field of applications and limitations, *CIRP Annals* 39 (1990) 61–64. [https://doi.org/10.1016/S0007-8506\(07\)61003-8](https://doi.org/10.1016/S0007-8506(07)61003-8).
- [96] Z.-C. Lin, D.-Y. Chen, A study of cutting with a CBN tool, *Journal of Materials Processing Technology* 49 (1995) 149–164. [https://doi.org/10.1016/0924-0136\(94\)01321-Q](https://doi.org/10.1016/0924-0136(94)01321-Q).
- [97] Y.K. Chou, C.J. Evans, M.M. Barash, Experimental investigation on CBN turning of hardened AISI 52100 steel, *Journal of Materials Processing Technology* 124 (2002) 274–283. [https://doi.org/10.1016/S0924-0136\(02\)00070-5](https://doi.org/10.1016/S0924-0136(02)00070-5).
- [98] P. Ettmayer, Hardmetals and cermets, *Annual Review of Materials Science* 19 (1989) 145–164. <https://doi.org/10.1146/annurev.ms.19.080189.001045>.
- [99] H. Ida, Y. Iyori, N. Shima, Cermet alloy, Patent Number US4957548A, USA, 1990.

- [100] D. Mari, Cermets and hardmetals, in: K.H. Jürgen Buschow, M.C. Flemings, E.J. Kramer, P. Veyssi re, R.W. Cahn, B. Ilschner, S. Mahajan (Eds.), *Encyclopedia of Materials: Science and Technology*, Elsevier, Oxford, UK, 2016: pp. 1118–1122. <https://doi.org/10.1016/B978-0-12-803581-8.02365-1>.
- [101] W. Lengauer, F. Scagnetto, Ti (C, N)-based cermets: Critical review of achievements and recent developments, *Solid State Phenomena* 274 (2018) 53–100. <https://doi.org/10.4028/www.scientific.net/SSP.274.53>.
- [102] K.J. Brookes, *World Directory and Handbook of Hardmetals and Hard Materials*, 5th ed., International Carbide Data, London, UK, 1992.
- [103] E.D. Whitney, *Ceramic Cutting Tools: Materials, Development and Performance*, William Andrew, Park Ridge, New Jersey, USA, 1994.
- [104] D.W. Richerson, Industrial applications of ceramic matrix composites, in: A. Kelly, C. Zweben (Eds.), *Comprehensive Composite Materials*, Pergamon Elsevier, Oxford, UK, 2000: pp. 549–570. <https://doi.org/10.1016/B0-08-042993-9/00133-9>.
- [105] J. Zhao, The use of ceramic matrix composites for metal cutting applications, in: I.M. Low (Ed.), *Advances in Ceramic Matrix Composites*, 2nd ed., Woodhead Publishing, Cambridge, UK, 2014: pp. 537–569. <https://doi.org/10.1533/9780857098825.3.537>.
- [106] J. Garc a, V. Collado Cipr s, A. Blomqvist, B. Kaplan, Cemented carbide microstructures: a review, *International Journal of Refractory Metals and Hard Materials* 80 (2019) 40–68. <https://doi.org/10.1016/j.ijrmhm.2018.12.004>.
- [107] R. Kieffer, F. Benesovsky, *Hartmetalle*, Springer, Vienna, Austria, 1965. <https://doi.org/10.1007/978-3-7091-8127-0>.
- [108] P. Wild, A. Perdrix, S. Romazini, J.-J. Moulin, F. Pellet, Lung cancer mortality in a site producing hard metals, *Occupational and Environmental Medicine* 57 (2000) 568–573. <https://doi.org/10.1136/oem.57.8.568>.
- [109] B. Gries, L.J. Prakash, Acute inhalation toxicity by contact corrosion – the case of WC–Co, in: *Proceedings Euro PM2007-Hard Material 1*, The European Powder Metallurgy Association, Toulouse, France, 2007: pp. 189–196.
- [110] V. Richter, A. Potthoff, W. Pompe, M. Gelinsky, H. Ikonomidou, S. Bastian, K. Schirmer, S. Scholz, J. Hofinger, Evaluation of health risks of nano- and microparticles, *Powder Metallurgy* 51 (2008) 8–9. <https://doi.org/10.1179/174329008X286640>.
- [111] S. Bastian, W. Busch, D. K hnel, A. Springer, T. Meißner, R. Holke, S. Scholz, M. Iwe, W.

- Pompe, M. Gelinsky, Toxicity of tungsten carbide and cobalt-doped tungsten carbide nanoparticles in mammalian cells in vitro, *Environmental Health Perspectives* 117 (2009) 530–536. <https://doi.org/10.1289/ehp.0800121>.
- [112] P. Ettmayer, H. Kolaska, W. Lengauer, K. Dreyer, Ti(C,N) cermets - metallurgy and properties, *International Journal of Refractory Metals and Hard Materials* 13 (1995). [https://doi.org/10.1016/0263-4368\(95\)00027-G](https://doi.org/10.1016/0263-4368(95)00027-G).
- [113] A. Bellosi, R. Calzavarini, M.G. Faga, F. Monteverde, C. Zancolò, G.E. D'Errico, Characterisation and application of titanium carbonitride-based cutting tools, *Journal of Materials Processing Technology* 143–144 (2003) 527–532. [http://dx.doi.org/10.1016/S0924-0136\(03\)00339-X](http://dx.doi.org/10.1016/S0924-0136(03)00339-X).
- [114] H. Ida, K. Kojo, A. Negishi, Cermet alloy and process for its production, Patent Number US5149595A, USA, 1992.
- [115] K. Nishigaki, H. Doi, Effect of additional carbon content on mechanical and cutting properties of TiC_{0.7}N_{0.3}-15Ni-8Mo alloy, *Journal of the Japan Society of Powder and Powder Metallurgy* 27 (1980) 130–136.
- [116] M. Fukuhara, H. Mitani, Mechanisms of grain growth in Ti (C, N)–Ni sintered alloys, *Powder Metallurgy* 25 (1982) 62–68. <https://doi.org/10.1179/pom.1982.25.2.62>.
- [117] H. Suzuki, K. Hayashi, H. Matsubara, K. Tokumoto, High temperature strength of TiC-Mo₂C-Ni alloys containing nitrogen, *Journal of the Japan Society of Powder and Powder Metallurgy* 30 (1983) 106–111. <https://doi.org/10.2497/JJSPM.30.106>.
- [118] W.W. Gruss, Cermets, in: *Machining*, ASM International, Russell Township, Ohio, USA, 1989: pp. 90–97. <https://doi.org/10.31399/asm.hb.v16.a0002125>.
- [119] C.F. Davidson, M.B. Shirts, D.D. Harbuck, Production of titanium nitride, carbide, and carbonitride powders, Patent Number US4812301A, USA, 1989.
- [120] M. Leparoux, Y. Kihn, S. Paris, C. Schreuders, Microstructure analysis of RF plasma synthesized TiCN nanopowders, *International Journal of Refractory Metals and Hard Materials* 26 (2008) 277–285. <https://doi.org/10.1016/j.ijrmhm.2007.06.003>.
- [121] B. Wittmann, W.-D. Schubert, B. Lux, WC grain growth and grain growth inhibition in nickel and iron binder hardmetals, *International Journal of Refractory Metals and Hard Materials* 20 (2002) 51–60. [http://dx.doi.org/10.1016/S0263-4368\(01\)00070-1](http://dx.doi.org/10.1016/S0263-4368(01)00070-1).
- [122] E. Gordo, B. Gómez, E.M. Ruiz-Navas, J.M. Torralba, Influence of milling parameters on the manufacturing of Fe–TiCN composite powders, *Journal of Materials Processing*

- Technology 162–163 (2005) 59–64. <http://dx.doi.org/10.1016/j.jmatprotec.2005.02.154>.
- [123] L. Prakash, B. Gries, WC hardmetals with iron based binders, in: L. Sigl, P. Rödhammer, S. Wildner (Eds.), *Proceeding of the 17th International Plansee Seminar*, Reutte, Austria, 2009: pp. 1–13.
- [124] M. de Nicolás, H. Besharatloo, P. Alvaredo, J.J. Roa, L. Llanes, E. Gordo, Design of alternative binders for hard materials, *International Journal of Refractory Metals and Hard Materials* 87 (2020) 105089. <https://doi.org/10.1016/j.ijrmhm.2019.105089>.
- [125] A.P. Umanskii, Titanium carbonitride composite with iron—chromium binder, *Powder Metallurgy and Metal Ceramics* 40 (2001) 637–640. <https://doi.org/10.1023/A:1015248407568>.
- [126] H.-O. Andrén, Microstructures of cemented carbides, *Materials & Design* 22 (2001) 491–498. [https://doi.org/10.1016/S0261-3069\(01\)00006-1](https://doi.org/10.1016/S0261-3069(01)00006-1).
- [127] Z. Guo, J. Xiong, M. Yang, J. Wang, L. Sun, Y. Wu, J. Chen, S. Xiong, Microstructure and properties of Ti (C, N)–Mo₂C–Fe cermets, *International Journal of Refractory Metals and Hard Materials* 27 (2009) 781–783. <https://doi.org/10.1016/j.ijrmhm.2009.01.003>.
- [128] P. Alvaredo, M. Dios, B. Ferrari, E. Gordo, Understanding of wetting and solubility behavior of Fe binder on Ti (C, N) cermets, *Journal of Alloys and Compounds* 770 (2019) 17–25. <https://doi.org/10.1016/j.jallcom.2018.07.243>.
- [129] H. Besharatloo, M. de Nicolás, J.J. Roa, M. Dios, A. Mateo, B. Ferrari, E. Gordo, L. Llanes, Assessment of mechanical properties at microstructural length scale of Ti(C,N)–FeNi ceramic-metal composites by means of massive nanoindentation and statistical analysis, *Ceramics International* 45 (2019) 20202–20210. <https://doi.org/10.1016/j.ceramint.2019.06.292>.
- [130] J. Gurland, New scientific approaches to development of tool materials, *International Materials Reviews* 33 (1988) 151–166. <https://doi.org/10.1179/imr.1988.33.1.151>.
- [131] M. Dios, I. Kraleva, Z. González, P. Alvaredo, B. Ferrari, E. Gordo, R. Bermejo, Mechanical characterization of Ti (C, N)-based cermets fabricated through different colloidal processing routes, *Journal of Alloys and Compounds* 732 (2018) 806–817. <https://doi.org/10.1016/j.jallcom.2017.10.274>.
- [132] M. Dios, Z. González, P. Alvaredo, R. Bermejo, E. Gordo, B. Ferrari, Novel colloidal approach for the microstructural improvement in Ti (C, N)/FeNi cermets, *Journal of Alloys and Compounds* 724 (2017) 327–338. <https://doi.org/10.1016/j.jallcom.2017.07.034>.

- [133] P. Alvaredo, S.A. Tsipas, E. Gordo, Influence of carbon content on the sinterability of an FeCr matrix cermet reinforced with TiCN, *International Journal of Refractory Metals and Hard Materials* 36 (2013) 283–288. <https://doi.org/10.1016/j.ijrmhm.2012.10.007>.
- [134] P. Alvaredo, D. Mari, E. Gordo, High temperature transformations in a steel-TiCN cermet, *International Journal of Refractory Metals and Hard Materials* 41 (2013) 115–120. <https://doi.org/10.1016/j.ijrmhm.2013.02.012>.
- [135] Y. Zhao, Y. Zheng, W. Zhou, J. Zhang, Q. Huang, W. Xiong, Effect of carbon addition on the densification behavior, microstructure evolution and mechanical properties of Ti (C, N)-based cermets, *Ceramics International* 42 (2016) 5487–5496. <https://doi.org/10.1016/j.ceramint.2015.12.097>.
- [136] H.E. Exner, Physical and chemical nature of cemented carbides, *International Metals Reviews* 24 (1979) 149–173. <https://doi.org/10.1179/imtr.1979.24.1.149>.
- [137] B. Roebuck, E.A. Almond, Deformation and fracture processes and the physical metallurgy of WC–Co hardmetals, *International Materials Reviews* 33 (1988) 90–112. <https://doi.org/10.1179/imr.1988.33.1.90>.
- [138] J.M. Tarragó, D. Coureaux, Y. Torres, F. Wu, I. Al-Dawery, L. Llanes, Implementation of an effective time-saving two-stage methodology for microstructural characterization of cemented carbides, *International Journal of Refractory Metals and Hard Materials* 55 (2016) 80–86. <https://doi.org/10.1016/j.ijrmhm.2015.10.006>.
- [139] B. Roebuck, K.P. Mingard, H. Jones, E.G. Bennett, Aspects of the metrology of contiguity measurements in WC based hard materials, *International Journal of Refractory Metals and Hard Materials* 62 (2017) 161–169. <https://doi.org/10.1016/j.ijrmhm.2016.05.011>.
- [140] E. Jiménez-Piqué, M. Turon-Vinas, H. Chen, T. Trifonov, J. Fair, E. Tarrés, L. Llanes, Focused ion beam tomography of WC-Co cemented carbides, *International Journal of Refractory Metals and Hard Materials* 67 (2017) 9–17. <https://doi.org/10.1016/j.ijrmhm.2017.04.007>.
- [141] J. Gurland, P. Bardzil, Relation of strength, composition, and grain size of sintered WC-Co alloys, *Journal of The Minerals, Metals and Materials Society* 7 (1955) 311–315. <https://doi.org/10.1007/BF03377497>.
- [142] S.K. Bhaumik, G.S. Upadhyaya, M.L. Vaidya, Properties and microstructure of WC–TiC–Co and WC–TiC–MO₂C–Co (Ni) cemented carbides, *Materials Science and Technology* 7 (1991) 723–727. <https://doi.org/10.1179/mst.1991.7.8.723>.
- [143] G.E. Spriggs, A history of fine grained hardmetal, *International Journal of Refractory*

- Metals and Hard Materials 13 (1995) 241–255. [https://doi.org/10.1016/0263-4368\(95\)92671-6](https://doi.org/10.1016/0263-4368(95)92671-6).
- [144] A.M. Human, H.E. Exner, The relationship between electrochemical behaviour and in-service corrosion of WC based cemented carbides, *International Journal of Refractory Metals and Hard Materials* 15 (1997) 65–71. [https://doi.org/10.1016/S0263-4368\(96\)00014-5](https://doi.org/10.1016/S0263-4368(96)00014-5).
- [145] G.S. Upadhyaya, *Cemented Tungsten Carbides: Production, Properties and Testing*, Noyes Publications, New Jersey, USA, 1998.
- [146] F. Akhtar, I.S. Humail, S.J. Askari, J. Tian, G. Shiju, Effect of WC particle size on the microstructure, mechanical properties and fracture behavior of WC–(W, Ti, Ta) C–6 wt% Co cemented carbides, *International Journal of Refractory Metals and Hard Materials* 25 (2007) 405–410. <https://doi.org/10.1016/j.ijrmhm.2006.11.005>.
- [147] L.H. Zeferino, A.C. Buriti, S.N. Monteiro, A.G.P. da Silva, Determination of the WC grain size in hardmetals using stereology—A critical analysis, *International Journal of Refractory Metals and Hard Materials* 26 (2008) 367–371. <https://doi.org/10.1016/j.ijrmhm.2007.08.011>.
- [148] J.M. Tarragó Cifre, *Damage tolerance of cemented carbides under service-like conditions*, Ph.D. Thesis, Universitat Politècnica de Catalunya, Barcelona, Spain, 2016.
- [149] Sandvik new developments and applications, [http://www2.sandvik.com/SANDVIK/0130/Internet/SE03460.NSF/Index/4321fa9f60f7f648c1257%0A21300411c4c/\\$FILE/CCRD.pdf](http://www2.sandvik.com/SANDVIK/0130/Internet/SE03460.NSF/Index/4321fa9f60f7f648c1257%0A21300411c4c/$FILE/CCRD.pdf). (accessed October 30, 2020).
- [150] W. Horvath, W. Prantl, H. Stroißnigg, E.A. Werner, Microhardness and microstructure of austenite and ferrite in nitrogen alloyed duplex steels between 20 and 500°C, *Materials Science and Engineering A* 256 (1998) 227–236. [https://doi.org/10.1016/S0921-5093\(98\)00839-9](https://doi.org/10.1016/S0921-5093(98)00839-9).
- [151] S. Hertzman, J. Charles, On the effect of nitrogen on duplex stainless steels, *Revue de Métallurgie* 108 (2011) 413–425. <https://doi.org/10.1051/metal/2011071>.
- [152] A. Tahchieva, N. Llorca-Isern, J.-M. Cabrera, Duplex and superduplex stainless steels: microstructure and property evolution by surface modification processes, *Metals* 9 (2019) 347. <https://doi.org/10.3390/met9030347>.
- [153] R.W. Cahn, G. Ertl, J. Heydenreich, Microstructural characterization of materials: An assessment, in: F. Ernst, M. Rühle (Eds.), *High-Resolution Imaging and Spectrometry of Materials*, Springer, Berlin, Heidelberg, 2003: pp. 419–433. <https://doi.org/10.1007/978-3->

[662-07766-5_10](#).

- [154] R. Mondal, S.K. Bonagani, A. Lodh, T. Sharma, P. V Sivaprasad, G. Chai, V. Kain, I. Samajdar, Relating general and phase specific corrosion in a super duplex stainless steel with phase specific microstructure evolution, *Corrosion* 75 (2019) 1315–1326. <https://doi.org/10.5006/3091>.
- [155] ISO 4499-2: Metallographic determination of microstructure. Part 2: measurement of WC grain size, Geneva, Switzerland, 2008.
- [156] J.H. Schmitt, New trends in austenitic stainless steel flat products for structural applications, in: *Proceedings of the 4th European Stainless Steel Science and Market Congress*. (Vol. 2), Paris, France, 2002.
- [157] S. Zhou, W. Zhao, W. Xiong, H. Zhongguo, Thermodynamics of the formation of contiguity between ceramic grains and interface structures of Ti (C, N)-based cermets, *International Journal of Refractory Metals and Hard Materials* 27 (2009) 740–746. <https://doi.org/10.1016/j.ijrmhm.2008.12.005>.
- [158] H.-C. Lee, J. Gurland, Hardness and deformation of cemented tungsten carbide, *Materials Science and Engineering* 33 (1978) 125–133. [https://doi.org/10.1016/0025-5416\(78\)90163-5](https://doi.org/10.1016/0025-5416(78)90163-5).
- [159] S. Luyckx, A. Love, The dependence of the contiguity of WC on Co content and its independence from WC grain size in WC–Co alloys, *International Journal of Refractory Metals and Hard Materials* 24 (2006) 75–79. <https://doi.org/10.1016/j.ijrmhm.2005.04.012>.
- [160] A.V. Shatov, S.S. Ponomarev, S.A. Firstov, R. Warren, The contiguity of carbide crystals of different shapes in cemented carbides, *International Journal of Refractory Metals and Hard Materials* 24 (2006) 61–74. <https://doi.org/10.1016/j.ijrmhm.2005.03.003>.
- [161] B. Roebuck, E.G. Bennett, Phase size distribution in WC/Co hardmetal, *Metallography* 19 (1986) 27–47. [https://doi.org/10.1016/0026-0800\(86\)90005-4](https://doi.org/10.1016/0026-0800(86)90005-4).
- [162] K.K. Sobiya, Hard turning of martensitic AISI 440B stainless steel, Ph.D. Thesis, University of the Witwatersrand, Johannesburg, South Africa, 2015.
- [163] M.R. VanLandingham, Review of instrumented indentation, *Journal of Research of the National Institute of Standards and Technology* 108 (2003) 249. <https://doi.org/10.6028/jres.108.024>.
- [164] G. Oncins, J.J. Roa, E. Rayón, J. Díaz, M. Morales, M. Segarra, F. Sanz, Friction, hardness and elastic modulus determined by AFM-FS and nanoindentation techniques for advanced

- ceramics materials, in: J.J. Roa, M. Segarra Rubi (Eds.), *Recent Advances in Ceramic Materials Research*, Nova Science Publishers, New York, USA, 2013: pp. 215–249.
- [165] E. Broitman, Indentation hardness measurements at macro-, micro-, and nanoscale: a critical overview, *Tribology Letters* 65 (2017) 23. <https://doi.org/10.1007/s11249-016-0805-5>.
- [166] L. Malet, C.W. Sinclair, P. Jacques, S. Godet, Grain scale analysis of variant selection during the gamma-epsilon-alpha' phase transformation in austenitic steels, *Solid State Phenomena* 172 (2011) 84–89. <https://doi.org/10.4028/www.scientific.net/SSP.172-174.84>.
- [167] E. Jiménez-Piqué, Y. Gaillard, M. Anglada, Instrumented indentation of layered ceramic materials, *Key Engineering Materials* 333 (2007) 107–116. <https://doi.org/10.4028/www.scientific.net/KEM.333.107>.
- [168] J.J. Roa, X.G. Capdevila, M. Segarra, Mechanical characterization at nanometric scale of ceramic superconductor composites, in: H. Tovar, J. Fortier (Eds.), *Superconducting Magnets and Superconductivity: Research, Technology and Applications*, Nova Science Publishers, New York, USA, 2009: pp. 77–168.
- [169] ISO 14577-1: Metallic materials—Instrumented indentation test for hardness and materials parameters—Part 1: Test method, UK, 2002.
- [170] E.L. Tobolski, A. Fee, Macroindentation hardness testing., in: H. Kuhn, D. Medlin (Eds.), *Mechanical Testing and Evaluation*, Vol. 8, ASM International, Ohio, USA, 2000. <https://doi.org/10.31399/asm.hb.v08.a0003271>.
- [171] W.C. Oliver, G.M. Pharr, An improved technique for determining hardness and elastic modulus using load and displacement sensing indentation experiments, *Journal of Materials Research* 7 (1992) 1564–1583. <https://doi.org/10.1557/JMR.1992.1564>.
- [172] W.C. Oliver, G.M. Pharr, Measurement of hardness and elastic modulus by instrumented indentation: Advances in understanding and refinements to methodology, *Journal of Materials Research* 19 (2004) 3–20. <https://doi.org/10.1557/jmr.2004.19.1.3>.
- [173] M.F. Doerner, W.D. Nix, A method for interpreting the data from depth-sensing indentation instruments, *Journal of Materials Research* 1 (1986) 601–609. <https://doi.org/10.1557/JMR.1986.0601>.
- [174] I.N. Sneddon, The relation between load and penetration in the axisymmetric Boussinesq problem for a punch of arbitrary profile, *International Journal of Engineering Science* 3 (1965) 47–57. [https://doi.org/10.1016/0020-7225\(65\)90019-4](https://doi.org/10.1016/0020-7225(65)90019-4).

- [175] ISO 14577-2: Metallic materials — Instrumented indentation test for hardness and materials parameters — Part 2: Verification and calibration of testing machines, Switzerland, 2002.
- [176] J.J. Roa, X.G. Capdevila, M. Martínez, F. Espiell, M. Segarra, Nanohardness and Young's modulus of YBCO samples textured by the Bridgman technique, *Nanotechnology* 18 (2007) 385701. <https://doi.org/10.1088/0957-4484/18/38/385701>.
- [177] G.M. Pharr, E.G. Herbert, Y. Gao, The indentation size effect: a critical examination of experimental observations and mechanistic interpretations, *Annual Review of Materials Research* 40 (2010) 271–292. <https://doi.org/10.1146/annurev-matsci-070909-104456>.
- [178] W.D. Nix, H. Gao, Indentation size effects in crystalline materials: a law for strain gradient plasticity, *Journal of the Mechanics and Physics of Solids* 46 (1998) 411–425. [https://doi.org/10.1016/S0022-5096\(97\)00086-0](https://doi.org/10.1016/S0022-5096(97)00086-0).
- [179] A.C. Fischer-Cripps, Factors affecting nanoindentation test data, in: *Nanoindentation. Mechanical Engineering Series*, Springer, New York, USA, 2004: pp. 69–93. https://doi.org/10.1007/978-1-4757-5943-3_4.
- [180] A.C. Fischer-Cripps, *Handbook of Nanoindentation*, Fischer-Cripps Laboratories Pty Ltd, Forestville, Australia, 2013.
- [181] G. Constantinides, K.S. Ravi Chandran, F.J. Ulm, K.J. Van Vliet, Grid indentation analysis of composite microstructure and mechanics: Principles and validation, *Materials Science and Engineering A* 430 (2006) 189–202. <http://dx.doi.org/10.1016/j.msea.2006.05.125>.
- [182] G. Constantinides, F.-J. Ulm, The nanogranular nature of C–S–H, *Journal of the Mechanics and Physics of Solids* 55 (2007) 64–90. <https://doi.org/10.1016/j.jmps.2006.06.003>.
- [183] J.H. Westbrook, H. Conrad, *The Science of Hardness Testing and Its Research Applications*, American Society for Metals, Metals Park, Ohio, USA, 1973.
- [184] K. Durst, M. Göken, H. Vehoff, Finite element study for nanoindentation measurements on two-phase materials, *Journal of Materials Research* 19 (2004) 85–93. <https://doi.org/10.1557/jmr.2004.19.1.85>.
- [185] G.Z. Voyiadjis, R. Peters, Size effects in nanoindentation: an experimental and analytical study, *Acta Mechanica* 211 (2010) 131–153. <https://doi.org/10.1007/s00707-009-0222-z>.
- [186] M. Liu, C. Lu, K.A. Tieu, C.-T. Peng, C. Kong, A combined experimental-numerical approach for determining mechanical properties of aluminum subjects to nanoindentation, *Scientific Reports* 5 (2015) 15072. <https://doi.org/10.1038/srep15072>.

- [187] S. Kucharski, D. Jarzabek, A. Piątkowska, S. Woźniacka, Decrease of nano-hardness at ultra-low indentation depths in copper single crystal, *Experimental Mechanics* 56 (2016) 381–393. <https://doi.org/10.1007/s11340-015-0105-2>.
- [188] J.J. Roa, E. Jiménez-Piqué, C. Verge, J.M. Tarragó, A. Mateo, J. Fair, L. Llanes, Intrinsic hardness of constitutive phases in WC–Co composites: Nanoindentation testing, statistical analysis, WC crystal orientation effects and flow stress for the constrained metallic binder, *Journal of the European Ceramic Society* 35 (2015) 3419–3425. <https://doi.org/10.1016/j.jeurceramsoc.2015.04.021>.
- [189] P. Sudharshan Phani, W.C. Oliver, A critical assessment of the effect of indentation spacing on the measurement of hardness and modulus using instrumented indentation testing, *Materials & Design* 164 (2019) 107563. <https://doi.org/10.1016/j.matdes.2018.107563>.
- [190] G. Constantinides, F.-J. Ulm, K. Van Vliet, On the use of nanoindentation for cementitious materials, *Materials and Structures* 36 (2003) 191–196. <https://doi.org/10.1007/BF02479557>.
- [191] C.A. Schuh, Nanoindentation studies of materials, *Materials Today* 9 (2006) 32–40. [https://doi.org/10.1016/S1369-7021\(06\)71495-X](https://doi.org/10.1016/S1369-7021(06)71495-X).
- [192] M. de Nicolás, H. Besharatloo, J.M. Wheeler, M. de Dios, P. Alvaredo, J.J. Roa, B. Ferrari, L. Llanes, E. Gordo, Influence of the processing route on the properties of Ti (C, N)-Fe₁₅Ni cermets, *International Journal of Refractory Metals and Hard Materials* 87 (2020) 105046. <https://doi.org/10.1016/j.ijrmhm.2019.105046>.
- [193] J.A. Escribano, B. Ferrari, P. Alvaredo Olmos, E. Gordo Odériz, A.J. Sánchez-Herencia, Colloidal processing of Fe-based metalceramic composites with high content of ceramic reinforcement, *Boletín de La Sociedad Española de Cerámica y Vidrio* 52 (2013) 247–250. <https://doi.org/10.3989/cyv.312013>.
- [194] J.A. Escribano, J.L. García, P. Alvaredo, B. Ferrari, E. Gordo, A.J. Sánchez-Herencia, FGM stainless steel-Ti (C, N) cermets through colloidal processing, *International Journal of Refractory Metals and Hard Materials* 49 (2015) 143–152. <https://doi.org/10.1016/j.ijrmhm.2014.05.008>.
- [195] P. Parente, A.J. Sánchez-Herencia, M.J. Mesa-Galan, B. Ferrari, Functionalizing Ti-surfaces through the EPD of hydroxyapatite/nanoY₂O₃, *The Journal of Physical Chemistry B* 117 (2012) 1600–1607. <https://doi.org/10.1021/jp305176h>.
- [196] R.G. Neves, B. Ferrari, A.J. Sánchez-Herencia, E. Gordo, Colloidal approach for the design of Ti powders sinterable at low temperature, *Materials Letters* 107 (2013) 75–78. <https://doi.org/10.1016/j.matlet.2013.05.015>.

- [197] ASTM E 3-01: Standard practice for preparation of metallographic specimens, USA, 2001. <https://doi.org/10.1520/E0003-01>.
- [198] L. Reimer, Scanning Electron Microscopy: Physics of Image Formation and Microanalysis, Springer, Berlin, Germany, 1998. <https://doi.org/10.1007/978-3-540-38967-5>.
- [199] J.I. Goldstein, D.E. Newbury, J.R. Michael, N.W.M. Ritchie, J.H.J. Scott, D.C. Joy, Scanning Electron Microscopy and X-Ray Microanalysis, Springer, New York, USA, 2003. <https://doi.org/10.1007/978-1-4615-0215-9>.
- [200] R. Mehta, Interactions, imaging and spectra in SEM, in: V. Kazmiruk (Ed.), Scanning-Electron-Microscopy, IntechOpen, Moscow, Russia, 2012: pp. 17–30. <https://doi.org/10.5772/35586>.
- [201] F.J. Gil Mur, J.M. Manero Planella, Metalografía, Universitat Politècnica de Catalunya Iniciativa Digital Politècnica, Barcelona, Spain, 2005.
- [202] V.E. Cosslett, P. Duncumb, Micro-analysis by a flying-spot X-ray method, Nature 177 (1956) 1172–1173. <https://doi.org/10.1038/1771172b0>.
- [203] K.F.J. Heinrich, Electron Beam X-Ray Microanalysis, Van Nostrand Reinhold Company, California, USA, 1981.
- [204] C. Merlet, X. Llovet, F. Salvat, Measurements of the surface ionization in multilayered specimens, X-Ray Spectrometry: An International Journal 33 (2004) 376–386. <https://doi.org/10.1002/xrs.757>.
- [205] C. Merlet, X. Llovet, O. Dugne, S. Brémier, W. Van Renterghem, R. Restani, Virtual standard for wavelength-dispersive electron-probe microanalysis, Microchimica Acta 161 (2008) 427–432. <https://doi.org/10.1007/s00604-007-0856-2>.
- [206] Electron Probe Micro Analyzer, <https://www.jeol.co.jp/en/science/epma.html> (accessed October 20, 2020).
- [207] A.J. Schwartz, M. Kumar, B.L. Adams, D.P. Field, Electron Backscatter Diffraction in Materials Science, Springer, New York, USA, 2009. <https://doi.org/10.1007/978-0-387-88136-2>.
- [208] S. Swapp, Integrating Research and Education, Geochemical Instrumentation and Analysis, Electron Backscatter Diffraction (EBSD), https://serc.carleton.edu/msu_nanotech/methods/ebbsd.html (accessed October 10, 2020).
- [209] P.R. Munroe, The application of focused ion beam microscopy in the material sciences,

- Materials Characterization 60 (2009) 2–13. <https://doi.org/10.1016/j.matchar.2008.11.014>.
- [210] R. Wirth, Focused Ion Beam (FIB) combined with SEM and TEM: Advanced analytical tools for studies of chemical composition, microstructure and crystal structure in geomaterials on a nanometre scale, *Chemical Geology* 261 (2009) 217–229. <https://doi.org/10.1016/j.chemgeo.2008.05.019>.
- [211] J. Orloff, L.W. Swanson, M. Utlaut, Fundamental limits to imaging resolution for focused ion beams, *Journal of Vacuum Science & Technology B: Microelectronics and Nanometer Structures Processing, Measurement, and Phenomena* 14 (1996) 3759–3763. <https://doi.org/10.1116/1.588663>.
- [212] V. Castaldo, C.W. Hagen, B. Rieger, P. Kruit, Sputtering limits versus signal-to-noise limits in the observation of Sn balls in a Ga⁺ microscope, *Journal of Vacuum Science & Technology B: Microelectronics and Nanometer Structures Processing, Measurement, and Phenomena* 26 (2008) 2107–2115. <https://doi.org/10.1116/1.3013306>.
- [213] Scanning Electron Microscopy / Focuses Ion Beam, http://www.brucherseifer.com/html/sem_fib.html (accessed November 3, 2020).
- [214] D.K. Shetty, I.G. Wright, P.N. Mincer, A.H. Clauer, Indentation fracture of WC-Co cermets, *Journal of Materials Science* 20 (1985) 1873–1882. <https://doi.org/10.1007/BF00555296>.
- [215] P.O. Malta, B.L. Condé, R.F. Assumpção, D.B. Perasoli, D.C. Sicupira, D.B. Santos, Effect of annealing temperature on mechanical behavior, pitting resistance and grain boundary character of a 2304 lean duplex stainless steel, *Metallurgical and Materials Transactions A* 50 (2019) 2665–2677. <https://doi.org/10.1007/s11661-019-05193-1>.
- [216] M. Breda, K. Brunelli, F. Grazzi, A. Scherillo, I. Calliari, Effects of cold rolling and strain-induced martensite formation in a SAF 2205 duplex stainless steel, *Metallurgical and Materials Transactions A* 46 (2015) 577–586. <https://doi.org/10.1007/s11661-014-2646-x>.
- [217] C. Tromas, N. Ouabadi, V. Gauthier-Brunet, M. Jaouen, S. Dubois, Mechanical properties of nanolaminate Ti₃SnC₂ carbide determined by nanohardness cartography, *Journal of the American Ceramic Society* 93 (2010) 330–333. <https://doi.org/10.1111/j.1551-2916.2009.03412.x>.
- [218] A.M. Korsunsky, M.R. McGurk, S.J. Bull, T.F. Page, On the hardness of coated systems, *Surface and Coatings Technology* 99 (1998) 171–183. [https://doi.org/10.1016/S0257-8972\(97\)00522-7](https://doi.org/10.1016/S0257-8972(97)00522-7).
- [219] H. Sachdev, Influence of impurities on the morphology and Raman spectra of cubic boron

- nitride, *Diamond and Related Materials* 12 (2003) 1275–1286. [https://doi.org/10.1016/S0925-9635\(03\)00072-4](https://doi.org/10.1016/S0925-9635(03)00072-4).
- [220] H. Besharatloo, M. Carpio, J.-M. Cabrera, A.M. Mateo, G. Fargas, J.M. Wheeler, J.J. Roa, L. Llanes, Novel mechanical characterization of austenite and ferrite phases within duplex stainless steel, *Metals* 10 (2020) 1352. <https://doi.org/10.3390/met10101352>.
- [221] Y. Xiao, H. Besharatloo, B. Gan, X. Maeder, R. Spolenak, J.M. Wheeler, Combinatorial investigation of Al–Cu intermetallics using small-scale mechanical testing, *Journal of Alloys and Compounds* 822 (2020) 153536. <https://doi.org/10.1016/J.JALLCOM.2019.153536>.
- [222] H. Besharatloo, M. de Nicolás, J.M. Wheeler, A. Mateo, B. Ferrari, E. Gordo, L. Llanes, J.J. Roa, Carbon addition effects on microstructure and small-scale hardness for Ti(C,N)-FeNi cermets, *International Journal of Refractory Metals and Hard Materials* 85 (2019) 105064. <https://doi.org/https://doi.org/10.1016/j.ijrmhm.2019.105064>.
- [223] H. Besharatloo, S. Gordon, T. Rodriguez-Suarez, A. Can, W.C. Oliver, L. Llanes, J.J. Roa, Small-scale mechanical properties of constitutive phases within a polycrystalline cubic boron nitride composite, *Journal of the European Ceramic Society* 39 (2019) 5181–5189. <https://doi.org/10.1016/J.JEURCERAMSOC.2019.08.023>.
- [224] M.D. Uchic, D.M. Dimiduk, J.N. Florando, W.D. Nix, Sample dimensions influence strength and crystal plasticity, *Science* 305 (2004) 986–989. <https://doi.org/10.1126/science.1098993>.
- [225] D. Kiener, C. Motz, G. Dehm, Micro-compression testing: A critical discussion of experimental constraints, *Materials Science and Engineering A* 505 (2009) 79–87. <https://doi.org/10.1016/j.msea.2009.01.005>.
- [226] C.M. Byer, B. Li, B. Cao, K.T. Ramesh, Microcompression of single-crystal magnesium, *Scripta Materialia* 62 (2010) 536–539. <https://doi.org/10.1016/j.scriptamat.2009.12.017>.
- [227] E. Lilleodden, Microcompression study of Mg (0 0 0 1) single crystal, *Scripta Materialia* 62 (2010) 532–535. <https://doi.org/10.1016/j.scriptamat.2009.12.048>.
- [228] D.R.P. Singh, N. Chawla, G. Tang, Y.-L. Shen, Micropillar compression of Al/SiC nanolaminates, *Acta Materialia* 58 (2010) 6628–6636. <https://doi.org/10.1016/j.actamat.2010.08.025>.
- [229] P.R. Howie, S. Korte, W.J. Clegg, Fracture modes in micropillar compression of brittle crystals, *Journal of Materials Research* 27 (2012) 141–145. <https://doi.org/10.1557/jmr.2011.256>.

- [230] F. Iqbal, J. Ast, M. Göken, K. Durst, In situ micro-cantilever tests to study fracture properties of NiAl single crystals, *Acta Materialia* 60 (2012) 1193–1200. <https://doi.org/10.1016/j.actamat.2011.10.060>.
- [231] M. Sebastiani, K.E. Johanns, E.G. Herbert, G.M. Pharr, Measurement of fracture toughness by nanoindentation methods: Recent advances and future challenges, *Current Opinion in Solid State and Materials Science* 19 (2015) 324–333. <https://doi.org/10.1016/j.cossms.2015.04.003>.
- [232] M. Ghidelli, M. Sebastiani, K.E. Johanns, G.M. Pharr, Effects of indenter angle on micro-scale fracture toughness measurement by pillar splitting, *Journal of the American Ceramic Society* 100 (2017) 5731–5738. <https://doi.org/10.1111/jace.15093>.
- [233] J. Ast, M. Ghidelli, K. Durst, M. Göken, M. Sebastiani, A.M. Korsunsky, A review of experimental approaches to fracture toughness evaluation at the micro-scale, *Materials & Design* 173 (2019) 107762. <https://doi.org/10.1016/j.matdes.2019.107762>.